Quantum Phase Transitions in CoCl2 salts, and the Nature of the Co-existance of Magnetism and Superconductivity in Y9Co7 and La2-xSrxCuO4+y

Larsen, Jacob; Christensen, Niels Bech; Niedermayer, Christof; Vegge, Tejs

Publication date:
2013

Document Version
Publisher's PDF, also known as Version of record

Quantum Phase Transitions in $CoCl_2$ salts, and the Nature of the Co-existence of Magnetism and Superconductivity in Y_9Co_7 and $La_{2-x}Sr_xCuO_{4+y}$

Jacob Larsen

Technical University of Denmark
Institute of Physics
30-06-2013

Abstract

In this thesis I present two studies of magnetism. First, I present a study of a transverse field quantum phase transition in the quasi-Ising antiferromagnetic $CoCl_2$ salts. Second, I present various studies of phase separation between magnetic and superconducting regions, in the low temperature superconductor Y_9Co_7 and in high temperature superconductors with chemical formula $La_{2-x}Sr_xCuO_{4+y}$.

In the first part of this thesis Neutron scattering is used to study the quasi-Ising antiferromagnet $CoCl_2 \cdot 2D_2O$. As a consequence of crystal field and spin-orbit effects in the monoclinic crystal structure of $CoCl_2 \cdot 2D_2O$, its low-temperature magnetic properties can be considered to approximate an effective $S = 1/2$ model with anisotropic, primarily Ising-like, exchange interactions and anisotropic g-factors. The dominant interactions are ferromagnetic and couple nearest neighbor spins forming chains. Weaker interchain interactions give rise to commensurate antiferromagnetic order below $T_N = 17.2$K. Theory predicts that the spin wave excitation spectrum of Ising magnets softens as a magnetic field is applied transverse to the preferred spin direction. This has been observed in the three-dimensional dipolar coupled ferromagnet $LiHoF_4$ and in $CoNb_2O_6$, which like $CoCl_2 \cdot 2D_2O$ consists of weakly coupled ferromagnetic Ising-like chains. Comparing $CoCl_2 \cdot 2D_2O$ to $CoNb_2O_6$ one might expect some similarities in the excitation spectra. However, different ratios of interchain to intrachain interactions and different degrees of deviation from the ideal Ising spin Hamiltonian, can also be expected to modify the spin waves.

We provide evidence that the spin wave mode indeed softens at $\mu_0 H_c$, and spin excitations reappear at field larger than $\mu_0 H_c$. Our findings are compared with RPA theory that reaches excellent agreement with our data. These studies indicate that $CoCl_2 \cdot 2D_2O$ shares more characteristics with an anisotropic Heisenberg magnet in transverse field than the pure Ising model. We have also addressed the possibility to lower the critical field by chemically substitute NH_3 for H_2O in $CoCl_2$ salts, in order to search for optimal experimental conditions within a certain class of materials using density functional theory.

The second part of this thesis is subdivided into three separate studies, all focusing on phase separation in superconductors. In the first part I present a muon spin rotation study of the magnetic properties of Y_9Co_7 - an example of a system displaying evidence for weak itinerant ferromagnetism and low temperature i.e. phonon driven superconductivity. With the highest quality sample available, our results provide evidence that the sample phase separates on a length scale of more than 30Å. Phase separation on this length scale or larger is also observed in the superoxygenated Lanthanum based high-temperature superconductor $La_{2-x}Sr_xCuO_{4+y}$ which separates into an incommensurate magnetic phase similar to the so-called '1/8' stripe phase observed in other Lanthanum-based cuprate compounds such as $La_{1.88}Ba_{0.12}CuO_4$ and $La_{1.48}Nd_{0.4}Sr_{0.12}CuO_4$, and a superconducting phase similar to optimally doped $La_{2-x}Sr_xCuO_4$. We are able to

extract the magnetic transition temperature, the superconducting transitions temperature and respective volume fraction of the magnetic and superconducting regions. Using transverse field muon spin rotation, we present an analysis which is consistent with previously published results but in addition, we extract the penetration depth which allows for a direct comparison of the superconducting phase in these samples and with other superconductors. We find very similar values regardless of Strontium doping in $La_{2-x}Sr_xCuO_{4+y}$. Finally, we have combined zero field and transverse field muon spin rotation with neutron spin echo spectroscopy to study the spin freezing process in oxygen-stoichiometric $La_{1.88}Sr_{0.12}CuO_4$ which does not phase separate on a length scale visible to the muon spin rotation technique. In this compound the onset temperature of incommensurate magnetic order is dependent on the time scale of the experimental technique used to probe it. Using the ultra-high resolution of the spin echo technique, we present measurements of the quasi-elastic energy width of an incommensurate Bragg peak in $La_{1.88}Sr_{0.12}CuO_4$. Our results on $La_{1.88}Sr_{0.12}CuO_4$ illustrate the complementary aspects of the local probe of muon spin rotation and neutron scattering.

Abstract

I denne afhandling præsenterer jeg to studier over magnetismen. Først vil jeg fremlægge et studie af en kvante-faseovergang i Ising lignende antiferromagnetiske CoCl2 salte i transvers felt. Dernæst, præsenterer jeg forskellige undersøgelser af faseadskillelse mellem magnetiske og superledende områder i lav-temperatur superlederen Y9Co7 og høj-temperatur superledere med kemisk den formel LA2-xSrxCuO4+y.

I første del af denne afhandling bruges neutronspredning til at studere den Ising lignende antiferromagnet CoCl2o2D2O. Grundet krystal felt og spin-orbit kobling i den monokline CoCl2o2D2O krystalstruktur, kan de magnetiske egenskaber lav temperatur anses for en effektiv S = 1/2 model med anisotropisk, primært Ising-lignende, vekselvirkninger og anisotrope g-faktorer. De dominerende nærmeste-nabo vekselvirkninger er ferromagnetiske og danner kæder. Svagere inter-kæde vekselvirkninger giver anledning til kommensurabel antiferromagnetiske orden under TN = 17,2 K. Teori viser, at spin bølge ekscitations-spektret fra Ising magneter svækkes når et magnetfelt påføres på tværs af den foretrukne spin retning. Dette er blevet observeret i den tredimensionelle dipol-koblede ferromagnet LiHoF4 og i CoNb2O6, der ligesom CoCl2o2D2O består af svagt koblede ferromagnetiske Ising-lignende kæder. Sammenlignes CoCl2o2D2O med CoNb2O6 kunne man forvente visse ligheder i ekscitations-spektret. Dog må det anderledes forhold mellem interkæde til intrakæde vekselvirkninger og graden af afvigelse fra den ideelle Ising spin-Hamilton, forventes at ændre spin bølgerne. Vi giver bevis for, at spin bølge tilstanden faktisk svækkes helt ved Hc og at spin ekscitationer kommer igen ved felter højere end Hc. Vore resultater sammenlignes med RPA teori, der passer glimrende med vores data. Disse undersøgelser viser at CoCl2o2D2O deler flere karakteristika med en anisotropisk Heisenberg magnet i transvers felt end med den rene Ising model. Vi adresserer også muligheden for at sænke det kritiske felt ved kemisk substitution af NH3 i stedet for D2O i CoCl2 salte, og således søge efter optimale eksperimentelle betingelser inden for en bestemt klasse af materialer ved hjælp af tætheds-funktional teori.

Anden del af denne afhandling er opdelt i tre separate studier, der alle fokuserer på faseadskillelse i superledere. I den første del præsenterer jeg et muon spin-rotation studie af de magnetiske egenskaber af Y9Co7 - et eksempel på et system det udviser tegn på svage itinerant ferromagnetisme og lav-temperatur, dvs. fonon drevet, superledning. Med en prøve af den højeste tilgængelige kvalitet, giver vores resultater bevis for at prøven faseadskilles over en længdeskala på mere end 30Å. Faseadskillelse på denne længdeskala eller større er også observeret i den superoxygenated Lanthan baseret høj-temperatur superleder La2-xSrxCuO4+y der fordeler sig i en ikke-kommensurabel magnetisk fase der ligner den såkaldte '1/8' stribe fase observeret i andre Lanthan-baserede cuprate materialer såsom La1.88Ba0.12CuO4 og La1.48Nd0.4Sr0.12CuO4, og en superledende fase ligner optimalt doteret La2-xSrxCuO4. Vi er i stand til at udtrække den magnetiske overgangstemperatur, den superledende overgange temperatur og respektive volumenfraktion af de magnetiske og superledende områder. Ved

brug transvers felt muon spin rotation præsenterer vi en analyse, som er i overensstemmelse med tidligere offentliggjorte resultater, men derudover finder vi gennemtrængnings dybden, som giver mulighed for en direkte sammenligning af den superledende fase i disse prøver og med andre superledere. Vi finder meget sammenlignende værdier, uanset Strontium niveauet i La2-xSrxCuO4+y. Endelig har vi kombineret nul-felt og transvers felt muon spin rotation med neutron spin-ekko spektroskopi til at studere spin fryseprocessen i ilt-støkiometrisk La1.88Sr0.12CuO4 som ikke faseseparerer på en længdeskala synligt med muon spin rotations teknikken. I dette materiale, er temperaturen for en ikke-kommensurable magnetiske orden afhængig tidsopløsningen af den eksperimentelle teknik som anvendes til at undersøge det. Ved brug af den ultra-høje opløsning af spin-ekko teknikken, præsenterer vi målinger af den kvasi-elastiske energibredde af en ikke-kommensurable Bragg top i La1.88Sr0.12CuO4. Vores resultater på La1.88Sr0.12CuO4 belyser de komplementære aspekter mellem den lokale muon spin-rotation teknik og neutronspredning.

Contents

List of Figures

CHAPTER 1

Introduction

Today a major, and largely still unsolved, problem in physics is the working mechanism behind high temperature superconductivity. Always appearing in close proximity with magnetism in the phase diagram spanned by temperature and chemical hole or electron doping, many speculate if, and if so how, high temperature superconductivity and magnetism are intimately connected to each other in these materials.

In this two part thesis, I present the work I have done during my time as a PhD student.

In the first part, I present the results of neutron scattering investigations into the nature of a magnetic quantum phase transition in the quasi-Ising ferromagnetic chain. Quantum phase transitions have drawn much attention in recent years as increasingly more sophisticated theoretical model have emerged. This particular study will focus on similarities and differences when going from the world of isolated pure Ising chains and into world of real crystals with both intra chain- and inter chain interactions.

In the second part, I present the results of primarily muon spin rotation experiments of superconductors which in some way or another is connected by the question of phase separation i.e. if the superconductivity and the magnetism which are known to co-exist in these samples, does so on a microscopic or a macroscopic level.

Chapter 1: In this chapter I present a brief discussion of the fundamentals of magnetism and superconductivity.

Chapter 2: In this chapter I present the basics of neutron scattering technique.

Chapter 3: In this chapter I present my neutron scattering studies on $CoCl_2 \cdot 2D_2O$

Chapter 4: In this chapter I present density functional theory calculation on the chemical bond lengths in $CoCl_2 \cdot 2NH_3$

Chapter 5: In this chapter I present the muon spin rotation technique.

Chapter 6: In this chapter I present my studies on Y_9Co_7

Chapter 7: In this chapter I present my studies on $La_{2-x}Sr_xCuO_{4+y}$

Chapter 8: In this chapter I present my studies on $La_{2-x}Sr_xCuO_4$

In the final words of this introduction, I would like to express my gratitude to a number of people who have contributed to or assisted my work during my time as a student. First or all, my three thesis supervisors Niels B. Christensen, Tejs Vegge and Christof Niedermayer for all their invaluable help understanding the physics and methods presented in this thesis.

Others who have been involved in my numerous experiments include Sonja (The Munich Maneuver) Holm, Ane K. Baden, Sigrid S. Adsersen, Johannes Beil, Maria N. Gastiasoro, Anders Bakke, Jonas O. Birk, Gitte Stieper, Henrik Jacobsen, Linda Udby, Neda Nikseresht, Louise F. Frellsen, Morten Sales, Rasmus Toft-Petersen, Klaus Habicht, Klaus Kiefer, Duc Le, Skoulatos Markos, Thomas Keller, Andrew Walters, Astrid Schneidewind, Enrico Faulhaber, Mark Laver, Amy Poole, Oksana Zaharko, Lukas Keller, Christian Bernhard, Tomasz Klimczuks, Pamela Knupp, Georg Ehlers, Andrey Podlesnyak, Matthias Frontzek, Hubertus Luetkens, James Lord, Mark Telling Stéphane Rols, Russell Ewings, Martin v. Zimmermann, Markus Hücker, Johan Chang, Alex Holmes, Ted Forgan, Jens W. Andreasen, Bente Lebech, Peter K. Willendrup, Erik Knudsen and Niels Hessel Andersen.

For help getting acquainted with the nuts and bolts of DFT calculations I thank espcially Steen Lysgaard, Jakob Howalt and Peter Bjerre Jensen.

I thank Sara Eisenhardt for help correcting the written word and I thank the staff and students at the previous department of materials research at Risø DTU, National Laboratory for Sustainable Energy and the staff and students at the DTU physics for good company. Erik Brok, Jelena Jordanovic, Anders Wulff, Tim B. Van Driel, Christian Rein, Elisabeth T. Ulrikkeholm and Kreuff.

Additionally I would like to thank Kim Lefmann for drawing my attention to this fascinating research field in the first place and for many years of fruitful collaboration, for always being ready to help when it is needed and for answering all questions this author have presented to him over the years. I would also like to thank Jens Jensen for theoretical support and helpful discussions regarding the theory of magnetic systems and further I would like to thank Turi Schäffer for making her skills as a chemist available for me, and doing the tedious job of growing CoCl2.2D2O crystals. Finally, outside the workplace I am grateful for all my friends and my loving family for their great support through the years.

CHAPTER 2

Magnetism and Superconductivity

In this chapter we shall review the most important concepts of magnetism and superconductivity. Emphasizing what is known about the high temperature superconductors. In the first part, focusing on magnetism we introduce the basic theory and apply it directly to the hydrated salt $CoCl_2 \cdot 2D_2O$ as an example. $CoCl_2 \cdot 2D_2O$ is the subject of investigations in the later chapter 5 in connection with my studies of quantum phase transitions.

2.1 Magnetism

Magnetism is an intrinsic quantum mechanical concept. The Bohr-van Leeuwen theorem [2] concludes that within classical physics of circulating currents, it is not possible to obtain equilibrium magnetically ordered states in condensed matter. This, however, is in striking disagreement with our everyday experience, where permanent magnets are frequently used.

Magnetism arises from the uncompensated spin or orbital angular momentum of unpaired electrons. In quantum mechanics the size of a spin, $\mathbf{S}$ is quantized in units of $\hbar$ and the total length of the spin is calculated in the basis states $|S, m_S\rangle$ by the eigenvalue equation $\mathbf{S}^2 |S, m_S\rangle = S(S+1) |S, m_S\rangle$ where S is either an integer or a half integer and the magnetic quantum number m_S ranges from $-S$ to $+S$. Electrons are spin half particles, $S = \frac{1}{2}$. Similar to the quantized orbital angular momentum, the three components of the spin $\mathbf{S} = (S_x, S_y, S_z)$ may not be simultaneously well defined. The operator S_z may be specified by the eigenvalue equation $S_z |S, m_S\rangle = m_S |S, m_S\rangle$ at the expense of precise knowledge of the eigenvalues S_x and S_y. Instead, the ladder operators $S_x = S_x + iS_y$ and $S_y = S_x + iS_y$, which in themselves do not correspond to any observable quantity, are introduced to from a complete theory.

Interacting electrons on adjacent ions in a solid form a very challenging many-body

problem in theoretical physics. However, in the limit of localized spins [3], many useful theoretical predictions can be made to support the vast amount of experimental data taken over the years. The concept of an exchange interaction between electrons can be illustrated nicely with the isolated spin-dimer. This the simplest non-trivial spin system, consisting of only two spins located close enough to each other for their wave function to have non-vanishing overlap integral [2]. Consider the exchange Hamiltonian $\mathcal{H} = \mathcal{J}\mathbf{S}_1 \cdot \mathbf{S}_2$. According to the rule of combining quantized angular momenta, the four possible dimer states are

$$S_1 + S_2 \leq S \leq |S_1 - S_2| = \begin{cases} S = 0 & \frac{1}{\sqrt{2}}\left(|\uparrow\downarrow\rangle - |\downarrow\uparrow\rangle\right) \\ S = 1 & \begin{cases} |\uparrow\uparrow\rangle \\ \frac{1}{\sqrt{2}}\left(|\uparrow\downarrow\rangle + |\downarrow\uparrow\rangle\right) \\ |\downarrow\downarrow\rangle \end{cases} \end{cases}$$

The energy of the singlet state with $S = 0$ is $-3\mathcal{J}/4$, which in this case is the true ground state of the dimer. The triplet with $S = 1$ has the energy $\mathcal{J}/4$. The separation of the singlet ground state and the triplet excited states is exactly $\mathcal{J}$. The sign of $\mathcal{J}$ thus determines how the two spins orientate with respect to each other.

In this short reviewed the quantum mechanics of quantized spin, focusing on the special case of the electron which is an $S = 1/2$ particle. Ions with unpaired electrons are at the heart of magnetism in condensed matter physics.

2.1.1 Magnetic Ions in Condensed Matter

The most profound quantum effects are observed in spin half systems. Like the example mentioned above, as the elementary building blocks were just two spins with $S = 1/2$. The situation is less straight-forward in condensed matter where an assembly of many interacting spins must be considered. An isolated magnetic ion is described by states that are mixtures of the single particle states of the individual electrons. The total degeneracy of available single particle states in an ion with spin S and orbital angular momentum L is $(2L + 1) \times (2S + 1)$. Out of this manifold of states the ground state can often be found from F. Hund's empirical rules [2]

1. The electronic spin of the combined system arrange to maximize S.
2. The orbital angular momenta of the combined system arrange to maximize L.
3. The total angular momentum is given by $J = |L - S|$ if the shell is less than half filled and $J = |L + S|$ if it is more than half filled.

Here the last rule is due to the non-vanishing contribution from the spin-orbit coupling, $\mathcal{H} = \lambda\mathbf{S} \cdot \mathbf{L}$.

In the later chapter we will focus on Cobalt salts. Therefore we now discuss Co as an example of the above. The electronic structure of Co is $[\mathrm{Ar}]4\mathrm{s}^2 3\mathrm{d}^7$, and the predicted ground state of Co^{2+} has $S = 3/2$, $L = 3$ and $J = 9/2$ and an ordered moment of $g\mu_B\sqrt{J\left(J+1\right)} = 6.6\mu_B$, a value which is larger than what is typically found in

experiments. This simple picture of isolated ions is thus not sufficient for a successful description of magnetism in condensed matter. The electrostatic environment of a magnetic ion from the surrounding ligands must also be included. This is known as the crystal field, $V(\mathbf{r}) = e\int \mathrm{d}\mathbf{r}' \frac{\rho(\mathbf{r}')}{|\mathbf{r}-\mathbf{r}'|}$, where $\rho(\mathbf{r}')$ is the charge density of the surrounding electrons. The crystal field Hamiltonian, $\mathcal{H}_{\mathrm{cf}}$, may be formulated is terms the so-called Steven's operators $\mathcal{O}_l^m(J_z, J_\pm)$ [4, 5, 6, 7, 8]

$$\mathcal{H}_{\mathrm{cf}} = \sum_l \sum_{m=-l}^{l} B_l^m \mathcal{O}_l^m(J_z, J_\pm) \tag{2.1}$$

where $l = 2, 4, 6, ...$ should be chosen to reflect the symmetry of the lattice and the ion-ligand complex coordination.

If the spin-orbit coupling is large compared to the crystal field, which is the case for the rare earth materials, $J = L + S$ is a good quantum number with well defined states and the true value of J can be calculated from Hund's third rule. But in the transition metals the spin-orbit coupling is small compared to the crystal field, and the effect known as orbital quenching may occur. Orbital quenching means that J no longer is a good quantum number, because the ground states matrix elements of L are smaller then expected from Hund's rules, and sometimes zero. Orbital quenching is a direct consequence of the broken rotational symmetry induced by the crystal field, and that fact that the crystal field, as given by 2.1, is a real-valued function (see ref [2]). In many cases the spin-orbit coupling is, however, not completely negligible and stats with non-zero L are mixed into the ground state. The result is a partially quenched state.

2.1.2 Magnetic ground states and excitations

The all-important consequence of the quantum many-body problem in the emergence of quantum ground states with no classical analogues. This is illustrated by the dimer example in the first section. Here, the ground state is a superposition of antiferromagnetic spin arrangements, the so-called Néel state. This can be generalized to magnetic ions in condensed matter, where the ions are arranged in periodic lattices. The magnetic ground state is always the spin arrangement which minimizes the total (free) energy of all the interacting spins. Assuming an isotropic exchange energy the total energy is given by the Heisenberg Hamiltonian

$$\mathcal{H} = -\mathcal{J}\sum_{i\neq j} \mathbf{S}_i \cdot \mathbf{S}_j. \tag{2.2}$$

The sum is typically performed over nearest neighbor spins. However, also the next nearest, $\mathcal{J}_{\mathrm{nn}}$, and even next-next nearest, $\mathcal{J}_{\mathrm{nnn}}$, neighbors can have observable consequences. In many real crystals the magnetic ground state is not simply ferromagnetic or antiferromagnetic in all direction. In addition, the exchange energy is generally not isotropic but a second rank tensor with anisotropic $\mathcal{J}$-values along the diagonal and

occasionally even off diagonal elements, see e.g. [4]. Depending on the crystal structure the resulting spin system can have reduced spatial dimensionality.

The chemical bond lengths between the magnetic ions and interstitial ligands as well as the bond angle form a network of so-called superexchange paths, hereby giving which spins that may interact strongly with each other. In general it is complicated to work out exactly how the super exchange give rise to the different exchange energies, but the (semi) empirical Goodenough-Kanamori rules [9, 10, 11, 12, 13] gives some qualitative insight into what the nature of the result will be, see figure 2.1.

The Goodenough-Kanamori rules are usually formulated as follows (1) There is strong antiferromagnetic exchange interaction if the unfilled orbital of two magnetic ions overlap with an empty or filled orbital of the interstitial ligand at an angle close to 180° (See figure 2.1) and (2) There is a weak ferromagnetic exchange interaction if the half-filled orbital of two magnetic ions overlap with an empty or filled orbital of the interstitial ligand at an angle close to 90° (See figure 2.1). The super exchange is responsible for most of the magnetic interactions in magnetic insulators.

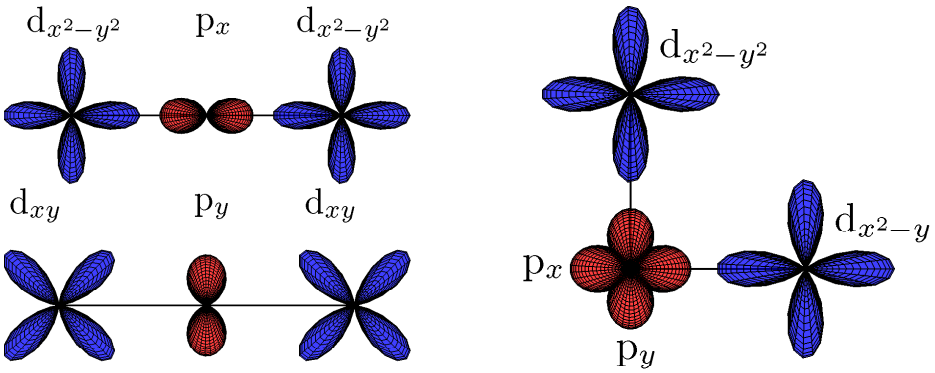

Figure 2.1: ***Left:*** *Examples where an antiferromagnetic interaction is expected from the Goodenough-Kanamori rules.* ***Right:*** *An examples where a ferromagnetic interaction is expected from the Goodenough-Kanamori rules.*

The Heisenberg Hamiltonian (2.2) with a three dimensional spin $\mathbf{S}$ mentioned above is, however, not always the case. The spin can have an effective reduced dimension. In the case where only the S^z operator is relevant, the exchange Hamiltonian takes the form

$$\mathcal{H} = -\mathcal{J} \sum_{i \neq j} S_i^z S_j^z \tag{2.3}$$

which is known as the Ising Hamiltonian. Depending on the ground state, which is determined by the crystal field and the spin-orbit coupling, magnetic systems might approximate this Hamiltonian. Consider the extreme case where the crystal field is dominated by an $\mathcal{O}_2^0$ type term, $\mathcal{H} = -\mathcal{J} \sum_{i \neq j} \mathbf{S}_i \cdot \mathbf{S}_j - D \sum_i (S_i^z)^2$ with a large D.

The ground state is a doublet, which is separated from the first excited state by the energy gap Δ. If $k_BT << \Delta$ only the ground state is populated and the resulting magnetic ion can be described as an effective $S = 1/2$ Ising model.

2.1.3 Magnetic Phase Transitions

The most fundamental physical process related to all materials is the phase transition, where a symmetry of the system is changed concomitant to a new energetically favorable ground state. Materials have very complicated phase diagrams where parameters such as chemical composition, pressure and temperature from a manifold of different ground states/phases of solids, liquids and gases. The set of parameters where a phase transition occurs is called the critical point. The magnetic ground state is also the result of a phase transition.

L. Landau constructed a simple mathematical theory of exactly this type of phase transitions in 1937 [2]. Within Landaus theory the free energy functional is a polynomial function of a temperature dependent scalar field, the so-called order parameter. The prefactors to the different powers of the order parameter is determined by the symmetries of the emerging ordered ground states.

Quantum mechanical fluctuations exists in the magnetic ground state. The one-dimensional Heisenberg antiferromagnet with $S = 1/2$ is an example where these fluctuation prevent long range order at $T = 0$ entirely. The so-called classical phase transitions are driven by thermal fluctuations which requires a finite temperature. However, many systems also show phase transitions at $T = 0$. Instead the transition is driven by some non-thermal parameter e.g. pressure, chemical doping or magnetic field which control the strength of the zero point fluctuations which are always present due to Heisenberg's uncertainty principle, $\left\langle (A - \langle A \rangle)^2 \right\rangle \left\langle (B - \langle B \rangle)^2 \right\rangle \geq \frac{1}{4} \left| \langle [A, B] \rangle \right|^2$ where $[A, B]$ is the commutator between the two quantum mechanical operators A and B. Such a transition is called a quantum phase transition (QPT) and the point in parameter space where it occurs is called the quantum critical point (QCP). To understand how a QPT may occur [14], consider a Hamiltonian which varies as a function of some non-thermal parameter g which couples to a conserved quantity in the Hamiltonian $\mathcal{H} = \mathcal{H}_0 + g\mathcal{H}_1$. In this case $\mathcal{H}_0$ and $\mathcal{H}_1$ can be diagonalized simultaneously and the resulting eigenstates must themselves be independent of g. However, the eigenfunction of $\mathcal{H}$ will depend on g, then there can be a value $g = g_C$ where a level crossing happens and the first excited state becomes the new ground state. Quantum critical behavior is often associated with a typical energy scale which is the energy gap Δ between the ground state and the first excited state, $\Delta \propto \xi^z$, and $\xi \propto (g - g_C)^{-\nu}$ in analogy with the classical phase transitions.

The simplest realization of a non-trivial QPT mechanism is the $S = 1/2$ one-dimensional Ising model/Ising chain in a transverse field (TFIM)

$$\mathcal{H} = -J \sum_i \left[S_i^z S_{i+1}^z + g S_i^x \right]. \tag{2.4}$$

The constant $J > 0$ determines the energy scale of the system and favors ferromagnetic

alignment of the spins. The $g > 0$ is the tuning parameter that eventually will cause the QPT. notice that g enters the Hamiltonian in the same way as an applied magnetic field in in the Zeeman Hamiltonian. For calculating purposes the Ising chain has lattice constant a and we assume cyclic boundary conditions.

Assuming now $T = 0$, in the limit $g \to 0$ the first term in (2.4) dominates and the ground state is given by either $|0\rangle_{g\to 0} = \prod_i |\uparrow\rangle_i$ or $\prod_i |\downarrow\rangle_i$. At any finite temperature entropy prohibits order in the Ising chain. Consider again the free energy $F = U - TS$. The first excited state create only one domain wall and flips the whole remaining segment of the chain. The energy cost of creating one domain wall in the chain is $U = J/2$. Because the energy cost is independent of the number of spin flipped after the domain wall, the number of different configurations i.e positions on the chain where the domain wall can reside is $N - 1$ where N is the number lattice sites in the chain. The probability distribution p_i which maximizes the entropy $S = -\sum_i p_i \ln(p_i)$ follows directly from the Lagrange multiplier method, we find $p_i = 1/w$ where w is the number of different configurations and $S = \ln(w)$. The free energy $F = J/2 - T\ln(N-1) < 0$ for $T > 0$ in the limit $N \to \infty$. This is a special case of the Mermin-Wagner theorem, which was proven in 1966 by D. Mermin and and H. Wagner [15, 16, 17]. This theorem states that no long range magnetic order exists at non-zero temperature in one- and two-dimensional Heisenberg systems with finite exchange interactions.

Turning on g, the second term of (2.4), $\mathcal{H} = g\sum_i S_i^x = g/2\sum_i \left(S_i^+ + S_i^-\right)$, induces spin flips in the chain. In the limit $g \to \infty$, the entire chain is polarized along the direction of the field and the ground state is given by $|0\rangle_{g\to\infty} = \prod_i |\rightarrow\rangle_i$ where $|\rightarrow\rangle_i = \frac{1}{\sqrt{2}}(|\uparrow\rangle_i + |\downarrow\rangle_i)$. In this polarized phase the elementary excitations are single spin flips. The excitation spectrum of the ideal $S = 1/2$ Ising chain in a transverse field should not be interpreted as bosonic spin wave but rather spinless fermions hopping between lattice sites. The Hamiltonian (2.4) may be transformed into fermion creation- ($\mathbf{c}_i^\dagger$) and annihilation ($\mathbf{c}_i$) operators through the Jordan-Wigner transformation [18, 19, 20]. The final diagonal form of (2.4) is

$$\mathcal{H} = \sum_{\mathbf{q}} \hbar\omega_{\mathbf{q}} \left[\gamma_{\mathbf{q}}^\dagger \gamma_{\mathbf{q}} - \frac{1}{2}\right] \tag{2.5}$$

where

$$\hbar\omega_{\mathbf{q}} = 2J\sqrt{1 + g^2 - 2g\cos(\mathbf{q}\cdot\mathbf{a})}. \tag{2.6}$$

The dispersion (2.6) satisfies $\hbar\omega_{\mathbf{q}} \geq 0$ for all q. Hence the ground state of the Hamiltonian (2.5) corresponds to a state with no quasi particles and zero point energy $-\frac{1}{2}\sum_{\mathbf{q}} \hbar\omega_{\mathbf{q}}$. The minimal quasi particle energy gap at $q = 0$ equals $\Delta = \hbar\omega_{\mathbf{q}=0} = 2J|1-g|$, see figure 2.2, leading to a gap closing at $g_C = 1$, see figure 2.3. Below g_C the system is dominated by the exchange energy and has long range magnetic order. Above g_C the system is in a polarized state but no longer dominated by the exchange energy. This state is often called a quantum paramagnet. As argued above the one-dimensional TFIM have $\Delta \propto |1-g|$ i.e. $z\nu = 1$. The critical exponent of the magnetization $m = (1-g)^\beta$ was calculated by R. Elliott, P. Pfeuty and C. Wood in

[21]. They find $\beta = 1/8$. These values of β and $z\nu$ are equivalent with those found by L. Onsager in 1949 for a classical magnetic phase transition in the two-dimensional Ising model, see e.g. [22]. In general, the universality class of a $d+1$-dimensional magnetic phase transition from classical statistical mechanics at finite temperature can be mapped onto a d-dimensional quantum phase transition [23, 24, 14].

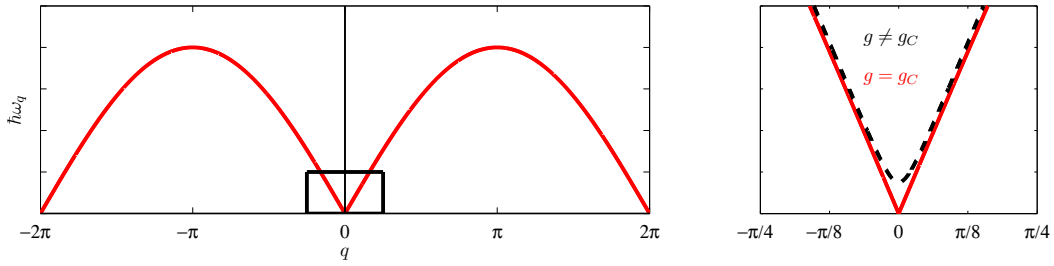

Figure 2.2: ***Left:*** *The dispersion relation of the Transverse field Ising model using* $g = g_C$. ***Right:*** *the gap minimum at* $q = 0$ *for* $g = g_c$ *and* $g \neq g_c$.

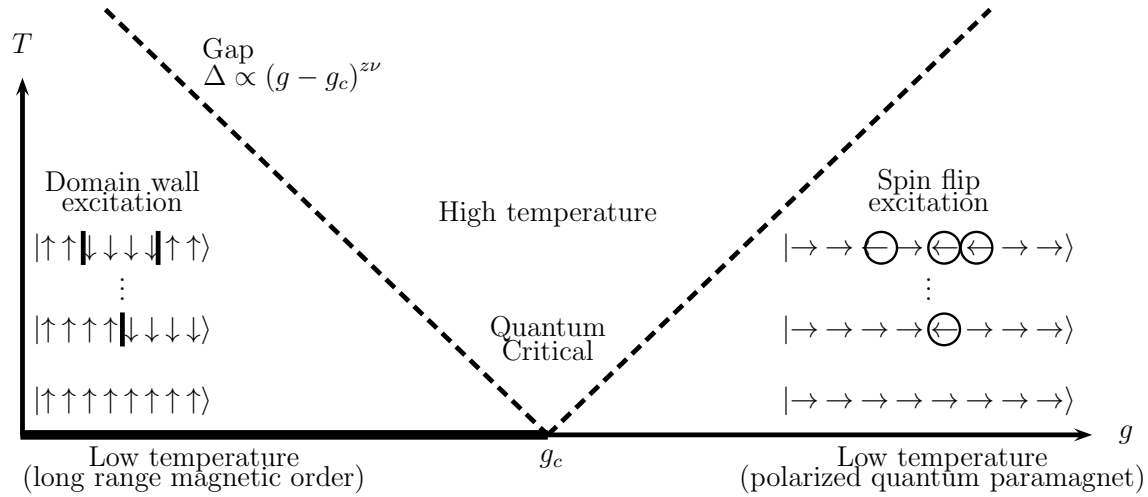

Figure 2.3: *Phase diagram of the one-dimensional TFIM (2.4) as a function of the coupling* g *and temperature* T. *There is a QPT at* $T = 0$, $g = g_c$ *with exponents* $z = 1$ *and* $\nu = 1$. *Magnetic long range order* $m \neq 0$ *exists only for* $T = 0$, $g < g_c$ *and the elementary excitations are domain walls. The ground state for* $g > g_c$ *is a quantum paramagnet which is fully polarized parallel to the applied field and the excitations are spin flips. There is an energy gap above the ground state for all* $g \neq g_c$.

2.2 Superconductivity

In this section we introduce the basic idea of superconductivity i.e. the state where matter loses all electrical resistivity. In a superconductor the electrons pair up into so-called Cooper pairs which constitute bosonic particles instead of a fermion and a gap opens in the band structure, see e.g. section 2.4.

The term 'low temperature superconductor' refers here to materials which does not fall under the same category as high temperature superconductors, introduced later in section 2.5. In some low temperature superconductors, then Cooper pairing mechanism is well understood i.e. those driven by phonon's, to be described in section 2.4. The mechanism of high temperature superconductors, however, is still a highly debated topic.

Becoming a superconductor has profound consequences for the thermodynamics and the electrodynamics of such materials. Superconductors are interesting in themselves from a purely academic point of view, but also as vital part of many already successful technologies in science and medicine and some technologies still in their infancy, like superconducting tapes and wires. In this thesis I focus on the coexistence between superconductivity and magnetism, a state of matter which is primarily found in the high temperature superconductors and a few low temperature superconductors . Many books dealing with solid state physics also deal with superconductivity, see e.g. [25, 26] or these books only on superconductivity [27, 28]. This chapter is largely based on the latter.

It was discovered by the laboratory team of K. Onnes in Leiden in 1911, only three year after their first successful liquefaction of Helium, that Mercury lost all electrical resistance below a critical temperature $T_c = 4.2\text{K}$ [29]. At the time, the electrical resistance ρ of a metal was expected to saturate below some temperature, on a finite value determined by the density of impurities and lattice imperfections. Mercury was therefore the ideal choice of material when investigating the electrical properties at low temperatures, owning to its low melting point, Mercury is a liquid at ambient conditions and can be purified by the distillation process. It was therefore a great mystery when superconductivity appeared, and it even turned out that superconductivity was a common feature of metals throughout the periodic system.

Following [25, 26], if a material is an insulator, the band structure has an energy gap ϵ_{gap}, between the highest filled band below the Fermi level ϵ_{Fermi} (valance band) and the lowest empty band above the Fermi level (conduction band), which is so large that the thermal fluctuations can not, unassisted, excite electrons into the conduction band. A filled band does not conduct current because there are no empty states below the Fermi level, and the Pauli principle forbids two electrons to occupy the same quantum state. The probability to excite en electron into the conduction band is proportional to $\exp\left(-\epsilon_{\text{gap}}/k_B T\right)$ and the electrical resistivity becomes huge at low temperature, see figure 2.4. On the other hand, in a metal, the band structure has an unfilled band with unoccupied states at low temperature. The famous Ohms law, $\mathbf{J} = \sigma\mathbf{E}$, is known to describe a current $\mathbf{J}$ caused by an electric field $\mathbf{E}$ in metals very well. The conductivity, $\sigma = 1/\rho$, is given by $ne^2\tau/m_e$ where e and m_e are the

electron charge and mass respectively and τ is a phenomenological parameter which is given as the time between electron scattering events. n is the density of electrons in the conduction band. The electron moves through the metal in Bloch waves [25]

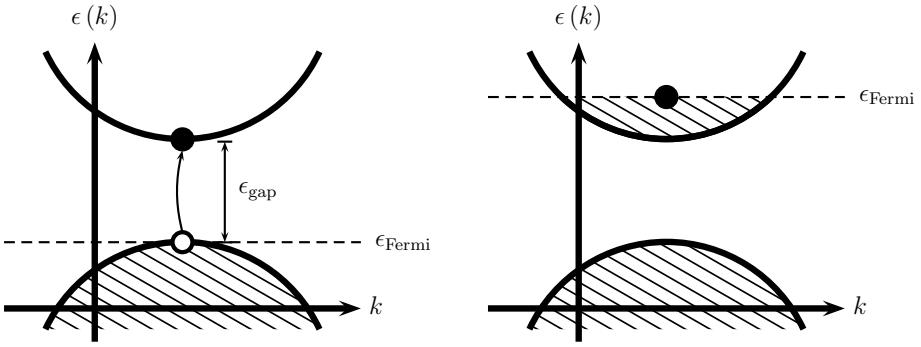

Figure 2.4: *Simplified picture of band structure.* ***Left:*** *The typical semiconductor or insulator. The highest band below the Fermi level is filled and the lowest band above the Fermi level is empty. They are separated by ϵ_{gap}.* ***Right:*** *The typical metal, where the conduction band is partially filled.*

and does as such not scatter from the lattice ions. However, lattice imperfections and impurities are expected to contribute the temperature independent ρ_0 to the resistivity at $T = 0$, electron-phonon scattering (T^{-5}) and electron-electron scattering (T^{-2}) also contributes at finite temperature. A material which could be cleaned completely of impurities and lattice imperfections would be a perfect conductor in the sense that at $T = 0$ the resistivity would be zero even without superconductivity. However, the critical temperature for superconductivity is found to be strictly non-zero. In conclusion, superconductivity with $\rho = 0$ at $T_c > 0$ can not be explained from simple energy band theory and phonon scattering alone.

Much of the theory for superconductors is based on phenomenological models based directly on observations. In the following section, I present some aspects of these, which are important for my muon spin rotation data analysis in the later chapter 7 - 10. We are going to introduce type-I and type-II superconductors and to introduce the London penetration depth and superconducting coherence length which are material-dependent length-scales characterizing the superconductors.

2.3 Electrodynamics of Superconductors

Many years after the first observation of superconductivity, in 1933, W. Meissner and R. Ochsenfeld [30, 25] reported another defining property of superconductors. Below T_c a superconductor develops perfect diamagnetism with $\chi = -1$ and expels all magnetic field lines from the interior of the superconductor, see figure 2.5. This in known as the Meissner effect. A metal, even assuming it to be a perfect conductor, does not expel flux in this manner. Superconductivity was evidently a new phase in condensed

matter characterized by $\mathbf{E} = 0$ (zero resistivity with a finite current) and $\mathbf{B} = 0$ (Meissner effect) below a critical temperature T_c. In 1934, shortly after the discovery of the Meissner effect, F. London and H. London [31, 25] published a theory for the electrodynamics of the superconducting phase. The London theory build on the two fluid model put fourth by C. Gorter and H. Casimir [32, 33]. In the two fluid model only a fraction n_s of the total number of electrons n conducts resistance free currents in the superconducting phase, the remaining fraction $n - n_s$ is assumed to constitute an 'electron fluid' similar to normal metals. The main achievement of the London's was to derive the so-called London equation $\boldsymbol{\nabla} \times \mathbf{J} = -\frac{n_s e^2}{m_e c}\mathbf{B}$ which was consistent with the observations. A constant magnetic field is not a solution to the London equation unless it is zero. Instead a magnetic field inside a superconductor is predicted to decay away within a thin layer of thickness λ of the surface according to

$$\boldsymbol{\nabla}^2\mathbf{B} - \mathbf{B}/\lambda \;=\; 0 \tag{2.7}$$

where $\lambda = \sqrt{m_e c^2/4\pi n_s e^2}$ is known as the London penetration depth. London theory still provides a very successful and useful approach to many applications of superconductivity, and the London penetration depth is one of the fundamental parameters used to characterize superconductors. However, it does not in itself give any insight into the microscopic mechanism which drives a material to become a superconductor.

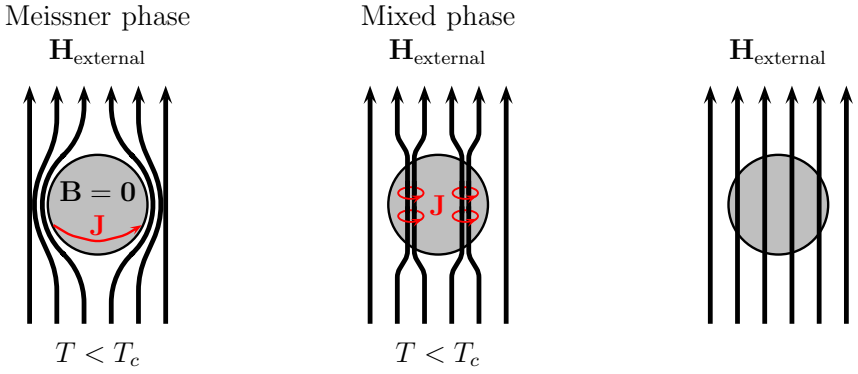

Figure 2.5: ***Left:*** *A type I superconductor in an external field. The magnetic field is expelled below T_c.* ***Middle:*** *A type II superconductor in an external field. For $H_{c1} < H < H_{c2}$ magnetic flux is allowed to penetrate the sample through vortices.* ***Right:*** *A non-superconducting material in an external field.*

In 1950 V. Ginzburg and L. Landau formulated a different theory focusing on the thermodynamics of the superconducting phase [25, 33]. This theory assumes the existence of an order parameter, which in the case of a superconductor is the density of Cooper pairs, n_s, which is zero above T_c. Building on the idea originally put forth by the London's the superconducting electron density is described in terms of a complex wave function $\psi(\mathbf{r}) = \sqrt{n_s(\mathbf{r})}\exp(-i\phi(\mathbf{r}))$, where $|\psi(\mathbf{r})|^2 = n_s$. The free energy

functional is given by an expansion in powers of $|\psi(\mathbf{r})|$

$$F - F_0 = \int \frac{\mathrm{d}\mathbf{r}^3}{V} \left[\frac{1}{2m} \left| \left(i\hbar \boldsymbol{\nabla} + \frac{q}{c} \mathbf{A}(\mathbf{r}) \right) \psi(\mathbf{r}) \right|^2 + A(T) |\psi(\mathbf{r})|^2 + \frac{B(T)}{2} |\psi(\mathbf{r})|^4 + \frac{B^2}{8\pi} \right], \tag{2.8}$$

where $\mathbf{A}(\mathbf{r})$ is the vector potential originating from the magnetic field, $\boldsymbol{\nabla} \times \mathbf{A} = \mathbf{B}$, and F_0 is the free energy of the normal phase. The free energy (2.8) includes no odd order terms of $|\psi(\mathbf{r})|$ because the free energy should always be a real quantity. The first term in (2.8) represents the increase in kinetic energy caused by a spatially variating order parameter. The terms $A(T)|\psi(\mathbf{r})|^2$ and $B(T)|\psi(\mathbf{r})|^4/2$ are phenomenological terms. The last term in (2.8) is the energy cost caused by the expulsion of magnetic flux from the superconductor.

Consider first a superconductor in zero external field i.e. $\mathbf{B} = 0$. At $T > T_c$ where $|\psi(\mathbf{r})| = 0$ the free energy (2.8) reduces to $F = F_0$, as expected. If however, $T < T_c$, minimizing the free energy (2.8) yields the 'Schrödinger like' equation $\left(1 + (B(T)/A(T)) |\psi(\mathbf{r})|^2\right) |\psi(\mathbf{r})| - \xi(T) \nabla^2 |\psi(\mathbf{r})| = 0$ and defining the coherence length $\xi(T) = \hbar/2\sqrt{mA(T)}$. The coherence length of the superconducting wave function describes the distance over which the wave function can vary without generating kinetic energy that lowers the density of superconducting charge carriers.

Consider now a superconductor in an external magnetic field. As the magnetic field is turned on, the superconductor creates shielding currents that cancels the field inside the superconductor. The shielding currents are associated with an increase in energy. If the applied field exceeds a certain critical field H_c, it becomes energetically favorable to revert back into the normal phase and allowing the magnetic field to penetrate. In general, the geometry of the superconductor is an impotent factor in the energy calculation due to the demagnetization factor. The difference between the free energy of the normal- and the superconducting phase is in general given by $H_c(T)/2\mu_0$. Superconductors where the entire volume is either in the normal or in the superconducting (Meissner) phase are known as type I, see figure 2.8. Type I superconductors are generally characterized by $\lambda < \xi$. However, a different behavior is observed in many superconducting materials. In fact most superconductors found to this day are not of type I. Below a lower critical field, H_{c1}, the entire volume of the superconductor is in the Meissner phase. Above H_{c1} but below the upper critical field, H_{c2}, there is a partial penetration of magnetic field through well defined tubes which are themselves in the normal phase. These are individually shielded from the rest of the superconductor be shielding currents, known as flux vortices. Every vortex encloses exactly one 'flux quantum', $\Phi_0 = h/2e$. The regime between H_{c1} and H_{c2} is known as the mixed phase. Above H_{c2} the remaining volume also reverts back into the normal phase. These materials are known as type II superconductors, see figure 2.8. The details of the Type II superconductor was worked out by A. A. Abrikosov [27, 33].

A vortex at $\mathbf{r}_0$ can be described within London theory by adding $\Phi_0 \delta(\mathbf{r} - \mathbf{r}_0)\hat{z}$ to

the right hand side of (2.7)

$$\boldsymbol{\nabla}^2\mathbf{B} - \mathbf{B}/\lambda \;=\; \Phi_0\delta\left(\mathbf{r}-\mathbf{r}_0\right)\hat{z}. \tag{2.9}$$

The solution of (2.9) is shown in figure 2.6. Abrikosov originally predicted a square lattice [34], but this was later corrected to a triangular lattice by W. H. Kleiner et al. [35]. The arrangement of vortices into a triangular lattice is not an intrinsic property of equation (2.9), it must be enforced as an assumption. Also a square arrangement is know to occur. Given an external field B_0, the number of vortices within a unit cell equals $N = B_0/\Phi_0$. Additionally, assuming a triangular vortex lattice every vortex is surrounded by a hexagonal array of other vortices, with a nearest neighbor inter vortex distance $d = (4/3)^{1/4}\left(\Phi_0/B_0\right)^{1/2}$.

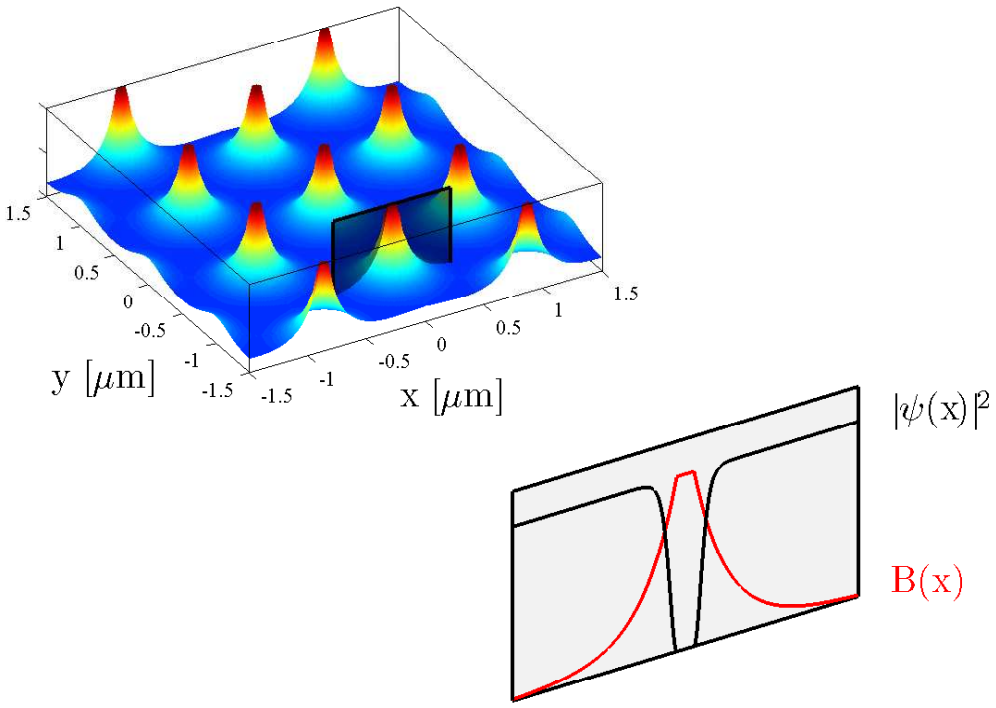

Figure 2.6: *The solution of equation (2.9) on a triangular lattice. From every vortex the magnetic field falls of on a length scale equal to λ and the superconducting wave function builds up from zero inside the vortex core to its full value over a length scale equal to ξ.*

Type II superconductors are generally characterized by $\lambda > \xi$. It was shown that a hexagonal vortex lattice minimizes the free energy, see figure 2.6. Defining $\kappa = \lambda/\xi$, Abrikosov showed that [27, 33]

$$\kappa = \begin{cases} \leq \frac{1}{\sqrt{2}} & \text{Type I} \\ > \frac{1}{\sqrt{2}} & \text{Type II} \end{cases}$$

The London penetration depth in many conventional superconductors are of the order ~ 100Å and the coherence length is ~ 1000Å. This is opposite in the high temperature superconductors discussed in the later chapters 9 and 10.

2.4 Cooper Pairing and BCS Theory

The same year as Abrikosov published his results on the vortex lattice, J. Bardeen, L. Cooper and J. Schrieffer published another paper, explaining the now famous BCS theory of superconductivity [36], in succession to a paper published by L. Cooper in 1956 [37]. The BCS theory successfully explained all the superconductors known at the time and it united experiments like the Isotope effect ($T_c \propto m_{\text{ion}}^{-\alpha}$ where m_{ion} is the mass of the lattice ions), with the unique electrodynamics of the superconductors. The following discussion is largely based on [27, 38, 39].

In his 1956 paper, L. Cooper proposed the existence of a new type of bound state in an electron gas. At zero temperature the Fermi sea is completely inert, but at any finite temperature there will be vacancies very close to the Fermi surface due to thermally excited electrons. These have a lifetime $1/\tau_{\mathbf{k}} \propto (k_B T/\epsilon_{\text{F}})^2$ before they relax back into the Fermi sea. Consider a typical superconducting transition temperature $T \approx 10$K (typical with respect to the superconductors known at that time) which is quite small compared to a typical Fermi energy 1eV≈ 11600K. The excited electrons thus live only within a very thin shell around the Fermi energy surface (characterized by the Fermi wave vector $k_{\text{F}} = \sqrt{2m\epsilon_{\text{F}}}/\hbar$). These electrons, which all satisfy $k > k_{\text{F}}$, form a very dilute electron gas in the crystal. According to the Born-Oppenheimer Approximation the lattice ions move much slower than the electrons and for all practical purposes they can be imagined as static on the timescale of electron dynamics. In effect the ions react by contracting the lattice slightly along the electron paths, dragging other electrons along. This creates an effective attractive interaction between electrons in the material which is mediated by phonons. The effective Hamiltonian including both the electron-electron coulomb interaction and the electron-phonon interaction is $\mathcal{H} = T_e + \sum_{\mathbf{k},\sigma,\mathbf{k}',\sigma',\mathbf{q}} V_{\text{eff}}(\mathbf{q},\omega)\, c^\dagger_{\mathbf{k}+\mathbf{q},\sigma} c^\dagger_{\mathbf{k}'-\mathbf{q},\sigma'} c_{\mathbf{k},\sigma} c_{\mathbf{k}',\sigma}$ where the fermion creation operator $c^\dagger_{\mathbf{k},\sigma}$ creates an electron with energy $\epsilon_{\mathbf{k}}$ and spin σ, T_e is the kinetic energy of the electrons and the effective electron-electron interaction $V_{\text{eff}}(\mathbf{q},\omega) = \langle \mathbf{k}' | V_{\text{eff}} | \mathbf{k} \rangle = V_{\text{el-el}}(\mathbf{q}) + V_{\text{el-ph}}(\mathbf{q})\, \omega_{\mathbf{q}}^2 / \left(\omega^2 - \omega_{\mathbf{q}}^2\right)$ where $\omega_{\mathbf{q}}$ is the phonon frequency. Both the Coulomb interaction $V_{\text{el-el}}$ and the phonon interaction $V_{\text{el-ph}}(\mathbf{q})$ are positive quantities. Note that when $\omega^2 < \omega_{\mathbf{q}}^2$ the electron-phonon interaction becomes negative i.e. attractive. It even diverges as ω comes sufficiently close to $\omega_{\mathbf{q}}$ and hence, there will always exist conditions for which the attractive phonon interaction overcomes the repulsive Coulomb interaction. If a small attractive interaction is present between electrons, they form Cooper pairs of two time reversed electrons i.e. $|\mathbf{k},\uparrow\rangle$ and $|-\mathbf{k},\downarrow\rangle$, with zero net momentum and spin. This is because the spin singlet state $\left(|\uparrow\downarrow\rangle - |\downarrow\uparrow\rangle\right)/\sqrt{2}$ is energetically favorable over the triplet states. As explained above, such two electron must evidently appear within a very thin energy shell above the Fermi surface, $|\epsilon_{\mathbf{k}} - \epsilon_{\text{F}}| < \hbar\omega_D$ where ω_D is the typical frequency for phonons in

the lattice, given by the Debye frequency.

By assuming an effective model for the electron-phonon interaction $\langle \mathbf{k}' | V_{\text{eff}} | \mathbf{k} \rangle = V_0$ (See figure 2.7) if $|\epsilon_{\mathbf{k}} - \epsilon_{\text{F}}| < \hbar\omega_D$ and zero otherwise, J. Bardeen, L. Cooper and J. Schrieffer was able to show the following relation for T_c: $k_B T_c = 1.14\hbar\omega_D \exp\left(-1/D\left(\epsilon_{\text{F}}\right) V_0\right)$, which also nicely explains the isotope effect by the relation $\omega_D \propto m_{\text{ion}}^{-1/2}$. Additionally, in the limit $T \to 0$, the size of the superconducting gap was shown to follow a similar form, $\Delta = 2\hbar\omega_D \exp\left(-1/D\left(\epsilon_{\text{F}}\right) V_0\right)$.

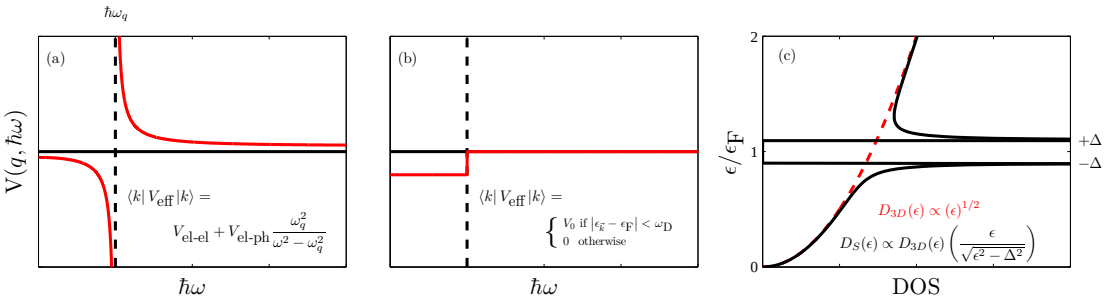

Figure 2.7: *(a) Sketch of the effective electron-electron interaction including the electron-phonon interaction. V_{el-ph} (b) Sketch of the effective electron-electron interaction in BCS theory. (c) Sketch of the superconducting density of states.*

The quasiparticle density of states, D_S, is modified when the superconducting gap opens. BCS theory gives the expression $D_S\left(\epsilon\right) = D\left(\epsilon\right)\left(\epsilon/\sqrt{\epsilon^2 + \Delta^2}\right)$ if $|\epsilon| < \Delta$ and zero otherwise. On both sides of the gap the density of states peaks because the total number of states must remain unaltered [33], see figure 2.7 for an illustration of D_S, assuming the normal state to be given by the same expression as for the free electron gas.

In this section the phonon driven Cooper pairing mechanism was discussed. This mechanism can explain properties of conventional superconductors within the framework of the BCS theory. The highest T_c among the conventional superconductors is found in MgB_2 with $T_c = 39$K [40]. In this thesis I have investigated Y_9Co_7 which is also a conventional superconductor, see chapter 8, where superconductivity ($T_c = 2.5$K) and magnetism ($T_C = 4.25$K) was reported to coexists [41], however, as it turns out this system most likely phase separated into macroscopic regions of each phase. In the next section I will introduce the so-called high temperature- or unconventional superconductors. The high temperature superconductors are not well described by the phonon driven Cooper pairing mechanism, and to this day, a correct alternative theory remains to be found. A leading candidate to the unconventional pairing 'glue' in high temperature superconductors are the magnetic fluctuations which are found to coexists (partially) with superconductivity, and a common features in many of these materials [42].

2.5 High Temperature Superconductivity

In 1986 J. Bednorz and K. Müller discovered superconductivity in the ceramic material $La_{5-x}Ba_xCu_5O_{5(3-y)}$ below $T_c = 30$K, [43, 44], the first so-called high temperature superconductor (HTC). In fact, when purified, the superconducting phase turned out to be $La_{2-x}Ba_xCuO_4$ (LBCO). Soon after the discovery of Bednorz and Müller, R. Cava et. al. reported superconductivity in $La_{2-x}Sr_xCuO_4$ (LSCO) below $T_c = 36.2$K [45] and M. Wu et. al. found superconductivity in $(Y_{1-x}Ba_x)_2CuO_{4-\delta}$ below $T_c = 93$K [46]. This discovery instantly triggered an enormous attention due to its particularly high T_c, which is well beyond the boiling point of liquid nitrogen (77K). $YBa_2Cu_3O_{6+x}$ (YBCO) still remains one of the most promising candidates for technical applications, such as superconducting wires used e.g. for turbines in the wind energy sector.

The three HTC materials mentioned above belong to a common group of materials known as cuprates, which are materials build up of copper and oxygen. The cuprates include also non-superconductors. A commons structural feature of the HTC cuprates, are quadratic planes of copper-oxide (CuO_2). The highest T_c, found among the HTC material known at present, came in 1995 where superconductivity was reported in $Hg_{1-x}Tl_xBa_2Ca_{n-1}Cu_nO_{2n+2+\delta}$ below $T_c = 138$K [47, 48]. The BCS theory described in the previous section can account for Cooper pairing below roughly 40K, thus following the original report of HTC and especially high T_c's reported soon after, it became clear that some other mechanism is behind Cooper pairing in these materials. Other classes of HTC's have been discovered. Notable among these are the recently discovered pnictides [49].

In the coming sections, I will try to condense the vast literature on HTC's into a text which on one hand sums up the general features of these systems, to the extent that such have reached a level of common agreement in the scientific community, and on the other hand, focuses on the aspect of coexistence between superconductivity and magnetism, which sets the scene for my investigations in the later chapters 9 and 10.

2.5.1 Cuprate Crystal Structures and Phase Diagram

One of the striking common features of the cuprate superconductors are the electronically active planes of the CuO_2 found in crystal structure. In these planes, the Cu^{2+} ions are arranged in a nearly square lattice i.e. the angle Cu-O-Cu is very close to 180°, that are well separated by one or even severals isolating layers of spacer ions in the unit cell. The superconductivity appears when either electrons or holes are doped into these spacer layers. It is strictly within these CuO_2 planes that the Cooper pairs are formed. Surrounding the Cu^{2+} ions are O^{2-} ligands. In the case of LSCO discussed below these ligands are arranged in an octahedral, CuO_6, which constitute a cubic crystal field on the Cu ion site.

In this thesis I have investigated various members of the $La_{2-x}Sr_xCuO_4$ (LSCO) family. The crystal structure of the LSCO parent compound La_2CuO_4, shown in figure 2.8, following [50], the structure displays two phases: a high temperature tetragonal phase (HTT) above ~ 500K, with space group I4/mmm (#139) and lattice parameters

$a = b < c$ and a low temperature orthorhombic (LTO) phase below $\sim$ 500K with space group Cmca (#64) and lattice parameters $a < b < c$. In LSCO $a = 5.3$Å, $b = 5.4$Åand $c = 13.2$Åin the orthorhombic structure. However, it is conventional to used the isomorphic notation where HTT is called F4/mmm and LTO is called Bmab [50, 51]. The so-called HTT-to-LTO transition temperature is dependent on the strontium doping x in LSCO and no trace of the LTO phase is observed above $x \sim 0.2$ [50, 51].

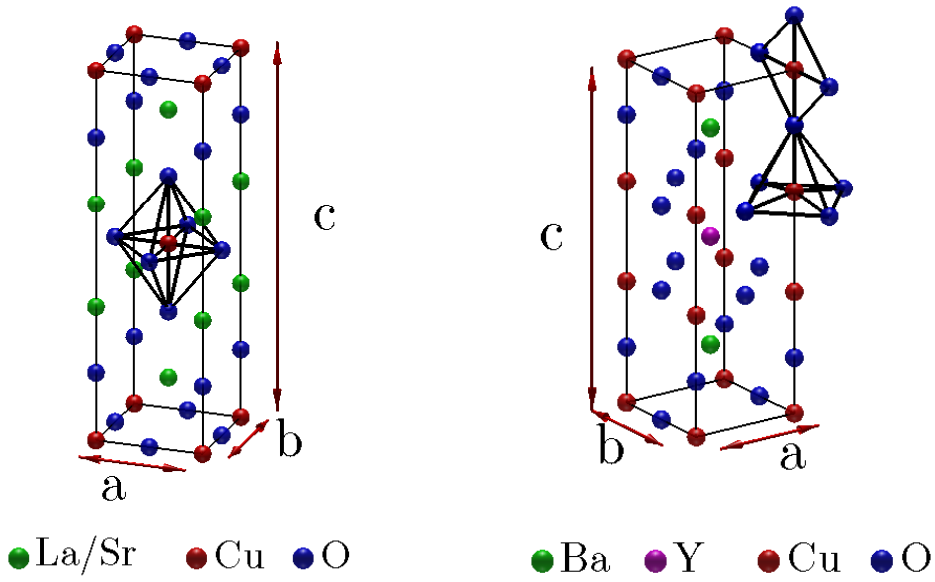

Figure 2.8: ***Left:*** *The tetragonal crystal structure of La_2CuO_4 (LCO). The space group of La_2CuO_4 is #139 (I4/mmm) [51].* ***Right:*** *The crystal structure of $YBa_2Cu_3O_7$. The space group of $YBa_2Cu_3O_{6+x}$ is #47 (P4/mmm) [52, 53]. YBCO belongs with the cuprates, but due to its different crystal structure e.g. the ligands are arranged in pyramids, some physical properties are also different between YBCO and e.g. LSCO.*

The sketch of the phase diagram for LSCO is shown in figure 2.9 compiled from information in e.g. [33, 51, 54, 55]. As function of hole doping, the HTC's display a rich variety of structural and electrical phases, see the sketched phase diagram 2.9. The LCO parent compound is an long-range antiferromagnet, and upon doping with Strontium, $La_{2-x}Sr_xCuO_4$ the long-range antiferromagnetic order is observed in the range $0 < x < 0.02$. In addition, experiments using muon spin rotation [54] observe a secondary spin freezing of the spin of the doped holes. The freezing temperature T_f in this regime follows $T_f \propto x$. Beyond the level of doping where long range magnetic order is completely suppressed, short ranged magnetic correlations persists in a spin-glass-like phase. Muon spin rotation experiments show that this spin-glass phase can be explained in terms of a phase separated electronic state where holes

form metallic domains leaving large hole poor regions with strongly correlated antiferromagnetism. Based on this picture, the spin-glass transitions temperature is expected to vary as $T_g \propto 1/x$ which is consistent with the measurements [54]. The incommensurate spin-glass regime, $0.02 < x < 0.10$, extends into the superconducting regime, $0.05 < x < 0.28$, see section 2.5.2. It is useful to separate the superconducting regime into two section. The doping level which gives the highest possible T_c is known as optimal doping. For LSCO optimal doping is approximately $x = 0.15$ leading to $T_c \approx 40$K and subsequently, the ranges $0.05 < x < 0.15$ and $0.15 < x < 0.28$ are known as underdoped and overdoped respectively. In the underdoped regime T_c is partially suppressed around $x \approx 0.125$, and concomitant, a sharp increase of the incommensurate magnetism develops in this range, see section 2.5.2. This is known as the 1/8 anomaly. The region of the phase diagram above T_c around optimal doping is known as the strange metal regime. The resistivity of the strange metal obeys $\rho \propto T$, in contrast to a normal metal resistivity $\rho \propto T^2$ seen at $x > 0.28$. The normal metal state is well described as a Fermi liquid. Another profound observation in the underdoped regime,

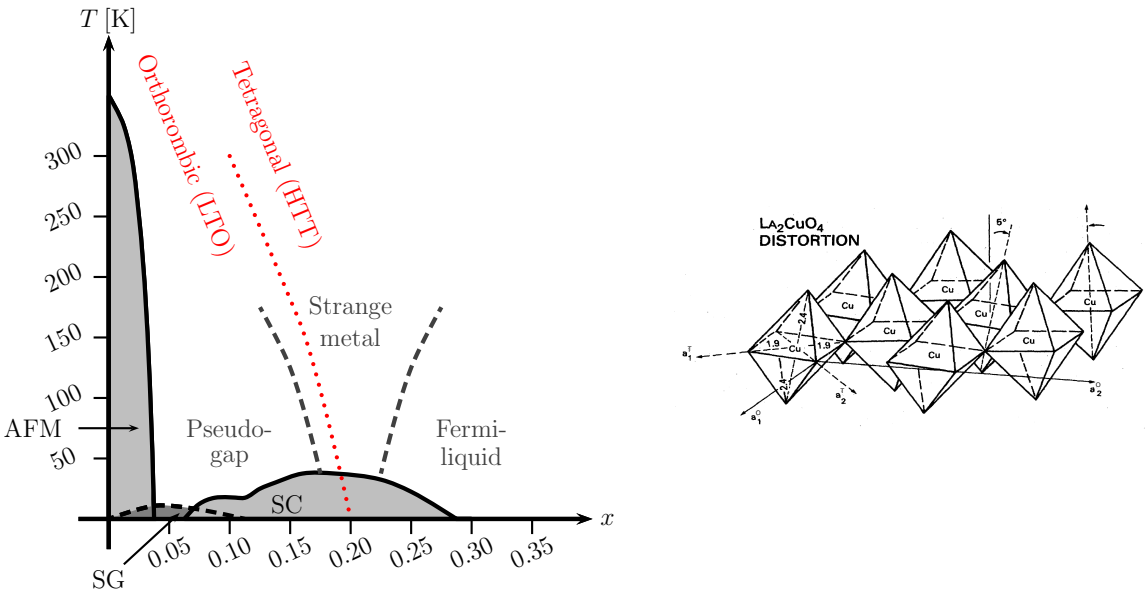

Figure 2.9: ***Left:*** *Generic cuprate phase diagram based on LSCO [33], including the low-temperature-orthorhombic (LTO) seen only in some cuprates. AFM denotes the long range antiferromagnetically ordered phase of the undoped compound. SG denotes a spin-glass like phase and SC denotes the superconducting phase, forming what is known as the superconducting dome. Around $x = 0.125$ the superconducting transition temperature is suppressed. Superconductivity is completely suppressed above $x \approx 0.28$ where the material acquire transport properties similar to those of a normal metal.* ***Right:*** *The lattice distortion associated with the HTT-to-LTO transition. The CuO_6 octahedra spontaneously tilt below the transition. Taken from [56].*

is the pseudogap regime, which appears in the non-magnetic and non-superconducting

state above the superconducting transition temperature [57]. The exact nature of the pseudogap is currently not known and hence no precise definition of the pseudogap transition temperature, T^*, has been established. In LSCO it ranges from 100K to 800K depending on the doping level and the experimental technique [57]. Below T^* the materials exhibits a partial suppression of low-energy density of states, as compared to what is expected from a Fermi liquid metallic state [57, 58, 59]. The onset of decreasing resistivity from the linear behavior of the strange metal have be used to determine T^* [60, 58]. However no clear definition of the pseudogap temperature exists today.

In recent years, evidence that the pseudogap in cuprates might be coupled to changes in the Fermi surface. Quantum oscillation experiments in high fields (20-50T) of YBCO confirm the existence of coherent electronic quasi particles with a small Fermi surface [61, 62], known as Fermi pockets. Additionally, measurements of a negative (electron like) Hall coefficient, $R_H = -1/en$, confirms that the charge carriers are indeed electron-like at low temperature and low doping. The quantum oscillation disappear below $p_c \approx 0.08$ (p is used here to refers to the total hole doping, which is called x in LSCO). In 2011, D. LeBoeuf et. al. [60] published results on both resistivity and Hall coefficient over the range of hole concentration $p = 0.078$ to 0.152 in YBCO. The low temperature Hall coefficient changes sign at $p = p_c$ such that $R_H < 0$ for $p < p_c$ and $R_H > 0$ for $p > p_c$. The high temperature ($T > 100K$) Hall coefficient however, remains positive (hole like) over the entire doping range. The above presented results hints to a doping dependent Fermi surface modulation in YBCO at low temperature and high magnetic field.

One mechanism which can facilitate such a Fermi surface scheme, is the appearance of a spin- or charge density wave order. Various theoretical models support that a spin-density wave type order can produce small electron pockets similar to the observations by techniques like ARPESS. The interested reader is referred to the recent article by M. Vojta [59].

A few possible explanations of the pseudogap have been put fourth over the years. One idea is that the suppression of low-energy density of states is a precursor of superconductivity, where phase-incoherent Cooper-pairs are formed. Evidence of Cooper pair formation above T_c has been reported in [63]. A major objection to this idea is that the onset temperature of pairing fluctuations found in experiments are significantly below T^*. Another theory points to various ordering phenomena i.e. spin- or charge-density waves, nematic or orbital circulating-currents orders. However, T^* does not seem to be associated with a thermodynamic phase transition [59]. However, as mentioned above, the exact nature of the pseudogap is heavily debated.

The richness of physics in the phase diagram of many cuprates, some of which was presented above, hints to the complexity that any successful electronic theory must encapsulate. No such theory currently exists, but in the next section some fundamental aspects of the experimentally known ground state are discussed.

2.5.2 Cuprate Electronic Structure and Magnetic Properties

The crystal structure of the different cuprates, like LSCO, LBCO and YBCO, leads to electronic structures with many common characteristics, however there are also differences. In LSCO the copper ions residing in slightly distorted octahedra, whereas in YBCO there are two different types of copper ion layers. In the following we focus on the ground states and doping mechanism of LSCO.

Consider the parent compound $LaCuO_4$ where the d-orbitals of a free Cu^{2+} are split by the octahedral crystal field [56]. The electronic structure of a copper ion is $[\mathrm{Ar}]\, 3d^{10}4s^1$, thus the outer shell of Cu^{2+} accommodates nine electrons distributed among the five d-orbitals, see figure 2.10. An unpaired electron resides on the Copper site in a hybridized state between the $3d_{x^2-y^2}$ orbital from the Copper ion and the $2p_x$ (or equivalently $2p_y$) from the oxygen. The magnetic ground state in La_2CuO_4 is known as a Mott insulator [56, 42, 39], due to the Coulomb interaction which tends to localize exactly one electron with $S = 1/2$ on the each copper site.

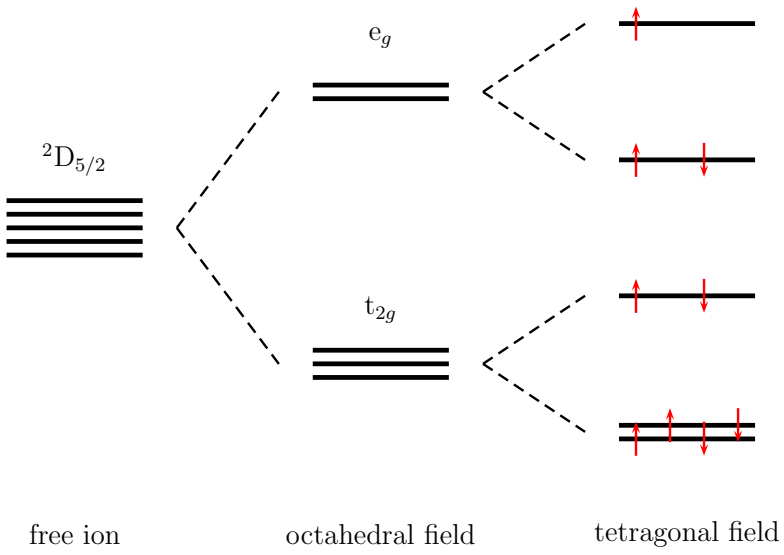

Figure 2.10: ***left:*** *The electronic states of Cu^{2+} in LSCO.*

P. W. Anderson suggested [42] a minimal model for the electronic structure of cuprate superconductors at low doping, including only a single electronic band in the Hubbard model [64]

$$\mathcal{H} = -t \sum_{\langle i,j\rangle,\sigma} \left(c^\dagger_{i\sigma} c_{j\sigma} + c^\dagger_{j\sigma} c_{i\sigma} \right) + U \sum_i n_{i\uparrow} n_{i\downarrow} - \mu \sum_{i\sigma} n_{i\sigma} \tag{2.10}$$

where the first term represents the kinetic energy. Following [65, 42, 28], the kinetic energy is described by tight-binding one-electron hopping between copper ion sites.

The operators $c^\dagger_{i\sigma}$ and $c_{i\sigma}$ annihilates or creates respectively an electron on site i with spin σ. As a first approximation the summation only includes nearest neighbors sites. The second terms represents the so-called on-site Coulomb interaction. The operator $n_{i\sigma} = c^\dagger_{i\sigma} c_{i\sigma}$ counts the number of electrons at site i with spin σ. The eigenvalue of $n_{i\sigma}$ is 1 if an electron with spin σ is at site i or 0 if not. The third term is the chemical potential. Consider first the situation with $U = 0$. The Hamiltonian (2.10) may be diagonalized directly by Fourier transformation yielding $\mathcal{H} = \sum_{\mathbf{k}\sigma} \xi_{\mathbf{k}} c^\dagger_{\mathbf{k}\sigma} c_{\mathbf{k}\sigma}$ where $\xi_{\mathbf{k}} = -2t\left(\cos\left(k_x\right) + \cos\left(k_y\right)\right) - \mu$. Now, including the strong on-site Coulomb interaction, i.e. $t << U$, a gap opens up in the quasi-particle spectrum, $\epsilon_{\mathbf{k}} = \pm\sqrt{\xi^2_{\mathbf{k}} + \Delta^2_{\mathbf{k}}}$. The HTC's are believed to have a so-called d-wave gap function $\Delta_{\mathbf{k}} = 2\Delta_0\left(\cos\left(k_x\right) - \cos\left(k_y\right)\right)$. It can be shown, that the ground state of the Hamiltonian (2.10) is a spin singlet, $\left(c_{i\uparrow} c_{j\downarrow} + c_{i\downarrow} c_{j\uparrow}\right)/\sqrt{2}$, which is intrinsic antiferromagnetic.

Consider now, doping by Strontium into $LaCuO_4$. A La^{3+} ion is replaced by Sr^{2+}, which causes the CuO_2 plane to donate an extra electron to the insulating spacer layer. In effect, this process create one additional holes in the CuO_2 plane. Building on the work of P. Anderson, F. Zhang and T. Rice [65] argued that the extra hole primary resides on the oxygen $2p_x/2p_y$ sites, forming a so-called Zhang-Rice singlet with the hole already present on the copper $3d_{x^2-y^2}$ site. Upon adding this hybridization to the Hamiltonian (2.10) F. Zhang and T. Rice showed that the resulting Hamiltonian, known as the $t - \mathcal{J}$ model, also has an antiferromagentic ground state.

The rich range of phenomena associated with the ground state of both the Hubbard model (2.10) and the $t - \mathcal{J}$ model is still an active research field within theoretical physics. In 2010 S. Raghu, S. Kivelson and D. Scalapino [66] established that d-wave superconductivity could be derived from the Hubbard model alone in the limit $U/t \to 0$, whereas the work of S. Sorella et. al. [67] finds d-wave superconductivity in the $t - \mathcal{J}$ model using quantum Monte Carlo simulations. Many papers have indeed been published on this subject, but so far, not one single consistent approach have successfully captured the full complexity of the cuprates seen in experiments.

As mentioned above, the magnetic ground state of the undoped material is an antiferromagnet with long range order. This was confirmed in 1988 by D. Vaknin et. al. [68] who performed elastic neutron scattering on an oxygen reduced sample of $LaCuO_{4-y}$. They found[1] $\mathbf{Q}_{\mathrm{AFM}} = \left(\frac{1}{2}\ \frac{1}{2}\ 0\right)$. It was further concluded that the individual spins point along the orthorhombic [010] axis and the ordered moment within each of the two sublattices amount to $0.48 \pm 0.15\mu_B/Cu^{2+}$. From the electronic structure discussed in the previous section, an ordered moment of $g\mu_B S = 1.14\mu_B/Cu^{2+}$ was expected given $g = 2.28$ [68], thus the experimentally determined value is only about half of the expected value. This reduction is reduction of the ordered moment is consistent with theories for two-dimensional Heisenberg antiferromagnets [69, 70].

The magnetic excitation in LCO, LBCO and LSCO are well described by spin wave theory, see e.g. [71, 72, 73, 74] with exchange constant of the order 100meV [74]. Recently A. T. Rømer et al. [75] published evidence of a so-called anisotropy

[1] The ordering vector quoted here is given in the tetragonal lattice units, where the tetragonal lattice vectors are along the Cu-O-Cu bonds. Another common notation is the orthorhombic where $\left(\frac{1}{2}\ \frac{1}{2}\ 0\right)_T = \left(1\ 0\ 0\right)_O$

gap in $La_{1.88}Sr_{0.12}CuO_4$. In LNSCO less is known about the excitations, however, at 5meV they has bee shown [76] to be either one dimensionally modulated and collinear, consistent with the stripe model or two dimensionally modulated with a noncollinear structure.

Early in the studies of $La_{2-x}Sr_xCuO_4$, evidence was published of inelastic incommensurate magnetic correlations at low temperature [77, 78]. Four peaks was measured around the antiferromagnetic Bragg point with incommensurability δ (above $x = 0.055$) defined by the ordering vectors $\mathbf{Q}_{\mathrm{AFM,IC}} = \left(\frac{1}{2}\ \frac{1}{2}\ 0\right) \pm (\delta\ 0\ 0)$ and $\mathbf{Q}_{\mathrm{AFM,IC}} = \left(\frac{1}{2}\ \frac{1}{2}\ 0\right) \pm (0\ \delta\ 0)$. In 1995 J. Tranquada et al. [79] published evidence of elastic incommensurate spin correlations in LNSCO. Tranquada explained their finding of $\delta \approx x$ in terms of a so-called stripe phase, shown in figure 2.11, where a spin super lattice of period 8 forms in real space, corresponding to incommensurate peaks with $\delta = 1/8$. Additionally, a charge super lattice of period 4 forms in real space, corresponding to incommensurate peaks with $\zeta = 2\delta$ [79].

The variation of incommensurability with doping for $x > 0.055$ was collected by K. Yamada [80], later known as the Yamada plot, see figure 2.12. It was found that in the range $0.055 < x < 0.125$ the incommensurability obeys $\delta \approx x$ but saturated at $\delta = 0.125$ above $x = 0.125$.

In the range $0.02 < x < 0.055$ the magnetic order is a spin glass, as was mentioned above. In this phase, there are only two incommensurate peaks appearing around the antiferromagnetic Bragg point [81, 82] and they are rotated by 45° relative to the stripes described above. The incommensurability δ is then defined by $\mathbf{Q}_{\mathrm{AFM,IC}} = \left(\frac{1}{2}\ \frac{1}{2}\right) \pm (\delta\ \delta)$.

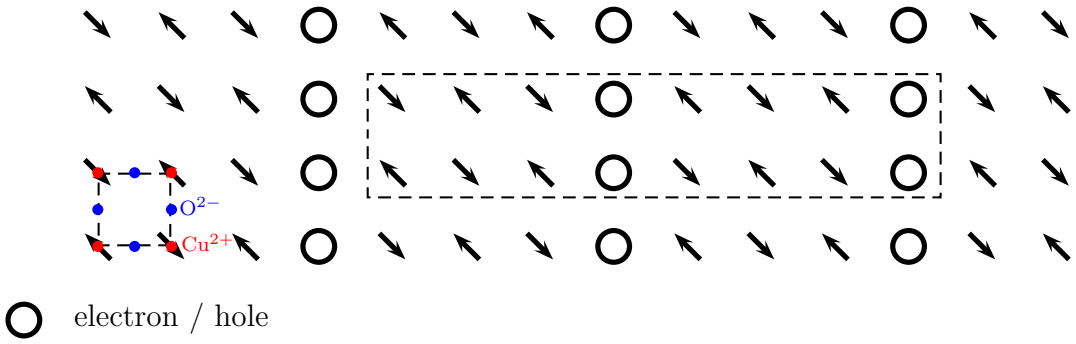

Figure 2.11: *Schematic picture of stripes at $x = 0.125$ from the original work by J. Tranquada et. al. [79], where one dimensional stripes of charges are acting as antiferromagnetic domain walls. The dashed lines encapsulate the super structure which would give $\delta = 1/8$. Later alternative models with the same symmetry and ordering vector has been proposed [74].*

The data acquired on $La_{2-x}Sr_xCuO_4$, show that magnetic order persists far into the superconducting underdoped regime [55]. In general the magnetic onset temperature

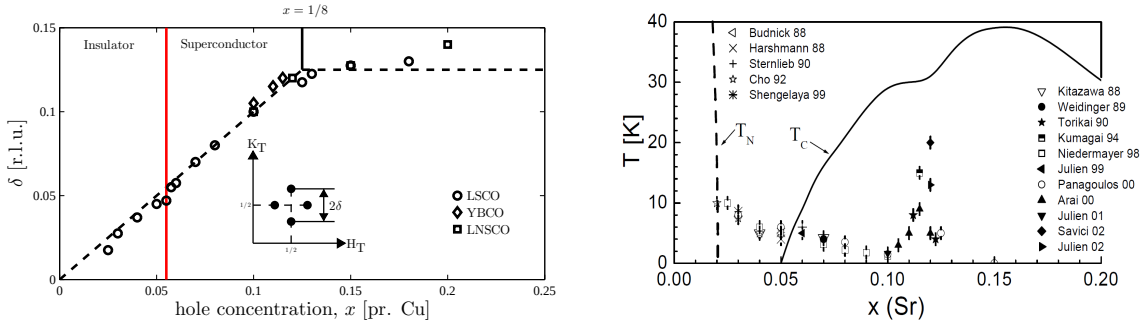

Figure 2.12: ***Left:*** *The Yamada plot including the three important HTC's LSCO, LNSCO and YBCO. Adopted from [80].* ***Right:*** *Measurements of T_N. From [55].*

T_N (T_f) does not coincide with T_c. Concomitant to a partial suppression of T_c around $x = 0.12$, the magnetic onset temperature show a very abrupt increase within a very narrow doping range. The magnetic correlation length is shortest at $x = 0.06$ ($\xi = 20$Å) and longest at $x = 0.12$ ($\xi > 200$Å) [55]. Also the size of the ordered moment show an anomaly at $x = 0.12$. The ordered moment starts decreasing from its $x = 0$ value above $x \sim 0.03$ and reached zero at $x = 0.09$. However, in LNSCO with $x = 0.125$ the moment reappears at a value around 80% of its $x = 0$ value [54, 83]. In LSCO the ordered moment reaches only 50%. This indicates a direct competition between superconductivity and magnetis in LSCO with $x = 0.125$.

We end this review of cuprate physics, with a few words on the effect of magnetic fields on the properties mentioned above. In 2000 Katano et al. [84] showed that the intensity of the IC-AFM Bragg peaks measured by elastic neutron scattering increased in a magnetic field, see also [85, 83]. Also the excitations are affected by field. As mentioned above, what is known about the excitation in the cuprates, indicates that they are well described by spin wave theory. In LSCO12 the excitations are gaped by an anisotropy gap and hence not by a superconducting gap, which is the case away from $x = 0.12$, see e.g. [86, 87] (above $x = 0.12$) and [88] (below $x = 0.12$), where the gap is presumably due to superconductivity. In table 2.1 shown below, some properties are listed for various Lanthanum based HTC materials. This is done as an attempt to highlights both similarities and differences which will form the basis of a discussion in the later chapters on LSCO+O (9) and LSCO12 (10).

Crystal Structure $T = 0$	Sample	IC-AFM peaks Sharp ($\xi > 100$Å) Broad ($\xi < 50$Å)	Field-induced or enhanced IC-AFM peaks	Charge order	T_c	Ref's.
LTT ([89])	LBCO 9.5%	Sharp ([89])	No ([89])	No ([89])	27K ([89])	[89]
LTLO ([90])				Yes ([90])	32K ([90])	[90]
LTT	LBCO 12%	Sharp	No / small	Yes	5K	[91] [92]
LTT	LNSCO 12%	Sharp	No	Yes	5K	[79] [83] [93]
LTO	LCO+O[a]	Sharp	Yes ([94])	No Report	42K	[94] [95]
LTO	LSCO+O[b]	Sharp	No	No Report	40K	[96] [97] [98]
LTO	LSCO 10.5%	Broad	Yes (enhanced)	No Report	30K	[83]
LTO[c]	LSCO 12%	Sharp	Yes (enhanced)	Yes ([99])	27K	[83] [99]
LTO	LSCO 14.4%	Sharp	Yes (induced) Above 3T	No report	35K	[100]
LTO	LSCO 14.5%	Sharp	Yes (induced) Above 7T	No report	36K	[83] [101]

Table 2.1: [a] *Sacici et al. [95] reported phase separation in this sample.* [b] *Mohottala et al. [96] and Udby et al. [97, 98] reported phase separation in this sample, see also chapter 9.* [c] *The data proving charge order in LSCO 12% is unpublished and the interpretation is unclear due to weak signatures of an LTT phase also observed in this experiment.*

CHAPTER 3

Density Functional Methods of Electronic Structure Calculations

In this chapter we introduce the concepts of density functional theory (DFT). DFT is a numerical technique developed over the last 50 years, which in its essence can be used to approximate the ground state properties of solids, liquids, single molecules etc. Over the decades the computer power have increased and the approximations made in DTF have become less severe, which allows for increasing precision of the final calculation.

In chapter 6 we will utilize DFT, as a tool which produce an educated guess for the structure of $CoCl_2 \cdot 2NH_3$ when coming from the structure of $CoCl_2 \cdot 2D_2O$ and change the so-called spacer molecule water from ammonia. This is a simple approach to screening different materials which have similar structural properties, but slightly different chemical bond lengths which translates into different exchange couplings. In an experiment, the critical points associated with various phase transitions, may be out of range for one particular choice of spacer molecule and within range for another. If insufficient literature exists, DFT is simple the best available tool for a useful assessment in such a question.

Many good texts exists on the fundamentals of DFT. This chapter largely follows the approach in ref. [102].

3.1 The Many-Body Problem in Condensed Matter

In this section we introduce the general Hamiltonian governing all phenomena in condensed matter physics, and eigenvalue problem facing scientists who are tries to solve it. Following the general discussion below, the numerical technique for approximate solutions to the eigenvalue problem known as density functional theory (DFT) is explained.

A condensed matter system is made up of as set of nuclei and their electrons. The quantum mechanical Hamiltonian describing all Coulomb interactions (V) and the

kinetic energies (T) of the particles reads [102, 38]

$$\mathcal{H} = T_{\text{el}} + V_{\text{el-el}} + T_{\text{nuc}} + V_{\text{nuc-nuc}} + V_{\text{el-nuc}} \tag{3.1}$$

where

$$T_{\text{el}} + V_{\text{el-el}} = \sum_{\sigma} \int \mathrm{d}\mathbf{r} \Psi_{\sigma}(\mathbf{r}) \left(-\frac{\hbar^2}{2m_e} \nabla_{\mathbf{r}} \right) \Psi_{\sigma}(\mathbf{r}) + \frac{1}{2} \sum_{\sigma\sigma'} \int \mathrm{d}\mathbf{r} \int \mathrm{d}\mathbf{r}' \Psi^{\dagger}_{\sigma}(\mathbf{r}) \Psi^{\dagger}_{\sigma'}(\mathbf{r}') \left(\frac{e^2}{|\mathbf{r} - \mathbf{r}'|} \right) \Psi_{\sigma'}(\mathbf{r}') \Psi_{\sigma}(\mathbf{r}) \tag{3.2}$$

$$T_{\text{nuc}} + V_{\text{nuc-nuc}} = \int \mathrm{d}\mathbf{R} \Psi(\mathbf{R}) \left(-\frac{\hbar^2}{2m} \nabla_{\mathbf{R}} \right) \Psi(\mathbf{R}) + \frac{1}{2} \int \mathrm{d}\mathbf{R} \int \mathrm{d}\mathbf{R}' \Psi^{\dagger}(\mathbf{R}) \Psi^{\dagger}(\mathbf{R}') \left(\frac{ZZ'e^2}{|\mathbf{R} - \mathbf{R}'|} \right) \Psi(\mathbf{R}') \Psi(\mathbf{R}) \tag{3.3}$$

$$V_{\text{el-nuc}} = \sum_{\sigma} \int \mathrm{d}\mathbf{r} \int \mathrm{d}\mathbf{R} \Psi^{\dagger}_{\sigma}(\mathbf{r}) \Psi^{\dagger}(\mathbf{R}) \left(-\frac{Ze^2}{|\mathbf{r} - \mathbf{R}|} \right) \Psi(\mathbf{R}) \Psi_{\sigma}(\mathbf{r}) \tag{3.4}$$

where $\mathbf{r}$ and $\mathbf{R}$ denotes the positions of the n electrons of mass m_e and the N nuclei of mass m respectively, and Z is the atomic number of the nucleus corresponding to its total number of elementary charges Ze. $\Psi_{\sigma}(\mathbf{r})$ and $\Psi^{\dagger}_{\sigma}(\mathbf{r})$ are second quantized field operators that annihilate or create a fermion[1] at position $\mathbf{r}$ and with spin σ.

Now we consider a macroscopic crystalline material, which contains of order 10^{23} nuclei. The ground state wave function of this enormous many-body system is $|\Phi\rangle = |\{(\mathbf{r}_1, \mathbf{r}_2, \mathbf{r}_3, ..., \mathbf{r}_n\}, \{\mathbf{R}_1, \mathbf{R}_2, \mathbf{R}_3, ..., \mathbf{R}_N)\}\rangle$. The wave function gives the probability of any particular configuration of electrons and nuclei occurring at any particular time. It must reflect the symmetry of the lattice, which essentially is a result of minimizing $T_{\text{nuc}} + V_{\text{nuc-nuc}}$. But must also include the motion of all the electrons which generally is influenced by interactions between the electrons themselves, $V_{\text{el-el}}$, as well as interaction with the lattice nuclei, $V_{\text{el-nuc}}$. The ground state energy is in principle obtainable by solving the Schrödinger equation $\mathcal{H}|\Phi\rangle = \epsilon|\Phi\rangle$. This is however far from straightforward.

Since the early days of quantum mechanics, many approximation schemes have been devised in the effort to solve the Schrödinger equation in cases with more complexity than the harmonic oscillator or the hydrogen atom. Among these, perturbation theory and variational calculus have been particularly successful for small problems dealing with few degrees of freedom. In 1927 M. Born and R. Opperheimer studied the Hamiltonian (3.1) in the case of a molecule using perturbation theory [103]. They expanded (3.1) in the electron-nucleus mass ratio $\kappa = (m_e/m)^{1/4}$, and showed, that due to the large mass difference $m_e/m \approx 1/2000$, there is essentially no changes in the electronic part of the wave function as a result of interactions with the nuclei. As a result hereof,

[1] $\Psi_{\sigma}(\mathbf{r})$ and $\Psi^{\dagger}_{\sigma}(\mathbf{r}')$ are fermionic fields if they satisfy the commutator relation $\left\{\Psi_{\sigma}(\mathbf{r}), \Psi^{\dagger}_{\sigma}(\mathbf{r}')\right\} = \delta_{\sigma\sigma'}\delta(\mathbf{r} - \mathbf{r}')$ and bosonic fields if they satisfy the anti-commutator relation $\left[\Psi_{\sigma}(\mathbf{r}), \Psi^{\dagger}_{\sigma}(\mathbf{r}')\right] = \delta_{\sigma\sigma'}\delta(\mathbf{r} - \mathbf{r}')$.

the motion of electrons takes place on a much faster time scale than the motion of the nuclei, and the nuclei can be treated separately and the electrons. The electrons can be then be imagined as moving in a potential, V_{ex}, which is external to the electron system, originating from the lattice (+ any other potential which might be enforced on the whole system). This is known as the Born-Oppenheimer Approximation. The electronic part of the Hamiltonian (3.1) thus reduces to $\mathcal{H} = T_{\text{el}} + V_{\text{el-el}} + V_{\text{ex}}$. The remaining difficulty stems primarily from the Coulomb interaction $V_{\text{el-el}}$ between the electrons themselves.

A first approach, which is widely known in condensed matter physics, provide much useful insight by ignoring the $V_{\text{el-el}}$ completely. Assuming a non-interacting electron gas to exist within a periodic external potential, $V_{\text{ex}}(\mathbf{r}+\mathbf{T}) = V_{\text{ex}}(\mathbf{r})$ where $\mathbf{T}$ is a translation vector of the lattice, the electron wave functions becomes the so-called Bloch waves [38].

Ignoring $V_{\text{el-el}}$ is however insufficient for a comprehensive understanding of many material properties. Hence a fully fledged ab initio methods have been developed over the years based on the single particle electron density [102]

$$n(\mathbf{r}) = \sum_{\sigma} \langle \Phi | \Psi_{\sigma}^{\dagger}(\mathbf{r}) \Psi_{\sigma}(\mathbf{r}) | \Phi \rangle . \tag{3.5}$$

Generally, the approach to solving the Schrödinger equation for the Hamiltonian (3.1) based on the electron density as opposed to the wave function itself is known as density functional theory (DFT). The fundamentals of DFT will be considered in detail in the next section.¨The interactions (3.3)-(3.4) can also expressed in terms of electron density, using the identity [102]

$$\sum_{\sigma\sigma'} \langle \Phi | \Psi_{\sigma}^{\dagger}(\mathbf{r},) \Psi_{\sigma'}^{\dagger}(\mathbf{r}') \Psi_{\sigma'}(\mathbf{r}') \Psi_{\sigma}(\mathbf{r}) | \Phi \rangle = n(\mathbf{r}) n(\mathbf{r}') g(\mathbf{r},\mathbf{r}') \tag{3.6}$$

where $g(\mathbf{r},\mathbf{r}')$ is the pair-correlation function. For the Coulomb interaction between the electrons we find

$$V_{\text{el-el}} = V_{\text{c}} + V_{\text{xc}} \tag{3.7}$$

where

$$\begin{aligned} V_{\text{c}}[n] &= \frac{e^2}{2} \int \mathrm{d}\mathbf{r} \int \mathrm{d}\mathbf{r}' \frac{n(\mathbf{r}) n(\mathbf{r}')}{|\mathbf{r}-\mathbf{r}'|}. \\ V_{\text{xc}}[n] &= \frac{e^2}{2} \int \mathrm{d}\mathbf{r} \int \mathrm{d}\mathbf{r}' \frac{n(\mathbf{r}) n(\mathbf{r}')}{|\mathbf{r}-\mathbf{r}'|} [g(\mathbf{r},\mathbf{r}') - 1] . \end{aligned}$$

The first term, V_{c}, describe a mean field theory for $V_{\text{c}}[n]$, which is also known as the Hartree approximation. The second term $V_{\text{xc}}[n]$ represents the many-body effects which beyond the Hartree approximation, it is known as the exchange-correlation potential. In this term, much of the difficulty of solving the eigenvalue problem of (3.1) is hidden. In the next section, DFT is introduced, along with the different approximations to the exchange-correlation energy used in practical calculations.

3.2 Density Functional Theory

In this section we develop the formal notions of DFT, which first of all is a numerical technique. However, even thou the machine power of laptop computers increase almost on an annual basis, DFT calculations with high accuracy still requires a modern super computer.

DFT begins with the problem discussed in previous section. Consider a solid or molecule within the Born-Oppenheimer Approximation. The Coulomb interaction between electrons is given by (3.7), in terms of the electron single particle density. The wave function, also described by the electron density $|\Phi[n(\mathbf{r})]\rangle$, give rise to the following energy functional

$$\begin{aligned} \epsilon[n(\mathbf{r})] &= \langle \Phi[n(\mathbf{r})]| T_{\mathrm{el}} + V_{\mathrm{c}} + V_{\mathrm{xc}} + V_{\mathrm{ex}} |\Phi[n(\mathbf{r})]\rangle \\ &= T_{\mathrm{el}}[n(\mathbf{r})] + V_{\mathrm{c}}[n(\mathbf{r})] + V_{\mathrm{xc}}[n(\mathbf{r})] + V_{\mathrm{ex}}[n(\mathbf{r})] \end{aligned} \tag{3.8}$$

In 1964 the development of density functional theory gained momentum when P. Hohenberg and W. Kohn proved that a specific electron density of a non-degenerate ground state uniquely determines the external potential $V_{\mathrm{ex}}[n]$, acting upon the electron system, up to an additive constant [102, 104]. This is known as the Hohenberg-Kohn theorem. It follows from the theorem, that the only variable of interest to this problem indeed is the electron density, and when it is known, all ground state properties including the ground state wave function is directly obtained from it. The force on each nucleus can be calculated from the potential created by the electrons, and the positions of each nuclei can sequentially be relaxed by an iterative process.

For a particular external potential, the ground state energy $\epsilon_0[n]$ is obtained by minimizing the energy functional (3.8) with respect to the electron density $n(\mathbf{r})$. The density that minimizes the functional is then the exact ground state electron density $n_0(\mathbf{r})$. The explicit density dependence of the kinetic energy of the electrons is generally not known. In 1965 W. Kohn and L. Sham devised a way around this [102, 105]. Consider instead a system of non-interacting electrons (Kohn-Sham particles), where the wave functions are Slater determinants i.e. antisymmetrized products of single particle wave functions $\left|\psi_i^{\mathrm{KS}}\right\rangle$, known as Kohn-Sham orbitals. The electron density is in this case given by $n(\mathbf{r}) = \sum_i \left|\left\langle \psi_i^{\mathrm{KS}} \mid \psi_i^{\mathrm{KS}} \right\rangle\right|^2$ and also the kinetic energy can be calculated in this case. The Kohn-Sham particles are completely fictitious, but if the ground state wave function of these particles coincidentally results in the same electron density $n_0(\mathbf{r})$ as the full many body solution, then by the Hohenberg-Kohn theorem, the external potential V_{ex} can be found.

The Kohn-Sham particles are affected by a effective potential, V^{KS}, which is different from V_{ex} in (3.8) and constructed in such a way, as to minimize the Kohn-Sham energy functional

$$\epsilon^{\mathrm{KS}}[n(\mathbf{r})] = T_{\mathrm{el}}^{\mathrm{KS}}[n(\mathbf{r})] + V_{\mathrm{c}}[n(\mathbf{r})] + V_{\mathrm{xc}}^{\mathrm{KS}}[n(\mathbf{r})] + V_{\mathrm{ex}}[n(\mathbf{r})] \tag{3.9}$$

where the modified exchange-correlation functional $V_{\mathrm{xc}}^{\mathrm{KS}}[n]$ includes both $V_{\mathrm{xc}}[n]$ from the original many-body problem (3.8) and the part of the kinetic energy originating

from the interactions. $T_{\mathrm{el}}^{\mathrm{KS}}[n]$ is the kinetic energy of the fictitious non-interacting Kohn-Sham particles. The Kohn-Sham eigenenergies and orbitals is thus defined through the Schrödinger equation

$$\left[-\frac{\hbar^2}{2m_e}\nabla_{\mathbf{r}}^2 + V^{\mathrm{KS}}(\mathbf{r})\right]\left|\psi_i^{\mathrm{KS}}\right\rangle = \epsilon_i\left|\psi_i^{\mathrm{KS}}\right\rangle \tag{3.10}$$

where

$$V^{\mathrm{KS}}(\mathbf{r}) = \frac{\delta V_{\mathrm{c}}[n(\mathbf{r})]}{\delta n(\mathbf{r})} + \frac{\delta V_{\mathrm{xc}}^{\mathrm{KS}}[n(\mathbf{r})]}{\delta n(\mathbf{r})} + \frac{\delta V_{\mathrm{ex}}[n(\mathbf{r})]}{\delta n(\mathbf{r})}. \tag{3.11}$$

The equations (3.9), (3.10) and (3.11) are solved self-consistently until the density converges via the scheme shown in figure 3.1.

Up to this point, no attentions was paid to the difference between those orbitals occupied by spin up and spin down electrons. However, to obtain a magnetic ground state, the electron density of spin up and spin down must be considered separately [102]. The treatment is, however, no different from what is outlined in figure 3.1.

$$n(\mathbf{r}) = n^{\uparrow}(\mathbf{r}) + n^{\downarrow}(\mathbf{r}). \tag{3.12}$$

The magnetization of the ground state is obtained as $\mu_B\left(n^{\uparrow}(\mathbf{r}) - n^{\downarrow}(\mathbf{r})\right)$ [2].

In the next section, we discuss the elusive exchange-correlation energy. It appears in the Kohn-Sham equations as a derivative in (3.11), but explicit is unknown. In order to obtain useful result from DFT, a wide variety of approximations to the exchange-correlation energy have been developed over the years.

3.2.1 Exchange-Correlation Energy Functionals

The validity of the methods described above for finding approximate solutions to the quantum mechanical many-body problem, rests on knowing a suitable approximation to the initially unknown exchange-correlation energy functional $V_{\mathrm{xc}}^{\mathrm{KS}}[n(\mathbf{r})]$. The simplest approach is called the local density approximation (LDA). It was proposed already by W. Kohn and L. J. Shams in 1965 [102, 105]. The LDA assumes a local homogeneous electron gas within a small sub-volume of the electron system as the solution to the generally inhomogeneous problem. This is a harsh approximation, but computationally fast and simple to implement. In the LDA, the exchange-correlation energy is given by

$$V_{\mathrm{xc}}^{\mathrm{LDA}}[n(\mathbf{r})] = \int \mathrm{d}^3\mathbf{r}\, n(\mathbf{r})\, e_{\mathrm{xc}}[n(\mathbf{r})] \tag{3.13}$$

where $e_{\mathrm{xc}}[n(\mathbf{r})]$ is the exchange-correlation density per electron. Using (3.12) the local spin-dependent density approximation (LSDA) follows trivially from (3.13) [102]

$$V_{\mathrm{xc}}^{\mathrm{LSDA}}\left[n^{\uparrow}(\mathbf{r}), n^{\downarrow}(\mathbf{r})\right] = \int \mathrm{d}^3\mathbf{r}\left(n^{\uparrow}(\mathbf{r}) + n^{\downarrow}(\mathbf{r})\right) e_{\mathrm{xc}}\left[n^{\uparrow}(\mathbf{r}), n^{\downarrow}(\mathbf{r})\right] \tag{3.14}$$

The main limitation of the LDA are; (i) inhomogeneities in the system are never included, (ii) non-local exchange and correlation are never included and even strong local correlations does not reproduce in LDA. To improve the LDA, the electron density can be expanded in terms of the density gradient [102]

$$V_{\mathrm{xc}}^{\mathrm{GGA}}\left[n\left(\mathbf{r}\right)\right]=\int \mathrm{d}^{3}\mathbf{r}n\left(\mathbf{r}\right)e_{\mathrm{xc}}\left[n\left(\mathbf{r}\right)\right]F_{\mathrm{xc}}\left[n\left(\mathbf{r}\right),\nabla_{\mathbf{r}}n\left(\mathbf{r}\right)\right], \tag{3.15}$$

which is known as a generalized gradient approximation (GGA) [102, 106]. Including the density gradient allows for inhomogeneities in the electron system to be included. The enhancement factor F_{xc} is to a large extent arbitrary, and can be chosen to favor optimize calculation accuracy within a group of materials. Today many functionals have been developed to describe a wide range of systems. The standard 'initial guess' for a GGA functional is the Perdew-Burke-Ernzerhof (PBE) functional [103]. The enhancement factor in the PBE functional is a function of $s=\nabla_{\mathbf{r}}n\left(\mathbf{r}\right)/2k_{\mathrm{F}}n\left(\mathbf{r}\right)$ has the form $F_{\mathrm{xc}}=1+\kappa-\kappa/\left(1+\mu s^{2}/\kappa\right)$ where $\kappa=0.804$ and $\mu=0.21951$.

Many more advanced GGA related functionals, such as revPBE [107] and the meta-GGA's [103], are available in all modern DFT implementations. Further accuracy, especially when dealing with molecules, have been archived through the introduction of the hybrid-GGA's functional [103]. The rationale behind a hybrid-GGA, is that DFT and the analytical Hartree-Fock theory [103] typically introduce errors in opposite directions in the calculation, thus a suitable average between the two, $V_{\mathrm{xc}}^{\mathrm{hybrid}}\left[n\left(\mathbf{r}\right)\right]=\alpha V_{\mathrm{xc}}^{\mathrm{HF}}\left[n\left(\mathbf{r}\right)\right]+\left(1-\alpha\right)V_{\mathrm{xc}}^{\mathrm{DFT}}\left[n\left(\mathbf{r}\right)\right]$, will come very close to the experimental result.

Finally, in this thesis we have mainly performed DFT calculations using the non-local van der Waals (vdW) functional [108, 109], $V_{\mathrm{xc}}^{\mathrm{vdW\text{-}DF}}\left[n\left(\mathbf{r}\right)\right]$, which provide high accuracy in systems like graphite and water, but also metal amines and hydrates. The long range behavior of a correctly described vdW interaction should approach the classical dipole-dipole interaction $V\left(\mathbf{r},\mathbf{r}'\right)=-C/\left|\mathbf{r}-\mathbf{r}'\right|^{6}$ [103]. This interaction originates due to the electric field generated by fluctuations of the electron density in different parts of the systems. No local functional can capture this behavior. The vdW functional (vdW-DF) used in this thesis is made from three different parts [110]

$$V_{\mathrm{xc}}^{\mathrm{vdW\text{-}DF}}\left[n\left(\mathbf{r}\right)\right]=V_{\mathrm{x}}^{\mathrm{GGA}}\left[n\left(\mathbf{r}\right)\right]+V_{\mathrm{c}}^{\mathrm{LDA}}\left[n\left(\mathbf{r}\right)\right]+V_{\mathrm{c}}^{\mathrm{nl}}\left[n\left(\mathbf{r}\right)\right] \tag{3.16}$$

where the exchange energy $V_{\mathrm{x}}^{\mathrm{GGA}}\left[n\left(\mathbf{r}\right)\right]$ is taken from a GGA such as the revPBE functional, which was used for this work. The local part of the correlation energy $V_{\mathrm{c}}^{\mathrm{LDA}}\left[n\left(\mathbf{r}\right)\right]$ is sufficiently well described by a standard LDA when a non-local correction energy $V_{\mathrm{c}}^{\mathrm{nl}}\left[n\left(\mathbf{r}\right)\right]$ is added on top. $V_{\mathrm{c}}^{\mathrm{nl}}\left[n\left(\mathbf{r}\right)\right]$ is given by the overlap between two electrons in real space [108, 103]

$$V_{\mathrm{c}}^{\mathrm{nl}}\left[n\left(\mathbf{r}\right)\right]=\frac{1}{2}\int \mathrm{d}\mathbf{r}\int \mathrm{d}\mathbf{r}'n\left(\mathbf{r}\right)\Phi\left(\mathbf{r},\mathbf{r}'\right)n\left(\mathbf{r}'\right) \tag{3.17}$$

where the integration kernal $\Phi\left(\mathbf{r},\mathbf{r}'\right)=\Phi\left(q\left(n\left(\mathbf{r}\right),\nabla_{\mathbf{r}}n\left(\mathbf{r}\right)\right),q\left(n\left(\mathbf{r}'\right),\nabla_{\mathbf{r}'}n\left(\mathbf{r}'\right)\right)\right)$ is expressed in terms of a function q [].

The different electrons in the problem falls into two groups. I) Core electrons, which remain close to the nucleus and which do not play any role in the chemical properties

of the atom. The core electrons are treated as 'frozen', meaning that they are treated similar as in the isolated atom. 2) Valance electrons, responsible for making chemical bonds in solids and molecules and for the magnetic ground state observed in systems with $3d$, $4f$ or $5f$incomplete shells. These can not be treated as frozen. In the next section we introduce a method to describe both of these types of electrons, the so-called The Projected Augmented Wave (PAW) Method.

3.2.2 The Projected Augmented Wave Method

In order to perform a DFT calculation, a proper set of basis functions must be chosen to represent the single-particle wave functions in the Kohn-Shams equations (3.10).

The simplest effective description of the true many-body wave functions of a periodic system in real space, such as a solid, is by a plane wave expansion. The number of plane wave needed for a completely accurate description is in principle infinite, however, in reality the plane wave expansion can be truncated at a finite number without introducing any fatally large errors. In effect, all plane waves with kinetic energy lower than some cut-off, $\hbar^2\mathbf{k}^2/2m_e \leq \epsilon_{\text{cut-off}}$, are included and those above are not. The Γ-point ($\mathbf{k}$=$\mathbf{0}$) thus defines a sphere in reciprocal space of wave vectors with radius $\sqrt{2m_e\epsilon_{\text{cut-off}}/\hbar^2}$. The error introduced by this truncation scales directly with the size of the cut-off. This works best for the loosely bound valance electrons. However, the tightly bound core electrons in solids typically have many nodes and vary violently in small regions of space, thus they require an enormous number of plane waves for a decent accuracy, corresponding to a large kinetic energy cut-off.

Computationally, it is desirable to operate with as few basis function as possible, and various schemes have been developed over the years to describe the core state electrons in terms of smooth so-called pseudo-potentials instead of trying to capture the actual nature of the wave functions. Since the fundamental assumption of the pseudo-potentials are that the wave function of the core electron essentially does not matter, any aspects of the system involving these can not be accurately described. However, in recent years the Projected Augmented Wave method has proven to be a steady and precise alternative to the pseudo-potentials []. The PAW method treats the many electron wave function as a linear transformation of a smooth effective wave function, $|\psi\rangle = T|\tilde{\psi}\rangle$, and can as such include the original many-body wave function in the effective description. The smooth part of the many-body wave function are still described by plane wave, $\left|\tilde{\psi}\right\rangle = \sum_m c_m \left|\tilde{\psi_m}\right\rangle$. The many-body wave function is thus written as

$$|\psi\rangle = \left|\tilde{\psi}\right\rangle + \sum_m c_m \left[|\psi_m\rangle - \left|\tilde{\psi_m}\right\rangle\right] \tag{3.18}$$

leading to the electron density

$$n(\mathbf{r}) = \tilde{n}(\mathbf{r}) + n^1(\mathbf{r}) - \tilde{n}^1(\mathbf{r}) \tag{3.19}$$

where

$$\begin{aligned}
\tilde{n}(\mathbf{r}) &= \sum_i f_i \left|\tilde{\psi}_i(\mathbf{r})\right|^2, \\
n^1(\mathbf{r}) &= \sum_i f_i \sum_{mm'} \left\langle \tilde{\psi}_i \,\middle|\, \tilde{\psi}_m \right\rangle \psi_m^*(\mathbf{r})\, \psi_{m'}(\mathbf{r}) \left\langle \tilde{\psi}_{m'} \,\middle|\, \tilde{\psi}_i \right\rangle, \\
\tilde{n}^1(\mathbf{r}) &= \sum_i f_i \sum_{mm'} \left\langle \tilde{\psi}_i \,\middle|\, \tilde{\psi}_m \right\rangle \tilde{\psi}_m^*(\mathbf{r})\, \tilde{\psi}_{m'}(\mathbf{r}) \left\langle \tilde{\psi}_{m'} \,\middle|\, \tilde{\psi}_i \right\rangle.
\end{aligned}$$

A similar expressions can be derived for the total energy.

3.3 GPAW implementation

The DFT work presented in this thesis was performed with the using the real space grid-based projector-augmented wave method (GPAW) GPAW is an open source code developed for a large part in the physics department at DTU In a GPAW calculation, the electron density is evaluated directly on a real space grid using the PAW method, making the calculations easy to parallelize. The PAW method was described in section 3.2.2.

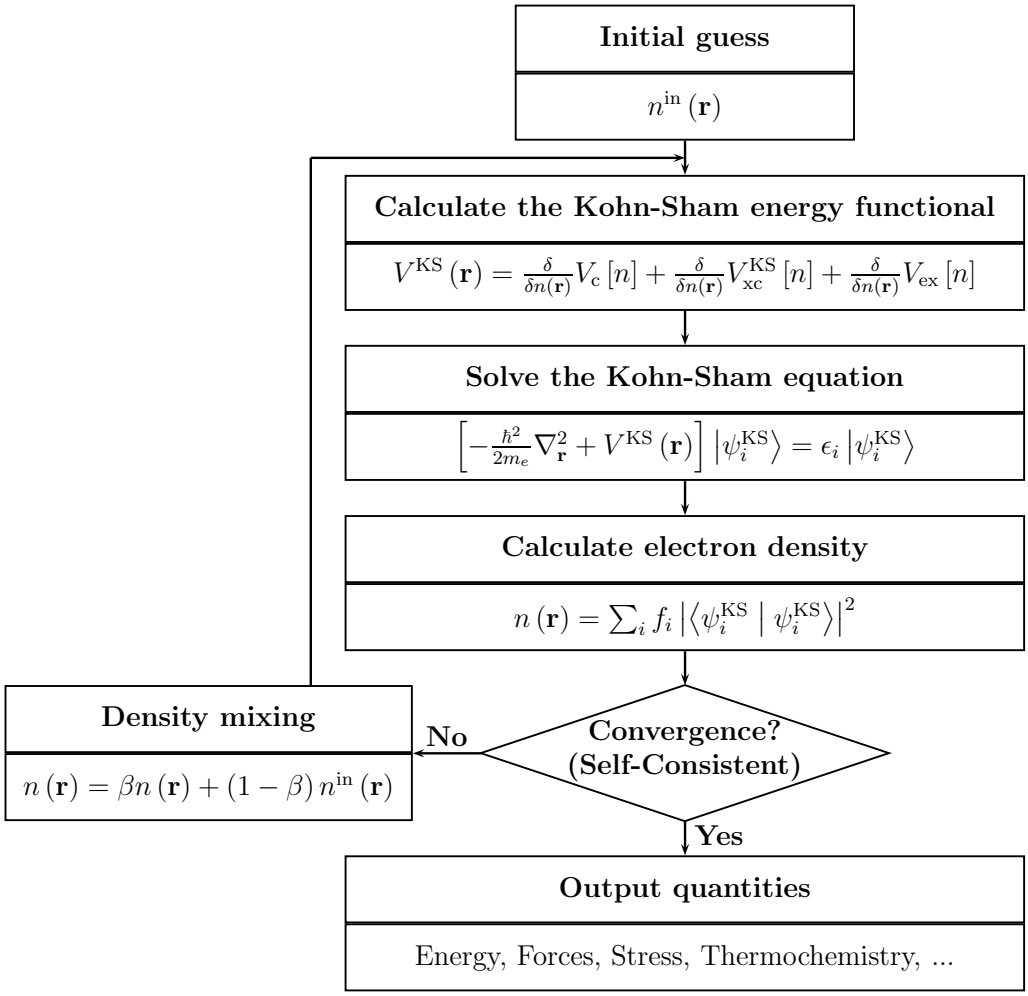

Figure 3.1: *The (simplified) algorithm used by most DFT codes. The Kohn-Sham equations are solved in a self-consistent loop until the forces of each atom are below a certain value. To avoid the so-called charge slushing, where the algorithm oscillates around the ground state without achieving convergence, the density obtained from the Kohn-Sham equations in step n is mixed with the density of step $n-1$. This figure is adapted from [102].*

CHAPTER 4

Introduction to Neutron Scattering

In this chapter we review the basic theory of neutron scattering needed to understand the later chapters of this thesis.

When the Nobel prize in physics was awarded to C. G. Shull and B. N. Brockhouse in 1994 for pioneering the field of neutron scattering as a probe to study solids and liquids. In the presentation speech of the 1994 Nobel prize in physics, the following famous quote appeared [111], *in simple terms, one could say that Shull answered the question of where atoms 'are' while Brockhouse answered the question of what they 'do'.* Still to this day, neutron scattering is the most direct way to obtain knowledge of both the structure and dynamical properties of magnetic systems.

Many excellent books are found on the various techniques in neutron scattering. I found these particularly helpful [112, 113, 114].

4.1 Basic Properties of the Neutron

The existence of the neutron was proven in 1932 by Sir James Chadwick, who was awarded the Nobel price in 1935 for the discovery. The neutron consists of three quarks, with the composition (udd) and as a result hereof it has no net electrical charge. The free neutron (outside the nucleus) is unstable, with a mean lifetime of about 15 min. The mean lifetime of the neutron is much longer than the flight-time a neutron spends in a typical scattering instrument and for all practical purposes, we can safely disregard all effects of decay in our experiments. Some basic properties of the neutron is listed in table 4.1. It is the internal motion of the quarks, that allows the neutron to have a magnetic moment even though it is electrically neutral.

Neutrons, used in typical scattering experiments, are produced in two ways. Neutrons can either be extracted from the core of fissions reactors or so-called spallations sources, where high energy protons (or a similar massive particle) collide with a heavy

target resulting in a burst of many particles, including neutrons. The typical values for a monochromatic neutron flux on the sample position are $10^8 \mathrm{cm}^{-2}\mathrm{s}^{-1}$. In comparison, a monochromatic photon flux from a third generation synchrotron X-ray source are in the range $10^{18}\mathrm{cm}^{-2}\mathrm{s}^{-1}$. Neutrons are much less abundant than photons, so neutron experiments are often more time consuming than X-ray experiments.

In both fission reactors and spallations sources, the created neutrons have kinetic energies in the MeV range. This in not desirable for condensed matter physics. In crystals the typical interatomic distances are measured in Å, and the quasi particle excitation energies, like magnons and acoustic phonons, are typically measured in meV.

The kinetic energy of the neutron are brought down by successive inelastic collisions in a so-called moderator. A moderator is a material which is a strong scatterer (high probability for e neutron to scatter from the nucleus) with a low absorption. Neutron absorption is a result of neutron induced nuclear reactions which merge the neutron with the atomic nucleus and emits other types of radiation instead. Typically, liquid water ($\sim$ 3004K) or liquid deuterium ($\sim$ 30K) are used to obtain thermal or cold neutrons respectively. Due to practical limitation or the moderator, the energy distribution of moderated neutrons will be a sum of Maxwellian distributions with the majority of the weight centered around the moderator energy.

Quantity	Value
mean lifetime	881.5 s
decay	$\mathrm{n}^0 \rightarrow \mathrm{p}^+ + \mathrm{e}^- + \bar{\nu}_\mathrm{e}$
rest mass	939.6 MeV/c^2
	1.675×10^{-24} g
spin	$\frac{1}{2} \times \hbar$
magnetic moment	$1.913\times\mu_\mathrm{N}$
charge	$0\times e$

Table 4.1: *Basic properties of the neutron*

4.2 Scattering Theory

In this section we introduce the the fundamental aspects of scattering. This is something which is found in most textbooks on quantum mechanics [115, 38], but typically not found in textbook on neutron scattering []. Figure 4.1 shows a generic scattering experiment.

Consider a monochromatic beam of neutrons with wave vector $\mathbf{k}_\mathrm{i}$. Sufficiently far away from the source, the spacial extent of the neutron wave function is well described by plane waves, i.e. $\psi_\mathrm{i}(\mathbf{r}) \propto e^{i\mathbf{k}_\mathrm{i}\cdot\mathbf{r}}$. Formally, the plane wave is obtained as the solution to the time-independent Schrödinger equation in the absence of any potential energy which could scatter the neutron.

$$\left(\nabla^2 + k_\mathrm{i}^2\right)\psi_\mathrm{i}(\mathbf{r}) = 0. \tag{4.1}$$

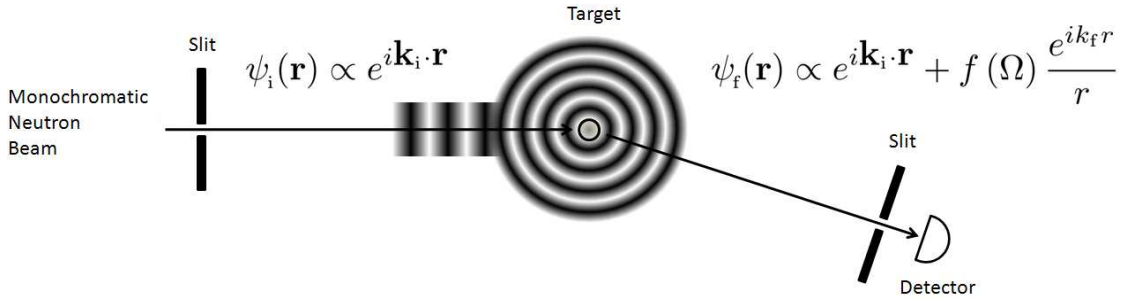

Figure 4.1: *A plane monochromatic neutron wave impinges on a sample, which produces a spherical wave. The spherical wave is weighted by the scattering amplitude, which is a function of a solid angle.*

Now we introduce a potential energy $V(\mathbf{r})$ in (4.1). A particular choice of $V(\mathbf{r})$ mimics a particular sample, in sections 4.4 and 4.5 we will present concrete examples, which are of relevance for the work in this thesis. $V(\mathbf{r})$ introduces scattering from the initial plane wave with $\mathbf{k}_{\mathrm{i}}$ into a new wave function with a different wave vector $\mathbf{k}_{\mathrm{f}}$. The time-independent Schrödinger equation (4.1) now takes the form

$$\left(\nabla^2 + k_{\mathrm{f}}^2\right)\psi(\mathbf{r}) = V(\mathbf{r})\,\psi(\mathbf{r}). \tag{4.2}$$

The solution of inhomogeneous equation (4.2) is added to the initial plane wave, which was the solution to the homogeneous equation (4.1), yielding

$$\psi(\mathbf{r}) = \psi_{\mathrm{i}}(\mathbf{r}) + \int \mathrm{d}\mathbf{r}' G(\mathbf{r},\mathbf{r}')\,V(\mathbf{r})\,\psi(\mathbf{r}'), \tag{4.3}$$

when $G(\mathbf{r},\mathbf{r}')$ is a so-called Green function. It must satisfy

$$\left(\nabla^2 + k_{\mathrm{k}}^2\right)G(\mathbf{r},\mathbf{r}') = \delta(\mathbf{r}-\mathbf{r}'). \tag{4.4}$$

Equation (4.4) has the solution

$$\begin{aligned} G(\mathbf{r},\mathbf{r}') &= -\frac{1}{4\pi}\frac{e^{ik_{\mathrm{f}}|\mathbf{r}-\mathbf{r}'|}}{|\mathbf{r}-\mathbf{r}'|} \\ &= -\frac{1}{4\pi}\frac{e^{ik_{\mathrm{f}}r}}{r}e^{-i\mathbf{k}_{\mathrm{f}}\cdot\mathbf{r}'}, \end{aligned} \tag{4.5}$$

8 where the last step is valid far away from the sample ($r >> r'$). Equation (4.5) is the wave function of a spherical wave. The integral equation (4.3) may be solved self-consistently by iterations. The resulting infinite series is known as the Born series

[38]. The first few terms in the Born series are as follows

$$\begin{aligned}
\psi^0(\mathbf{r}) &= \psi_{\mathrm{i}}(\mathbf{r}) && (4.6)\\
\psi^1(\mathbf{r}) &= \psi_{\mathrm{i}}(\mathbf{r}) + \int \mathrm{d}\mathbf{r}' G(\mathbf{r},\mathbf{r}') V(\mathbf{r}) \psi_{\mathrm{i}}(\mathbf{r}') && (4.7)\\
\psi^2(\mathbf{r}) &= \psi_{\mathrm{i}}(\mathbf{r}) + \int \mathrm{d}\mathbf{r}' G(\mathbf{r},\mathbf{r}') V(\mathbf{r}) \psi_{\mathrm{i}}(\mathbf{r}') && (4.8)\\
&\quad + \int\int \mathrm{d}\mathbf{r}''\mathrm{d}\mathbf{r}' G(\mathbf{r},\mathbf{r}') V(\mathbf{r}) G(\mathbf{r}',\mathbf{r}'') V(\mathbf{r}') \psi_{\mathrm{i}}(\mathbf{r}') && (4.9)\\
\psi^3(\mathbf{r}) &= \dots
\end{aligned}$$

Neutron scattering experiment are well described within the first Born approximation, which including terms up to first order in the series ψ^1. Using (4.3) and (4.5) and the first Born approximation, the solution of (**??**) is directly written as [115]

$$\begin{aligned}
\psi(\mathbf{r}) &= \psi_{\mathrm{i}}(\mathbf{r}) - \frac{1}{4\pi}\frac{e^{ik_{\mathrm{f}}r}}{r}\int \mathrm{d}\mathbf{r}' e^{-i\mathbf{k}_{\mathrm{f}}\cdot\mathbf{r}'} V(\mathbf{r}) e^{i\mathbf{k}_{\mathrm{i}}\cdot\mathbf{r}} && (4.10)\\
&= \psi_{\mathrm{i}}(\mathbf{r}) - \frac{1}{4\pi}\frac{e^{ik_{\mathrm{f}}r}}{r}\int \mathrm{d}\mathbf{r}' e^{i\mathbf{Q}\cdot\mathbf{r}'} V(\mathbf{r}),
\end{aligned}$$

where we have introduced the momentum transfer $\mathbf{Q} = \mathbf{k}_{\mathrm{i}} - \mathbf{k}_{\mathrm{f}}$.

Scattering experiments falls within two main categories. Elastic scattering from a crystal has $|\mathbf{k}_{\mathrm{i}}| = |\mathbf{k}_{\mathrm{f}}| = k$ and if the Bragg condition, $\mathbf{Q} = \boldsymbol{\tau} = \mathbf{k}_{\mathrm{i}} - \mathbf{k}_{\mathrm{f}}$ where $\boldsymbol{\tau}$ is a reciprocal lattice vector, is satisfied, we obtain the relation known as Bragg's law $\tau = 2k\sin(\theta)$ where 2θ is the angle between the incident and the final neutron wave vectors.

Inelastic scattering has $|\mathbf{k}_{\mathrm{i}}| \neq |\mathbf{k}_{\mathrm{f}}|$ and is in addition associated with an energy transfer $\hbar\omega = \epsilon_f - \epsilon_i$ between the neutron and an excitation in the crystal. If $\mathbf{k}_{\mathrm{f}} > \mathbf{k}_{\mathrm{i}}$ and $\hbar\omega > 0$ energy is transfered from the neutron to the crystal, and in this process an excitation can be created. However, if $\mathbf{k}_{\mathrm{f}} < \mathbf{k}_{\mathrm{i}}$ and $\hbar\omega < 0$ energy is in stead transfered to the neutron from the crystal, and an excitation can be annihilated. The momentum transfer of such a process is given by $\mathbf{Q} = \boldsymbol{\tau} + \mathbf{q} = \mathbf{k}_{\mathrm{i}} - \mathbf{k}_{\mathrm{f}}$ where $\mathbf{q}$ is the excitation momentum within the first Brillouin zone.

4.3 The Neutron Scattering Cross-Section

The fundamental quantity, which is measured during a neutron scattering experiment, is the scattering cross section. We call this quantity σ. If Ψ is a constant flux[1] of neutrons impinging on a sample which is covered by detectors in the entire (solid

[1] A flux of any kind of particle beam is defines as

$$\Psi = \frac{\text{number(\#) of particles impinging on a surface per second}}{\text{surface area normal to the particle beam}}.$$

angle) 4π, then the neutron cross section σ is simply the total number of scattered neutron (including all energies) from the sample normalized by Ψ. However, Not even the largest neutron detectors cover 4π, instead, the differential neutron cross section $\mathrm{d}\sigma/\mathrm{d}\Omega$ include only neutrons scattered into a certain solid angle $\mathrm{d}\Omega$, but the differential neutron cross section still including all energies.

Many real world experiments are inelastic, the point of an inelastic scattering experiment is exactly to analyze the energy of the scattered neutrons. Further below discuss some instrumentation for inelastic neutron scattering, and to deal with these, we introduce the partial differential cross section $\mathrm{d}\sigma^2/\mathrm{d}\Omega\mathrm{d}\epsilon_f$ which takes into account the energy dependence of the scattered neutrons.

The probability for a neutron to scatter by the potential V from the initial quantum state $|i\rangle$ into the a final quantum state $|f\rangle$ with different momentum and energy, is given by Fermi's golden rule [115]

$$\Gamma_{i\to f} = \frac{2\pi}{\hbar}\frac{\mathrm{d}n}{\mathrm{d}\epsilon_f}\left|\langle f|\,V\,|i\rangle\right|^2\delta\left(\epsilon_i-\epsilon_f\pm\hbar\omega\right) \tag{4.11}$$

where the energy conservation dictates the excitation $\hbar\omega=\epsilon_f-\epsilon_i$, and $\frac{\mathrm{d}n}{\mathrm{d}\epsilon_f}$ is the density of final states for the neutron. The expression (4.11) is generally valid for inelastic ($\hbar\omega\neq 0$) as well as elastic ($\hbar\omega=0$) scattering. The partial differential cross section follows directly from (4.11)

$$\begin{aligned}\frac{\mathrm{d}^2\sigma}{\mathrm{d}\Omega\mathrm{d}\epsilon_f} &= \frac{1}{\Psi}\frac{\Gamma_{i\to f}\text{ into }\mathrm{d}\Omega}{\mathrm{d}\Omega}\\ &= \frac{k_f}{k_i}\left(\frac{m_n}{2\pi\hbar}\right)^2\left|\langle f|\,V\,|i\rangle\right|^2\delta\left(\epsilon_i-\epsilon_f\pm\hbar\omega\right)\end{aligned} \tag{4.12}$$

where k_i and k_f are the size neutron wave vector before and after the scattering respectively.

From the partial differential cross section one can obtain the energy independent differential cross section and the total cross section by the relations [112, 113, 114]

$$\frac{\mathrm{d}\sigma}{\mathrm{d}\Omega} = \int \mathrm{d}\epsilon_f\frac{\mathrm{d}^2\sigma}{\mathrm{d}\Omega\mathrm{d}\epsilon_f} \tag{4.13}$$

$$\sigma = \int\int \mathrm{d}\epsilon_f\mathrm{d}\Omega\frac{\mathrm{d}^2\sigma}{\mathrm{d}\Omega\mathrm{d}\epsilon_f} \tag{4.14}$$

4.4 Neutron-Nucleus Interaction

In this section we introduce the scattering potential of a single atomic nucleus. The interaction between neutrons and the atomic nuclei is via the strong nuclear force which is very short ranged. The typical extent of the atomic nucleus is of the order fm (10^{-15}m). This is very small compared to the wavelength of neutrons typically used in scattering experiments, which is of the order of Å(10^{-10}m). Therefore the scattering potential may be approximated by a delta function without introducing any noticeable

error. Consider a single nucleus at the position $\mathbf{r}_d$. We can model the neutron-nucleus interaction by the so-called Fermi pseudopotential [112, 113, 114]

$$V_j(\mathbf{r}) = \frac{2\pi\hbar^2}{m_n} b_d \delta(\mathbf{r} - \mathbf{r}_d) \tag{4.15}$$

where the constant b_d is known as the scattering length. This number varies randomly throughout the periodic table and even within families of the isotopes and different spin states. This gives rise to both coherent scattering, from the mean value of $\langle b_d \rangle = \sum_d f_d b_d$ and incoherent scattering from the variance $\left(\langle b_d^2 \rangle - \langle b_d \rangle^2\right)^{1/2}$.

Because of the random nature of the scattering length, every nuclei should be assigned a distribution f_d of scattering lengths centered around b_d, where $\sum_d f_d = 1$. It is rare that all nuclei in a sample is exactly the same isotope. In special cases chemists can do a controlled synthesis and favor a certain isotope. This might be necessary if the majority of the naturally occurring isotopes is a strong absorber. However, the vast majority of samples studied with neutron scattering posses an intrinsic 'chemical randomness' of isotopes.

Also the temporally short lived bound state formed between the nuclear spin of every isotope and the unpolarized neutrons[2] randomizes the scattering length. Considering only a single isotope, the different number of quantum states associated with either adding a neutron with $s = 1/2$ (spin-triplet) or with $s = -1/2$ (spin-singlet) to the nuclear spin I result in a average scattering length $\langle b_d \rangle = ((I+1)b_d^{\text{triplet}} + I b_d^{\text{singlet}})/(2I+1)$.

In a neutron scattering experiment, the objective is most often to measure the coherent scattering σ_{coh}, while the incoherent scattering σ_{inc} manifest itself as undesirable background.

4.4.1 The Nuclear Scattering Cross Section

The general partial differential cross scattering for neutron-nuclear scattering presented below was originally derived by Van Hove in 1954 [116]. The derivation is presented in many textbooks [112, 113, 114], so we shall only quote the final expression here. Assuming a crystalline sample, we have

$$\frac{\mathrm{d}^2\sigma}{\mathrm{d}\Omega \mathrm{d}\epsilon_f} = \frac{k_f}{k_i} \mathcal{S}(\mathbf{Q}, \omega) \tag{4.16}$$

where

$$\begin{aligned} \mathcal{S}(\mathbf{q}, \omega) &= \frac{1}{2\pi\hbar} \int \mathrm{d}t e^{-i\omega t} \sum_{jd} \sum_{j'd'} b_d b_{d'} e^{-i\mathbf{Q}\cdot\left(\mathbf{r}_j - \mathbf{r}_{j'}\right)} e^{-i\mathbf{Q}\cdot(\mathbf{r}_d - \mathbf{r}_{d'})} \\ &\quad \times \left\langle e^{-i\mathbf{Q}\cdot\mathbf{u}_{jd}(0)} e^{i\mathbf{Q}\cdot\mathbf{u}_{j'd'}(t)} \right\rangle. \end{aligned} \tag{4.17}$$

Expression (4.17) is essentially a Fourier transform of the two-point density correlation function. In (4.17) $\mathbf{r}_j$ refers to the position of the j'th unit cell and $\mathbf{r}_d$ is the equilibrium

[2] A beam of neutrons containing on average an equal amount of neutrons with $s = 1/2$ and $s = -1/2$.

position of the d'th basis atom. If $\mathbf{a}$, $\mathbf{b}$ and $\mathbf{c}$ are the primitive unit vectors of the lattice, then any lattice vector is written as $\mathbf{r} = x\mathbf{a} + y\mathbf{b} + z\mathbf{c}$ where x, y and z are integers. The time-dependent operator $\mathbf{u}_{jd}(t)$ describe the thermal displacement of the d'th atom from $\mathbf{r}_d$. The expression 4.17 is generally valid for both elastic (diffraction) and inelastic (spectroscopic) nuclear scattering from e.g. phonons. However, scattering from phonons will not be discussed further in this thesis because it has not played a major role in our investigations.

The nuclear differential cross section is obtained directly from 4.16 by integration out the energy degree of freedom

$$\frac{\mathrm{d}\sigma}{\mathrm{d}\Omega} = N\frac{(2\pi)^2}{V_0}e^{-2W(\mathbf{Q})}\left|F_N(\mathbf{Q})\right|^2\sum_{\boldsymbol{\tau}}\delta(\mathbf{Q}-\boldsymbol{\tau}), \tag{4.18}$$

where the nuclear structure factor $|F_N(\mathbf{Q})|$ is given by

$$|F_N(\mathbf{Q})| = \sum_d \langle b_d\rangle\, e^{-i\mathbf{Q}\cdot\mathbf{r}_d}.$$

The exponential factor $\exp(-2W(\mathbf{Q}))$ is the Debye-Waller factor [114]. It is often a useful approximation that the Debye-Waller factor is equal to 1. The nuclear differential cross section (4.18) contains $\delta(\mathbf{Q}-\boldsymbol{\tau})$ meaning that it hold exclusively when the Bragg condition $\boldsymbol{\tau} = \mathbf{q}$ is satisfied. The set of integers h, k and l defining the reciprocal lattice vector $\boldsymbol{\tau} = h\mathbf{a}^* + k\mathbf{b}^* + l\mathbf{c}^*$ then represents the plane of atoms which is perpendicular to $\mathbf{Q}$.If $|F_N(\mathbf{Q}=\boldsymbol{\tau})| \neq 0$, the resulting peak in $(\mathbf{Q},\omega)$-space is known as a Bragg peak.

4.5 Neutron-Electron Interaction

The neutron has neutral net charge. As a consequence the neutron does not scatter from the Coulomb potential associated with the electron charge. However, the neutron does posses a magnetic moment $\boldsymbol{\mu}_n = -\gamma\mu_N\boldsymbol{\sigma}$ where $\gamma = 1.913$ and $\mu_N = 5.051\times10^{-27}\mathrm{Am}^2$.

The dipole field created by the neutron couples to the magnetic moment of an unpaired electron through the Zeeman Hamiltonian, which produces a finite probability for scattering the neutron.

Consider a single electron at position $\mathbf{r}_j$ with momentum $\mathbf{p}$. The dipole field at any other position $\mathbf{r}$ is given by $\mathbf{H} = \frac{\mu_0}{4\pi}\left[\nabla\times\left(\frac{\boldsymbol{\mu}_e\times(\mathbf{r}-\mathbf{r}_j)}{|\mathbf{r}-\mathbf{r}_j|^3}\right) - \frac{2\mu_B}{\hbar}\frac{\mathbf{p}\times(\mathbf{r}-\mathbf{r}_j)}{|\mathbf{r}-\mathbf{r}_j|^3}\right]$ where $\boldsymbol{\mu}_e = -g\mu_B\mathbf{S}_j$ is the magnetic moment of the electron where using $g = 2.002$ for free electrons and $\mu_B = e\hbar/2m_e = 6.274\times10^{-24}$ is the Bohr magneton. We arrive at the neutron-electron interaction [112, 113, 114]

$$\begin{aligned} V_j(\mathbf{r}) &= -\boldsymbol{\mu}_n\cdot\mathbf{H} \\ &= -(\gamma r_0)\,\boldsymbol{\sigma}_n\cdot\left[\nabla\times\left(\frac{\boldsymbol{\mu}_e\times(\mathbf{r}-\mathbf{r}_j)}{|\mathbf{r}-\mathbf{r}_j|^3}\right) - \frac{2\mu_B}{\hbar}\frac{\mathbf{p}\times(\mathbf{r}-\mathbf{r}_j)}{|\mathbf{r}-\mathbf{r}_j|^3}\right] \end{aligned} \tag{4.19}$$

where $r_0 = 2.818$fm and the first term describe the dipole interaction between the magnetic moment of the neutron and the magnetic moment of the electron (spin).

The second term describe the interaction due to the magnetic field created when the electron has non-zero angular momentum. A filled atomic shell have zero spin i.e. no unpaired electrons, and can not contribute to any magnetic response. Magnetism arise solely in systems with unfilled atomic shells.

4.5.1 The Magnetic Scattering Cross Section

Like with the nuclear partial differential cross scattering, the derivation of the general expression of the magnetic partial differential cross scattering is given in many textbooks [112, 113, 114], so we only quote the final result here. Assuming a magnetically ordered crystal, we have

$$\frac{\mathrm{d}^2\sigma}{\mathrm{d}\Omega\mathrm{d}\epsilon_f} = \frac{k_f}{k_i}\left(\gamma r_0\right)^2 e^{-2W(\mathbf{Q})}\left|\frac{g}{2}F\left(\mathbf{Q}\right)\right|^2 \sum_{\alpha\beta}\left(\delta_{\alpha\beta}-\hat{Q}_\alpha\hat{Q}_\beta\right)\mathcal{S}^{\alpha\beta}\left(\mathbf{Q},\omega\right) \quad (4.20)$$

where α and β run over the Cartesian coordinates, and

$$\mathcal{S}^{\alpha\beta}\left(\mathbf{Q},\omega\right) = \frac{1}{2\pi\hbar}\int \mathrm{d}t e^{-i\omega t}\sum_{jd}\sum_{j'd'} e^{-i\mathbf{Q}\cdot\left(\mathbf{r}_{jd}-\mathbf{r}_{j'd'}\right)}\left\langle S^\alpha_{jd}\left(0\right)S^\beta_{j'd'}\left(t\right)\right\rangle \quad (4.21)$$

is the dynamical scattering function, and

$$F\left(\mathbf{Q}\right) = 2\int \mathrm{d}\mathbf{r}\rho_s\left(\mathbf{r}\right)\exp\left(i\mathbf{Q}\cdot\mathbf{r}\right) \quad (4.22)$$

is the magnetic form factor with g being the Landé factor [112]. The dynamical scattering function (4.21) is essentially a Fourier transform of the two-point spin correlation function. If (4.21) is integrated over all energies inside the first Brillouin zone, one finds $\sum_{\alpha\beta}\int \mathrm{d}\omega\int \mathrm{d}\mathbf{Q}\mathcal{S}^{\alpha\beta}\left(\mathbf{Q},\omega\right) \propto S\left(S+1\right)$ which gives a qualitative measure of the distribution between elastic magnetic scattering and inelastic magnetic scattering. The elastic magnetic scattering is generally proportional to S^2 and hence dominates the scattering function.

The famous fluctuation dissipation theorem relates the dynamical scattering function to the linear response to a time and space varying magnetic field, expressed by the generalized susceptibility χ. We find the relation

$$\mathcal{S}^{\alpha\beta}\left(\mathbf{Q},\omega\right) = \left(n_{\mathrm{B}}\left(\omega\right)+1\right)\chi''_{\alpha\beta}\left(\mathbf{Q},\omega\right) \quad (4.23)$$

where χ'' is the imaginary part of the susceptibility and $n_{\mathrm{B}}\left(\omega\right)$ is the Bose occupation factor. Where experiments can measure the scattering function, theoretical model can often calculate the susceptibility. The most successful of these model is the random phase approximation (RPA), see chapter 5.

The geometrical factor $\sum_{\alpha\beta}(\delta_{\alpha\beta}-\hat{Q}_\alpha\hat{Q}_\beta)$ in (4.20) prohibits any scattering from spin direction parallel to $\mathbf{Q}$ from being observed with neutron scattering.

Similar to (4.18), the magnetic differential cross section is obtained from 4.20 by integrating out the energy degree of freedom

$$\begin{aligned}\frac{\mathrm{d}\sigma}{\mathrm{d}\Omega} &= N\frac{(2\pi)^2}{V_0}(\gamma r_0)^2 \exp\left(-2W(\mathbf{Q})\right)\left|\frac{g}{2}F(\mathbf{Q})\right|^2 |F_M(\mathbf{Q})|^2 \\ &\quad \times \sum_{\alpha\beta}\left(\delta_{\alpha\beta}-\hat{Q}_\alpha\hat{Q}_\beta\right)\sum_{\boldsymbol{\tau}}\delta(\mathbf{Q}-\boldsymbol{\tau}) \end{aligned} \tag{4.24}$$

where

$$F_M(\mathbf{Q}) = \sum_d e^{-i\mathbf{Q}\cdot r_d}\langle S_d\rangle \tag{4.25}$$

which is the magnetic structure factor. Similar to the nuclear differential cross section, its magnetic counterpart produces magnetic Bragg peaks from the lattice formed by ordered electronic spins. Ferromagnetic (FM) order would hence produce magnetic Bragg peaks on the exact same integer positions in the Brillouin zone as the nuclear Bragg peaks from an ordered crystal, but antiferromagnetic- (AFM) and any type of incommensurate order produce peaks at non-integer positions in the Brillouin zone.

4.6 Neutron Instruments

4.6.1 Triple-Axis Spectrometers

The Triple-axis Spectrometer (TAS) is the basic workhorse in neutron spectroscopy studies, available in the instrumentation toolbox. It has great flexibility i.e access to a large part of the $(\mathbf{Q}, \hbar\omega)$-space, and it can be used equally well for elastic and inelastic investigations. A typical layout of a TAS is shown in figure 4.6.1.

The TAS utilizes Bragg scattering, typically from pyrolytic graphite, to a monochromate and analyze the energy of the neutron beam. Before the sample the monochromator (ideally) select a single wavevector $\mathbf{k}_i$ from a white beam, and after the sample, the analyzer scans the energy of the scattered neutron beam. In reality, singling out a completely well defined wave vector, k, and transporting it through the instrument and the sample is not possible due to finite divergence and mosaicity.

The transmission function of every TAS component produces a sharply peaked distribution of wave vectors centered around the desired k, the convolution of these distributions defines an experimental resolution, $R(\mathbf{Q}'-\mathbf{Q}, \omega'-\omega)$, where $\mathbf{Q}' = \mathbf{Q} + \Delta\mathbf{Q}$ and $\omega' = \omega + \Delta\omega$. The resulting neutron intensity is given by a convolution of the neutron scattering cross section and the experimental resolution

$$I(\mathbf{Q},\omega) \propto \int \mathrm{d}\mathbf{Q}' \int \mathrm{d}\omega' \mathcal{S}(\mathbf{Q}',\omega') R(\mathbf{Q}'-\mathbf{Q},\omega'-\omega). \tag{4.26}$$

Various TAS instruments exists on user facilities around the world. During my PhD studies I have worked on RITA II at the Paul Scherrer Institute [117]. RITA II is a

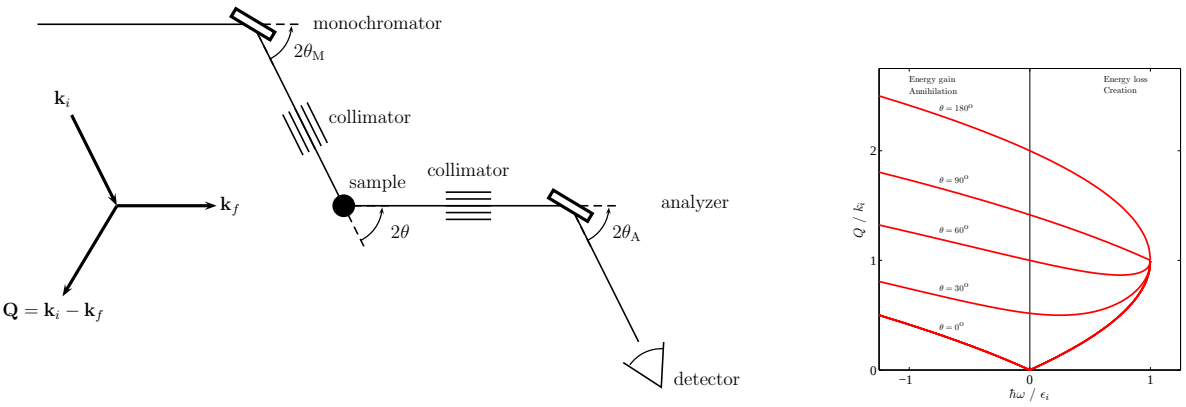

Figure 4.2: *Schematic layout of a triple axis spectrometer. The TAS own its name to the following threes rotations; The first axis of the TAS is defined by the rotated of the monochromator, $2\theta_M$, with respect to the initial beam direction. The second axis is defined by the rotation 2θ due to scattering by the sample. Finally, the third axis is defined by the rotation of the analyzer, with respect to the scattered beam direction. A collimator is an assembly of thin neutron absorbing sheets which helps to minimize beam divergence.*

so-called multi-analyzer TAS with 9 analyzer blades [118, 119]. FLEX (FLEXX) at the Helmholtz-Zentrum Berlin für Materialien und Energie. FLEX uses only a single analyzer blade, but has the unique possibility to apply a 17.5T magnetic field to the sample.

4.6.2 Spin-Echo Spectrometers

Neutron spin-echo (NSE) spectroscopy is performed using a modified version of the polarized TAS. It offers a greatly improved energy resolution in the μeV range, which is completely decoupled from the original TAS resolutions.

Figure 4.3 shows the basic layout of the NSE instrument TRISP. Two radio frequency (rf) coils are placed in front the sample position (front set) and two are placed after (back set).

Each coil produces two magnetic fields, a static field H_z which is directed perpendicular to the neutron beam direction, and an AC-field H_{xy} which is rotating in the (x, y)-plane at a frequency ω. The resulting field is equation of motion for the neutron spin is

$$\frac{\mathrm{d}\mathbf{S}}{\mathrm{d}t} = \mathbf{S} \times \gamma_N \mathbf{H} \tag{4.27}$$

where $\gamma_N = 183.3\text{MHz/T}$ and

$$\mathbf{H}(\mathbf{r},t) = H_z\hat{z} + H_{xy}\left(\cos(\omega t)\,\hat{x} + \sin(\omega t)\,\hat{y}\right) \tag{4.28}$$

This setup is used to produce so-called $\pi/2$ and π spin flip of the neutron [120]. One can show [120, 121] that the phase which is picked up by the neutron spin after passing a set of coils is $\phi = \omega L/v$ where L is the length between the coils and v is the velocity of the neutron. This phase would be exactly the same, if the neutron had passed a homogeneous effective magnetic field $H_{eff} = 2H_z$ which filled the entire region between the coils.

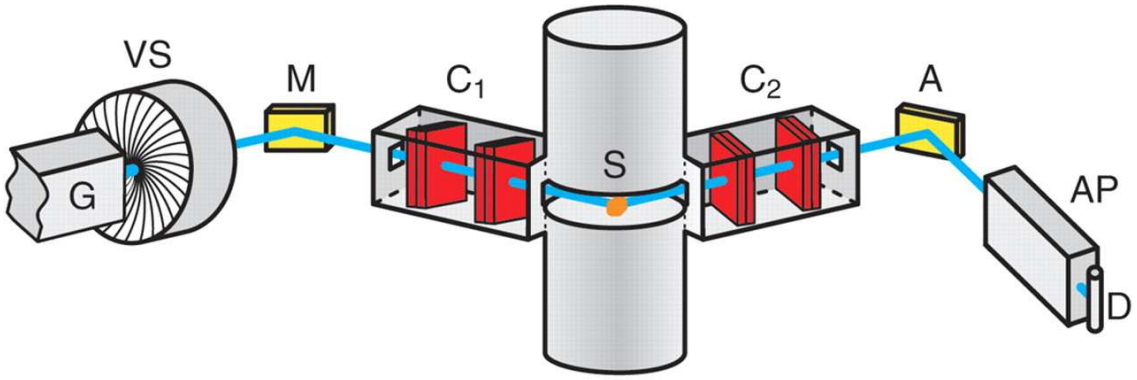

Figure 4.3: *Schematic layout of the NES instrument TRISP. A polarized neutron beam emerge from the supermirror guide (G) and is monochromatized by a PG(200) monochromator (M). The front set of coils (C_1) and the back set of coils (C_2) provide the effective field needed for the spin-echo. The neutron beam scatter of the sample (S) and into the PG(200) analyzer (A), and finally through the Heusler analyser (AP) and into the detector D.*

The effective field of the front and back set of coils are adjusted such that, if a neutron scatters elastically from the sample i.e. the initial velocity v_i is equal to the final velocity v_f, then the phase picked up in the front set coils is exactly countered by the back set.

If instead, a neutron scatters inelastically from the sample, the final velocity v_f is different from the initial velocity v_i, and the phase of the neutron spin have acquired a net phase after having traveled both sets of coils. This phase is defined by the relation [120, 121]

$$\phi = \omega\tau_\text{NSE} \tag{4.29}$$

where the so-called spin echo time is given by

$$\begin{aligned}\tau_\text{NSE} &= \frac{\hbar\omega_\text{L}L}{m_\text{N}v_\text{i}^3} \\ &= 1.864\times10^{-12}\times H_{eff}\,[\text{T}]\times L\,[\text{cm}]\times\lambda^3\,[\text{Å}]\,.\end{aligned} \tag{4.30}$$

The polarization of the neutron spin can subsequently be analyzed using a Heusler analyzer. We expect the polarization e.g. parallel to the x-axis, to vary as function of spin-echo time according to

$$P(\tau_{\mathrm{NSE}}) = \int \mathrm{d}\omega \mathcal{S}(\mathbf{Q},\omega)\cos(\omega\tau_{\mathrm{NSE}}), \tag{4.31}$$

which is the cosine Fourier transform of the dynamical scattering function $\mathcal{S}(\mathbf{Q},\omega)$ with respect to energy. A quasi elastic Bragg peak is well described by a Lorentzian peak shape

$$S(\mathbf{0},\omega) = \frac{\Gamma}{\Gamma^2 + (\hbar\omega)^2}, \tag{4.32}$$

leading to an exponential (de)polarization of the neutron spin as function of spin-echo time

$$P(\tau_{\mathrm{NSE}}) = \exp(-\Gamma\tau_{\mathrm{NSE}}). \tag{4.33}$$

During my studies I have worked on the NSE instrument TRISP, which is located on the FRM II thermal reactor source. The neutron beam is polarized be means of a supermirror. TRISP's main use falls within the study of excitation lifetimes in solids, where the excellent energy resolution is more impotent than the $\mathbf{Q}$ resolution.

I have used TRISP to study the quasi elastic linewidth of the incommensurate antiferromagnetic order in $La_{2-x}Sr_xCuO_4$ with $x = 0.12$. I have done this to make a direct comparison of the magnetic transition temperature obtained with muon spin rotation, see chapter 10.

4.6.3 Time of Flight Neutron Scattering

Time-of-flight (TOF) neutron scattering uses a wall covered in detectors to cover as large a part of $(\mathbf{Q},\hbar\omega)$-space as possible and the, instead of using an analyzer crystal to scan the energy of the scattered neutrons, TOF uses the flight time of the neutron to discriminate in energy. The TOP principle discussed below is also referred to as a 'direct geometry'. Figure 4.4 shows the basic layout of the TOF instrument Cold Neutron Chopper Spectrometer (CNCS).

A TOF instrument uses neutron/Fermi choppers, which are rotating mechanical discs designed to block the neutron beam for some fraction of each revolution of the chopper. the Fermi chopper transmit a very narrow pulse of neutrons with a well defined (initial) energy. In addition, the detectors are placed in a semi-circle around the sample position, so the total flight distance L is the same for all neutrons. From the initial velocity, and the time difference between the neutron pulse leaves the Fermi chopper and the neutrons are registered in one of the detectors, the final velocity can be calculated. If $\hbar\omega = 0$ the neutron arrive at the detector at the time $t_0 = v_{\mathrm{i}}/L$. So-called Bandwidth choppers placed in close connection with the Fermi choppers to further narrow the pulse.

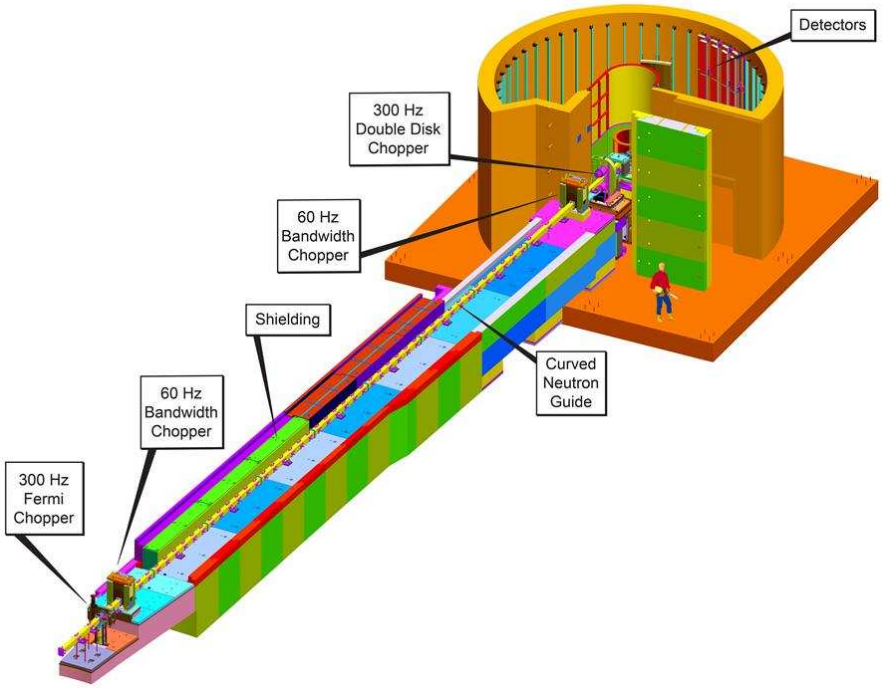

Figure 4.4: *Schematic layout of the TOF instrument CNCS. The chopper systems create a well defined pulse of neutrons with a well defined velocity. The flight time is used to analyze the energy of the neutron after scattering from the sample.*

If $\hbar\omega < 0$ the neutrons gained energy when scattered off the sample, they arrive before t_0, wheres if $\hbar\omega > 0$ the neutrons lost energy when scattered off the sample and they arrive after t_0.

During my studies I have worked on the TOF instrument CNCS, which is located on the SNS spallation source. CNCS provide great flexibility and can be used to study a vast variety of scientific problems. The incident wavelength can be chosen in the range $0.5 - 80$meV and the wave vector transfer cover $0.05 - 10$Å^{-1}. The detector coverage is $-50°$ to $+135°$ horizontally and $\pm 16°$ vertically. I have used CNCS to study the spin wave dispersion in $CoCl_2 \cdot 2D_2O$.

CHAPTER 5

Neutron Scattering studies of a Quantum Phase Transition of the Quasi-Ising Antiferromagnet $CoCl_2 \cdot 2D_2O$

In this chapter I present my studies of the field tuned quantum phase transition in $CoCl_2 \cdot 2D_2O$ at low temperature.

We started this study to investigate how similar $CoCl_2 \cdot 2D_2O$, a reported Ising-like chain system [122, 123, 124], was to $CoNb_2O_6$ which had recently been published showing a rich excitation spectrum as function of transverse field that could be explained as Ising chain with non-vanishing interchain interaction [125]. It was originally shown by [124] that $CoCl_2 \cdot 2D_2O$ does display a transverse field quantum phase transition at $\mu_0 H_c = 16.2$T.

The low-temperature magnetic properties of $CoCl_2 \cdot 2D_2O$ can to a good approximation be described by an effective $S = 1/2$ model with anisotropic, primarily Ising-like, exchange interactions and anisotropic g-factors. The dominant interactions are ferromagnetic and couple nearest neighbor spins lying on chains oriented along the crystallographic c-axis [126]. Weaker inter-chain interactions give rise to commensurate antiferromagnetic order below T_N=17.2 K. $CoCl_2 \cdot 2D_2O$ is then in the same quasi-1D Ising-like symmetry class as $CoNb_2O_6$ [125]. Indeed, as will be shown below $CoCl_2 \cdot 2D_2O$ and $CoNb_2O_6$ share remarkably similar phase diagrams in an applied field longitudinal to the spin direction. However, the spectrum will be modified by the different ratio of inter-chain to intra-chain couplings, and by differences associated with the degree to which the dominant intrachain interaction can be approximated by the pure Ising model.

5.1 Crystal and Magnetic Structure of $CoCl_2 \cdot 2D_2O$

The crystal structure of $CoCl_2 \cdot 2D_2O$ was investigated using X-ray diffraction by B. Morosin and E. Graeber [127] and the masgnetic structure, using neutron diffraction,

by D. Cox et al. [128]. The crystal structure is monoclinic, belonging to the space group C2/m (#12), with lattice constants $a = 7.256$Å, $b = 8.575$Å, $c = 3.554$Å and $\beta = 97.60°$. The Co atoms sits in the center of edge-sharing octahedra that are arranged in ferromagnetic chains chains along the tilted c-axis. The Co atoms are separated from each other by chloride anions and each chloride is shared by two Co atoms. All atomic positions within the unit cell containing two chemical formula units are listed in table 5.1.

Element	Wyckoff	$x/a, y/b, z/c$	$x/a, y/b, z/c$
Co	2a	$0, 0, 0$	
Cl	4i	$0.237, 0, 0.558$	$-0.237, 0, -0.558$
O	4g	$0, 0.237, 0$	$0, -0.237, 0$
D	8j	$0.090, 0.309, 0.139$	$-0.090, -0.309, -0.139$
		$0.090, -0.309, 0.139$	$-0.090, 0.309, -0.139$

Table 5.1: *Atomic positions within the unit cell of $CoCl_2 \cdot 2D_2O$. Referenced from [128].*

The magnetic structure of $CoCl_2 \cdot 2D_2O$ is shown in figure 5.1. The two Co^{2+} ions are antiferromagnetically aligned below $T_N = 17.2$K, with the spin oriented along the **b**-axis. Every Co^{2+} ion sits in a distorted octahedral coordination of four chloride and two oxygen atoms. The minimal crystal field model, describing the ground state of Co^{2+} includes crystal field parameters up to order $l = 4$ as well as the spin-orbit coupling [129, 4]

$$\begin{aligned} \mathcal{H}_{\text{cf}} &= \mathrm{B}_4 \left[\mathcal{O}_4^0 \left(J_z, J_\pm\right) + 5\mathcal{O}_4^4 \left(J_z, J_\pm\right)\right] \\ &\quad + \mathrm{B}_2^0 \mathcal{O}_2^0 \left(J_z, J_\pm\right) + \mathrm{B}_2^2 \mathcal{O}_2^2 \left(J_z, J_\pm\right) + \lambda \mathbf{S} \cdot \mathbf{L} \end{aligned} \tag{5.1}$$

where

$$\begin{aligned} \mathcal{O}_2^0 &= 3J_z^2 - X \\ \mathcal{O}_2^2 &= \frac{1}{2}\left[J_+^2 + J_-^2\right] \\ \mathcal{O}_4^0 &= 35J_z^4 - \left(30X - 25\right)J_z^2 + 3X^2 - 6X \\ \mathcal{O}_4^4 &= \frac{1}{2}\left[J_+^4 + J_-^4\right] \end{aligned}$$

and $X = J\left(J+1\right)$. It has been found that values $\mathrm{B}_2^0 = -2.9$meV, $\mathrm{B}_2^2 = 3.6$meV, $\mathrm{B}_4 = -2.3$meV and $\lambda = -21.82$meV generally gives a good agreement with experiments, see e.g. [130]. A schematic of the electronic levels are shown in figure 5.2

From precise knowledge of the exchange paths, which is most often archived through neutron scattering measurements, the magnetic ground state can be found. Following [131, 132, 133, 134], the main ferromagnetic interchain exchange path $\mathcal{J}_0$ of the hydrated salt $CoCl_2 \cdot 2D_2O$ introduced above is mediated along the crystallographic (001)

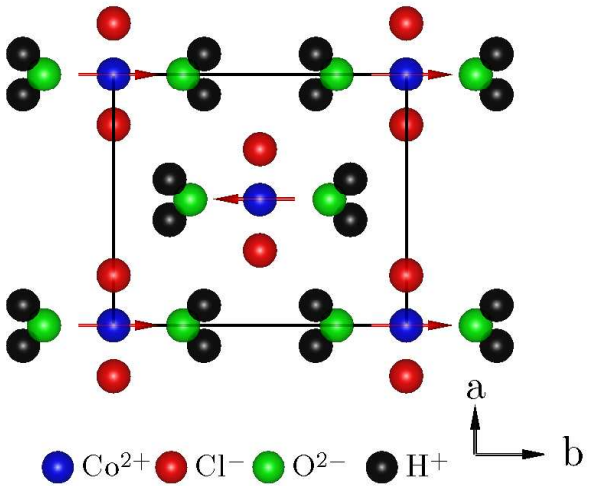

Figure 5.1: *The (**a**,**b**)-plane of $CoCl_2 \cdot 2D_2O$ showing both the two chemical formula units and the surrounding units in the unit cell. The red arrows indicate the spin direction.*

direction by the interstitial chloride ion, Co-Cl-Co, at an angle very close to 90°. In agreement with the Goodenough-Kanamori rules this interaction is indeed ferromagnetic, it is however not weak compared to the other interactions in the system. The antiferromagntic intrachain exchange $\mathcal{J}_1$ involves the Co-Cl-Cl-Co bridge which contributes equally for both the nearest neighbor and next nearest neighbor Cobalt ion of the nearest adjacent chain along the (110) direction. The interaction to the next nearest adjacent chains along the (100) $\mathcal{J}_2$ and (010) $\mathcal{J}_3$ directions are also mediated by a Co-Cl-Cl-Co bridge [131]. They are much weaker than the ferromagnetic intrachain interaction and effectively antiferromagnetic. The complete network of exchange paths in $CoCl_2 \cdot 2D_2O$ is shown on figure 5.3. The resulting spin arrangement of $CoCl_2 \cdot 2D_2O$, below a critical temperature $T_N = 17.2$K, have a spin easy axis along the b-axis [128]. The all dominating ferromagnetic intrachain interaction is along the c-axis and an effective antiferromagnetic nearest-interchain- and ferromagentic next-nearest-interchain interaction.

The magnetic excitations are collective fluctuation relative to the ground state. From the completely idealized models of true low dimensional spin and structure, which can have very exotic excitation spectra (See 2), to the more three-dimensionally ordered materials, where the excitations are precessions of the ordered moments around their equilibrium position, abbreviated spin waves or magnons due to their bosonic nature. These excitation can be studied by e.g. neutron scattering and have been investigated intensely over the last decades. The spin wave dispersion relation of a given spin system is calculated as eigen-modes of the bilinear form of the Heisenberg

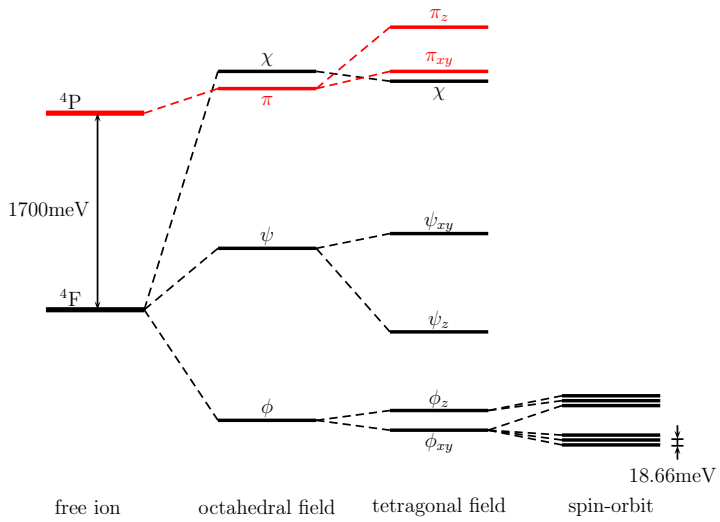

Figure 5.2: ***Left:*** *The energy levels obtained from (5.1). This model provide a realistic description of Co^{2+} in hydrated salts, from [129]. All Co^{2+} ions sits in distorted octahedral coordination formed by the nearly perfect square planar arrangement of four Cl^- and completed by the hydrate O^{2-}. At very high temperature another electronic level ^4P with the same symmetry as ^4F is also mixed into the ground state, see [129].*

Hamiltonian. Consider the Hamiltonian

$$\begin{aligned}\mathcal{H} &= -\sum_{i\delta}\left[\mathcal{J}_\delta^z S_i^z S_{i+\delta}^z + \frac{\mathcal{J}_\delta^\perp}{2}\left(S_i^+ S_{i+\delta}^- + S_i^- S_{i+\delta}^+\right)\right. \\ &\left. + \frac{\mathcal{J}_\delta^{\mathrm{A}}}{2}\left(S_i^+ S_{i+\delta}^+ + S_i^- S_{i+\delta}^-\right)\right], \end{aligned} \tag{5.2}$$

The bilinear form of (5.2) may be shown to be [126]

$$\begin{aligned}\mathcal{H} &= \sum_{\mathbf{q}}\left[A_{\mathbf{q}}\left(a_{\mathbf{q}}a_{\mathbf{q}}^\dagger + b_{\mathbf{q}}b_{\mathbf{q}}^\dagger\right) + B_{\mathbf{q}}\left(a_{\mathbf{q}}a_{-\mathbf{q}} + a_{\mathbf{q}}^\dagger a_{-\mathbf{q}}^\dagger + b_{\mathbf{q}}b_{-\mathbf{q}} + b_{\mathbf{q}}^\dagger b_{-\mathbf{q}}^\dagger\right)\right. \\ &\left. + C_{\mathbf{q}}\left(a_{\mathbf{q}}b_{\mathbf{q}}^\dagger + b_{\mathbf{q}}a_{\mathbf{q}}^\dagger\right) + D_{\mathbf{q}}\left(a_{\mathbf{q}}b_{-\mathbf{q}} + b_{-\mathbf{q}}^\dagger a_{\mathbf{q}}^\dagger\right)\right] \end{aligned} \tag{5.3}$$

where

$$\begin{aligned} A_{\mathbf{q}} &= 2\mathcal{J}_0^z - 8\mathcal{J}_1^z + 2\mathcal{J}_2^z + 2\mathcal{J}_3^z \\ &\quad -2\mathcal{J}_0^\perp\cos(\mathbf{q}\cdot\mathbf{c}) - 2\mathcal{J}_2^\perp\cos(\mathbf{q}\cdot\mathbf{a}) - 2\mathcal{J}_3^\perp\cos(\mathbf{q}\cdot\mathbf{a}) && (5.4) \\ B_{\mathbf{q}} &= -\mathcal{J}_0^{\mathrm{A}}\cos(\mathbf{q}\cdot\mathbf{c}) - \mathcal{J}_2^{\mathrm{A}}\cos(\mathbf{q}\cdot\mathbf{a}) - \mathcal{J}_3^{\mathrm{A}}\cos(\mathbf{q}\cdot\mathbf{b}) && (5.5) \\ C_{\mathbf{q}} &= -4\mathcal{J}_1^\perp\left[\cos(\mathbf{q}\cdot\mathbf{a}/2)\cos(\mathbf{q}\cdot\mathbf{b}/2) + \cos(\mathbf{q}\cdot\mathbf{a}/2)\cos(\mathbf{q}\cdot\mathbf{b}/2)\cos(\mathbf{q}\cdot\mathbf{c})\right. \\ &\quad \left. -\sin(\mathbf{q}\cdot\mathbf{a}/2)\cos(\mathbf{q}\cdot\mathbf{b}/2)\sin(\mathbf{q}\cdot\mathbf{c})\right] && (5.6) \\ D_{\mathbf{q}} &= -4\mathcal{J}_1^{\mathrm{A}}\left[\cos(\mathbf{q}\cdot\mathbf{a}/2)\cos(\mathbf{q}\cdot\mathbf{b}/2) + \cos(\mathbf{q}\cdot\mathbf{a}/2)\cos(\mathbf{q}\cdot\mathbf{b}/2)\cos(\mathbf{q}\cdot\mathbf{c})\right. \\ &\quad \left. -\sin(\mathbf{q}\cdot\mathbf{a}/2)\cos(\mathbf{q}\cdot\mathbf{b}/2)\sin(\mathbf{q}\cdot\mathbf{c})\right] && (5.7) \end{aligned}$$

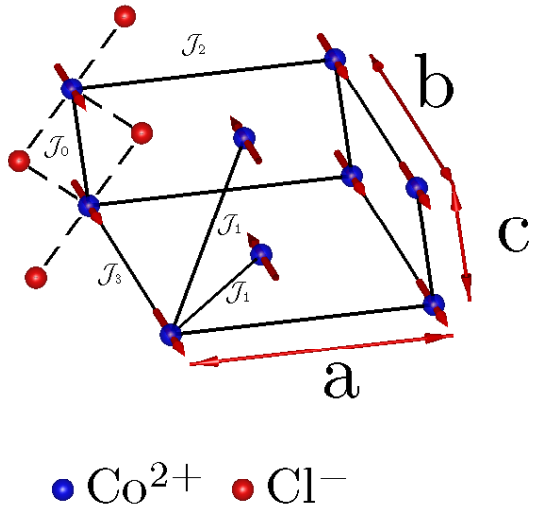

Figure 5.3: *Sketch of the main exchange paths in $CoCl_2 \cdot 2D_2O$. The ferromagnetic intrachain exchange is a result of super exchange via the Cobalt atoms (blue circles) and the interstitial Chloride (red circles).*

The Hamiltonian 5.3 can be brought into diagonal form by using the methods described in [135], yielding two spin wave excitations branches, see figure 5.4, with dispersions

$$\hbar\omega_{\mathbf{q}}^{\pm} = \sqrt{\left(A_{\mathbf{q}} \pm C_{\mathbf{q}}\right)^2 - \left(B_{\mathbf{q}} \pm D_{\mathbf{q}}\right)^2} \tag{5.8}$$

where

Parameters	Ref. [122]	Ref. [126]
$\mathcal{J}_0^z - 8\mathcal{J}_1^z + 2\mathcal{J}_2^z + 2\mathcal{J}_3^z$	2.30 ± 0.02	2.48 ± 0.005
$\mathcal{J}_0^{\perp}$	0.24 ± 0.02	0.47 ± 0.005
$\mathcal{J}_0^{\mathrm{A}}$	0.16 ± 0.02	0.33 ± 0.06
$\mathcal{J}_1^{\perp}$	-0.056 ± 0.002	-0.12 ± 0.02
$\mathcal{J}_1^{\mathrm{A}}$	-0.032 ± 0.004	0.00 ± 0.005
$\mathcal{J}_2^{\perp}$	-0.024 ± 0.001	-0.022 ± 0.007

Table 5.2: *Exchange constants wich have been reported for $CoCl_2 \cdot 2D_2O$ in the literature. The parameters $\mathcal{J}_2^A$, $\mathcal{J}_3^{\perp}$ and $\mathcal{J}_3^A$ were in both cases [122, 126] reported to be zero.*

Figure 5.5 shows the susceptibility in the paramagnetic state and the magnetization curves in $CoCl_2 \cdot 2D_2$. The magnetization process can be understood in terms of an approximate Ising model [137, 138].

If a magnetic field is applied along the crystallographic *b*-axis, longitudinal to the spin, in the magnetically ordered state below 17.2K. The magnetization is found to

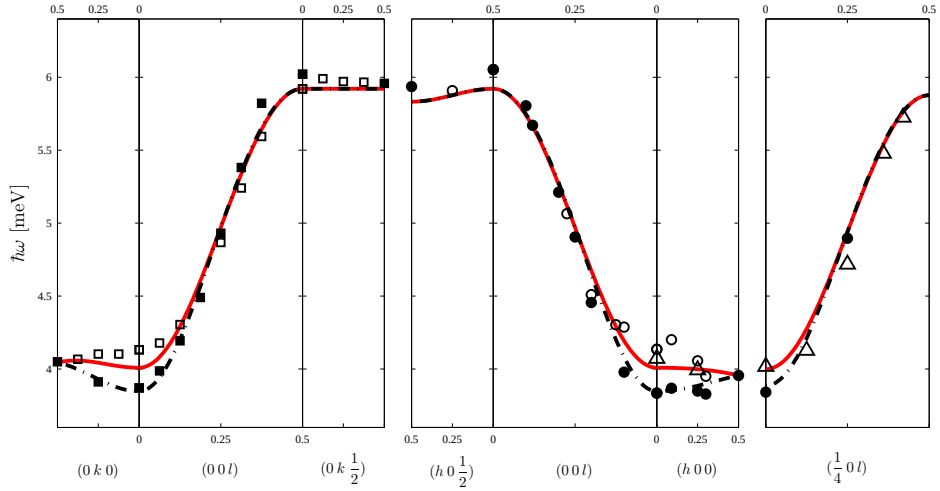

Figure 5.4: *The spin wave excitation energies in the ordered state of $CoCl_2 \cdot 2D_2O$ for $T < 7K$. The measurements reported in [126] are denoted by filled circles. The filled and unfilled squares are taken from [133] and the unfilled triangles are from [136]. The lines are calculated from (5.8) using the values from reference [126] shown in the table 5.2.*

have a two step dependence on the applied field [124]. The increases in magnetization happens at the critical fields $H_{C1} = 3.2$T and $H_{C2} = 4.6$T, see figures **??** and 5.5. In fields higher than H_{C2}, the system is fully polarized in a ferromagnetic state with an ordered/saturated moment of $\sim 3.4\mu_B/\mathrm{Co}^{2+}$. Between H_{C1} and H_{C2} the system is in an intermediate ferrimagnetic state with an ordered moment of only $\sim 1.0\mu_B/\mathrm{Co}^{2+}$ i.e. very close to 1/3 of the saturation magnetization. This partial magnetic order is analyzed in numerous paper including [134, 137, 138, 139] and is a feature of some quasi-Ising systems like $CoCl_2 \cdot 2H_2$, $CoBr_2 \cdot 2H_2O$ [134], $CoNb_2O_6$ [139] and related systems [140].

If a magnetic field is applied transverse to the spin direction in $CoCl_2 \cdot 2H_2O$ only one antiferromagnetic-to-paramagnetic transition is observed, see figure 5.5. A detailed investigation of the (a, c)-plane anisotropy reveal a minimum critical field $H_{Cx} = 16.2T$ (easy axis) along a direction which very nearly coincides with the shortest Co-Cl bond and a maximum (hard axis) critical field $H_{Cy} = 37.0T$ along the orthogonal Co-Cl bond. The ordered moment, m^α, is obtained by extrapolating the magnetization curves above the critical field down to zero. The anisotropic g-values, $g^\alpha = m^\alpha/\mu_B S$, are consistent with those previous published by A. Narath [132] if an effective $S = 1/2$ model is assumed. H. Mollymoto finds $g^\alpha \mu_B S = 1.68, 0.94$ and $3.38\mu_B/\mathrm{Co}^{2+}$ for $\alpha = x, y$ and z respectively [124]. The magnetization curves are seen to increase even after the critical field, this indicates a non-negligible mixing of higher energy levels into the ground state. The susceptibility in the paramagnetic phase above 17.2K is shown in figure 5.5. It is observed that the easy axis (transverse) susceptibility is a factor 2-3 times lower than the susceptibility in the (longitudinal), z, direction which supports that the system is dominated by a strong uniaxial anisotropy.

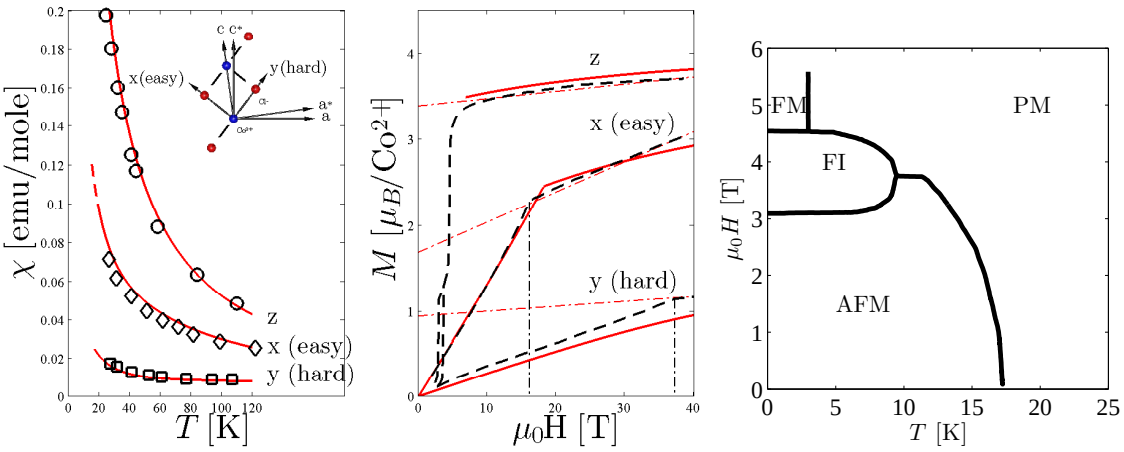

Figure 5.5: ***Left:*** *The paramagnetic susceptibility obtained by A. Narath [132] (the black data points) of* $CoCl_2 \cdot 2D_2O$ *along the crystallographic b-axis (z) and along the easy (x) and hard (y) magnetic axises in the* (a, c)*-plane. The red lines are* $\chi = m/\mu_B H$*, based on the calculated magnetization curves shown on the right figure.* ***Middle:*** *Magnetization curves obtained by H. Mollymoto [124] (the black dashed curves). The red lines are obtained by numerical calculations based on the model of the* Co^{2+} *ion using (5.1), see [130] for details.* ***Right:*** *The phase diagram in longitudinal field. From [126]. The ferromagnetic state corrosponds to the first increase in magnetization with the external field along* **b**

For the experiments described in this thesis, the external magnetic field was applied close to the direction of the magnetic easy axis, **y**. The magnets available typically apply a vertical field, thus the sample alingment was alway as shown in figure 5.6. Due to the monoclinic unit cell of $CoCl_2 \cdot 2D_2O$, the angle between **a** and $\mathbf{a}^*$ is 7.6°. By bringing the two reflections (010) and (201) into a horizontal scattering plane, the external field is makes an angle of 1.8° to **y**, which is acceptable because the variations of the critical field with respect to this angle is very small [124]. With this configuration, we can reach the magnetic (211) Bragg peaks.

5.2 $CoNb_2O_6$

In recent years, one compound stands out in the study of the the magnetic properties of materials consisting of Ising ferromagnets chains. As we shall see below, the frustrated columbite $CoNb_2O_6$ shows nice chain characteristics as well as a complex excitation spectrum originating from the interchain couplings confining the domain wall excitations of the Ising model into quantized states.

The crystal structure of $CoNb_2O_6$ is shown in figure 5.7 and the atomic positions of all elements in the unit cell are shown in table 5.3. $CoNb_2O_6$ belongs to the orthorombic

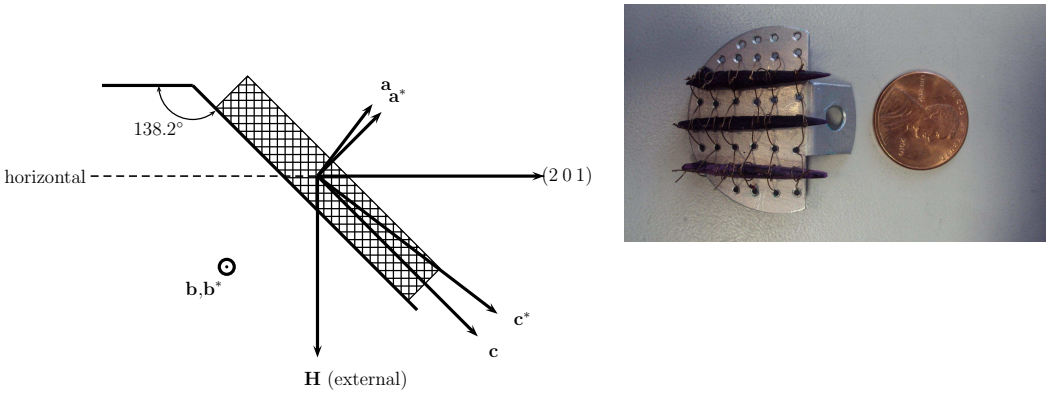

Figure 5.6: *Left: Drawing of the orientation of $CoCl_2 \cdot 2D_2O$, used in my experiments. Right: A picture of the three co-aligned sample initially used at the SNS experiment. An American penny is provided to set the scale.*

space-group #60 (Pbcn) with lattice parameters $a = 14.1337$Å, $b = 5.7019$Å and $c = 5.0382$Å.

Corresponding to the two crystallographically inequivalent octahedral CoO_6 orientations, there also exists two different magnetic easy axes. Below $T_N = 1.97$K the spins align along $(\pm \sin(\gamma)\ 0\ \pm \cos(\gamma))$ where $\gamma = 31°$, where the sign alternates depending on the four Co sites in the unit cell [141], see figure 5.7 A. $CoNb_2O_6$ and $CoCl_2 \cdot 2D_2O$

Element	Wyckoff	$x/a, y/b, z/c$
Co	2c	$0, 0.165, 0.250$
Nb	8d	$0.1600, 0.3193, 0.7518$
O1	8d	$0.0949, 0.3948, 0.4268$
O2	8d	$0.0796, 0.1161, 0.9041$
O3	8d	$0.2558, 0.1236, 0.5784$

Table 5.3: *The atomic positions in the unit cell of $CoNb_2O_6$ with four chemical elements. Adapted from [139].*

have a number of similarities, which will be presented in this section. The similarities between $CoNb_2O_6$ and $CoCl_2 \cdot 2D_2O$ are the motivation for the studies we have done on $CoCl_2 \cdot 2D_2O$, in order to quantify exactly how the differences may manifest themselves. They are both quasi one-dimensional in the sense that Co^{2+} ions form ferromagnetic chain along the orthorhombic **c**-axis, but the overall three-dimensional magnetic ground state is antiferromagnetic.

In $CoNb_2O_6$ Co forms so-called zig-zag chain by edge sharing octahedra along the orthorhombic **c**-axis via the 90° Co^{2+}-O^{2-}-Co^{2+} superexchange interaction $\mathcal{J}_0$. The Co^{2+} are arranged in an isosceles triangular lattice in the (**a**,**b**)-plane, see figure 5.7 B. Within the (**a**,**b**)-plane the nearest-neighbor interchain superexchange interaction, $\mathcal{J}_1$, is along the orthorhombic **b**-axis mediated by a Co^{2+}-O^{2-}-O^{2-}-Co^{2+} bridge. The next-nearest-neighbor interchain superexchange interaction, $\mathcal{J}_2$, also in the (**a**,**b**)-plane

is mediated Co^{2+}-Nb^{2-}-Nb^{2-}-Co^{2+} bridge. Notice that in $CoNb_2O_6$ the triangular arrangement of the Co atoms the interchain coupling give rise to geometrical frustration between the chains.

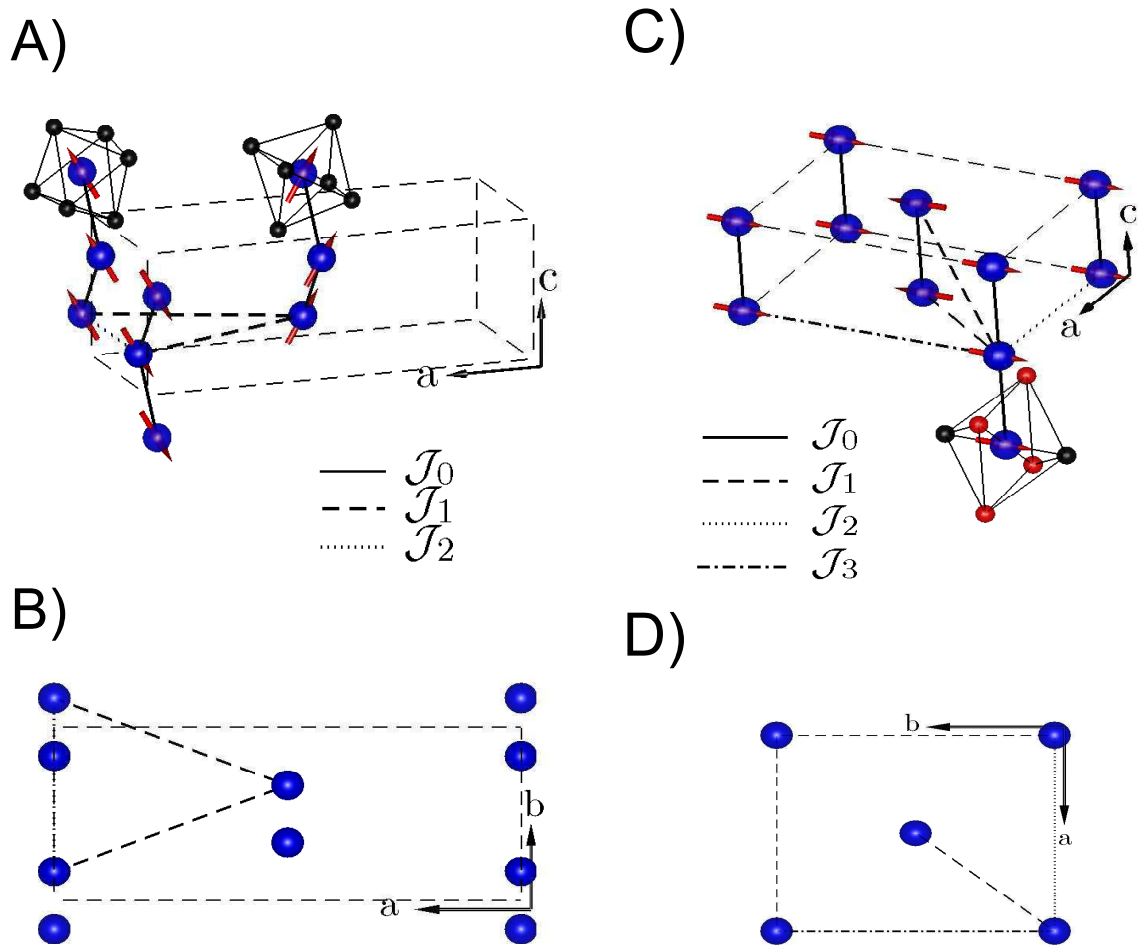

Figure 5.7: *The common rule in all these figures is that the blue circles shows the Co atomic positions and other atoms have been removed for clarity. The red arrows show the spin direction in the ordered state.* ***A*** *The crystal structure of $CoNb_2O_6$ with exchange paths. Examples of the two inequivalent octahedral CoO_6 orientations are shown.* ***B*** *The (a,b)-plane of $CoNb_2O_6$. An isosceles triangle is made of two Co atoms in the unit cell and one outside.* ***C*** *The crystal structure of $CoCl_2 \cdot 2D_2O$ with exchange paths. The distorted octahedral, consisting of four chloride atoms (red circles) and two oxygen (black circles) is also shown* ***D*** *The (a,b)-plane of $CoCl_2 \cdot 2D_2O$.*

The ordered moment of $CoNb_2O_6$ in the AFM phase is $3.2\mu_B/Co^{2+}$. This value is very similar to the corresponding ordered moment in $CoCl_2 \cdot 2D_2O$ indicating a similar incomplete quenching of the orbital angular momentum in the Co ions in the two materials, see chapter 2.

An applied magnetic field along the orthorhombic **c**-axis reveal a rich (H,T)-phase diagram whereof the commensurate AFM phase, with ordering vector $\mathbf{Q} = (0\ 1/2\ 0)$, turns out to be only a small part.

The magnetization as function applied field along the the **c**-axes (close to the magnetic easy axes) increases in steps. First to 1/3 of the saturation magnetization, as the system enters an incommensurate magnetic phase (denoted IC in figure 5.8). Before reaching a spin flip, SF1, phase between 0.03T< $\mu_0 H$ <0.32T, characterized by the ordering vector $\mathbf{Q} = (0\ 1/3\ 0)$. In the SF1 phase the magnetization is approximately constant. Above $\mu_B H = 0.32$T the magnetization grow to its full saturation value during another spin flip phase, SF2, characterized by the ordering vector $\mathbf{Q} = (0\ 1/2\ 0)$. Finally, above $\mu_B H = 0.38$T the magnetization is constant but the magnetic long range order is completely suppressed.

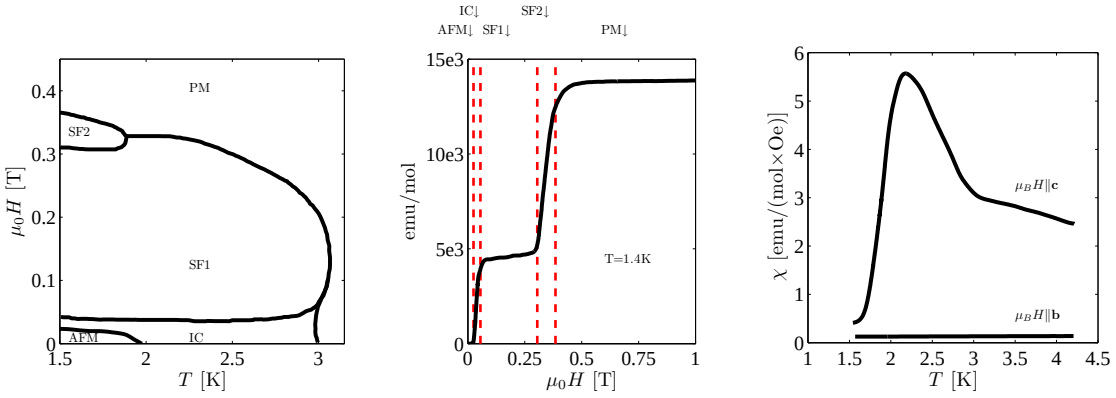

Figure 5.8: *This figure shows the bulk characteristics of* $CoNb_2O_6$. ***Left:*** *(T,H)-phase diagram.* ***Middle:*** *Magnetization as function of applied field at 1.4K* ***Right:*** *Susceptibility as function of temperature above* T_N *of the AFM phase seen in the (T,H)-phase diagram below 2K. A large difference between* $\mathbf{H}||\mathbf{c}$ *and* $\mathbf{H}||\mathbf{b}$ *is also observed in Figure 5.5 for* $CoCl_2 \cdot 2D_2O$.

All these field induced metamagnetic transitions at low temperature are analogous to the one (the ferrimagnetic phase) in $CoCl_2 \cdot 2D_2O$. This behavior, as mentioned above, is typical for one-dimensional materials in a field applied along the magnetic easy axis [137, 138], and the phase diagram shown in figure 5.8 is another example of similarities between the two systems. The susceptibility, shown in figure 5.8, is measured with a field along the orthorhombic **b**- and **c**-axes. The susceptibility along **c** only partially reflects the longitudinal susceptibility, due to the $\pm 31°$ angle between the **c** and the true magnetic easy axes. However, the susceptibility along **b** is the transverse susceptibility. The transverse susceptibility is almost completely negligible compared to the longitudinal susceptibility at T_N, this is an indication of a strong uniaxial anisotropy and the same is seen in $CoCl_2 \cdot 2D_2O$ [131], see figure 5.5. The strong uniaxial anisotropy supports the notion of $CoCl_2 \cdot 2D_2O$ and $CoNb_2O_6$ as effective Ising spin systems.

If an external magnetic field is applied transverse to the direction of the ordered moment in $CoCl_2 \cdot 2D_2O$ and $CoNb_2O_6$, they are both expected to exhibit excitation spectra specific to that of the one dimensional Ising model in transverse field. The simple theory of the TFIM presented in chapter 2 is, however, complicated further in the presence of non-zero interchain interaction. Flipping an entire segment of the chain after a domain wall would be associated with a very large amount of energy due to all the broken bonds to the neighboring chains. The lowest excitation in an Ising chain with finite, but small, interchain couplings create, in stead, a pair of independent domain walls flipping only a single spin, also known as a soliton [142]. If the domain walls propagate away from each other, the process upsets a new set of bonds to the neighboring chains, and is therefor associated with an additional energy cost that grow linearly with the domain wall separation, $V(x) = \lambda |x|$, in this model λ is equivalent to an effective string tension known from classical mechanics. The confined state, with propagating domain walls, stabilize discrete excitations with energies specific to an E_8 Lie group symmetry [125]. The energy eigenstates can be calculated as $\epsilon_j = \epsilon_0 + z_j \lambda^{2/3} \left(\hbar^2/\mu\right)^{1/3}$ where μ is the reduced mass in the center-of-mass frame of the two domain walls, z_j is given as zeros to the Airy function $\mathrm{Ai}(z_j) = 0$, $z_j = 2.33, 4.08, 5.52, 6.78, 7.94, ...$ [125], see figure 5.9. In $CoNb_2O_6$, the string tension λ originates from an small longitudinal field h^z enforced upon the chain by the neighboring chains. The regime between Ising and Heisenberg models in reduced dimensions have been studied intensively in recent years. Starting from an isolated Ising chain, weak three-dimensional interactions to the neighboring chains is known to produce a small longitudinal field $-h^z \sum_i S_i^z$ where $h^z = \sum_\delta \mathcal{J}_\delta m$ is summed only over the interchain exchange couplings [143, 144]. The supporting material of [125] quotes a value of $h^z = 0.020\mathcal{J}$ where $\mathcal{J} = 1.94$meV in $CoNb_2O_6$.

An effective Ising model was proposed for $CoCl_2 \cdot 2D_2O$ by Torrance and Tinkham in [122], to explain their observations of magnetic excitation by far-infrared transmission spectroscopy. Adapting Tinkhams model for a single chain putting $\delta = 0$ (this is discussed below),

$$\mathcal{H} = -\mathcal{J} \sum_i \left[S_i^z S_{i+1}^z + \beta \left(S_i^+ S_{i+1}^- + S_i^- S_{i+1}^+ \right) + \delta \left(S_i^+ S_{i+1}^+ + S_i^- S_{i+1}^- \right) \right], \quad (5.9)$$

we achieve a model for $CoCl_2 \cdot 2D_2O$ comparable to the model used by R. Coldea for $CoNb_2O_6$ [125]. Using the exchange interactions presented in [133], $\mathcal{J} = 1.6$meV, $\beta = 0.15$ and the ordered moment $m = 3.4\mu_B/Co^{2+}$ from [124] we arrive at $h^z = 0.012\mathcal{J}$ for $CoCl_2 \cdot 2D_2O$ which is about half of the value in $CoNb_2O_6$. From the naive picture of magnetization and paramagnetic susceptibility measurements and the model parameters extracted from an anisotropic Heisenberg Hamiltonian the two systems candidate to have similarly excitation spectra. However, there are also differences between $CoCl_2 \cdot 2D_2O$ and $CoNb_2O_6$, the interchain interactions in the latter give rise to geometric frustration which was demonstrated in [145] to be intimately connected to quantum criticality in $CoNb_2O_6$ and related systems. Further, neglecting the contribution from the interchain anisotropy $\mathcal{J}^A = 2\mathcal{J}\delta = 0.33$meV in $CoCl_2 \cdot 2D_2O$ is also an over-simplification which will modify the excitation spectrum, the value of $\mathcal{J}^A$ is

only slightly lower than $J^{\perp} = 2J\beta = 0.48$meV. Finally the doublet ground state of the crystal field in $CoCl_2 \cdot 2D_2O$ does have non-zero matrix elements S^x and S^y and hence will not behave like idealized Ising spins.

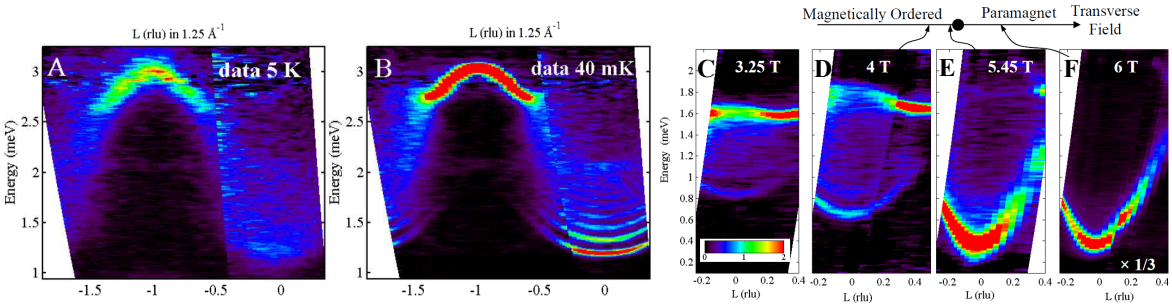

Figure 5.9: *A collection of figures from [125].* ***A*** *show zero-field spin excitations at 5K. The observed scattering shows a broad continuum near $L = 0$ due to scattering by pairs of domain walls.* ***B*** *show zero-field spin excitations at 40mK. The continuum splits into discrete excitations as a result of interchain interaction.* ***C*** *to* ***F*** *show Inelastic neutron measurements of $CoNb_2O_6$ Spin excitations along the chain near the critical field $\mu_0 H_c = 5.5T$.* ***C*** *to* ***E*** *are in the ordered phase below H_c R. Coldea et. al. observes a continuum originating from scattering between pairs of domain walls. Near the critical field the spectrum of the ferromagnetically polarized phase above H_c, showing a single strong spin flip excitation, mixes into the continuum.*

In chapter 2, the one-dimensional Ising model in transverse field was presented as a simple example of a quantum phase transition. However, the scientific question remains as how much of the pure Ising characteristics that remain in real crystals. $CoNb_2O_6$ which was introduced in this section shows an excitation spectrum which can be interpreted as Ising spin flips with interchain interaction, see figure 5.9.

5.2.1 The Random Phase Approximation

In this section we review the essentials of the Random Phase Approximation (RPA). This computational technique is used to construct a model of $CoCl_2 \cdot 2D_2O$, which is solved by numerical methods using a standard PC. This numerical model will serve as a comparison with our measurements. All RPA calculations used in this thesis was made by J. Jensen.

The RPA is described in textbooks such as J. Jensen and A. R. Mackintosh [4]. The ground state electron configuration of a magnetic Co ion in a relevant crystal field was discussed above in section 5.1. To improve calculation time, the calculations presented here assume that only two doublets lowest in energy of the Co ion are populated. The energy of the ground state doublet is (by convention) chosen as the energy zero point and the excited doublet is then found at $\epsilon_0 = 18.66$meV. To mimic the one

dimensionality of the physical crystal, a cluster of three Co ions is solved without further approximation and subsequently the cluster is coupled to the three dimensional surroundings using mean field theory[1]

This model assumes a set of exchange interactions which differs slightly from the model presented in 5.1. This model allows for different next-nearest ($\mathcal{J}_1$) and next-next-nearest neighbor ($\mathcal{J}_{\tilde{1}}$) interactions, which is consistent with the model presented in [133]. Now introducing the two sub-lattices of the antiferromagnet, $\mathbf{a}\in\{\mathbf{1},\mathbf{2}\}$ and $\mathbf{b}\in\{\mathbf{1},\mathbf{2}\}$, the susceptibility is given by the averaged response function

$$\overline{\overline{\chi}}(\mathbf{q},\omega)=\frac{1}{2}\sum_{\mathbf{ab}}\overline{\overline{\chi}}^{\mathbf{ab}}(\mathbf{q},\omega)\,. \tag{5.10}$$

The susceptibility

$$\begin{pmatrix}\sum_{\mathbf{a}}\overline{\overline{\chi}}^{\mathbf{1a}}(\mathbf{q},\omega)\\ \sum_{\mathbf{a}}\overline{\overline{\chi}}^{\mathbf{2a}}(\mathbf{q},\omega)\end{pmatrix}=\left[\overline{\overline{1}}-\overline{\overline{M}}(\mathbf{q},\omega)\right]\begin{pmatrix}\overline{\overline{\chi}}^{0}_{\mathbf{1}}(\omega)\\ \overline{\overline{\chi}}^{0}_{\mathbf{2}}(\omega)\end{pmatrix}. \tag{5.11}$$

where

$$\overline{\overline{M}}(\mathbf{q},\omega)=\begin{pmatrix}\overline{\overline{\chi}}^{0}_{\mathbf{1}}(\omega)\,\overline{\overline{\mathcal{J}}}_{\mathbf{11}}(\mathbf{q}) & \overline{\overline{\chi}}^{0}_{\mathbf{1}}(\omega)\,\overline{\overline{\mathcal{J}}}_{\mathbf{12}}(\mathbf{q})\\ \overline{\overline{\chi}}^{0}_{\mathbf{2}}(\omega)\,\overline{\overline{\mathcal{J}}}_{\mathbf{21}}(\mathbf{q}) & \overline{\overline{\chi}}^{0}_{\mathbf{2}}(\omega)\,\overline{\overline{\mathcal{J}}}_{\mathbf{22}}(\mathbf{q})\end{pmatrix}, \tag{5.12}$$

is the characteristic 6×6 coupling matrix. The non-interacting susceptibility, χ^0, is given in ([4]. The magnetic excitations are calculated as poles of the susceptibility.

To investigate the similarities and differences between the magnetic properties of $CoNb_2O_6$ and $CoCl_2\cdot 2D_2O$ we have carried out a series of neutron scattering experiments on $CoCl_2\cdot 2D_2O$. These are presented below.

5.3 The $CoCl_2\cdot 2D_2O$ Order Parameter and Phase Diagram

To determine H_c and investigate the phase diagram we used elastic neutron scattering to

In zero applied magnetic field, $CoCl_2\cdot 2D_2O$ becomes magnetically ordered below $T_N = 17.2$K [124]. However, at the quantum critical point $T_N = 0$K. Some points indicating this evolution are shown in figure 5.10. The point at H_c was taken at the FLEX instrument in Berlin in connection with this work using the Dy-booster to obtain a maximum field on the sample position of 17.3T. All other points in figure 5.10 were take using the triple axis spectrometer RITA-II located at the Swiss Spallation

[1]The mean field approximation is described in many text books dealing with magnetism e.g. [2]. In essence, the term $\mathbf{S}_i\cdot\mathbf{S}_j$ in the Heisenberg model is replaced by $\mathbf{S}_i\cdot\langle\mathbf{S}_j\rangle+\mathbf{S}_j\cdot\langle\mathbf{S}_i\rangle-\langle\mathbf{S}_i\rangle\cdot\langle\mathbf{S}_j\rangle$ as the term $(\mathbf{S}_i-\langle\mathbf{S}_i\rangle)\cdot(\mathbf{S}_j-\langle\mathbf{S}_j\rangle)$ is approximated to zero. This approximation is good in the ordered phase, but breaks down close to the critical points. Starting from the $-\frac{1}{2}\sum_{ij}\mathcal{J}_{ij}\mathbf{S}_i\cdot\mathbf{S}_j$ The 'mean field' Hamiltonian then reduces to $\mathcal{H}^{\mathrm{MF}}=-\sum_i\mathbf{S}_i\cdot\mathbf{H}_i^{\mathrm{eff}}$ where $\mathbf{H}^{\mathrm{eff}}=\sum_j\mathcal{J}_{ij}\langle\mathbf{S}_j\rangle$ where the constant term have been dropped.

Neutron Source SINQ and taken not in connection with this they are from [130]. We used elastic neutron scattering with $k_i = k_f = 1.55\text{Å}^{-1}$, and was able to reach (10.50.5) where second order neutrons from (2 1 1) can be used to study the elastic magnetic signal. We used a 15T Oxford Instruments cryo-magnet to get the field. We observe a smooth decrease of T_N from $T_N\,(H = 0) = 17.2\text{K}$ to $T_N\,(H = H_c) = 0\text{K}$. The phase boundary separates the three dimensional antiferromagnetic state from the disordered paramagnet.

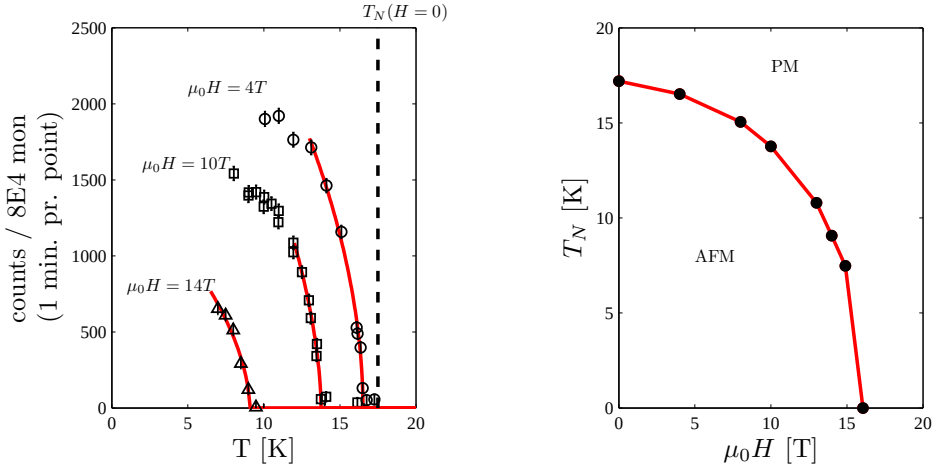

Figure 5.10: *Left: Three point scans as function of temperature for three values of field $\mu_0 H = 4T$, $10T$ and $14T$. Right: The (T,H)-phase diagram of $CoCl_2 \cdot 2D_2O$.*

The elastic data from a later experiment, shown in figure 5.11, was measured on the triple-axis spectrometer FLEX in Berlin in 2009 (before the recent update). We used $k_i = k_f = 2.367\text{Å}^{-1}$ which allowed us to reach both $Q = (201)$ and $Q = (020)$ with no second order contamination from the guide. The monochromator and the analyzer was pyrolytic graphite utilizing the [002] reflection. With this configuration $Q = (2\,1\,1)$ was within reach.

A 15T vertical field cryomagnet from Oxford Instruments (VM-1) with a Dy-booster insert was used to archive the high fields above H_c. The booster is fully magnetized already at 1T and adds a constant field of 2.5T to the field of the magnet. The downside of the booster, is a drastically reduced available sample space. The base temperature of the magnet was 1.6K and using the booster the maximum available field was 17.3T. For this experiment we had no way of measuring the sample mass accurately, but we estimate 0.1g. The sample was aligned as shown in figure 5.6 in a small aluminum pill using Araldite glue, then cut and polished to fit in the booster.

By performing a series of sample rotation θ angle scans at the position $\mathbf{Q}_{\text{AFM}} = (211)$ at different magnetic fields, the field dependence of the antiferromagnetic order parameter was determined. The magnetic Bragg peak at $\mu_0 H = 13.0\text{T}$ and $\mu_0 H = 17.3\text{T}$ is shown in figure 5.11. The line shape is slightly broadened towards higher

angles, presumably by mosaicity, but neither the width or the center show no detectable field dependence. The peak shape is sufficiently described by

$$I(\theta) = A\sum_{\xi=1}^{2} G_\xi(2\theta) + B \tag{5.13}$$

where G are Gaussians with width, center relative amplitudes determined in zero field. The constant A is the common amplitude Gaussians and B is the common background. The integrated intensity of (5.13) is $\sqrt{\pi/2}A\sum_{\xi=1}^{2}\sigma_\xi$. The field dependence of the integrated intensity is shown in figure 5.11. Close to the quantum critical point, $\mu_0 H > 15.5$T, we fit the integrated intensity to a power law, $I \propto (H_c - H)^{2\beta}$. We obtain $\mu_0 H = 16.05 \pm 0.04$T and $\beta = 0.45 \pm 0.09$.

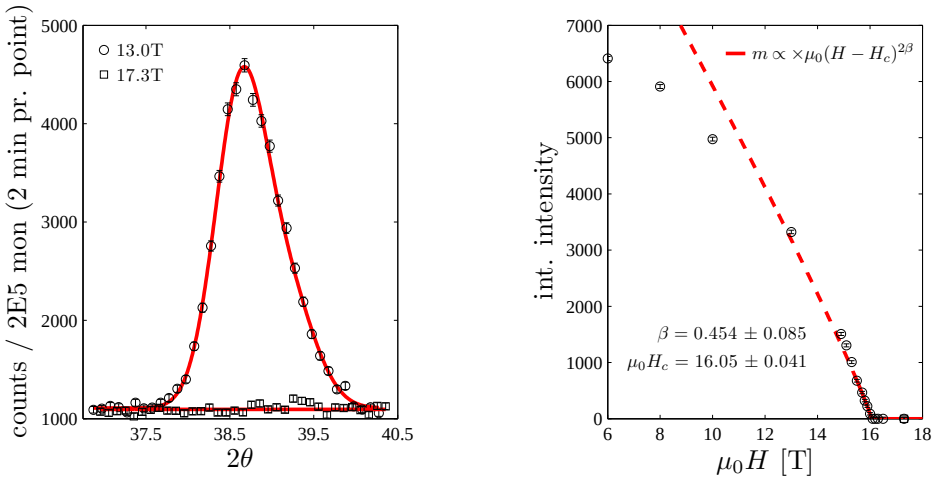

Figure 5.11: *Left: The magnetic Bragg peak (211) measured at $\mu_0 H = 13\,T$ and $17.3\,T$. Right: The integrated intensity of the magnetic Bragg peak (211) as function of applied field. The critical field is determined by a power law fit.*

5.4 Spin Waves in $CoCl_2 \cdot 2D_2O$ close to H_c

The zero transverse field spin waves were measured before [133, 126]. In the simple one dimensional Ising model in a transverse field, the excitation gap is expected to close at $H = H_c$. We present measurements of the spin wave like excitations in $CoCl_2 \cdot 2D_2O$ in the close vicinity of H_c.

In the three dimensional rare earth Ising magnet $LiHoF_4$, H. Rønnow et al. presented the softening of the magnetic spin flip excitation at $\mathbf{Q} = (1+\epsilon 01)$ at $T = 0.31$K. The exchange energy Hamiltonian is dominated by the dipole-dipole interaction except close to the critical point, where the hyperfine interaction, $\mathcal{H} = A\mathbf{I}\cdot\mathbf{J}$ with $A = 3.36\mu$eV, is the most significant contribution. The hyperfine energy scale in

$LiHoF_4$ is $2A \langle J \rangle I = 0.19$meV i.e almost a hundred times larger than the energy scale set by the temperature. As a result of the hyperfine interaction the gap remains open at $H = H_c$ and it also raises H_c from 3.6T to 4.2T due to mixing of the ground state and the higher excited states. In $CoCl_2 \cdot 2D_2O$, $A = 0.83\mu$eV indicating this interaction to be significantly less pronounced in $CoCl_2 \cdot 2D_2O$. In addition, our measurements where done around $T = 1.5$K which is larger than the hyperfine energy scale.

In $LiHoF_4$ the strong three dimensional couplings stabilizes spin-flip excitations, both in the ordered state and the quantum paramagnet. In $CoNb_2O_6$ Rado et. al. presented scattering from propagating domain wall excitations forming a bow-tie shaped continuum. The bandwidth of this continuum increases as the field rises and approaches H_c. At $H = H_c$ the shape of the spectrum changes into a single sharp excitation which lives on into the quantum paramagnetic state. Below H_c, the ground state of the ferromagnetic chain is two-fold degenerate, this favors the domain wall excitations. Above H_c, the degeneracy is lifted by the Zeeman energy, and the excitations are single spin reversals opposite to the applied field, leading to the single sharp mode. The domain wall excitation below H_c would not be observed in higher dimensions.

5.4.1 Excitation Dispersions Below H_c

We have performed an inelastic time-of-flight experiment on $CoCl_2 \cdot 2D_2O$. This technique allowed us to determine the excitation spectrum faster than using a triple axis spectrometer. We used the chopper spectrometer CNCS (Cold Neutron Chopper Spectrometer) located at the cold source at SNS (Spallation Neutron Source) under the Oak Ridge National Laboratory in Tennessee. The SNS cold source uses Liquid hydrogen as moderator. On CNCS, the user have the unique possibility to apply a 16T vertical magnetic field while still retaining a large sample space of 34mm in diameter. The magnet have a 8° opening angle and a base temperature of 1.5K. The detector coverage spans from $-50°$ to $+135°$ in the horizontal plane and $\pm 16°$ in the vertical. The source-to-sample distance is 36.2m and the sample-to-detector distance is 3.5m. We used an incident energy of 12meV and the following chopper settings; Fermi chopper 120Hz, bandwidth chopper 1 60Hz, bandwidth chopper 2 60Hz Double disk chopper 1 120Hz and Double disk chopper 2 120Hz, resulting in a measured energy resolution of 0.8711meV (FWHM).

Initially three samples where co-aligned within one degree, and fixed only with copper wire, see figure 5.6. However, due to internal strain induced by the external field, the crystals subdivided into small needle shaped crystals effectively ending the experiment prematurely, we were unable to produce a sustainable solution to this problem within the limits of one beam time. Since then, we have solved this problem and we have had a second beam time pending. However, due to technical problems with the 16T magnet, we have not been able to perform the second experiment yet.

The data range collected in our time of flight experiment is shown in figure 5.12. We observe a broad spurion emerging from the elastic signal above 0.8711meV and even continuing further into the inelastic regime above (1.50 0 0.75). We assume this spurion is due to multiple elastic scattering in the magnet shielding [146]. The spurion

is located in a very inconvenient spot for our investigations were it inevitably interferes with our excitation going soft, see figure 5.13. We measure the background using an empty can, to subtract the spurion from our data. In the following discussion, the background is subtracted from all plots.

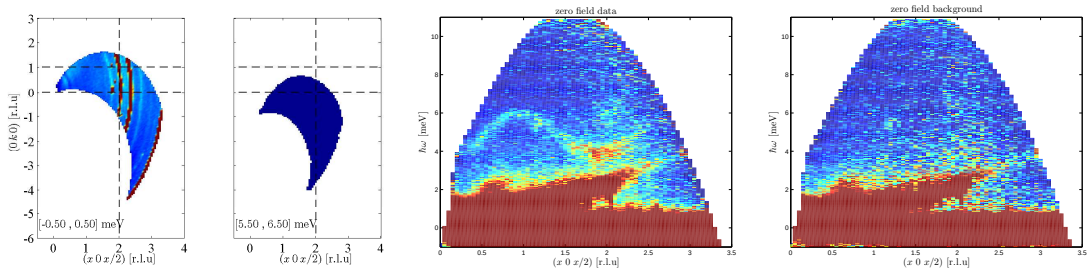

Figure 5.12: *Left: the measured data in reciprocal space at $\hbar\omega = 0$ and $\hbar\omega = 6$. Middle: the measured data projected along $(x0x/2)$ with three $CoCl_2 \cdot 2D_2O$ crystals in the beam. Right: the measured data projected along $(x\,0\,x/2)$ with an empty can.*

The collected spectra, projected onto $(x0x/2)$, are shown in figure 5.13. We observe a dispersive excitation with a bandwidth of about 2meV in zero field. The maximum of the dispersion is found at $[1\ 0\ \frac{1}{2}]$. In $\mu_0 H = 12$T the bandwidth widens to 3meV due to softening of the excitation. The RPA model described in section 5.2.1 closely reproduces the zero field band width. We include also the linear spin wave (LSW) model presented in section [126]. LSW predicts a small splitting of the modes at $x = 0, 2$ which is also consistent with the data presented in [126], but on the basis of our current data, we can not resolve the individual modes.

The spectra presented in figure 5.13 was integrated over the entire Brillouin zone along $(0\ k\ 0)$. This integration would introduce artifacts in the spectrum, if the excitations had any dispersion along $(0\ k\ 0)$. The collected spectra at $\mu_0 H = 0$T and $\mu_0 H = 12$T, projected onto $(0\ k\ 0)$ at $\mathbf{Q} = (1\ k\ 0.5)$ and $\mathbf{Q} = (2\ k\ 1)$, are shown in figure 5.14. We integrate $(x\ k\ x/2)$ in the range $0.75 < x < 1.25$ and $1.75 < x < 2.25$ respectively. Figure 5.14 A and B show data in zero field. We observe a very flat excitation, which is in qualitative agrees with both the RPA [147] and LSW theory [126], even though our resolution does not permit us to resolve the small splinting predicted by LSW. Figure 5.14 C and D show data in 12T. Along $\mathbf{Q} = (1\ k\ 0.5)$ we observe a broader mode whose width seems to be modulated along k. This disagrees with our RPA theory which predicts no such change in the width, see figure 5.14.

The width of the mode seen in figure 5.14 C might be artificially enhanced due to dispersion along the integration direction $(x\ k\ x/2)$. In order to investigate this

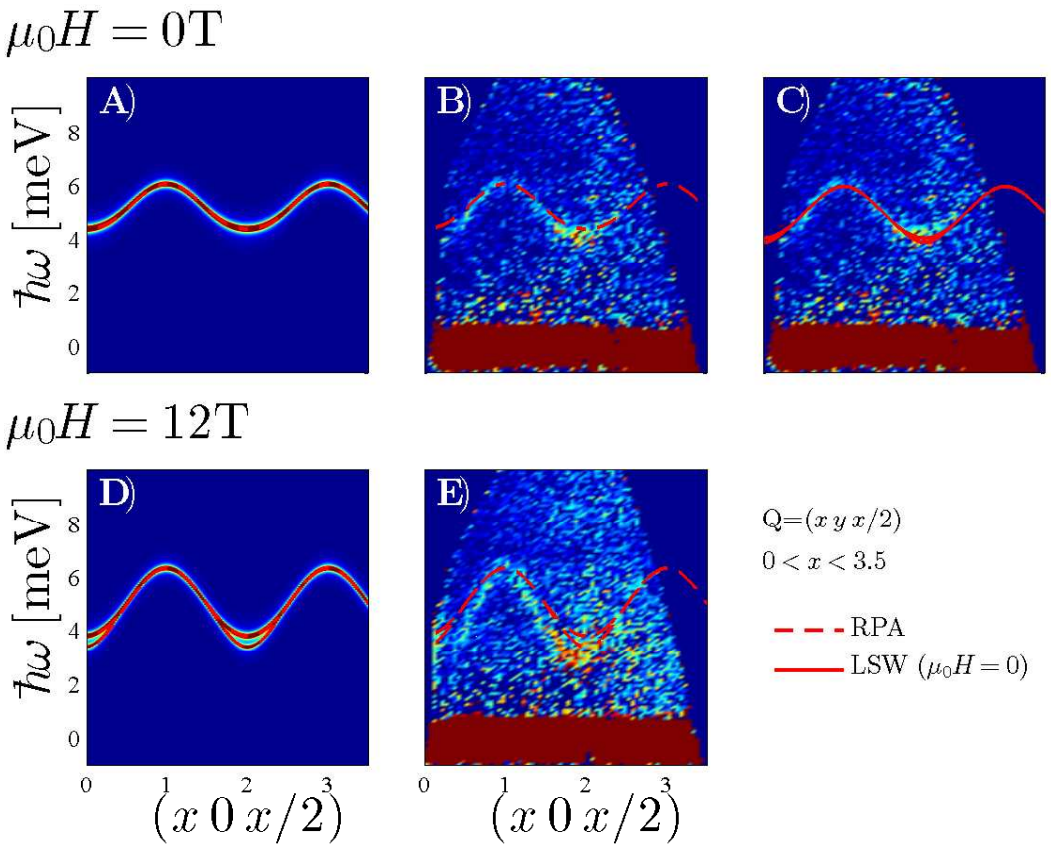

Figure 5.13: ***A*** *The RPA theory in zero field.* ***B*** *Our background subtracted measurements of* $CoCl_2 \cdot 2D_2O$ *in zero field with a red line indicating the RPA theory plotted on top.* ***C*** *The same as* ***B*** *but with the LSW theory plotted on top in stead.* ***D*** *The RPA theory in 12T.* ***E*** *Our background subtracted measurements of* $CoCl_2 \cdot 2D_2O$ *in 12T with a red line indicating the RPA theory plotted on top.*

possibility, we make three narrow cuts in the ranges $0.75 < x < 0.875$ and $1.125 < x < 1.25$ which are combined into a cut C1, and compared to a cut in the range $0.875 < x < 1.125$ which we will call C2, in both zero field and 12T. Figure 5.15 shows the resulting data at $\mathbf{Q} = (1\ 0\ 0.5)$ and $\mathbf{Q} = (1\ 0.5\ 0.5)$ fitted to single Gaussians. We observe very little difference between C1 and C2 at the two $\mathbf{Q}$-points in zero field, this is consistent with figure 5.14 A. However, in 12T we observe a large difference between C1 and C2 at $\mathbf{Q} = (1\ 0\ 0.5)$ and a significantly smaller difference at $\mathbf{Q} = (1\ 0.5\ 0.5)$. It seems likely on the basis of this data, that the width is broader in 12T $\mathbf{Q} = (100.5)$ due to our integration over a steeper dispersing mode along $(x\ k\ x/2)$ in 12T. In addition, we observe the the mode at 12T is broader at both $\mathbf{Q}$-points relative to zero field.

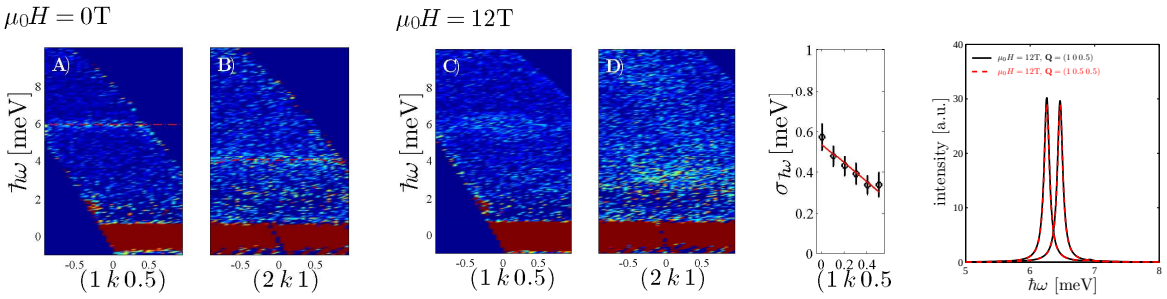

Figure 5.14: *left:* ***A*** *The measured data in zero field projected along* $\mathbf{Q} = (1\ k\ 0.5)$*, the excitation is seen at 6meV.* ***B*** *The measured data in zero field projected along* $\mathbf{Q} = (2\ k\ 1)$*, the excitation is seen at 4meV. Middle:* ***C*** *The measured data in 12T projected along* $\mathbf{Q} = (1\ k\ 0.5)$*, the excitation is again seen at 6meV.* ***D*** *The measured data in 12T projected along* $\mathbf{Q} = (2\,k\,1)$*, the excitation is seen at around 3meV, but the spurion subtraction make scattering this region appear very broad. Right: The width of the excitation seen in* ***C*** *between* $k = 0$ *and* $k = 0.5$ *and the RPA predictions showing that no difference in the excitation width is expected at these points.*

5.4.2 Excitation Dispersions Close to H_c

We have used the recently upgraded triple axis spectrometer V2/FLEXX in Berlin to measure the transverse spin waves in $CoCl_2 \cdot 2D_2O$. FLEXX is located on the BER-II cold source. To improve flux on the sample position and resolution FLEXX uses a double focusing monochromator and a horizontally focusing analyzer. We used $k_i = 1.55\text{Å}^{-1}$ resulting in a vanadium energy resolution (FWHM) of 0.18meV [148]. The new FLEXX is cleaned completely for second order contamination using a velocity selector right after the cold source, thus the use of any filter is unnecessary. We measured the incoherent background at wave vector $\mathbf{Q} = (1.87\ 1.61\ 0.94)$, above and below the critical field, to investigate any possible field dependence of the background. We found no systematic difference in our background measurements at 15.50T, 15.75T, 16.00T and 17.00T. Hence we have combined all background data into a single common dataset, see figure 5.16.

Examining at the background dataset, we observe the elastic signal to be significantly broaden into the quasi elastic regime. Fitting the data to a single Gaussian offers an insufficient description in the quasi elastic regime, in stead, we fit the data to the following model

$$I^{\text{BG}}(\hbar\omega) = A\left[G(\hbar\omega) + V(\hbar\omega)\right] + B, \tag{5.14}$$

where the Gaussian G describes the elastic incoherent signal, and the Voigtian V describe the quasi elastic signal we observe in the data. The constants A and B are

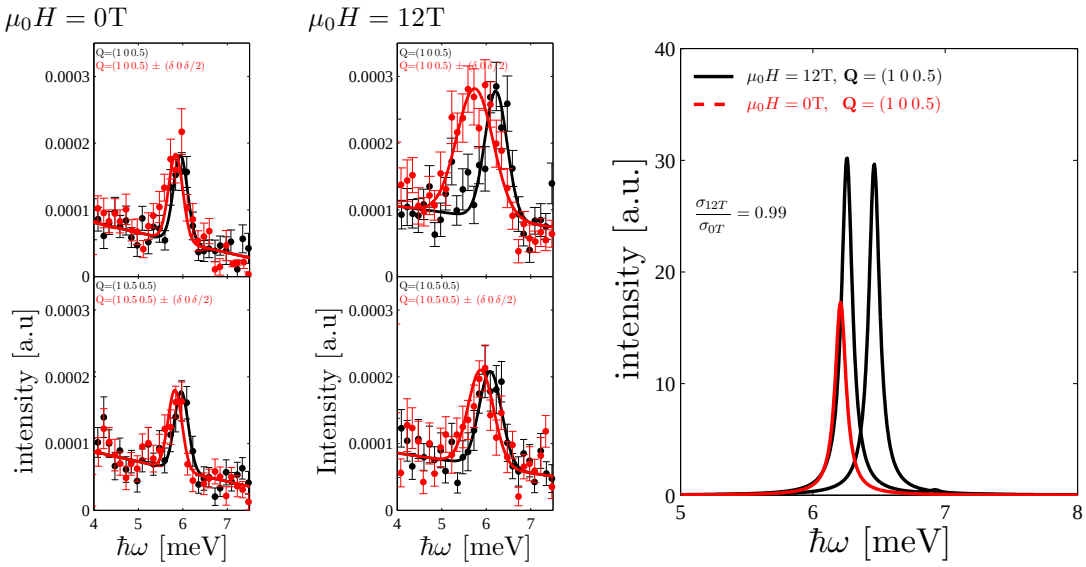

Figure 5.15: *Left: cuts at zero field comparing* $\mathbf{Q} = (1\,0\,0.5)$ *to* $\mathbf{Q} = (1\,0\,0.5) + (\delta\,0\,\delta/2)$ *and* $\mathbf{Q} = (1\ 0.5\ 0.5)$ *to* $\mathbf{Q} = (1\ 0.5\ 0.5) + (\delta\ 0\ \delta/2)$ *where* $\delta = 0.125$. *Middle: cuts at 12T comparing* $\mathbf{Q} = (1\ 0\ 0.5)$ *to* $\mathbf{Q} = (1\ 0\ 0.5) + (\delta\ 0\ \delta/2)$ *and* $\mathbf{Q} = (1\ 0.5\ 0.5)$ *to* $\mathbf{Q} = (1\ 0.5\ 0.5) + (\delta\ 0\ \delta/2)$ *where* $\delta = 0.125$. *Right: An RPA calculation showing that the width is expected to be the same in zero field and 12T but the intensity is expected to increase with increasing field.*

a common intensity and a common background respectively. We observe the strong incoherent elastic signal with onset 0.02 ± 0.0003meV from zero. This offset can be a result of the resolution ellipsoid collecting extra intensity from the dispersing excitation. In addition, we find the FWHM of the elastic incoherent contribution to be 0.19 ± 0.0002meV. This value is fairly consistent with the expected width.

The excitation dispersion was investigated by performing a series of constant-$\mathbf{Q}$ scans at $\mathbf{Q} = (2\ 1\ 1)$. The spectrum was recorded at the five magnetic fields 15.50T, 15.75T, 16.00T, 16.50T and 17.00T chosen below, very close to and above the critical field $\mu_0 H_c = 16.05$. The data is presented in figure 5.17. Approaching H_c from below, we observe a single well defined excitation clearly separated from the model background, and decreasing in energy between 15.50T and 15.75T. The intensity as well as the width of the peak increases with increasing field. At H_c we can not find any evidence of an excitation in our data. The energy resolution of the instrument prohibits us from making definitive statement about if the gap is completely closed, but our measurements shows that it is surely below 0.19meV. Above H_c we recover the single well defined excitation. In addition, the intensity and width is seen to increase again from 16.50T to 17.00T.

We have successfully verified that the magnetic excitation in $CoCl_2 \cdot 2D_2O$ indeed goes soft in field. At the critical field we observe no excitation above the elastic resolu-

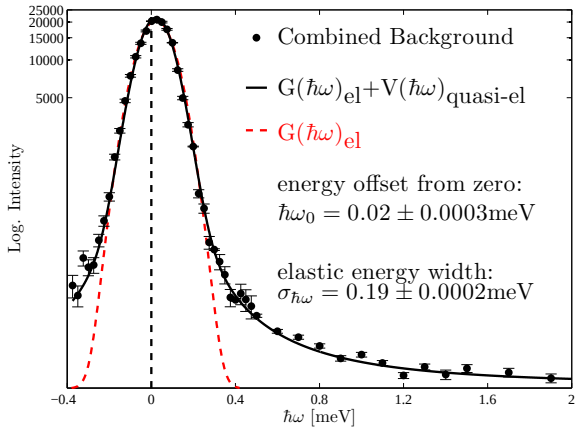

Figure 5.16: *The background data combined from measurements at 15.50T, 15.75T, 16.00T and 17.00T on the incoherent wave vector* $\mathbf{Q} = (1.87\ 1.61\ 0.94)$. *Two fit are shown, the single Gaussian (red line) and equation (5.14) (black line).*

tion. We observe the excitation emerging again above the critical field, in the so-called quantum paramagnetic phase. Our data agrees well with the qualitative behavior of RPA theory. We are thus able to describe both the bulk properties, see section 5.1, and the spin dynamics shown in figure 5.17 with the model described in section 5.2.1 which assumes an anisotropic one dimensional Heisenberg model in stead of an idealized Ising model. We observe magnetic excitations which can be characterized as transverse spin waves, which are not present in the Ising model, and the excitation spectrum which is characteristic of a one dimensional Ising system, see figure 5.9, are not seen in $CoCl_2 \cdot 2D_2O$ in our experiments.

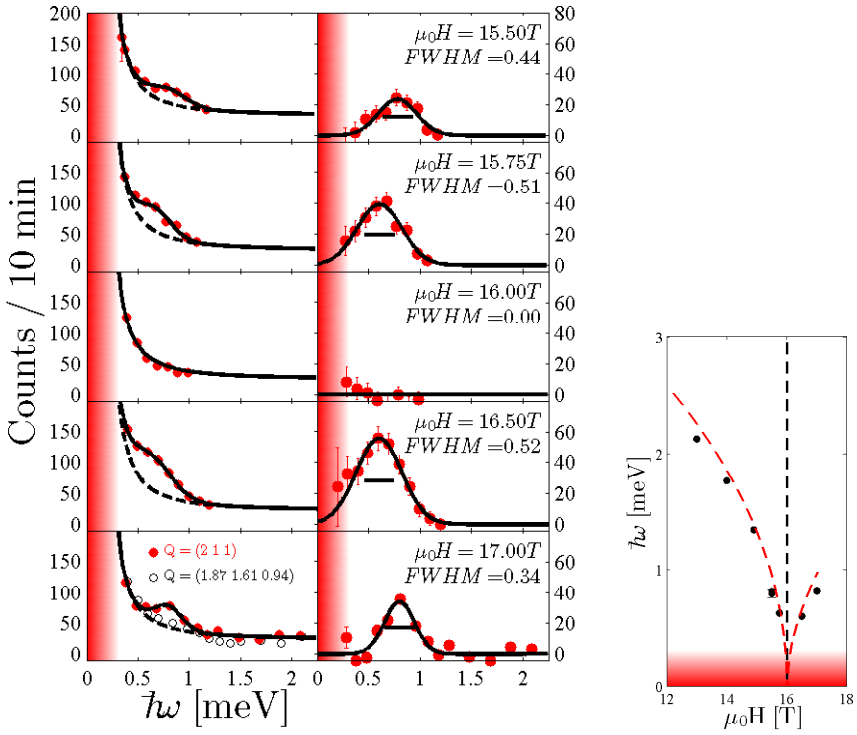

Figure 5.17: *Left: The excitation in $CoCl_2 \cdot 2D_2O$ measured by inelastic neutron scattering as function of increasing field. The left panel is the raw data (red points) with the fit to a single Gaussian (full black line) on top of the background described by (5.14) (dashed black line). The right panel shows the background subtracted data. Left: The excitation energy as function of applied field is shown as black points and the RPA calculation is shown as a dashed red line.*

CHAPTER 6

Computational Analysis of the Chemical Structure $CoCl_2 \cdot 2D_2O$ and $CoCl_2 \cdot 2NH_3$

In chapter 3, we presented the general electron structure problem in condensed matter physics, and the computational method density functional theory (DFT) as a way find approximate solutions to it. DFT have recently been used a tool to perform large screening studies of materials, see e.g. [149], where structural properties such as equilibrium positions of the lattice ions are calculated for a large groups of materials expected to have similar crystal structure allowing for their chemical stability to be analyzed.

In chapter 5 we described our experimental evidence for a quantum phase transition in $CoCl_2 \cdot 2D_2O$. Above a certain critical field, the low temperature magnetically ordered ground state in $CoCl_2 \cdot 2D_2O$ changes to a low temperature paramagnetic state. The interest in such quantum phase transitions have increased in recent years, but good candidate materials are still sparse. The critical field in $CoCl_2 \cdot 2D_2O$ was ~ 16T, which is just above the normal capabilities of typical available sample environment. We were only able to record the data shown in figure 5.17 because the HZB owns a special Dy-booster, which is unique in the world.

In this chapter we present a comparison of the ground state crystal structure of $CoCl_2 \cdot 2D_2O$ and $CoCl_2 \cdot 2NH_3$ obtained from DFT calculations. These two materials are expected to display similar magnetic characteristics [150]. The overall magnetic structure of ferromagnetic Co ions arranged in chains along the **c**-axis is expected in both cases and the size of the ordered moment should also be similar[150]. However the slightly different chemical bond lengths might result in different critical parameters, which are more favorable for experimenters. We make the simple assumption that the exchange integrals have a power law dependency of the bond lengths and we predict the change in the critical field expected in $CoCl_2 \cdot 2NH_3$ relative to the experimentally known value for $CoCl_2 \cdot 2D_2O$.

Another approximation in our study presented here, is that the spin-orbit coupling is typically not included at in DFT calculations. It remains to be seen to what extent this induces observable results. Our study here is limited to computations only. We have not at this time had a single crystal of $CoCl_2 \cdot 2NH_3$ available for experiments.

This work is currently being developed into an article (draft is added to this thesis).

6.1 Computational Methods

The DFT calculations were initialized using the structural information available for $CoCl_2 \cdot 2D_2O$ shown in table I, where H2O was exchanged for NH3, and subsequently, the atomic positions were relaxed to determine the structure and thermodynamic properties of the emergent ammine phase.

The calculations were performed in the ASE framework[1] using the GPAW code[2], which a real-space projector-augmented wave (PAW) method [151]. We use a vdW-DF [108] exchange correlation functional that accounts for the non-local van der Waals forces, which are essential in weakly bound systems as the metal halide hydrates and amines containing a large amount of hydrogen and which have long bond-lengths. All reported structures were tested for convergence of the energy for both k-points and grid spacing. The Brillouin-zone was sampled using a Monkhorste-Pack grid [152] with 6 k-points, the grid spacing was 0.18Å and all initial structures were allowed to relax the atomic coordinates by the quasi-Newton type optimization algorithm used the calculated DFT forces. We have performed all calculations both with and without spin polarization.

The energy of H_2O(g) and NH_3(g) was calculated by placing a molecule in a cube with a side length of 8Å, removing the periodic boundary conditions and using the same grid spacing as above. Finite enthalpy and entropy values are calculated by adding the calculated zero point energy and finite temperature corrections. For solids, the correction is found by summation of the mean energies of the vibrational frequencies calculated in the harmonic approximation.

The relaxation of the atomic positions is done via a three stage process. First, an initial relaxation of the atomic positions in a fixed unit cell, followed by a relaxation of the unit cell volume. The three axis a, b and c are relaxed independently. The optimal value is found by scaling each axis (both up scaling and down scaling) and fitting the resulting energy curve to the polynomial $\epsilon(V) = c_0 + c_1 t + c_2 t^2 + c_3 t^3$ where $t = V^{-1/3}$, known as the equation of state in ASE. Last the relaxation of the atomic positions is repeated in the new unit cell.

6.1.1 Thermodynamics

In ASE, the module thermochemistry contains functions which were used to obtain the free energy of water and ammonia in molecular gases and in solids. The following is a

[1] http://wiki.fysik.dtu.dk/ase/
[2] https://wiki.fysik.dtu.dk/gpaw/

short review of the approximations contained herein.

The thermodynamics of ideal gases are calculated by assuming that all spatial degrees of freedom are separable into translational, rotational, and vibrational degrees of freedom [153]. For the 3-dimensional ideal gas, this means that the heat capacity is separable i.e. $C_P = k_B + C_{V,\mathrm{trans}} + C_{V,\mathrm{rot}} + C_{V,\mathrm{vib}}$ where $C_{V,\mathrm{trans}} = 3/2k_\mathrm{B}$, and $C_{V,\mathrm{rot}} = 0$ for a monatomic gas, k_B for linear molecules, and $3/2k_B$ for the nonlinear molecules, and $C_{V,\mathrm{vib}}$ contains $3N-6$ degrees of freedom any nonlinear molecules and $3N-5$ degrees of freedom for linear molecules with N being the number of atoms. The vibrational degrees of freedom are treated in the Harmonic approximation [154]. The ideal gas enthalpy, at temperature T, is given by

$$H(T) = E_{DFT} + E_0 + \int_0^T \mathrm{d}T C_P, \tag{6.1}$$

where E_{DFT} is the total electronic energy obtained directly from the DFT calculation, and E_0 is a zero point energy from the Harmonic approximation. The entropy is also separable i.e. $S(T,P) = S_{\mathrm{trans}}(T,P^\circ) + S_{\mathrm{rot}}(T,P^\circ) + S_{\mathrm{vib}}(T,P^\circ) + S_{\mathrm{elec}}(T,P^\circ) - k_B \ln(P/P^\circ)$ where $P^\circ = 101325\mathrm{Pa}$. Explicit expressions for each part of the entropy are given in [153]. The free energy of the ideal gas, at temperature T and pressure P, is given by

$$G(T,P) = H(T) - TS(T,P). \tag{6.2}$$

For solids, where the interaction between between the particles can not be neglected, there are no rotational or translational degrees of freedom, instead, all $3N$ (vibrational) degrees of freedom are treated in the Harmonic approximation. The internal energy is calculated directly as $U(T) = E_{DFT} + E_0 + \sum_i n_B(\epsilon_i)\epsilon_i$ where ϵ_i is the vibrational energy levels from the Harmonic approximation. The entropy also only includes the a vibrational term. The free energy at temperature T and pressure P, is given by

$$G(T,P) = U(T) - TS(T,P). \tag{6.3}$$

6.2 Modelling the $CoCl_2 \cdot 2D_2O$ and $CoCl_2 \cdot 2NH_3$ Structures

The experimentally determined $CoCl_2 \cdot 2D_2O$ crystal structure was reported in [128, 127] and also discussed in chapter 5. Because of the two lone pairs in water, the D_2O molecule has a twofold rotational degree of freedom around the Co-O axis. Rotational ordering along the [001] is the cause of the small monoclinic distortion of the $CoCl_2 \cdot 2D_2O$ crystal structure [150]. This complication is generally not considered here. The NH_3 molecules in $CoCl_2 \cdot 2NH_3$ are rotationally disordered up to approximately 135K but the reported low temperature crystal structure remains orthorhombic in this case [150].

In order to mimic the antiferromagnetically aligned Co-chains of $CoCl_2 \cdot 2D_2O$, we set up a system with four chemical formula units an relax the atomic positions, by the

process described in section 6.1. Table 6.1 summarizes the final atomic positions. The $CoCl_2 \cdot 2NH_3$ structure is set up by exchanging the H_2O molecules for NH_3 whit the nitrogen atom on the oxygen site. Afterwards the atomic positions are relaxed again via the same procedure.

The relaxed chemical bond lengths in $CoCl_2 \cdot 2D_2O$ are summarized in table 6.3. We find an overall good agreement between the bond lengths we have calculated using GPAW and the experimental $CoCl_2 \cdot 2D_2O$ structure, with one exception, which is the Cl-Cl connecting the chains (interchain). The interchain Cl-Cl bond relaxes to a shorter bond length in the calculation than expected from [128, 127]. The same is true for the calculated $CoCl_2 \cdot 2NH_3$ bond lengths which are summarized in table 6.2.

To verify the calculated structures we find the binding energy of water and ammonia relative to the empty salt $CoCl_2$ i.e $G_{CoCl_2 \cdot 2D_2O} - (G_{CoCl_2} + 2 \times G_{H_2O})$ and similar for ammonia. We find binding energy of water to be 82.44kJ/mol and the binding energy of ammonia to be 78.18kJ/mol these values are consistent with our expectation from e.g. [155].

The ordered moment of the calculated ground state $CoCl_2 \cdot 2D_2O$ structure is $2.52\mu_B$/Co which is 20% below the experimental value from [124]. However, we only fint an ordered moment of 0.92 in the calculated $CoCl_2 \cdot 2NH_3$. This is not consisntent with the experimental value of $3.6\mu_B$/Co reported in [150]. The origin of this discrepancy is currently not understood.

Element	Wyckoff	x/a	y/b	z/c
Co	2a	0	0	0
Cl	4i	1.73	0.19	1.89
		−1.72	0.20	−1.89
O	4g	−0.24	2.10	0.06
		0.26	−2.10	−0.06
H	8j	0.49	2.66	0.43
		−0.66	−0.66	−0.65
		0.68	−2.61	0.66
		−0.46	−2.67	−0.43

Table 6.1: *The relaxed atomic positions of one chemical formula unit in the unit cell of $CoCl_2 \cdot 2D_2O$.*

Element	Wyckoff	x/a	y/b	z/c
Co	2a	0	0	0
Cl	4i	1.69	0.15	1.76
		−1.71	0.30	−1.77
N	4g	0.01	−2.01	0.04
		−0.02	2.09	−0.03
H	8j	−0.01	−2.37	−0.87
		−0.80	−2.39	0.55
		0.83	−2.40	0.53
		−0.39	2.39	−0.89
		0.89	2.44	0.09
		−0.61	2.43	0.70

Table 6.2: *The relaxed atomic positions of one chemical formula unit of $CoCl_2 \cdot 2NH_3$ in the unit cell $CoCl_2 \cdot 2D_2O$.*

6.2.1 The Superexchange Dependence on Bond Lengths and Critical Parameters

The super exchange interaction was discussed in chapter 2. In this section we discuss a simplified model for the exchange interactions dependence on chemical bond angle and bond length.

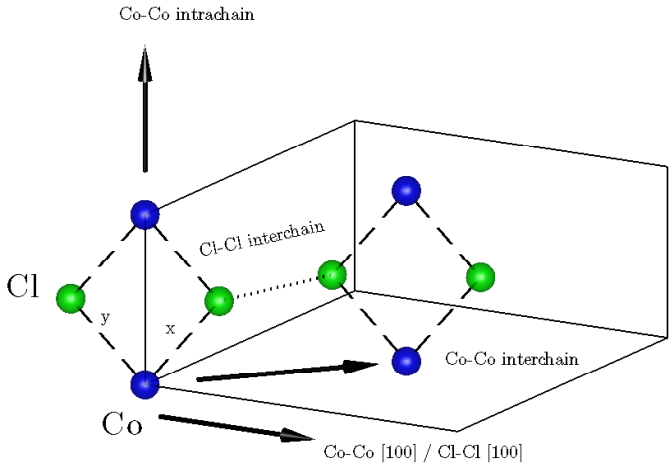

Figure 6.1: *Sketch of the interactions along different direction in the unit cell of* $CoCl_2 \cdot 2D_2O$. *The naming convention used here is also found in table 6.3. The 'Co-Co intrachain' connects two Co ions along the* **c***-axis involving a Co-Cl-Co bridge (dashed lines) with an angle close to 90°. The 'Co-Co interchain' connects two Co ions on neighboring chains via the Co-Cl-Cl-Co bridge (dottet line). The 'Co-Co [100]' connects Co ions on next nearest neighboring chains also via a Co-Cl-Cl-Co bridge.*

	Bond length [Å] $CoCl_2 \cdot 2D_2O$	Bond length [Å] $CoCl_2 \cdot 2NH_3$	Relative Difference [%]
Co-Co Interchain	5.61 (5.62)	5.71 (5.86)	+1.7 (+4.3)
Co-Co Intrachain	3.59 (3.55)	3.69 (3.71)	+2.6 (+4.5)
Co-Co [100]	7.27 (7.26)	7.59 (7.99)	+4.4 (+10.1)
Co-Cl x	2.57 (2.63)	2.56 (2.60)	-0.4 (-1.1)
Co-Cl y	2.42 (2.33)	2.48 (2.48)	+2.5 (+6.4)
Cl-Cl Interchain	3.89 (4.31)	4.27 (4.03)	+9.8 (-6.5)
Cl-Cl [100]	3.85 (3.84)	4.18 (4.53)	+8.6 (+18.0)
	Bond angle [°] $CoCl_2 \cdot 2D_2O$	Bond angle [°] $CoCl_2 \cdot 2NH_3$	
Co-Cl-Co intrachain	91.5 (92.3)	93.5	

Table 6.3:

The geometrical coordination of the magnetic ions and the interstitial ligand ion is known to affect the interaction in predictable ways [9, 10, 12, 13]. Following [156, 157, 158, 157] the chemical bond angle θ dependence of the exchange interaction follows the general rule $J(\theta) \propto t_{180^\circ} \cos^2(\theta) + t_{90^\circ} \sin^2(\theta)$ where the operator t depends on the inter-atomic distance r. This dependence was first systematically studied by B. Bloch [159], who found $t \propto r^{-\gamma}$ with $\gamma = 10$ which hold true for short distances i.e. 2-3Å . However, it was later shown by K. Shrivastava and V. Jaccarino [160] that in fact γ itself also depends on distance, and for long distances $t \propto e^{-\beta r}$ would be a better

description. For our current purpose, we will assume a power law dependence

$$J(r,\theta) = J_0 \times \begin{cases} r^{-\gamma}\cos^2(\theta) & \text{bond angle: } \sim 180^\circ \\ r^{-\gamma}\sin^2(\theta) & \text{bond angle: } \sim 90^\circ \end{cases} . \tag{6.4}$$

The exact value of γ is not known and many different value have been reported in the range 10-20 [161, 162]. For a bond length around 4Å , $\gamma = 10 - 12$ seems to be consistent with experiments on various ionic compounds [161]. We use 6.4 and the calculated bond lengths to estimate a new set of exchange parameters for both $\gamma = 10$ and $\gamma = 12$.

From Mollymoto et al. [124] we get an expression for the critical field, which is the field where all the spin in $CoCl_2 \cdot 2D_2O$ become polarized in the direction along the externally applied field

$$H_c = \frac{2\left(\mathcal{J}_0^{zz} - \mathcal{J}_0^{\alpha\alpha} + 2\left(\mathcal{J}_1^{zz} + \mathcal{J}_1^{\alpha\alpha}\right)\right)}{g^{\alpha\alpha}\mu_B} \tag{6.5}$$

where $\alpha = x, y$ and $\mathcal{J}_2$ and $\mathcal{J}_3$ terms have been neglected because they are much smaller than $\mathcal{J}_0$ and $\mathcal{J}_1$. Mollymoto et al. [124] finds that (6.5) overestimates the true critical field H_c by about 45% along the easy axis. The reason for this large discrepency is due to the so-called Van Vleck paramagnetism [2, 124] which is difficult to include in the calculation. For our present simplified purpose,we will use (6.5) to get an idea about the trend which we can expect for H_c when the exchange interactions change.

The magnetic ordering temperature T_N's dependency on the exchange interactions in low dimensional systems is a more difficult matter. A number of attempts to give a qualitative picture is presented in Yasuda et al. [163] using various numerical techniques. For a one dimensional Heisenberg model, similar to (5.2) Yasuda finds $T_N \propto J_0^{\alpha\alpha}/J_0^{zz}$ indicating a strong dependence on the J_0^{xx} and J_0^{yy} components.

Using $g^{xx} = 3.35$ and $g^{yy} = 1.87$ from ref. [124] and (6.4), we determine the change in critical field 6.5) expected due to the change of chemical bond lengths angles. We then normalize critical field found from the calculated $CoCl_2 \cdot 2D_2O$ structure to the measured value, 16.2T, from [124] and use the same ratio to calculate the critical field expected for our calculated $CoCl_2 \cdot 2NH_3$ structure. For $\gamma = 10$ we find the $H_c = 14.2$T and for $\gamma = 12$ we find $H_c = 13.8$T of $CoCl_2 \cdot 2NH_3$. This is a reduction of more than 2T.

6.3 Discussion and conclusion

We used DFT to calculate the equilibrium positions of the ions in $CoCl_2 \cdot 2NH_3$. This was done by exchanging ammonia for the water in $CoCl_2 \cdot 2D_2O$ and using GPAW to relax the structure. For all but one chemical bond we obtain correct trends between the two materials. This is the Cl-Cl bond between two Co chains. Currently, it is not knows what the origin of this discrepancy is not known.

We obtain a critical field H_c which is smaller in $CoCl_2 \cdot 2NH_3$ than in $CoCl_2 \cdot 2D_2O$ by about 12 However, the Néel temperature in $CoCl_2 \cdot 2NH_3$ was reported to be 26K

[150] which is above the 17.2K reported for $CoCl_2 \cdot 2D_2O$ [124]. This can be understood by the noting that the Néel temperature in coupled chains is expected to depend strongly on $\mathcal{J}^{xx}$ and $\mathcal{J}^{yy}$ in which direction the bond length contracts, whereas the critical field depend strongly on $\mathcal{J}^{zz}$ where the bond length expands.

To validate our approach we would need a single crystals sample of $CoCl_2 \cdot 2NH_3$ in order to determine the magnetization along different directions, just as Mollymoto et al. [124] does for $CoCl_2 \cdot 2D_2O$. By such a measurement we would get a final validation of the calculation done here.

CHAPTER 7

Introduction to Muon Spin Rotation

In this chapter we review the basic theory of muon spin rotation which is needed to understand the data analysis and the conclusions in later chapters of this thesis. There exists a few books on the topic whereof I have found [164, 22, 165] helpful. Muon spin rotation is also often referred to as muon spin relaxation, muon spin resonance or muon spectroscopy. Primary, these names highlights the similarities with well established techniques such as Nuclear Magnetic Resonance (NMR), Electron Spin Resonance (ESR), etc. whose range of application transcends many different branches of science.

7.1 Basic Properties of the Muon

In this section we introduce some fundamental aspects connected to muons and muon production. We will focus especially on the production of positive muons produced as so-called surface muons. Positive surface muons are used in muon spin rotation (μ-SR) experiments, where e.g. the temperature dependence of the ordered moment and the magnetic volume fraction in a condensed matter sample can be determined. The following section is mainly based on [22, 165]

The muon was first discovered by C. D. Anderson and S. Neddermeyer in 1937 during their studies of the cosmic radiation [166]. However the name 'muon' came later. The existence of the muon was subsequently confirmed later in 1937 by J. C. Street and E. C. Stevenson in a cloud chamber experiment [167]. Some fundamental values characterizing the muon is presented in table 7.1 in the end of this section.

In the laboratory, muons are created from a high energy proton beam impinged into a resting target, typically graphite. When a proton or neutron at rest are hit by a high energy proton whose energy exceeds a threshold of roughly two twice the pion

mass (139.6MeV/c^2) charged pions are produced via the elementary reactions

$$\begin{aligned} \mathrm{p}^+ + \mathrm{p}^+ &\rightarrow \pi^+ + \mathrm{p}^+ + \mathrm{n}^0, & (7.1)\\ \mathrm{p}^+ + \mathrm{n}^0 &\rightarrow \pi^+ + \mathrm{n}^0 + \mathrm{n}^0, & (7.2)\\ \mathrm{p}^+ + \mathrm{n}^0 &\rightarrow \pi^- + \mathrm{p}^+ + \mathrm{p}^+. & (7.3) \end{aligned}$$

The mean lifetime of a pion is 26ns. During this time, the pions moves through the target, which is designed to optimize the number of pions which come to rest near its surface. Positive pions do not interact with the target, but negative pions are captured by the target nuclei. Therefore mainly positive pions reaches the surface. They decay at rest, resulting in a monoenergetic (4.1MeV, 29.8MeV/c) beam of positive muons via the reaction

$$\pi^+ \rightarrow \mu^+ + \nu_\mu. \quad (7.4)$$

This is a two body decay with zero initial momentum, conservation of momentum dictates that the muon and the neutrino are emitted in exactly opposite directions in the rest frame of the pion.

Because the pion has spin zero and the neutrinos are exclusively left handed particles[1] - that is, their spin are antiparallel to their momentum - the muons produced in this way must also be left handed and the resulting beam of muons is very close to 100% spin polarized. Such spin polarized (surface) muon beams have proven very usefull in condensed matter physics using them as e.g. magnetic probes. In this thesis we have used muons to investigate the magnetic phases in high temperature superconductors.

Quantity	Value
mean lifetime	$2.197 \cdot 10^{-6}$s
decay	$\mu^- \rightarrow \mathrm{e}^- + \bar{\nu}_\mathrm{e} + \nu_\mu$ (muon)
	$\mu^+ \rightarrow \mathrm{e}^+ + \nu_\mathrm{e} + \bar{\nu}_\mu$ (anti muon)
rest mass	105.7MeV/c^2
	$1.884 \cdot 10^{-25}$g
spin	$\frac{1}{2}\hbar$
magnetic moment	$3.183\mu_\mathrm{N}$
charge	$\mp 1e$

Table 7.1: *Basic properties of the muon.*

7.2 Muon Spin Rotation

In this section we discuss the fundamental notions of μ-SR experiments. μ-SR experiments comes in three important categories, zero field, longitudinal field and trans-

[1] The projection of the spin $\mathbf{S}_\mu$ onto the momentum $\mathbf{p}$ is known in particle physics as helicity: $h = \frac{\mathbf{S}_\mu \cdot \mathbf{p}}{|\mathbf{p}|}$. The eigenvalue of the helicity is either $+1$ (right handed particle) or -1 (left handed particle) but all neutrinos are exclusively left handed.

verse field but we will mainly be concerned with zero field and transverse field μ-SR. The transverse field μ-SR technique have proved to be a powerful technique for studying the so-called superfluid density of high temperature superconductors, see e.g. [168, 169, 170, 171]. The following section is mainly based on [164, 22]

In a μ-SR experiment, positive muons are sequentially implanted into the bulk of a sample, only one at a time. The produced surface muons, as explained in the previous section, have a momentum of roughly $p = 30\text{MeV}/c$. The penetration depth of such muons varies from 0.1mm-1mm depending on the material density [172]. Every muon comes to rest at a specific position in the unit cell of the sample material, the muon site, determined by the electrostatic potential. For a detailed description of the different stages of the muon thermalisation process see [165]. The entire thermalisation process takes on the order of 10^{-10}-10^{-9}s and conserves the muons initial polarization. After a time, on average equal to the mean lifetime of the muon τ_μ, it decays via the weak decay process

$$\mu^+ \rightarrow \mathrm{e}^+ + \nu_\mathrm{e} + \bar{\nu}_\mu. \tag{7.5}$$

The positron can subsequently be detected using scintillators.

The power of μ-SR as a condensed matter probe rests on the parity violation [173, 174] of the weak interaction. Parity violation leads to a spatially asymmetric emission cross section of the decay positron with respect to the spin direction of the muon. This is shown in figure 7.1 and expressed by equation

$$\frac{\mathrm{d}^2\sigma}{\mathrm{d}\Omega\mathrm{d}\epsilon} \propto 1 + A(\epsilon)\cos(\Theta), \tag{7.6}$$

where Θ in the (azimuthal) angle between the emitted positron trajectory and the muon spin direction. $A(\epsilon)$ is known as the asymmetry parameter and ϵ is the energy of the positron. The number of positrons $\mathrm{d}N$ at time t emerging into the solid angle $\mathrm{d}\Omega = \sin(\Theta)\,\mathrm{d}\Theta\mathrm{d}\Phi$ is given by

$$\mathrm{d}N = \left(\frac{\mathrm{d}^2\sigma}{\mathrm{d}\Omega\mathrm{d}\epsilon}\right) N_\mu(t)\,\mathrm{d}t\mathrm{d}\epsilon\mathrm{d}\Omega, \tag{7.7}$$

where $N_\mu(t)$ is the number of muons present at time t. This number decreases according to the famous radioactivity decay law, $N_\mu(t) = N_\mu(0)\exp(-t/\tau_\mu)$. Typically in a muon spin rotation experiment, the energy of the positrons are not analyzed. Due to intrinsic mechanisms in the weak decay, when (7.7) is integrated over energy, the resulting energy-averaged asymmetry parameter $A_0 \approx 1/3$. In conclusion, the positrons are emitted preferentially in the direction parallel to the muon spin direction.

Consider the situation shown in figure 7.2. One positron detector is positioned in front (F) of a sample, relative to the muon beam direction, and another behind (B) the sample. This geometry is known as a longitudinal- (LF-μ-SR) or zero field μ-SR experiment (ZF-μ-SR). All external field, including the earth magnetic field, can be compensated by applying small opposing external fields on the sample position. The magnetic moment of the muon and the mean life-time have two very important

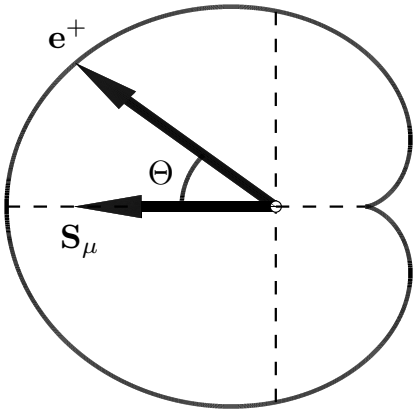

Figure 7.1: *Spatial distribution of positrons from the decay of a polarized muon.*

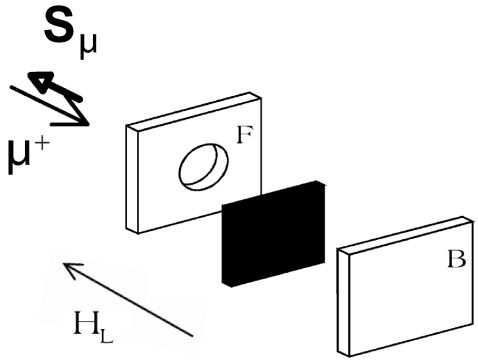

Figure 7.2: *The experimental geometry for ZF-μ-SR and LF-μ-SR. Adapted from [175].*

consequences in ZF-μ-SR. 1) muons are sensitive very small magnetic fields inside the sample, typically down to 10^{-4}T. 2) The time window in which muons are sensitive to the dynamics of the electronic moments, described by a characteristic correlation time, is typically slower than most neutron scattering techniques and typically faster than NMR. These probes thus complement each other nicely. An external so-called longitudinal field $\mathbf{H}_{\text{ext}}$ may also be applied parallel to the muon spin direction. Consider now, if there is an internal local magnetic field $\mathbf{H}_{\text{loc}}$ at the muon site in the sample. $\mathbf{H}_{\text{loc}}$ arise naturally in e.g. magnetically ordered systems due to the dipole-dipole interaction between the (static) ordered electronic moments and muon spin. The local field is then written as [22, 164]

$$\mathbf{H}_{\text{loc}} = \mathbf{H}_{\text{int}} + \mathbf{H}_{\text{ext}}, \tag{7.8}$$

where

$$\mathbf{H}_{\text{int}} = \mathbf{H}_{\text{dip}} + \mathbf{H}_{\text{dm}} + \mathbf{H}_{\text{l}} + \mathbf{H}_{\text{fermi}}. \tag{7.9}$$

If the sample has no net magnetization, such as antiferromagnets, the dominating contribution to the internal local field comes from ordered electronic moments which contribute via the dipole-dipole interaction

$$\mathbf{H}_{\text{dip}} = \frac{\mu_0}{4\pi} \sum_i \left[\frac{\boldsymbol{\mu}_\mu \cdot \boldsymbol{\mu}_e}{|\mathbf{r}_\mu - \mathbf{r}_i|^3} - \frac{3\left(\boldsymbol{\mu}_\mu \cdot (\mathbf{r}_\mu - \mathbf{r}_i)\right)\left(\boldsymbol{\mu}_e \cdot (\mathbf{r}_\mu - \mathbf{r}_i)\right)}{|\mathbf{r}_\mu - \mathbf{r}_i|^5} \right], \tag{7.10}$$

where i in principle is summed over all the electronic moments in the sample. However it is a good approximation to neglect all moments which are not within ≈ 30Å of the muon site. $\mathbf{H}_{\text{dm}} = -N\mathbf{M}$ is the demagnetization field stemming from any non-zero magnetization of the finite sample. $\mathbf{H}_{\text{l}} = \frac{4\pi}{3}\mathbf{M}$ is the Lorentz field which is produced by the opposing magnetization of a small spherical cavity around the muon site inside the

magnetized sample. These contributions are important in ferromagnetic samples. If the magnetization is caused by the external field then $\mathbf{M} = \chi \mathbf{H}_{\text{ext}}$. In metallic samples a field $\mathbf{H}_{\text{fermi}} \propto -|\psi_s(\mathbf{r})|^2 \boldsymbol{\mu}_e$ arising from the dipole interaction between the muon moment and the itinerant moment of the surrounding electron cloud, this is known as the Fermi contact interaction and due to its dependence of the s-wave function it is very short ranged.

The time evolution of each component of the muon spin $\mathbf{S}(t) = (S_x(t), S_y(t), S_z(t))$ follows the Larmor equation [2, 164]

$$\frac{\mathrm{d}\mathbf{S}(t)}{\mathrm{d}t} = \gamma_\mu \mathbf{S}(t) \times \mathbf{H}_{\text{loc}}, \tag{7.11}$$

where $\gamma_\mu = 135.5\text{MHz/T}$.

Assuming, without any loss of generality, a coordinate system where the local field is parallel to the $\hat{z}$ direction, and the muon initially spin makes an angle θ to the $\hat{x}$ direction in the $\hat{x}\hat{z}$-plane, see figure 7.3. The solution of (7.11) gives the following set of equations

$$S_x(t) = S\sin(\theta)\cos(\omega_\mu t), \tag{7.12}$$
$$S_y(t) = S\sin(\theta)\sin(\omega_\mu t), \tag{7.13}$$
$$S_z(t) = S\cos(\theta). \tag{7.14}$$

where $S = |S(0)|^2$ is the length of the muon spin. The Larmor frequency $\omega_\mu = \gamma_\mu H$.

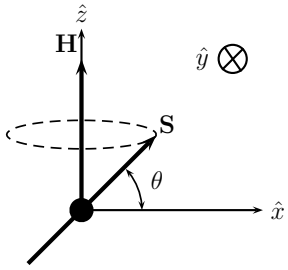

Figure 7.3: *This figure shows the external field along $\hat{z}$ and the muon spin precesses around it in the xy-plane.*

$\mathbf{H}_{\text{loc}}$ cause the muon spin to presses around $\hat{\mathbf{H}}_{\text{loc}}$, and thus depolarizes it from its original direction by a time dependent polarization $\mathbf{P}(t)$. The primary purpose of most μ-SR experiment is to determine the evolution of this polarization. Implanted muons in different parts of the sample effectively perform an ensemble average of the local field. In general, if the local magnetic field is given by the distribution $D(\mathbf{H}_{\text{loc}})$, $\mathbf{P}(t)$ is defined as the average over the muon ensemble normalized by the initial spin projected onto the initial direction of the muon spin [22]

$$\begin{aligned}\mathbf{P}(t) &= \int \mathrm{d}\mathbf{H}_{\text{loc}} D(\mathbf{H}_{\text{loc}}) \left[\frac{\mathbf{S}(t)\cdot\mathbf{S}(0)}{|\mathbf{S}(0)|^2}\right], \\ &= \int \mathrm{d}\mathbf{H}_{\text{loc}} D(\mathbf{H}_{\text{loc}}) \left[\cos^2(\theta) + \sin^2(\theta)\cos(\gamma_\mu H_{\text{loc}} t)\right]. \end{aligned} \tag{7.15}$$

When the polarization $\mathbf{P}(t)$ is introduced into equation (7.6) and (7.7), the asymmetry parameter $A_0 \rightarrow A_0\mathbf{P}(t)$. The time dependent positron count in a single detector placed in the direction $\hat{\mathbf{r}}$ ($|\hat{\mathbf{r}}| = 1$) is given by the expression [164, 22]

$$N(t) = N_\mu(0)\exp(-t/\tau_\mu)\left[1 + A_0\mathbf{P}(t)\cdot\hat{\mathbf{r}}\right] + \mathrm{B} \tag{7.16}$$

where B is a background parameter and $N_\mu(0)$ is initial muon count (in the following we skip the subscript μ). Consider again the situation shown in figure 7.2. The detector placed in front of the sample records the positron count $N_\mathrm{F}(t)$, and the detector placed behind the sample, i.e. 180° relative to $\hat{\mathbf{r}}$, records $N_\mathrm{B}(t)$. In the longitudinal geometry, the external field $\mathbf{H}_\mathrm{ext} = H_\mathrm{ext}\hat{z}$ and $\hat{\mathbf{r}} = \hat{z}$ are both parallel to the muon beam direction. The muon spin rotates around the sum $\mathbf{H}_\mathrm{loc} = \mathbf{H}_\mathrm{int} + \mathbf{H}_\mathrm{ext}$. Due to unavoidable intrinsic differences, the efficiency is not exactly the same for the two detectors. In general both the normalization and the background will not be the same. One can show the following relation between the positron count and the polarization

$$A_0P_z(t) = \frac{\left[N_\mathrm{F}(t) - \mathrm{B_F}\right] - \alpha\left[N_\mathrm{B}(t) - \mathrm{B_B}\right]}{\left[N_\mathrm{F}(t) - \mathrm{B_F}\right] + \alpha\left[N_\mathrm{B}(t) - \mathrm{B_B}\right]} \tag{7.17}$$

where, using $\alpha = N_\mathrm{F}(0)/N_\mathrm{B}(0)$

$$N_\mathrm{F}(t) = N_\mathrm{F}(0)\exp(-t/\tau_\mu)\left[1 + A_0P_z(t)\right] + \mathrm{B_F}. \tag{7.18}$$

$$N_\mathrm{B}(t) = \alpha^{-1}N_\mathrm{F}(0)\exp(-t/\tau_\mu)\left[1 - A_0P_z(t)\right] + \mathrm{B_B}. \tag{7.19}$$

where $P_z(t)$ is the polarization component along the muon spin direction. Apart from the constant A_0, the polarization can be deduced directly from the positron counts in the two detectors. $A_0P_z(t)$ is also known as the asymmetry function. Some examples are shown in the figures 7.4-7.6.

In a wide range of situations, the expected asymmetry function can be calculated theoretically, which in turn allows for meaningful numbers to be extracted from the data. In the following we shall discuss few important examples. These will serve a twofold purpose. 1) As concrete illustrations of the asymmetry function (7.17) for some simple field distributions. 2) The field distributions are directly used in the data analysis of our muon data, presented in chapter 9.

7.2.1 Uniform Internal Field

Consider first, the situation with a single well defined and static field H_0 on the muon site in a polycrystalline sample. Assuming a polycrystalline sample dictates a random orientation of the spatial crystallites and hence a random angle θ between the $\mathbf{H}_\mathrm{loc}$ and the implanted muon initial spin direction. The distribution $D(\mathbf{H}_\mathrm{loc}) = \delta(H_\mathrm{loc} - H_0)/4\pi H_0^2$ gives a particularly simple asymmetry function

$$P_z(t) = \frac{1}{3} + \frac{2}{3}\cos(\gamma_\mu H_\mathrm{loc}t), \tag{7.20}$$

where the numerical factors $\frac{1}{3}$ and $\frac{2}{3}$ reflect that fact that, for every implanted muon, one component of the local field will be parallel to- and two components will be perpendicular to the muon spin direction. The later will cause the muon spin to rotate and hence change the asymmetry into an oscillation with a frequency of oscillation given by the strength of the local field. The component of the field which is parallel to the muon spin direction does not result in any change of the initial asymmetry. If the sample would have been a crystal, the prefactors would generally differ from $\frac{1}{3}$ and $\frac{2}{3}$, but one finds that general from $a + (1-a)\cos(\gamma_\mu H_{\rm loc} t)$ where $0 < a < 1$ still holds. In

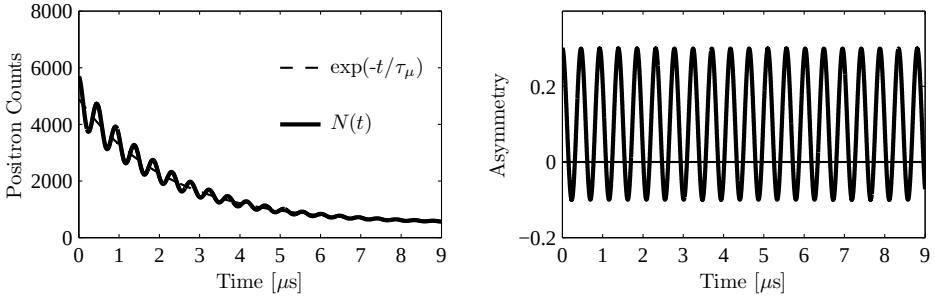

Figure 7.4: *Time evolution of equations (7.18) and (7.17) using (7.20) with* $H = 0.1\,T$ *and* $A_0 = 1/3$.

some cases, if the magnetic order forms a spin density wave the in zero field oscillation is best described by a Bessel function, see e.g. [176] and see also chapter 10.

7.2.2 Isotropic Random Internal Field

Next, consider the magnetic field distribution from random magnetic moments in the close vicinity of the muon site in a polycrystalline sample. We assume an isotropic Gaussian distribution with $\langle H_{\rm loc}\rangle = 0$ and variance $\langle H_{\rm loc}^2\rangle - \langle H_{\rm loc}\rangle^2 = (\sigma/\gamma_\mu)^2$ in all directions

$$D\left(\mathbf{H}_{\rm loc}\right) = \left(\frac{\gamma_\mu}{\sqrt{2\pi}\Delta}\right)^3 \exp\left(-\frac{1}{2}\left(\frac{\gamma_\mu H_x}{\sigma}\right)^2\right) \exp\left(-\frac{1}{2}\left(\frac{\gamma_\mu H_y}{\sigma}\right)^2\right) \exp\left(-\frac{1}{2}\left(\frac{\gamma_\mu H_z}{\sigma}\right)^2\right).$$

In this case, the asymmetry function gives

$$P_z\left(t\right) \;=\; \frac{1}{3} + \frac{2}{3}\exp\left(-\sigma^2 t^2/2\right)\left[1 - \sigma^2 t^2\right], \tag{7.21}$$

which is known as the Gaussian Kubo-Toyabe (KT) function [177]. This function describe e.g. data from samples with no ordered electronic moments, then the KT function expresses the field distribution of the randomly oriented nuclear moments.

7.2.3 Combined Isotropic Random- and Uniform Internal Field

In many real experiments, the situation is often more complicated than in the two examples presented above. We consider now, the situation where there is both a uniform

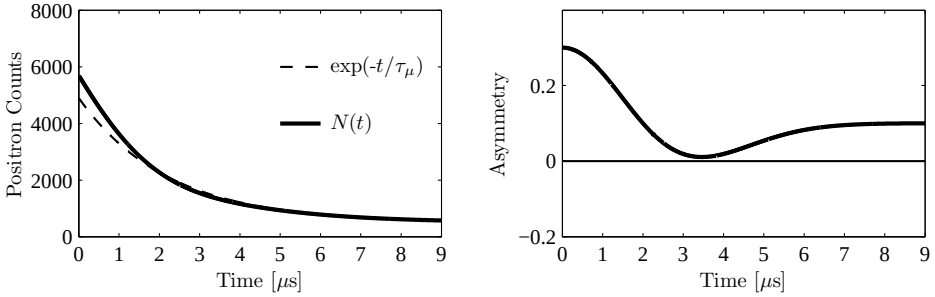

Figure 7.5: *Time evolution of equations (7.18) and (7.17) using (7.21) with* $\sigma = 0.5\mu s^{-1}$ *and* $A_0 = 1/3$.

static field and a Gaussian field distribution with finite variance. The finite variance could be due to chemical inhomogeneities or an intrinsic inhomogeneous magnetic phase in the sample. In experiments, this finite variance manifest itself as a damping of the different components of the asymmetry function. A Gaussian distribution is often sufficient. However, in special cases where the magnetic phase of the sample is diluted with non-magnetic impurities, a Lorentzian is often better. For a Gaussian field distribution the equation (7.20) modifies into

$$P_z(t) = \frac{1}{3}\exp\left(-\sigma_L^2 t^2/2\right) + \frac{2}{3}\exp\left(-\sigma_T^2 t^2/2\right)\cos\left(\gamma_\mu H_{\rm loc} t\right), \qquad (7.22)$$

where the longitudinal relaxation σ_L and transverse relaxation σ_T in general are expected to be different.

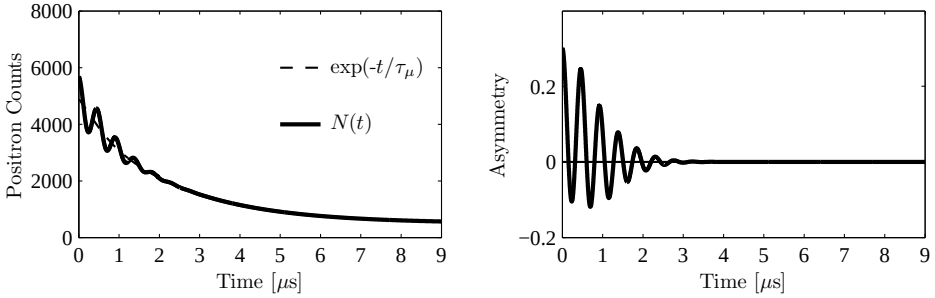

Figure 7.6: *Time evolution of equations (7.18) and (7.17) using (7.22) with* $\sigma_L = 2\sigma_T$, $\sigma_T = 1\mu s^{-1}$, $H = 0.1T$ *and* $A_0 = 1/3$.

7.3 Muon Spin Rotation in a Transverse Field

In this section we discuss muon spin rotation experiments performed in an external field which is perpendicular to the initial muon spin direction (TF-μ-SR). This section is mainly based on [164, 22]. The transverse geometry is seen in figure 7.7. For example, if we consider the same coordinate system as seen in figure 7.3, the initial muon spin

direction is rotated to the $\hat{x}$ direction, the field is again applied in the $\hat{z}$ direction and $\mathbf{P}(0) = P_x(0)$ and $P_y(0) = P_z(0) = 0$, the polarization $\mathbf{P}(t)$ precesses in the xy-plane. If the direction of observation $\hat{\mathbf{r}}$ is chosen in the xy plane the equation (7.16) modifies into

$$N(t) = N_\mu(0)\exp(-t/\tau_\mu)\left[1 + A_0 P_x(t)\cos(\gamma_\mu H_{\rm loc} t + \phi)\right] + \mathrm{B} \qquad (7.23)$$

where ϕ is the initial angle (phase) between $\mathbf{P}(0)$ and $\hat{\mathbf{r}}$. Assuming that the local field

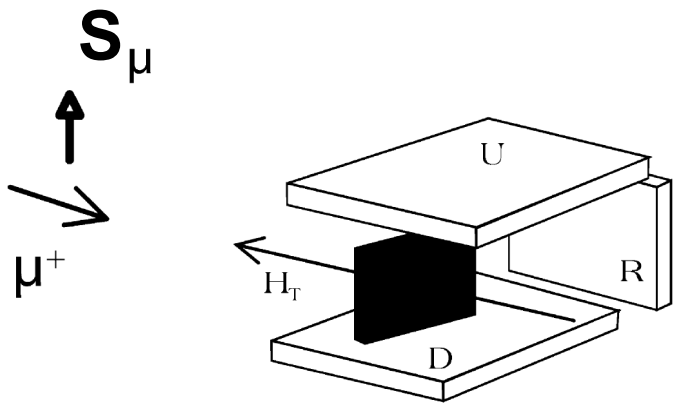

Figure 7.7: *The experimental geometry for TF-μ-SR. Adapted from [175].*

distribution to be Gaussian, the asymmetry function takes the form of a damped cosine function [164, 22]

$$P_x(t) = e^{\frac{1}{2}\sigma_{\rm TF}^2 t^2}\cos(\gamma_\mu H_{\rm ext} t + \phi) \qquad (7.24)$$

where the relaxation $\sigma_{\rm TF}^2 = \gamma_\mu^2\left(\langle H_{\rm loc}^2\rangle - \langle H_{\rm loc}\rangle^2\right)$ is determined by the variance of the local static field distribution. This relaxation rate is known as at $1/T_2$. In the following section we introduce the field distribution of a Type II superconductor where $\sigma_{\rm TF}$ can be calculated explicitly.

7.3.1 Muon Spin Rotation in Type-II Superconductors

Now we discuss the special case of muon spin rotation in type II superconductors. This section is based on E. H. Brandt [178]. In the mixed state of a type II superconductor the magnetic field is given by the solution of the London equation (2.9). In high temperature superconductors such as LSCO, which are of type II, the penetration depth spans much more that one unit cell and is as such an inhomogeneous magnetic phase from the μ-SR point of view. The solution of (2.9) gives the magnetic field $\mathbf{H}(\mathbf{r}) = H(\mathbf{r})\,\hat{z}$ at any point in space inside the bulk of the superconductor

$$H(\mathbf{r}) = H_0 \sum_{\mathbf{k}_{mn}} H_{\mathbf{k}_{mn}} \exp(-i\mathbf{k}_{mn}\cdot\mathbf{r}), \qquad (7.25)$$

where $\mathbf{k}_{mn}$ is a reciprocal lattice vector. $H_{\mathbf{k}_{mn}}$ is given by

$$H_{\mathbf{k}_{mn}} = \frac{1}{1+\lambda^2\left|\mathbf{k}_{mn}\right|^2}, \tag{7.26}$$

and $H_0 = n\Phi_0$ where n is the number of vortices per unit area and $\Phi_0 = 2.07\cdot 10^{-15}\mathrm{Tm}^2$ is the flux quantum [25]. From equation (7.25) we find the variance of this distribution

$$\left\langle H_{\mathrm{loc}}^2\right\rangle - \left\langle H_{\mathrm{loc}}\right\rangle^2 = H_0^2 \sum_{\mathbf{k}_{mn}\neq\mathbf{0}} \left|H_{\mathbf{k}_{mn}}\right|^2. \tag{7.27}$$

Noting that $\lambda^2\left|\mathbf{k}_{mn}\right|^2 >> 1$,the square of (7.26) can be approximated by $\left|H_{\mathbf{k}_{mn}}\right|^2 \approx 1/\lambda^4\left|\mathbf{k}_{mn}\right|^4$. Choosing an isoscalar triangular flux line lattice (FLL) where each vortex site is shared between two triangles, see the insert in figure 7.8, we find the lattice constant $d = \left(2\Phi_0/\sqrt{3}H_0\right)^{1/2}$ and $\mathbf{k}_{mn} = \left(16\pi^2/3d^2\right)\left(m^2+n^2+mn\right)$. Using this, we find

$$\left\langle H_{\mathrm{loc}}^2\right\rangle - \left\langle H_{\mathrm{loc}}\right\rangle^2 \approx 0.0037106\Phi_0^2\lambda^{-4} \tag{7.28}$$

The magnetic field distribution, shown in figure 7.8, follows from [22]

$$D\left(\mathbf{H}_{\mathrm{loc}}\right) = \frac{1}{A}\int_A \mathrm{d}\mathbf{r}\delta\left(H\left(\mathbf{r}\right) - H_{\mathrm{loc}}\right) \tag{7.29}$$

where the integral extends over one single unit cell of area A. This field distribution is often approximated be a Gaussian damping even though the bare distribution is highly non-Gaussian with an asymmetric line shape due to long tail towards very high fields, found inside the vortex cores, with a low probability due to the short spacial extent of the core region, this is indicated at point V in figure 7.8. However, disorder and flux pinning may smear the distribution into a more Gaussian type line shape.

The discussion now turns to the frequency of the cosine in (7.24). Following [179], we find the following relations for the minimum frequency ω_{min} in the system, seen at point M in figure 7.8 and the saddlepoint frequency ω_{sad} seen at point S in figure 7.8

$$\omega_{\mathrm{min}} = \omega_{\mathrm{ext}} - 0.79\frac{\gamma_\mu\Phi_0}{4\pi\lambda^2}\ln\left(2\right), \tag{7.30}$$

$$\omega_{\mathrm{sad}} = \omega_{\mathrm{ext}} - 0.67\frac{\gamma_\mu\Phi_0}{4\pi\lambda^2}\ln\left(2\right), \tag{7.31}$$

and for $H_{\mathrm{ext}} < H_{c2}$ the muon spin rotation frequency is expected to decrease when $T < T_c$ according to the equation

$$\omega - \omega_{\mathrm{ext}} = \frac{\omega_{c2}-\omega_{\mathrm{ext}}}{1+\beta_{\mathrm{G}}\left(2\kappa^2-1\right)}, \tag{7.32}$$

where $\omega_{\mathrm{ext}} = \gamma_\mu H_{\mathrm{ext}}$ and $\omega_{c2} = \gamma_\mu H_{c2}$. The geometrical parameter β_{G} takes the value 1.16 for a triangular lattice. A TF-μ-SR experiment thus directly determines T_c as the temperature where the frequency drops.

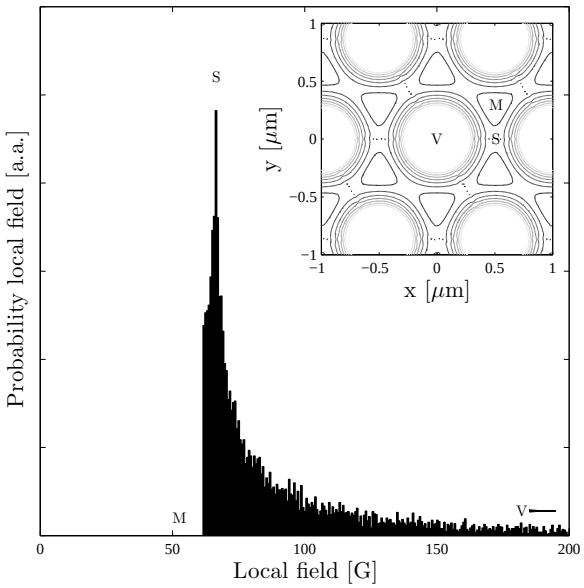

Figure 7.8: *The insert shows the FLL unit cell for the isotropic type II superconductor with $\lambda = 0.1318\mu m$ and an average field of 0.01T. The contour lines for local fields above 0.01T are left out for clarity. The main figure shows the corresponding μ-SR lineshape. The minimum field (marked 'M') is at the center of the triangle . The maximum field (marked 'V') is in the vortex core and the saddle point (marked 'S') has the highest probability.*

The transverse field relaxation rate from (7.24), is directly proportional to the variance of the field distribution originating from the magnetic vortices. This is given by (7.27) and depends on the penetration depth as $1/\lambda^2$. In the isotropic London theory presented in chapter 2 we find the relation

$$\frac{1}{\lambda^2} = \frac{4\pi n_s e^2}{m^* c^2}. \tag{7.33}$$

The relation (7.32) implicitly assumes the so-called clean limit where the mean free path is much larger than the coherence length. Y. J. Uemura proved that a universal linear relation between $\sigma \propto n_s/m^*$ and T_c within each of the different families of high temperature superconductors [180, 181, 182], see figure 7.9. This known as the Uemura plot. Above a certain value of n_s/m^* the critical temperature saturates and even decreases again at higher n_s/m^*. The linear part of the relation, can be explained if the energy scale of the Cooper pairing is of the same order as the Fermi energy, then one would expect $T_c \propto T_F$. In high temperature superconductors, the Cooper pairs are localized within the CuO_2 planes, and for a two dimensional electron gas the Fermi energy $\epsilon_F = k_B T_F = \pi\hbar^2 n_e/m^*$ where n_e is the two dimensional electron density. From the BCS gap function, we get $T_c \propto \hbar\omega_D$ and hence we obtain $T_c \propto n_e/m^*$ [180, 181]. The temperature dependence of the Cooper pair condensate density, and hence the muon relaxation rate, reflects the symmetry of the superconducting gap. From BCS

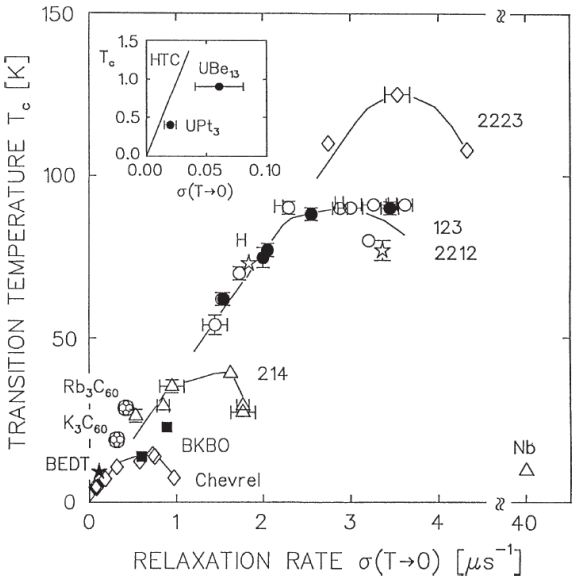

Figure 7.9: *This figure shows the Uemura plot from [180] which illustrate the (partially) linear relation* T_c *and* $\sigma(T \to 0) \propto n_s/m^*$.

theory, we get the temperature dependence of the so-called 'superfluid density' [39]

$$n_s(T) = n_s(0)\left(1 - \frac{1}{\pi k_B T}\int_0^{2\pi} \mathrm{d}\theta \int_0^{\infty} \mathrm{d}\epsilon n_F(\epsilon_{\mathbf{k}})\left[1 - n_F(\epsilon_{\mathbf{k}})\right]\right), \quad (7.34)$$

where $n_F(\epsilon_{\mathbf{k}}) = \left(1 + \exp\left(\sqrt{\epsilon_{\mathbf{k}}^2 + \Delta_{\mathbf{k}}(T,\theta)^2}/k_B T\right)\right)^{-1}$ is the Fermi occupation factor and the angle θ is the azimuthal angle in k-space, defined by $\tan(\theta) = k_y/k_x$. For the isotropic s-wave gap function $\Delta_{\mathbf{k}}(T,\theta) = \Delta_{\mathbf{k}}(T,0)$, and the anisotropic d-wave gap function $\Delta_{\mathbf{k}}(T,\theta) = \Delta_{\mathbf{k}}(T,0)\cos(2\theta)$, we obtain the following relations

$$\lambda_{s-wave}^{-2}(T) = \lambda^{-2}(0)\left(1 - \gamma\sqrt{\frac{1}{k_B T}}\exp\left(-\Delta_{\mathbf{k}}(T,0)/k_B T\right)\right), \quad (7.35)$$

$$\lambda_{d-wave}^{-2}(T) = \lambda^{-2}(0)(1 - \alpha T), \quad (7.36)$$

where α and γ are constants. We see from (7.36) that in the case of a d-wave superconductor, such as the High-T_c's, we expect the relaxation rate to have a linear dependence on temperature, at least for $T << T_c$. In disordered systems, however, the linear term may weaken, and following [183, 184] the presence of impurities in a d-wave superconductor, give rise to a quadratic term, that must be added to (7.34)

$$\lambda_{d-wave+imp}^{-2}(T) = \lambda^{-2}(0)(1 - \alpha T - \beta T). \quad (7.37)$$

In chapters 9 and 10, we will use (7.37) to obtain the penetration depth.

7.4 Manipulating μ-SR data

All μ-SR data analysis for this thesis was performed using the C++/ROOT based software musrfit which is available from the PSI Linux cluster llcsl5a [185].

In the practical interpretation of μ-SR data, two manipulation techniques are commonly used. The Fourier power spectrum of any μ-SR (asymmetry) spectrum is equivalent to the local magnetic field distribution. The Fourier power spectrum is directly obtained from the absolute values of each coefficient in the discrete Fourier transform. The resulting Fourier power spectrum forms a sum of peaks corresponding to the different muon spin rotation frequencies in the system. Due to the finite counting rates peak will always appear slightly broader that the actual field distribution and the spectrum will contain statistical noise. This noise can be eliminated using a suitable apodization. Apodization is described in [186] and on the on-line musrfit manual [185]. When using apodization, one must keep in mind that the apodization procedure itself also slightly broadens the peaks further.

When dealing with TF-μ-SR, the external field often result in a muon precession period $T \propto 1/H_{\mathrm{loc}} \propto 1/\omega$ which is so fast compared to the time structure of the histogram, that any meaningful visualization is impossible. Another important technique, mainly for visualization in my case, is the rotating reference frame (RRF). The RRF transformation expresses the static laboratory polarizations in a rotating frame which effectively reduced ω. The relation between the laboratory polarizations P_x and P_y and the RRF polarizations P_x^{RRF} and P_y^{RRF} is given by

$$\begin{pmatrix} P_x^{RRF}(t) \\ P_y^{RRF}(t) \end{pmatrix} = \begin{bmatrix} \cos(\omega_{\mathrm{RRF}} t) & \sin(\omega_{\mathrm{RRF}} t) \\ -\sin(\omega_{\mathrm{RRF}} t) & \cos(\omega_{\mathrm{RRF}} t) \end{bmatrix} \begin{pmatrix} P_x(t) \\ P_y(t) \end{pmatrix}. \tag{7.38}$$

7.5 Theory of Dynamical Relaxation

The following section deals with the relaxation caused be a time dependent magnetic environment around the muon site. The approach presented here is based on [187]. The motion for the muon spin in the presence of a fluctuating magnetic field is is no longer sufficiently described (7.11). A time dependent magnetic field can couple to the component muon spin which is parallel to the field by flipping it. The Zeeman Hamiltonian of this interaction reads $\mathcal{H} = -\hbar\gamma_\mu \mathbf{S}_\mu \cdot \mathbf{H}_{\mathrm{loc}}(t)$. The term spin relaxation, refers in this case to the characteristic time over which the muon spin direction is unchanged. The fluctuation rate of the magnetic surroundings usually increase with increasing temperature. Assuming simple Gaussian fluctuations with correlation time, τ_c, and the correlation function of the transverse field components reads

$$\langle H_{\mathrm{loc}}^x(0) H_{\mathrm{loc}}^x(t)\rangle = \langle H_{\mathrm{loc}}^y(0) H_{\mathrm{loc}}^y(t)\rangle = H_\perp \exp(-t/\tau_c). \tag{7.39}$$

The muon is a spin half particle and may be in either of the two orthogonal states, $|\uparrow\rangle$ or $|\downarrow\rangle$ corresponding to $S^z = +1/2$ and $S^z = -1/2$ respectively. The transverse field components $H^x = H^+ + iH^-$ and $H^y = H^+ - iH^-$ stimulate transitions between

the two muon spin states $|\uparrow\rangle$ and $|\downarrow\rangle$, and hereby causes a relaxation similar to the so-called spin-lattice relaxation in NMR.

The probability of inducing a transition between the two muon spin states is independent of whether the transition goes from $|\uparrow\rangle$ to $|\downarrow\rangle$ or vice versa. The time evolution of the populations $N_\uparrow(t)$ and $N_\downarrow(t)$ are then given by the following rate equations

$$\frac{\mathrm{d}}{\mathrm{d}t}N_\uparrow = WN_\downarrow(t) - WN_\uparrow(t) \qquad \frac{\mathrm{d}}{\mathrm{d}t}N_\downarrow = WN_\uparrow(t) - WN_\downarrow(t) \tag{7.40}$$

where the rate W is derived from Fermi's golden rule (4.11)

$$W = \gamma_\mu^2 \sum_{\alpha=\{x,y\}} \left|\langle S^z| S_\alpha \left|S^{z'}\right\rangle\right|^2 \int \mathrm{d}t e^{-i\omega t} \langle H^\alpha(0) H^\alpha(t)\rangle, \tag{7.41}$$

where ω is the Larmor frequency. The difference between $N_\uparrow(t)$ and $N_\downarrow(t)$ leads to a relaxation rate $T_1^{-1} = 2W$. Now, using (7.39), we can evaluate (7.41) and obtain

$$T_1^{-1} = \gamma_\mu^2 H_\perp^2 \frac{\tau_c}{1-(\omega\tau_c)^2}. \tag{7.42}$$

Knowledge about the temperature dependence of the relaxation rate $\sigma = 1/T_1$ (7.42) is obtained directly from the damping of the asymmetry function. When $1+(\omega\tau_c)^2 = 0$ the relaxation rate shows a peak. This is shown in figure 7.10. Such a peak is observed when the temperature dependent ω becomes equal to $1/\tau_c$ where τ_c is the 'muon timescale' i.e. the timescale below which the fluctuations seems static to the muon. This is a landmark of a magnetic phase transition as the correlation time of the electronic moments diverges exactly at the critical temperature. A typical τ_c in a muon spin rotation experiment is 10^{-8}s.

7.6 The General Purpose Surface-Muon Instrument

We have performed all measurements shown in this thesis, see chapters 8, 9 and 10, on the General Purpose Surface-Muon Instrument (GPS) at the Laboratory for Muon Spin Spectroscopy LMU on the Swiss Muon Source located at the Paul Scherrer Institute. GPS has five detectors; in front and behind the sample position, perpendicular, viewed along the muon beam direction (longitudinal detectors), above and below the sample position perpendicular to the muon beam direction and a single detector to the right of the sample position (transverse detector). The sample stick is inserted from the left.

GPS sits on the piM3.2 muon beam line that Positive muons with the standard momentum 28MeV/c. The muon beam is more than 95% polarized. GPS uses the technique of active collimation, this means that so-called veto detectors are placed both at the front detector and the back detector. The veto detectors remove any positon count from muons that do not impinge directly on the sample position and hence reduce background. The GPS has a so-called spin rotator which is used to direction of the spin $\sim 60^\circ$ with respect to muon momentum when doing transverse

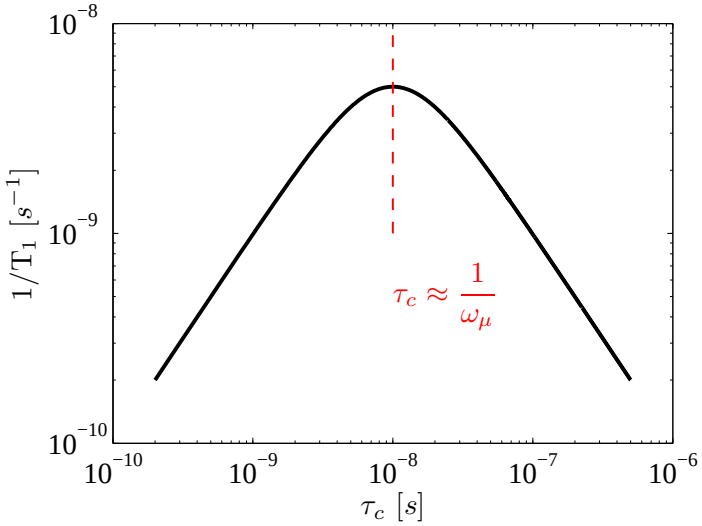

Figure 7.10: *A slowing down of magnetic fluctuations results in a maximum in the dynamical relaxation rate* $1/T_1$ *in a muon spin rotation experiment. The figure shows such a maximum if a muon timescale of* $10^{-8}s$ *is chosen.*

field μ-SR, meaning however that $\mathbf{S}_\mu$ is never fully perpendicular to the field,a s is was assumed in the ideaized calculation in section 7.3.

During the experiment, the samples were mounted on a silver (fork shaped) sample holder.

CHAPTER 8

A Study of Phase Separation between Itinerant Ferromagnetism and Superconductivity in the Hexagonal Intermetallic Y_9Co_7

The general question of co-existence of superconductivity and magnetism will be a recurrent theme in the next chapters. Since an antiferromagnetic phase is always found in close proximity of superconductivity in the high temperature superconductors, where the superconductivity is still largely not understood and where magnetic and superconducting phases are sometimes overlapping, it is natural to look at the few low temperature (or conventional) superconductors which shares these characteristics.

Y_9Co_7 was the first compound where superconductivity was confirmed to co-exist with ferromagnetism [41]. Even though the study of Y_9Co_7 is old, there are still a number of unsolved questions associated to it. This chapter is concerned with whether the co-existence microscopic i.e. the same electrons participate in both phenomena, or if it is macroscopic where the sample develops patches of superconductor and patches of magnetic regions which are spatially separate from each other. Previous μ-SR work suggested the latter [188].

The complex chemistry of the Y-Co alloy have often prohibited the fabrication of high quality samples in the past. However, in connection with this work T. Klimczuk (previously associated with the group of R. J. Cava at Princeton University and presently at Gdansk University of Technology), has managed to fabricate what is probably the purest and most homogeneous samples to date. Indeed Micro X-ray Fluorescence (μXRF) shows a completely homogeneous distribution of Y and Co on a micrometer length scale [189]. Another figure-of-merit confirming the high quality of this sample is the residual resistivity ratio (RRR), which was determined to be 35 for this sample [189]. Such high RRR values are considered state-of-the-art [41].

We report muon spin rotation (μ-SR) measurements in zero field and weak transverse field. Our experiments are similar to the previous work by Ansaldo et al. [188] who found evidence that superconductivity and magnetism phase separates macroscop-

ically. The magnetic part of the sample studied by Ansaldo in fact took up 75% of its volume. Since we believe we have samples of the highest quality, we were encouraged to redo these measurements, to firmly exclude the possibility of chemical inhomogenities as the cause for the phase seperation.

8.1 Introduction to Co-existence of Magnetism and Superconductivity in Y_9Co_7

After some controversy, partially due to the existence of several stable phases [190], the crystal structure of Y_9Co_7 is now believed to be hexagonal, Space group #176 ($P6_3/m$) with lattice parameters a=11.53Å and c=4.05Å (See Figure 8.1) [41]. The common structural feature of the various phases [190] is trigonal prisms of Yttrium atoms, with Cobalt atoms at their centers. In Y_9Co_7 the prisms form chains along the c-axis. Additional Co ions reside on the 2b sites, forming chains along c. These sites are only partially occupied [191]. NMR data indicate that only these Co ions are magnetic. Taking into account partial occupancy of the 2b sites, Takigawa and coworkers find local moments of 0.23 μ_B per occupied 2b site [192]

Y_9Co_7 is an example (of which there are very few) of conventional i.e. phonon driven superconductivity coexisting with weak itinerant ferromagnetism [194]. The magnetic and superconducting properties have been investigated by a variety of techniques. The superconducting properties below $T_c = 2.5$K are characterized by a coherence length of 315Å, penetration depth of 1750Å and critical fields $H_{c1} = 0.0092$T and $H_{c2} = 0.38$T [41]. The basic magnetic properties below the Curie temperature $T_C = 4.5$K are derived from a Curie-Weiss fit to the susceptibility giving a Curie-Weiss constant of (+)13.6K with a small effective moment of $0.14\mu_B$/Co suggesting itinerant magnetism [41].

The coexistence of superconductivity and magnetism in the samples studied in this chapter are evident from is evident from both the AC susceptibility and the specific heat (C/T) measurements shown in figure 8.2 prepared by T. Klimczuk [189]. The real part of the susceptibility drops drastically below T_c due to the diamagnetism of the Meissner state of the superconductor.

Note that the real part of the susceptibility starts to increase around 7.5K, but that Arrott plot analysis yields $T_C = 4.25K$ in our sample. The susceptibility signal between T_C and 7.5K likely corresponds to buildup of ferromagnetic correlations. The specific heat data displays two peaks, corresponding to the onset of ferromagnetism and superconductivity. T. Klimczuks analysis yields $T_c = 2.75$ K in our sample.

The itinerant ferromagnetism in Y_9Co_7 is believed to stem primarily from the partially occupied so-called 2b sites in the crystal structure [192, 193].

Note that in a sample characterized by a residual resistance ratio of 30, i.e. a sample of significantly better quality than the sample (RRR=10) used in the studies yielding the above H_{c1} and H_{c2} values, a much higher value of Hc2 was obtained: At T=0.1K, Sarkissian and Tholence find Hc2 *simeq* 2.2T [195]. It is clear from this difference in Hc2 that sample quality is of high importance for the physical properties of Y_9Co_7.

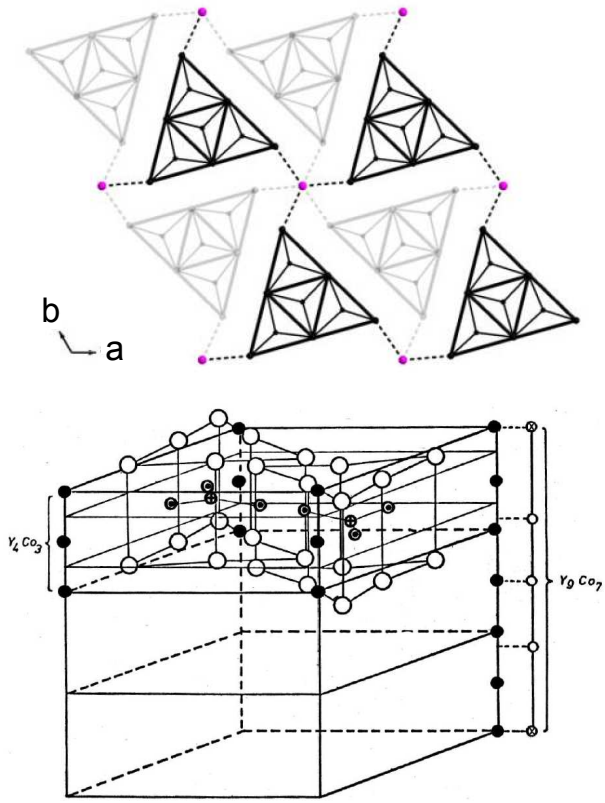

Figure 8.1: *This figure shows the presumed crystal structure of Y_9Co_7.* ***Top:*** *The prisms made of Yttrium atoms (large black circles) with Cobalt atoms (small black circles) inside shown in the (**a**,**b**)-plane. The red circles indicates the position of the partially occupied 2b Cobalt sites, these sites are believed to be the main source of the magnetism in this materials [192, 193] Another layer of Y-Co prisms are indicated in light gray. This figure was provided by T. Klimczuk [189].* ***Bottom:*** *The unit cell of Y_9Co_7. The open circles indicates the position of the Yttrium atoms in the prisms and the filled black circles indicate Co atoms. The Co atoms on the edge of the unit cell are the 2b sites. This figure is from [41].*

8.2 New μ-SR Y_9Co_7

We have performed zero field and weak transverse field ($H_{ext} = 0.005$T) muon spin rotation experiments on Y_9Co_7 between 1.6K and 13K. The experiments were performed using the GPS instrument, see section 7.6.

Figure 8.3 shows the zero field μ-SR data taken at various temperatures. Data at 1.6K is shown in upper panel. We observe a clear oscillation and a relaxation of the asymmetry from the magnetic part of the sample. Above 4.7K we no longer observe an oscillation but we still observe a large relaxation. This relaxed signal persists up to 6.7K where only a very small remanence can be seen below 0.5μs on top of a Kubo-Toyabe function (see chapter 7). Above 6.7K we no longer observe any clear signs of

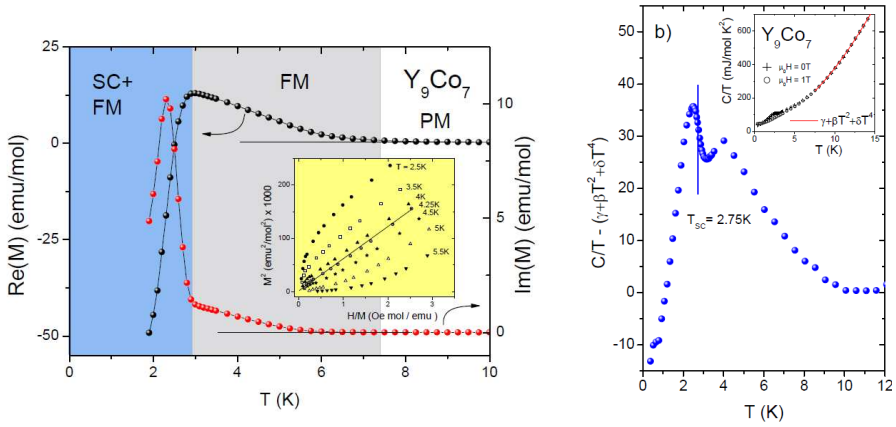

Figure 8.2: *These figures show susceptibility (**left**) and specific heat capacity (**right**) measurements of the Y_9Co_7 samples studied in this chapter. The insert in the left figure show a so-called Arrot plot which can be used to determine the critical temperature for ferromagnets. This sample displays a Curie temperature of 4.25K and a superconducting transition temperature of 2.75K. Both these figures were provided by T. Klimczuk [189].*

magnetism. At 12.9K the asymmetry is well described by a Kubo-Toyabe function.

The zero field μ-SR spectra at low temperature shown in figure 8.3, reveals a rapidly damped component with a clear oscillation below T_C. The oscillation corresponds to muons stopping at sites with a local field from ordered electronic moments which are static on the muon time scale. The tail of the magnetic component is seen to decay at times $t > 1\mu$s. This is due to dynamical relaxation, see chapter 7. This dynamic part of the magnetic signal persists up to about 6K. However, the oscillating signal does not account for the full asymmetry. In consistency with [188], a second slowly relaxing component must be added, corresponding to muons stopping at sites with only disordered nuclear moments. The fact that the μ-SR spectrum can not be described be a single component, indicates a phase separated ground state, consisting of a magnetic volume fraction and a non-magnetic volume fraction. The latter represents areas in the sample larger than ~ 30Å, which is roughly the extent of the dipole-dipole interaction, and hence the length scale away from a magnetic region where the muons would still feel the ordered electronic moments. Above 7K the asymmetry is well described by a single Kubo-Toyabe function, see chapter 7.

The sample was polycrystalline, hence the local ordered moment is randomly orientated relative to the direction of the muon spin. On average, only $\frac{1}{3}$ of the local fields are parallel and $\frac{2}{3}$ are perpendicular to the muon spin direction. Hence, we fit our zero field μ-SR data to the following model containing the two components described above

$$P_z(t) = \begin{cases} A_{\mathrm{m}}\left[\frac{2}{3}\cos(\omega t)\exp(-\lambda_{\mathrm{stat}}t) + \frac{1}{3}\exp(-\lambda_{\mathrm{dyn}}t)\right] & \\ +A_{\mathrm{nm}}\exp\left(-\frac{1}{2}\sigma^2t^2\right) & \text{for} \quad T \leq T_C \\ A_{\mathrm{nm}}\left(\frac{1}{3} + \frac{2}{3}\exp(-\sigma^2t^2/2)\left[1-\sigma^2t^2\right]\right) & \text{for} \quad T > T_C \end{cases} \tag{8.1}$$

Here ω is the muon spin rotation frequency, λ_{stat} and λ_{dyn} are the static and dynamic

relaxation rates of the magnetic component, respectively, and σ is the relaxation rate due to nuclear moments. The asymmetry $A_{\rm m}$ is converted to a magnetic volume fraction by $V_{\rm m} = A_{\rm m}/(A_{\rm m} + A_{\rm nm})$. In the limit $T \to 0$ we find also the superconducting volume fraction $V_{\rm sc} = 100\% - V_{\rm m}$. As examplified by the fits shown in figure 8.3, the model works well.

The zero field temperature dependence of the magnetic volume fraction in Y_9Co_7 is shown in figure 8.4. The two dashed lines in figure 8.4 indicate the Curie temperature $T_C = 4.25$K and the superconducting transition temperature $T_c = 2.75$K, see the previous section. We observe that the volume fraction raises gradually from roughly 7K to a final value of roughly 60%. This is consistent with the data shown in figure 8.2 where magnetic correlations are also seen to appear around the same temperature. We observe that the full asymmetry for the magnetic part of the sample develops not directly at T_C but rather close to 3K.

Weak transverse field μ-SR spectra are also shown in 8.3. Two distinctively different oscillations are observed in the data taken at 1.6K. Taking the zero field result as a point of departure we expect one oscillation to reflect the muons stopping in the diamagnetic superconducting regions and the other to reflect muons stopping in the magnetic regions. The oscillation due to muons stopping in the magnetic regions must be characterized by a more rapid relaxation than the oscillation due to superconducting regions. At high temperature a single oscillation fits the data nicely. We thus fit our weak transverse field data to the following model

$$P_x(t) = \begin{cases} A_{\rm m}\cos(\omega_{\rm fast}t + \delta)\exp\left(-\frac{1}{2}\sigma^2_{\rm fast}t^2\right) & \\ +A_{\rm nm}\cos(\omega_{\rm slow}t + \delta)\exp\left(-\frac{1}{2}\sigma^2_{\rm slow}t^2\right) & \text{for} \quad T \le T_C \\ A_{\rm nm}\cos(\omega_{\rm slow}t + \delta)\exp\left(-\frac{1}{2}\sigma^2_{\rm slow}t^2\right) & \text{for} \quad T > T_C \end{cases} \tag{8.2}$$

where the phase δ is a fixed number for all the fits. As exemplified by the data shown in figure 8.3 the model adequately describes the data.

From the temperature dependence of the fast relaxation rate $\sigma_{\rm fast}$, shown in figure 8.5, we observe the onset temperature of the magnetism to be $\sim 7K$. This is in full consistency with our zero field data and the data show in figure 8.2. We find $\sigma_{\rm fast}(T \to 0) \sim 4$MHz. By contrast, the slow relaxation show no clear temperature dependence below 6K.

The magnetic volume fraction measured by zero field μ-SR in this sample reached $\sim 60\%$ and there is no effect seen on the volume fraction when cooling below T_c. Hence no competition between the superconducting and magnetic order parameters can be infered from this data. This is an additional argument against any microscopic connection between the two phases. In transverse field we find a magnetic volume fraction approaching $\sim 52\%$, which is in fair agreement with the zero field analysis.

Figure 8.4 also shows the dynamic relaxation rate. We observe a peak at T_C which is caused by the magnetic phase transition, see chapter 7. Further, we observe that the dynamical relaxation rate, $\lambda_{\rm dyn}$, increases at low temperatures starting just below $T_{\rm sc}$ and continuing to the lowest temperatures probed. This effect could mark the onset of a Hebel-Slichter peak [196], but in the absence of data taken at sub-Kelvin

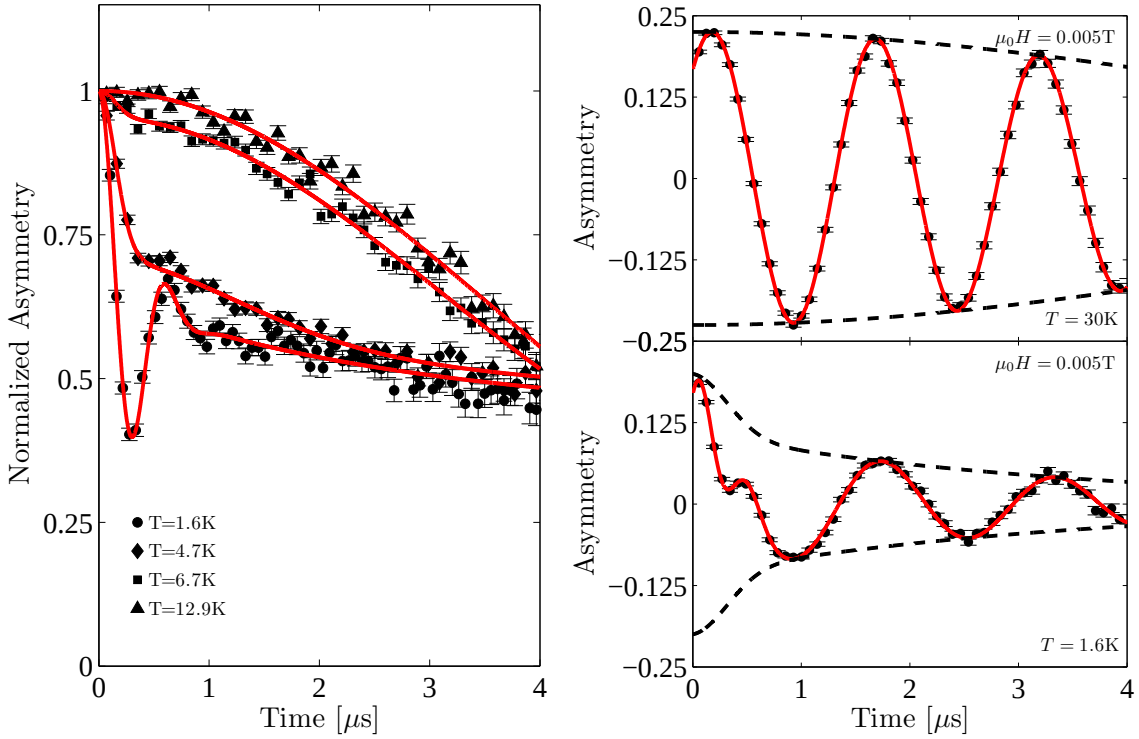

Figure 8.3: ***Left:*** *Shows raw zero field μ-SR data at the different temperatures where the spectrum from Y_9Co_7 changes behavior. At 1.6K we observe a clear frequency and a relaxation from the magnetic part of the sample. Above 4.7K we no longer observe the characteristic oscillation, but we still observe the relaxing magnetic contribution. Above 6.7K we only observe a single component which is well described by a Kubo-Toyabe function.* ***Right:*** *Shows raw weak transverse field μ-SR data at 1.6K and 30K. At 1.6K we observe two oscillations with different frequencies. At 30K we observe only one component with a frequency consistent with the external field.*

temperatures no firm conclusion can be drawn on this point. A Hebel-Slichter peak have been observed one before by μ-SR in Rb_3C_{60} [197, 198].

From equation (8.1), we obtain $\omega = (1.402 \pm 0.014)$MHz at 1.6K which corresponds to a local field of 0.0018T (110Oe). This value is in excellent agreement with the value quoted by Ansaldo [188]. What Ansaldo did not observe, but what is clear from our analysis is an anomaly in the temperature dependence of the muon spin rotation frequency shown in figure 8.4 and its inset: Below the superconducting transition temperature, T_c, the frequency tends to saturates around $\sim$ 1.4MHz. However, at temperatures near 2K it rises further to reach a value of 1.5 MHz at the lowest temperatures. This effect is a robust result of our analysis. A possible origin will be discussed below.

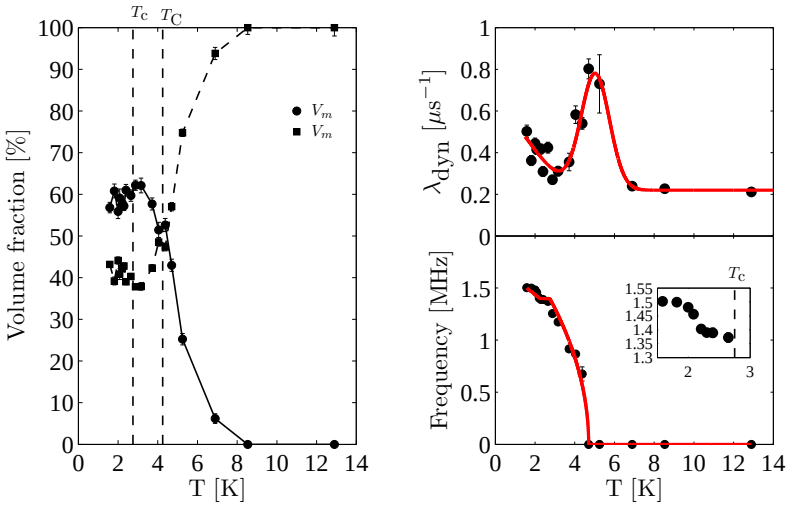

Figure 8.4: ***Left:*** *The magnetic and non-magnetic volume fractions measured by zero field μ-SR. The onset temperature for magnetism is found to be $\sim 7K$. No clear effect of competition between the superconducting and the magnetic order parameter is seen in this data.* ***Right:*** *The zero field frequency and dynamical relaxation rate, λ_{dyn}. Both the peak in the dynamical relaxation rate and the disappearance of the frequency confirms that T_C is 4.25 in this sample. We observe an anomaly below T_c which we believe can be explained in terms of a macroscopically phase separated picture, see the insert.*

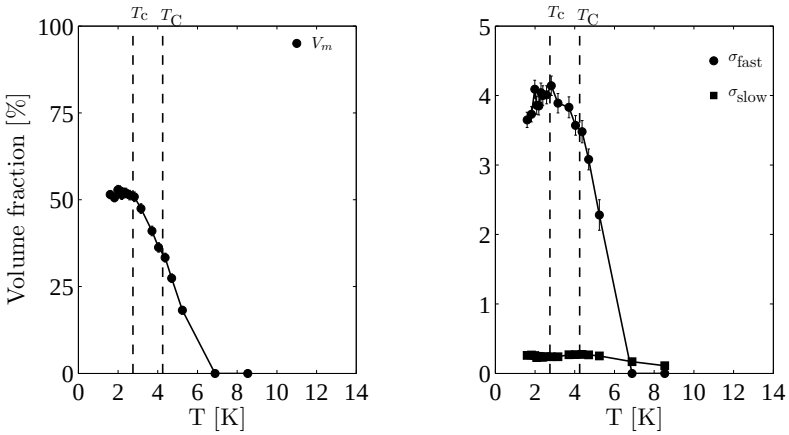

Figure 8.5: ***Left:*** *The magnetic volume fraction measured by transverse field μ-SR. We find general consistency between our transverse field and zero field data.* ***Right:*** *The fast and slow relaxation rates obtained from fits to the model (8.2). The slow rate σ_{slow} corresponds the non-magnetic/superconducting parts of the sample and has no clear temperature dependence. The fast rate σ_{fast} corresponds to the magnetic areas of the sample, and seems to decrease slightly at T_c. It is not currently known if/how this could be related to superconductivity.*

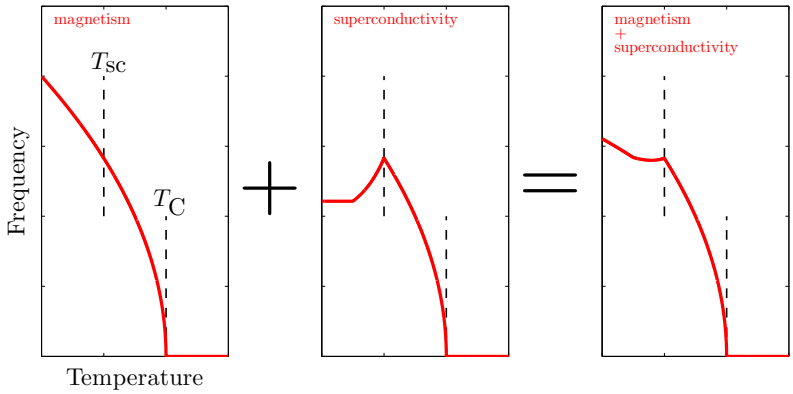

Figure 8.6: *These figures illustrate the idea which we think explains the behavior of the observed zero field frequency, ω seen in figure 8.4. The frequency signal of a magnetizing solid is assumed to follow a power law, this is shown in the left part of the figure. When a part of the sample turns into a superconductor, the interior of the these regions are diamagnetic with shielding currents in their surface to counteract the magnetism. The superconductor is known to change the frequency measured by the muon to a slightly lower value where it then flattens out, this is shown in the middle part of the figure. If the frequency behavior of the magnetic and the superconducting part of the sample is added, which is the case in a zero field Muon spin rotation experiment, we would observe a behavior close to what we find.*

8.3 Discussion and conclusion

Based on a simple physical picture of phase separation (See figure 8.6), we interpret this increase in frequency below T_c as caused by superconducting shielding currents. These currents act to reduce the local field seen by muons implanted near boundaries between magnetic and superconducting regions, as compared with the still increasing local field seen by muons implanted deep in the magnetic regions. If we assume that the ordered moment inside magnetic regions follows a simple power law i.e $\omega \propto (T_C - T)^{1/2}$ and that when superconductivity sets in, macroscopic parts of the sample become diamagnetic with no local field seen by muons stopping in the centers of these areas. Currents in the surface layer of the superconductor counteract the field of the surrounding magnet. This phenomenon is known from the study of flux lines lattices in high temperature superconductors to lower the effective local field, see chapters 9 and 10. The measured zero field frequency reflects the combined contributions from muons stopping inside the magnetic areas (which increases ω as temperature drops below T_C) and muons stopping in the superconducting areas within the penetration depth from the surface (which first decreases ω due to the shielding currents, and then saturates at lower temperatures). The sum of two such contributions can mimic the behavior of ω that we have observed (Compare figures 8.6 and 8.4).

We report that given the sample of Y_9Co_7 of the best quality available, μ-SR finds the superconducting and magnetic phases, which are well documented with various experimental techniques (See figure 8.2, to be phase separated on a length scale larger

than ~ 30Å . No effect is seen on the magnetic volume fraction upon cooling through T_c, which is further indication that the nature of the co-existence is not microscopic. These findings largely confirm those of Ansaldo et al. [188]. In addition, we observe an anomaly in the zero field μ-SR frequency, which we interpret as further evidence for macroscopic phase separation. Moreover, our data provide what might be a preliminary glimpse of a Hebel-Schlichter peak at temperatures of order 1K. Further experiments at sub-Kelvin temperatures would be needed to confirm or dismiss this possibility.

CHAPTER 9

Unique magnetic and superconducting phases in super-oxygenated $La_{2-x}Sr_xCuO_{4+y}$

In the previous chapter, we saw phase separation on a length scale which had to be larger than $\sim$ 30Å between a low temperature superconducting phase and a ferromagnetic phase. In this chapter we present a muon spin rotation study into the nature of the magnetic and superconducting phases in phase separated $La_{2-x}Sr_xCuO_{4+y}$, $x = 0.04, 0.065, 0.09$ (LSCO+O) [96]. Following Y. Lee et al. [94], B. Wells [199] and A. T. Savici et al. [1], the superoxygenated LSCO+O family have proved a fascinating specimen among the high temperature superconductors (HTC's). First of all, the oxygen doping of the non-superconducting parent compound La_2CuO_{4+y} (LCO+O) results in a superconductor with $T_c \approx 42$K which is the highest in the LSCO family. But LCO+O also shows sharp incommensurate antiferromagnetic magnetic (IC-AFM) Bragg peaks similar to the magnetic stripe order known from $La_{1.88}Ba_{0.12}CuO_4$ (LBCO12) and $La_{1.48}Nd_{0.4}Sr_{0.12}CuO_4$ (LNSCO12), see chapter 2, $La_{1.88}Sr_{0.12}CuO_4$ (LSCO12) in the next chapter. This long ranged magnetic order in LSCO+O appears below $T_N \approx T_c \approx 42$K.

A magnetic volume fraction of $\sim$ 40% in $La_2CuO_{4.11}$ (LCO4.11) was reported by Savici [1]. This was interpreted in a framework of nanoscopic phase separation into patches (or island) of magnetically ordered regions 15-30Å in size, coexsisting on a non-microscopic level with the surounding superconductor. These characteristics are largely preserved upon Strontium (co)doping. As we shall see, a systematic and detail-oriented study of the Sr evolution of both the magnetism- and superconducting phases is still in progress.

In connection with a study of the ordered moment [98] and staging [50] in LSCO+O performed by L. Udby et al., further evidence of the similarity between the superconducting phases of the LSCO+O samples with $x = 0.04, 0.065, 0.09$ was desired. In this chapter, we present a study of the temperature dependence of high transverse field

muon spin rotation spectra. This allows for direct quantitative comparison between the superconducting properties in LSCO+O. Our work builds directly upon the previously published results by H. Mohottala et al. [96]. All experiments were performed by H. Mohottala and C. Niedermayer.

This work has been submitted for publication in [98].

9.1 Magnetism in $La_{2-x}Sr_xCuO_{4+y}$

By the wet electrochemical process of superoxygenation, an excess non-stoichiometric amount of oxygen can be intercalated in the La_2CuO_4 structure. This process have many interesting consequences. All sample were superoxygenated until they showed a single sharp transition of $T_c^{\text{onset}} \approx 40$K in SQUID measurements [96]. All samples studied in this chapter was superoxygenated at the University of Connecticut in the group of B. Wells.

The process by which Sr and O doping atoms relax their position in the La_2CuO_4 unit cell is very different. When oxygen-stoichiometric LSCO is formed by cooling through the liquid-solid phase transition, the resulting material forms an homogeneous 'disordered' distribution of Sr on the La sites. This process takes place at very high temperature i.e. $>$ 1000K and is also refereed to as quenched disorder. However, the excess intercalated oxygen remains mobile down to much lower temperatures [200] where it tends to organize in well-ordered superstructures, with different magnetic properties as a result.

The phase diagram of this co-doping is shown in figure 9.1. In a large portion of this phase space, the compound is in the so-called miscibility gap where the superconducting phase and the magnetic phase are separated. The samples studied here are believed to fall in the region of hole doping between 0.12 and 0.16 base on the optimally doped superconducting properties (like $x = 0.16$) and the '1/8' type magnetic phase (like $x = 0.12$), as is described in chapter 2. The total hole content was determined only for the sample with $x = 0.065$ by the destructive Thermogravimetric analysis (TGA). TGA found that the excess oxygen was $y = 0.032$. Using the simple assumption that Sr doped one hole and O dopes two holes, a total hole doping of $p = x + 2y = 0.1284$ is obtained, and this value puts this sample just within the right region of the phase diagram. However, if this argument is true, the oxygen content of the $x = 0.04$ sample has to be significantly larger than in the $x = 0.065$ sample to fall within the same area of the phase diagram, see figure 9.1. The only way to fully understand what the actual hole doping is in these superoxygenated samples would be to perform TGA on all of them, who are unfortunately all very small and they would be destroyed in the process.

In LSCO, see chapter 2, the strontium doping level is known to affects the superconducting transition temperature, and also induces a profound change of the IC-AFM Bragg peaks, from having ordering vector (in tetragonal notation) $\mathbf{Q}_{\text{IC-AFM}} = \left(\frac{1}{2}\ \frac{1}{2}\right) \pm (\delta\ 0)$ below $x = 0.055$ to $\mathbf{Q}_{\text{IC-AFM}} = \left(\frac{1}{2}\ \frac{1}{2}\right) \pm (\delta\ \delta)$ above $x = 0.055$. In striking contrast with this conventional behavior, Udby [98] reports a quartet of IC-AFM peaks measured by elastic neutron scattering at the same Q positions i.e. same incommen-

surability δ and modulation direction, in all LSCO+O samples studied in this chapter, even though the Sr doping ranges from $x = 0.04$ to $x = 0.09$.

The IC-AFM peaks in LSCO+O, at $\mathbf{Q} = (1/2+\delta, 1/2+\delta, 0)$, are compared in figure 9.1. In these LSCO+O samples, regardless of Sr content, Udby [98] finds that the incommensurability is $\delta = 0.123 \pm 0.004$, corresponding to a spin superlattice structure of 8.1 unit cells parallel to the Cu-O bond similar to the situation in LSCO12, LBCO and LNSCO, see chapter 2. In addition, Udby [98] finds similar $T_{SDW} \approx 39$K for all LSCO+O samples using elastic neutron scattering. The temperature dependence of the IC-AFM Bragg peaks are also shown in figure 9.1. They are seen to follow very similar power laws.

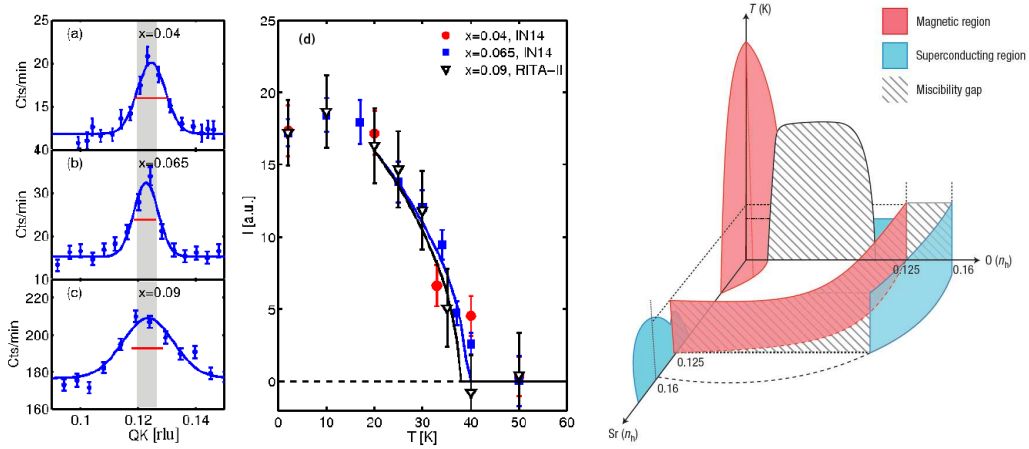

Figure 9.1: ***Left:*** *These three figures show the IC-AFM Bragg peak af* $\mathbf{Q} = (1/2 + \delta, 1/2 + \delta, 0)$ *in the three LSCO+O samples studied in this chapter. They are close to being resolution limited (the red line) and they are at the same position regardless of Sr doping. These figures are from [98]* ***Middle:*** *The temperature dependence of the scaled intensity which is very similar for the three samples. This figure is from [98]* ***Right:*** *The Sr/O-phase diagram. The red regions represent the magnetically ordered states, whereas the blue regions represent superconducting states. The hatched areas represent miscibility gaps. All of the oxygenated samples described in this chapter falls into the arc-shaped miscibility gap between 0.12 and 0.16. This figure is from [96]*

9.2 Previous μ-SR Studies of $La_{2-x}Sr_xCuO_{4+y}$

$La_{2-x}Sr_xCuO_{4+y}$ was originally studied by H. Mohottala et al. [96]. Mohottala presented zero field and so-called weak-transverse field μ-SR studies of the the magnetic and the superconducting volume fractions. The point of a weak transverse field study is to obtain information only about the magnetic properties of high temperature superconductors without the complication of a flux line lattice. The typical magnetic field strength during a weak-transverse field experiment is $H_{ext} \approx 0.01$T. In [96], overall agreement between zero field and weak transverse field results were found.

Mohottala fit the zero field μ-SR spectra to a model with two components, which is identical to the model used for superoxygenated LCO+O by Savici in [1]. The LSCO+O were generally found to phase separate into a magnetic (hole poor) phase with very similar properties to the 1/8 phase in LSCO12, see chapters 2 and 10, and an optimally doped superconducting (hole rich) phase with $T_c \approx 40$K. In contrast to our study of LSCO12, which will be discussed in the next chapter, no dynamical relaxation effect, see chapter 7, is observed by ZF-μ-SR in any of these samples.

For all LSCO+O samples investigated here, Mohottala find that a Bessel type oscillation appears below ~ 40K, and that the frequency of these Bessel functions fit to similar values within the standard error, and all consistent with an ordered electronic moment of $\sim 0.33\mu_B$/Cu. The oscillation proves that local magnetic order is static on the muon time scale, see chapter 7, and the Bessel type oscillation indicates that the order is incommensurate. Owning to these similarities, Mohottala conclude that the magnetic phase in these samples are identical.

Examples of zero field fits are shown in figure 9.2 for the specific samples studied in this chapter. The datasets shown in figure 9.2 were taken in a geometry where $H_{ext}||\mathbf{c}$, see [201, 1] and chapter 10. All these fits were done using the model described by Mohottala in the supplement of [96]. We obtain values for the magnetic volume fractions which are in full consistency with the values quoted in [96]. Also the muon spin rotation frequency, obtained from the fits shown in figure 9.2 are fully consistent with [96]. We have calculated the ordered electronic moments which are summarized in table 9.1.

In figure 9.2, the magnetic volume fraction is seen to vary randomly with Sr content. However, it follows a linear trend with the superconducting volume fraction obtained from DC field cooled magnetization measurements. The sum of the two does not add up to 100%. However, it is speculated that this is due to the superconducting volume fraction being underetsimated in magnetization measurements because of flux pinning [96]. It is thus desirable to obtain the superconducting volume fraction also from the method of μ-SR. In the supplementary of [96], some values are given for the samples with $x = 0.065$ and $x = 0.09$, but not for the sample with $x = 0.04$, also we find that a modification of the model described in [96] must be made to correct for a non-relaxting part of the signal, which we believe to originate mainly from muons stopping outside the sample, see section 9.3.

9.3 Transverse Field Studies of the Magnetic and Superconducting Phases in $La_{2-x}Sr_xCuO_{4+y}$

The high transverse field data was taken at a field of $H_{ext} \approx 0.3$T (weak transverse field typically only falls in the range 0.01-0.05T). Figure 9.3 shows the raw data at 1.6K and 45K. Below $T_c \approx T_N$, in consistency with the reported zero field and weak transverse field studies by Mohottala, we also observe two relaxing components in the high transverse field spectra. One oscillation is rapidly relaxing which corresponding to regions of ordered electronic moments, with properties similar to the stripe ordered

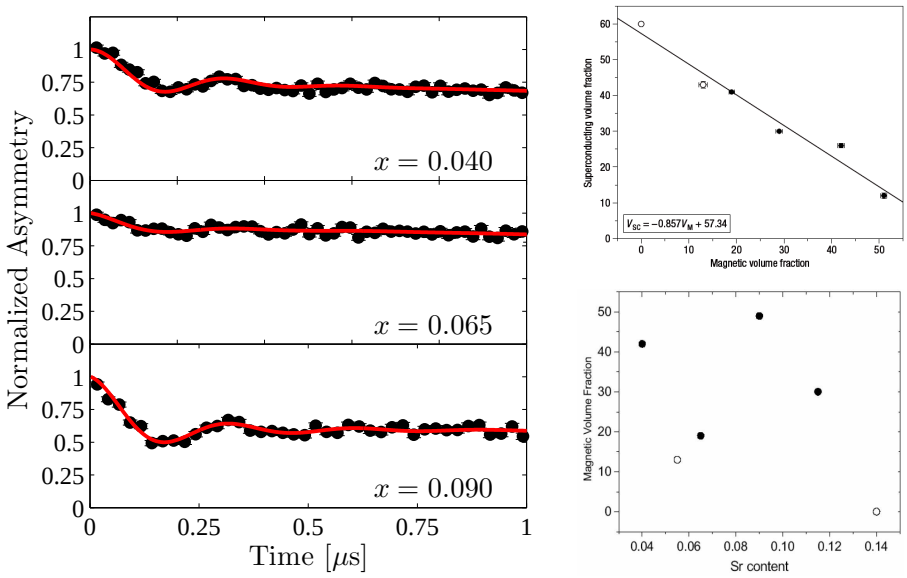

Figure 9.2: *This figure summarizes result from the zero field μ-SR presented in Ref. [96].* ***Left:*** *Zero field μ-SR spectra at base temperature for the three sample studied in this chapter. We observe a Bessel type oscillation with a frequency $\omega \approx 3.5MHz$ which is consistent with Ref. [96].* ***Right:*** *These two figures show the magnetic volume fraction as function of Sr doping, which shows no clear trend and the superconducting volume fraction as function of the magnetic volume fraction, which shows a linear trend. It is argued in [96] how these trends suggests a scenario of a phase separation between magnetic (hole poor) and superconducting (hole rich) regions. These figures are from Ref. [96].*

materials such as LBCO and LNSCO. The second oscillation is slowly relaxing, which corresponds to the superconducting regions, with properties similar to optimally doped LSCO, see chapter 2. However, we also observe a third, almost non-relaxing, component. This component is most pronounced in the sample with $x = 0.04$ where a clear oscillation is seen to persist for times even higher than 4μs. We speculate that this third component is a background originating not from muons stopping in the sample, but from muons stopping the the surrounding sample holder and cryostat wall. Neither the frequency, the small relaxation rate, or the volume fraction of the third component show any noticeable temperatures dependence. Both the muons stopping in the superconducting regions and in the background are well described by cosine oscillations with a simple Gaussian damping.

Figure 9.3 also shows the Fourier power spectrum, which describe the probability distribution of internal fields. Neither the sample with $x = 0.09$ or the sample with $x = 0.065$ are well described by simple Gaussian distributions at 1.6K, they are however perfectly Gaussian above T_c. Instead, for the temperatures below T_c we choose the skewed Gaussian [202] (9.1) which captures the essence of the asymmetric distribution shown in figure 9.3 much better than a normal Gaussian. The skewed Gaussian has two

relaxation rates, σ^- and σ^+ which describe the decay to the left and right respectively of the center position H_0

$$D\left(H_{\rm loc}\right) = \frac{1}{\sqrt{2\pi}\left(\sigma^- + \sigma^+\right)} \times \begin{cases} \exp\left(-\frac{1}{2}\left[\frac{H_{\rm loc}-H_0}{\sigma^+}\right]^2\right) & H_{\rm loc} \geq H_0 \\ \exp\left(-\frac{1}{2}\left[\frac{H_{\rm loc}-H_0}{\sigma^-}\right]^2\right) & H_{\rm loc} < H_0 \end{cases} . \tag{9.1}$$

Using (7.15) the polarization is obtained as the cosine Fourier transform of (9.1). In conclusion, we fit the high transverse field data below $T_c \approx T_N$, using the following model, containing all three components discussed above, and weighted by the asymmetry fractions A_m (magnetic component), A_{nm} (non-magnetic component) and A_{bg} (background) respectively

$$\begin{aligned} P_x\left(t\right) &= A_{\rm m}\left[\frac{1}{1+\eta^{-1}}\exp\left(-\left(\sigma^-_{\rm fast}t\right)^2/2\right)\left\{\cos\left(\omega_{\rm fast}t+\delta\right)+\sin\left(\omega_{\rm fast}t+\delta\right)\mathrm{Erfi}\left(\frac{\sigma^-_{\rm fast}t}{\sqrt{2}}\right)\right\}\right. \\ &\quad \left.+\frac{1}{1+\eta}\exp\left(-\left(\sigma^+_{\rm fast}t\right)^2/2\right)\left\{\cos\left(\omega_{\rm fast}t+\delta\right)-\sin\left(\omega_{\rm fast}t+\delta\right)\mathrm{Erfi}\left(\frac{\sigma^+_{\rm fast}t}{\sqrt{2}}\right)\right\}\right] \\ &\quad +A_{\rm nm}\exp\left(-\left(\sigma_{\rm slow}t\right)^2/2\right)\cos\left(\omega_{\rm slow}t+\delta\right) \\ &\quad +A_{\rm bg}\exp\left(-\left(\sigma_{\rm bg}t\right)^2/2\right)\cos\left(\omega_{\rm bg}t+\delta\right), \end{aligned} \tag{9.2}$$

where the pseudo-skewness $\eta = \sigma^-_{\rm fast}/\sigma^+_{\rm fast}$ and

$$\begin{aligned} \mathrm{Erfi}\left(x\right) &= \frac{2}{\sqrt{\pi}}\int_0^x e^{t^2}\mathrm{d}t \\ &= \frac{2}{\sqrt{\pi}}\sum_{k=0}^{\infty}\frac{x^{2k+1}}{k!\left(2k+1\right)}, \end{aligned}$$

is the imaginary error function. Above $T_c \approx T_N$ we observe only a single slowly relaxing component, that at high temperature becomes indistinguishable from the background.

To compare our model (9.2) with the typical values from the literature, see e.g. ref. [180], the second statistical moment of the skewed Gaussian distribution must be calculated. One can show [202]

$$\sigma_{\rm skewed} = \sigma^+_{\rm fast}\sqrt{\left[\pi\left(1-\eta+\eta^2\right)-2\left(\eta-1\right)^2\right]/\pi} \tag{9.3}$$

which has the same physical meaning as σ of a normal Gaussian.

The temperature dependence of the magnetic volume fraction (off the sample volume only) $V_{\rm m} = A_{\rm m}/\left(A_{\rm m}+A_{\rm nm}\right)$ for the three samples, are shown in figure 9.4. The non-magnetic volume fraction of each sample i.e. $V_{\rm nm} = 100\% - V_{\rm m}$ is also shown. For clarity, the background component has not been included in this plot. In the limit $T \to 0$ we interpretate $V_{\rm nm} = V_{\rm sc}$ as the superconducting volume fraction. For a similar three component intrepretation of μ-SR data see e.g. [203]

Figures 9.4 a-c show the temperature dependences of the volume fractions obtained from high transverse field measurements. We find the magnetic volume fraction to

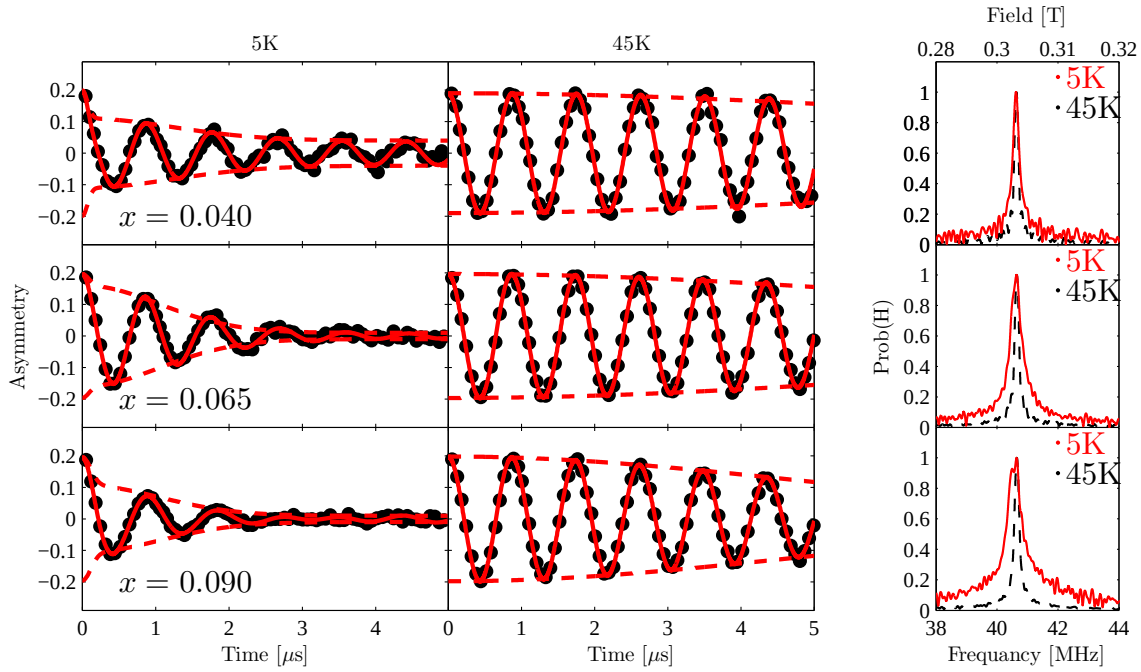

Figure 9.3: ***Left:*** *These figures show the raw data from $H_{ext} = 0.3T$ transverse field μ-SR and fits. At 5K we observe a magnetic component which is rapidly relaxing and a non-magnetic or superconducting component, but we also observe a third component which is most pronounced in the $x = 0.04$ sample. This is presumably a background from muons stopping outside the sample. The $x = 0.04$ sample was significantly smaller than the others. At $45K > T_N \approx T_c$ we observe only one slowly relaxing component.* ***Right:*** *The local field probability distribution on the muon site. The asymmetric field distribution which is particularly pronounced for the samples with $x = 0.09$ and $x = 0.065$ is a signature of magnetic flux lines, see chapter [**?**].*

appear below $\sim$ 40K. In table 9.1 our values for the magnetic volume fraction, the ordered moment in the limit $T \to 0$ and the Néel temperature are summarized for each sample. We find on overall good agreement between our values for the volume fraction and the those reported in [96]. The largest difference is found in the sample with $x = 0.04$, which is also the sample where the background component is most dominant. In this sample, we find $V_{\mathrm{m}} = 56 \pm 4\%$ which is around $14 - 16\%$ larger than what is reported in [96]. In table 9.2 we summerize the superconducting volume fraction, the penetration depth and the superconducting transition temperature of each sample. We find values for the superconducting volume fractions which are quite different from the values qouted in the suplementary of [96].

Figures 9.4 d-f show the relaxation rate of the non-magnetic component. It reaches a value in the limit $T \to 0$ which is in rough agreement with the expectation from the Uemura plot i.e. $\sigma\,(T \to 0) \approx 0.9\mu\mathrm{s}^{-1}$ for superconductors with $T_c \approx 40$K , see chapter 7. The shape of the temperature dependence is quite similar for the three samples studied in this chapter. We fit our data to the expression (7.36) with fitting parameters

$\lambda_{ab}^{x=0.04}(0) = 0.41 \pm 0.014\mu$m, $\lambda_{ab}^{x=0.065}(0) = 0.40 \pm 0.0006\mu$m and $\lambda_{ab}^{x=0.09}(0) = 0.37 \pm 0.0007\mu$m and a non-zero α and β, where $\alpha \approx 0.2\text{K}^{-1}$ and $\beta/\alpha \approx 10^{-2}\text{K}^{-1}$ for all the fits. The values found for the magnetic penetration depth is significantly larger than what have been we observed for LSCO12 in chapter 10 and which is found in e.g. optimally doped LSCO [204]. But our values are consistent with the magnetic penetration depth found in LCO+O by Ansaldo et al. [203]. A ratio between α and β similar to our result was found for $YBa_2Cu_3O_{6.95}$ in [183] although the absolute values themselves were different. The increased disorder from the intercalated oxygen in these samples, are a natural explanation for the appearance of a non-zero T^2 term.

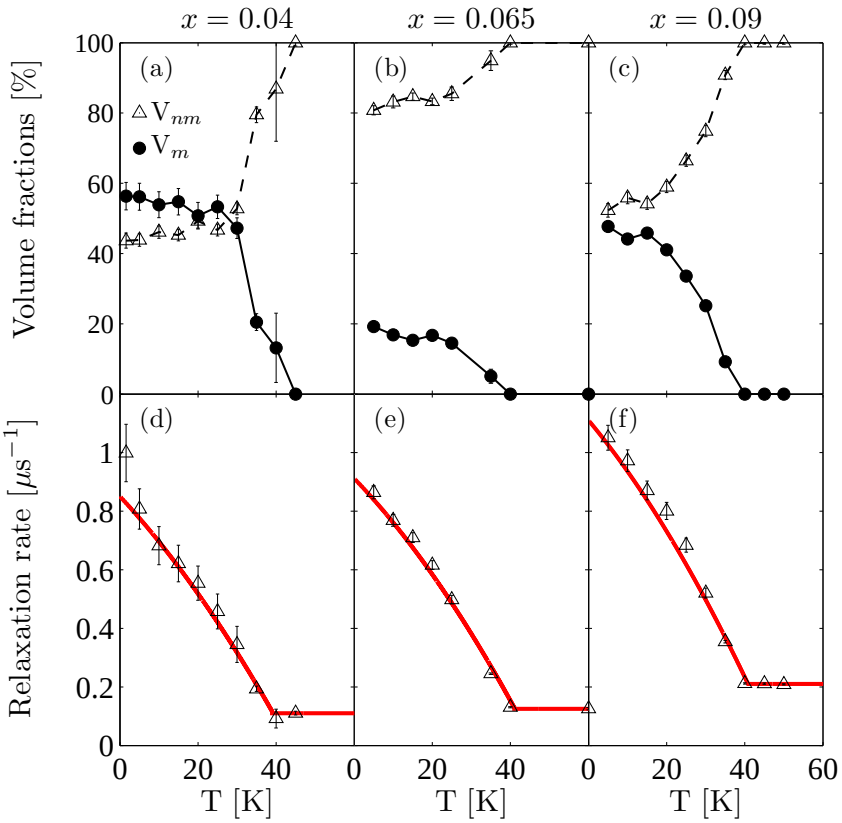

Figure 9.4: ***a-c*** *show the temperature dependence of volume fractions of the magnetic component (V_m) and the non-magnetic component ($V_{nm} = 100 - V_m$) for the three samples. We observe that the magnetic phase appears below $T_N \approx T_c \approx 40K$.* ***d-f*** *show the temperature dependence of the relaxation rate of the non-magnetic component. It reflects the magnetic penetration depth i.e. $\sigma \sim 1/\lambda_{ab}^2$, see chapter 2 and we extract similar values of λ_{ab} for the three samples, which are in excellent agreement with the value quoted for LCO+O by Ansaldo et al. [203].*

Figure 9.5 shows the frequency of the non-magnetic component of (9.2). We observe a decrease below $T_N \approx T_c \approx 40$K for all samples, which confirms that $T_N \approx T_c$ in these samples. The size of the decrease is given by κ and H_{c2}, see chapter 2 on superconductivity. However, accurate values for of either κ or H_{c2} for these sample

x	V_{m}^{HTF} [%]	V_{m}^{WTF} [%] [96]	V_{m}^{ZF} [%] [96]	$\lvert\boldsymbol{\mu}\rvert$ [μ_B/Cu]	T_N [98]
0.04	56 ± 4	40	42	0.32 ± 0.018	40
0.065	19 ± 1	15	19	0.33 ± 0.033	39 ± 1
0.09	47 ± 2	46	51	0.34 ± 0.0066	38 ± 2

Table 9.1: *Collected μ-SR- and elastic neutrons results for the magnetic properties at base temperature. Values for V_m^{HTF} and $\lvert\boldsymbol{\mu}\rvert$ were found in this chapter.*

x	V_{sc}^{HTF} [%]	V_{sc}^{HTF} [%] [96]	V_{sc}^{M} [%] [96]	λ_{ab} [μm]	T_c [98]
0.04	44 ± 1	–	26	0.41 ± 0.014	39 ± 1
0.065	81 ± 1	67	40	0.40 ± 0.006	38.7 ± 0.7
0.09	53 ± 1	48	12	0.37 ± 0.007	37.1 ± 0.5

Table 9.2: *Collected μ-SR- and DC magnetization measurement results for the superconducting properties at base temperature. Values for V_{sc}^{HTF} and λ_{ab} were found in this chapter.*

are not found in the literature and a further quantitative analysis of the temperature dependence of the frequency is not possible at this stage. The 'width' of the transition into the fully developed superconducting state seems broad in the $x = 0.065$ and $x = 0.04$ samples. This is inconsistent with the DC magnetization measurements shown in [96], which are all sharp. Above T_c we observe the frequency of the non-magnetic component of (9.2) goes towards the value given by the external field.

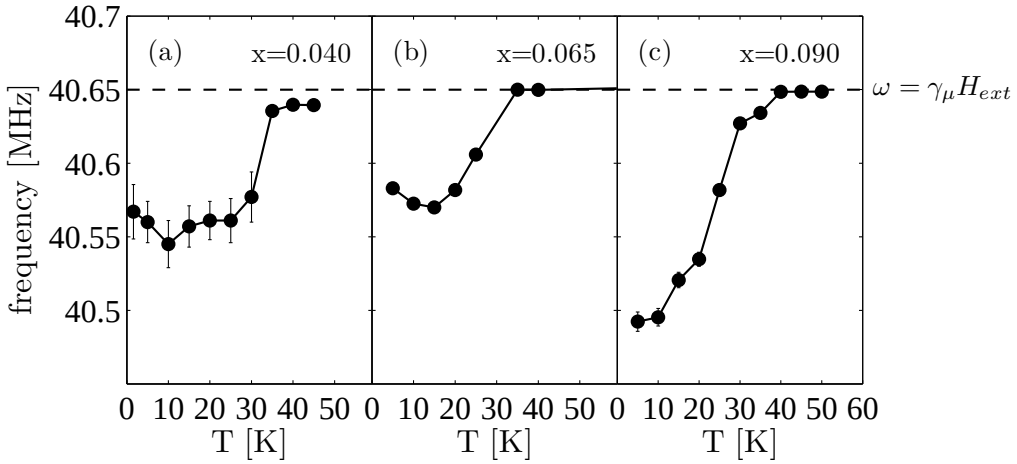

Figure 9.5: *This figure shows the frequency of the non-magnetic component. A decrease is observed at T_c. This is a well known landmark of superconductivity in μ-SR. Above T_c the frequency goes to the value given by the external field.*

Using the magnetic volume fraction from μ-SR, Udby [98] is able to conclude that within the standard error, the ordered electronic moments are the same in these three samples. This is another example of how the local probe of μ-SR and the global (vol-

ume averaging) probe of neutron scattering can supplement each other and provide complementary information. However, the absolute size of the ordered moment measured with μ-SR is about twice the value found from neutron scattering [98]. The origin of this discrepancy is not currently known.

9.4 Discussion

Our results confirms that $T_N \approx T_c \approx 40$K and that the superconducting phase in the three samples are indeed very similar. We determine $T_N \approx 40$ by measuring the magnetic volume fraction in a high (~ 0.3T) transverse field, which goes to zero above T_N. We determine T_c by measuring both the decrease in frequency of the non-magnetic component due to the diamagnetic response of the superconducting state, which develops below T_c, and the relaxation rate σ of the non-magnetic component which goes to zero at T_c. The value of $\sigma\left(T \to 0\right) \approx 0.9\mu\text{s}^{-1}$ found in this study is in general agreement with the Uemura plot, see chapter 2. We also obtain meaningful values of $\lambda_{ab} \approx 0.40\mu$m which are of the same order of magnitude as for LSCO12 and optimally doped LSCO and very close to the value found in LCO+O [203]. The magnetic volume fraction found by zero field and weak transverse field found by Mohottala et al. [96], are consistent with the the values found in this work.

Apart from the $x = 0.065$ sample, the exact hole content p is not known for these samples. In future work it would be very helpful for the interpretation of the analysis to know p.

CHAPTER 10

A Comparative Study Between Neutron Scattering and μ-SR of the Spin Freezing Temperature in $La_{2-x}Sr_xCuO_4$ with $x = 0.12$

In the last two chapter we saw examples on how superconductivity and magnetism phase separates on a length scale visible to muon spin rotation i.e. more than 30Å , first in the low-temperature superconductor Y9Co7, then in the high-temperature superconductor LSCO+O. We now turn to $La_{1.88}Sr_{0.12}CuO_4$ (LSCO12). From [83] (and the information later in this chapter) it is clear that the spins freeze into magnetic stripe order i.e. incommensurate antiferromagnetic order (IC-AFM) see chapter 2, below $T_f = 10 - 15$K when measured with muon spin rotation (μ-SR) and $T_N = 30$K when measured with elastic neutron scattering. This is due to the different time scales of the techniques [83].

LSCO12 shows a field-enhancement of the IC-AFM signal [83], but neither does $La_{1.48}Nd_{0.4}Sr_{0.12}CuO_4$ LNSCO12 [83] or LSCO+O [97] and $La_{1.88}Ba_{0.12}CuO_4$ (LBCO) have only a very small field effect if any [92]. However, the magnetic order which is observed in all these samples have correlation lengths above 100Å and is in that respect proper long ranged. Further, J. Chang et al. [205] have observed evidence of a Fermi surface reconstruction in LSCO12, which could indicate the presence of a static spin density wave, but could also be caused by the LTO structure itself. Finally N. B. Christensen et al. [99] have observed charge order of the same type which is seen in LBCO12 [91] and LNSCO12 [79].

The magnetic excitation in LSCO12 and LBCO12 are very similar, and well described as spin waves [75]. Also, in both systems there is no clear field effect on the spin waves down to about 0.3meV. This would indicate that the elastic magnetic signal observed by neutron scattering in the state between T_f and T_N are in fact low energy ($\hbar\omega < 0.3$meV) excitation which do have a field effect.

The evidence listed above indicates that the magnetism seen in LSCO12 is quite similar to the stripe phase of LBCO and LNSCO, and this encouraged us to investigate

the zero field and transverse field μ-SR on the sample used in [83], especially with respect to the superconducting properties which were not touched upon in [83].

In this chapter we present a comparative study between neutron scattering and μ-SR, of the compound $La_{2-x}Sr_xCuO_4$ $x = 0.12$ (LSCO12).

In the first section we will introduce some result of previous μ-SR experiments on various $La_{2-x}Sr_xCuO_4$ systems from the literature. This helps to set the scene for analysis of our μ-SR measurements, which are presented below. We report a full temperature dependence study of the μ-SR spectra, in both zero field and transverse field. From our data, we are able to extract additional information about T_{SDW}, T_c and the in-plane penetration depth (λ_{ab}) of this particular sample.

In the second section, we discuss a neutron spin-echo study of the IC-AFM Bragg peaks energy width. This study was inspired by the work of D. Haug et al. [206], who used the same technique to study underdoped $YBa_2Cu_3O_{6+x}$. Haug finds a finite energy broadening down to the resolution limit of the spin-echo technique. We were able to measure the energy width at three temperatures, and from our data we also observe a finite broadening above 10K. The fact that μ-SR and neutron scattering gives comparable information in this direct way, strengthens the claim from [83], that the IC-AFM peaks are a result of the spin degrees of freedom freezing out when the time scale of the measurement technique is equal to the time scale typical spin fluctuation in LSCO12. Note that in LSCO+O, this seems not to be the case. In LSCO+O $T_f = T_N = T_c$ [95, 96].

10.1 Introduction to μ-SR studies of $La_{2-x}Sr_xCuO_4$

$La_{2-x}Sr_xCuO_4$ has been investigated several times with μ-SR in the past. Freezing of the electronic moments into a Néel-type antiferromagnetic order was reported by e.g. D. R. Harshman et al. [207] in the underdoped regime. Their data was primary obtained from polycrystalline samples and showed more than an order of magnitude of difference between the Néel temperature for $x = 0$ ($\sim$ 200K) and for $x = 0.02$ ($\sim$ 10K). In [207] all samples for which $x \leq 0.02$ had $\sigma(T \to 0) \approx 5.5$MHz (see chapter 7) but the width of the field distribution, and hence the internal field inhomogeneity, increases with increasing x.

A single crystal sample with $x = 0.06$ was investigated by B. J. Sternlieb et al. [208]. Their $x = 0.06$ sample shows a freezing temperature of $\sim$ 6K from ZF-μ-SR, but using quasi-elastic neutron scattering Sternlieb found the IC-AFM correlations to appear already below $\sim$ 20K. These trends where shown to be shared between $La_{2-x}Sr_xCuO_4$ and $Y_{1-x}Ca_xBa_2Cu_3O_6$ by C. Niedermayer et al. [54] who studied a broad range of doping values $0 < x < 0.12$. At $x = 0.09$ the internal field is seen to be completely suppressed only to reappear at $x = 0.12$ [54, 209]. See also the review in [55].

We now turn to studies focused on LSCO at $x = 0.12$ where T_c is slightly suppressed. K. Kumagai et al. [209] reported ZF-μ-SR of an $x = 0.12$ sample showing IC-AFM order below $\sim$ 15K. The oscillation frequency (See chapter 7) observed by Kumagai et al. correspond to an ordered moment of $0.3\mu_B$/Cu. Later, A. T. Savici et al. [1]

published both zero field and transverse field μ-SR on a LSCO12 sample. Figure 10.1 shows the ZF-μ-SR obtained by Savici in [1]. Savici finds an ordered electronic moment which is consistent with Kumagai. However, only a small magnetic volume fraction, which is only $\sim 20\%$.

The LSCO12 sample used in our experiments, which are presented below, was studied previously by J Chang et al. [83]. Chang studied field-induced magnetism and the so-called mixed SDW+SC phase [210] in LSCO12, primary with neutron scattering. In contrast to Savici, Chang finds a very large magnetic volume fraction approaching 100%. The difference between the volume fraction found be Savici and Chang indicates that there might be sample dependency in these quantities.

The muon site has been determined for LSCO. The positive muon comes to rest a the interstitial position $(0.199d\ 0\ 0.171c)$ in the real space unit cell ($d = 3.779$Å and $c = 13.2$Å) [1] (see also Ref. [211, 212, 1]). Knowledge of the muon site is crucial for calculating the ordered moment from the zero field muon spin rotation frequency $\omega\,(T \to 0)$. Now, assuming the all dominating contribution to the dipole-dipole interaction to originate from the ordered electronic moment at (000), the ordered moment in μ_B/Co^{2+} can be calculated (using (7.10)) as $0.099386 \times \omega\,(T \to 0)$ [MHz].

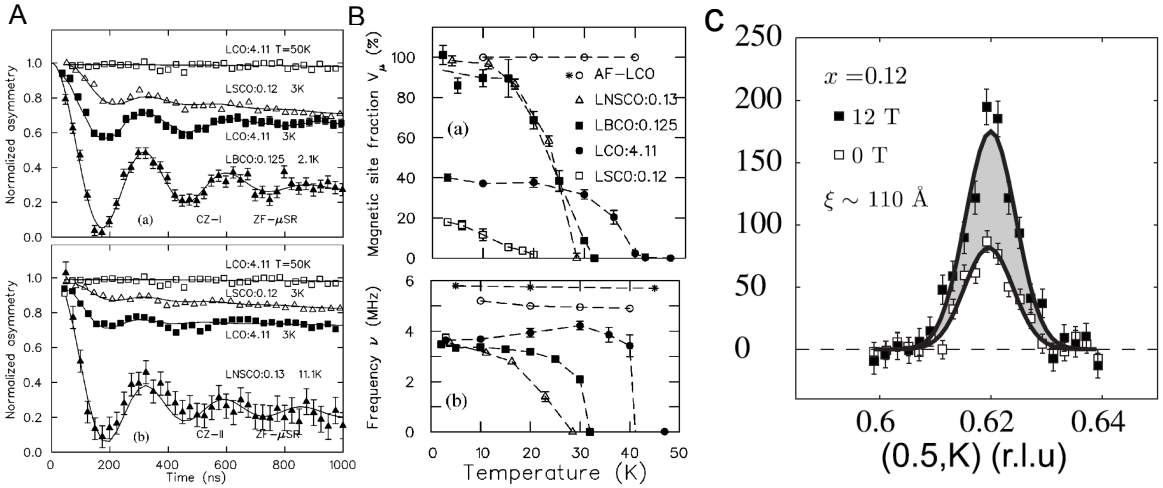

Figure 10.1: *These figures are adopted from Savici et al. [1].* ***A*** *shows the zero field μ-SR data with $\mathbf{S}_\mu(0)\,||\mathbf{c}$ called CZ-I (a) and $\mathbf{S}_\mu(0)\perp\mathbf{c}$ called CZ-II (b) respectively. Savici shows data from LCO, LCO+O, LNSCO, LBCO and LSCO12. The LSCO12 sample investigated by Savici show directly the small magnetic volume fraction i.e. it oscillates around a asymmetry value slightly lower than 1.* ***B*** *These figures show the Magnetic volume fraction (panel (a)) and oscillation frequency (panel (b)) extracted from the data analysis in [1]. (a) shows the dependence of the magnetic volume fractions and (b) shows the the temperature dependence of the frequencies.* ***C*** *The IC-AFM Bragg peak of the LSCO12 sample studied in this chapter. Adapted from [83]*

10.2 μ-SR results

In the following section we present our μ-SR findings. The experiments were performed using the GPS instrument, see section 7.6 and the LSCO12 single crystal sample is oriented such that $\mu_0\mathbf{H}_{ext}||\mathbf{c}$.

10.2.1 Temperature dependence of ZF-μ-SR spectra

Figure 10.2 shows our raw zero field μ-SR data at different temperatures of interest. Below $T \sim 8.6$K we observe an oscillation which correspond to magnetic order which is static on the muon time scale (See chapter 7). This oscillation is well described by a Bessel function (See chapter 9). Above 8.6K we still observe a rapid relaxation due to magnetism, however, the oscillation can no longer be seen. This is well described by a dynamical relaxation due to fluctuations in the local field at the muon site. Above 13K this component also goes to zero. Finally, above 15K we only see one slowly relaxing component. We model this component with a Gaussian, but we could just as well have chosen a Kubo-Toyabe function, see chapter 7. Including the components discussed here, we analyze our zero field μ-SR data using the model

$$P_z(t) = \begin{cases} A_{\mathrm{m}}\left[F_1 j_0(\omega t)\exp(-\lambda_{\mathrm{stat}}t) + F_2\exp(-\lambda_{\mathrm{dyn}}t)\right] & \\ +A_{\mathrm{nm}}\exp\left(-\frac{1}{2}\sigma^2t^2\right) & \text{for } T \le T_c \\ A_{\mathrm{nm}}\exp\left(-\frac{1}{2}\sigma^2t^2\right) & \text{for } T > T_c \end{cases} \tag{10.1}$$

where $F_1 + F_2 = 1$ and $A_{\mathrm{m}} + A_{\mathrm{nm}} = A_{\mathrm{total}}$. A_{total} and the efficiency parameter α were obtained from a high temperature transverse field spectrum, which is fitted to a single relaxing cosine. This parameters are subsequently fixed in the data fitting process. We find that $F_1 \approx 0.5$ for our data. This model gives very precise fits, see figure 10.2. Savici et al. [1] use a very similar model, however, Savici finds no evidence of the dynamical relaxation that we find.

The first component of (10.1), A_{m}, represent muons stopping at a site with non-zero local magnetic field. This component includes two terms: $j_0(\omega t)$ is the zeroth order Bessel function and represents the asymmetry fraction $A_{\mathrm{m}}F_1$ which oscillates due to ordered electronic moments. The Bessel function implies a spin density wave type order [213, 176]. The Lorentzian damping of the oscillation (λ_{stat}) is due to the finite width of the local field distribution ($1/T_2$), the second Lorentzian damping of the non-oscillating part (λ_{dyn}) is dynamic ($1/T_1$), see chapter 7.

The second component in (10.1), A_{nm}, represents the regions without a local field, and the slow damping of this term stems from the disordered nuclear dipolar fields.

In single crystal samples, it may happen that the spin direction of the majority of the implanted muons are parallel to the local field direction. This would wrongly imitate a large non-magnetic fraction of the sample. In this case, if the [001] direction in sample is then rotated 90° the situation would be completely opposite, showing instead, a large magnetic fraction of the sample. We must investigate both configurations to find the true magnetic volume fraction. Following [1] we denote the situation $\mathbf{S}_\mu(0)||\mathbf{c}$ for CZ-I and $\mathbf{S}_\mu(0)\perp\mathbf{c}$ for CZ-II. Due to the partial spin rotation in the transverse

geometry of the GPS instrument, we acquire both spectra simultaneously. As discussed in previous work [1, 95, 201], the true magnetic volume fraction is calculated by $V_{\mathrm{M}} = (V_{CZ-I}/2 + V_{CZ-II})$ where $V_{CZ-I,CZ-II} = A_{\mathrm{m}}/(A_{\mathrm{m}} + A_{\mathrm{nm}})$ for the two configurations CZ-I and CZ-II respectively.

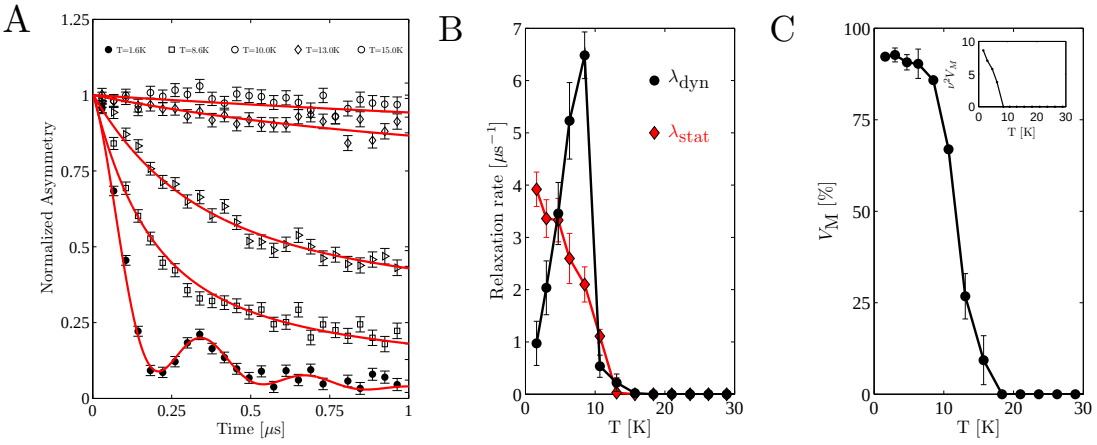

Figure 10.2: *(**A**) Zero field μ-SR spectra obtained on LSCO12 at a series of temperatures. They are normalized as $P(t)/P(0)$ (**B**) Temperature dependences of λ_{stat} and on λ_{dyn}. We observe a peak in the dynamical relaxation rate around 10K, indicating that the SDW becomes static on the muon time scale at this temperature. The static relaxation rate simply goes gradually to zero. (**C**) Temperature dependence of magnetic volume fraction. We observe a large magnetic volume fraction which is close to 100% at 1.6K.*

Figure 10.2 shows examples of raw zero field μ-SR spectra taken at a selection chosen to illustrate the temperature evolution. At 1.6K the Bessel function is clearly seen in the data. At 8.6K the oscillation is no longer visible, but the rapid relaxation still remains. In contrast to the results of both Savici et al. [1] and Kumagai et al. [209], we observe a very large magnetic volume fraction, which is close to 100% at 1.6K. At 9-10K the asymmetry begins to fall of to zero. The frequancy of the oscillation also drops rapidly to zero at 10K. Above 15K we observe no evidence of the magnetic component and we restict the model to only include the nuclear dipolar fields.

We point out that even though our zero field μ-SR results point to a near 100% magnetic volume fraction, the typical extent of the dipole-dipole interaction that muons are sensitive to, implies that inhomogeneity at a scale smaller than ~ 30Åmay still exist. Such a ground state, characterized as a nano-scale inhomogeneous state consisting of patches of superconducting and antiferromagnetic regions are discussed in Ref. [83].

We observe a muon spin rotation frequency equal to 3.1MHz at 1.6K. In terms of ordered moment, 3.1MHz gives $\sim 0.31\mu_B$/Co. This value is a little smaller than the 3.6MHz, which is the standard SDW frequency seen in LNSCO [83] which was also observed in LSCO12 by Savici. Our value seems, however, to be consistent with Kumagai in [209].

Figure 10.2 also shows that we observe a maximum in the dynamical relaxation

rate λ_{dyn} slightly below 10K, indicating that freezing temperature truly is 9-10K in this sample. This is close to the value found by Kumagai but significantly lower than the 15K quoted in Chang [83]. Concomitant, to the maximum in λ_{dyn}, λ_{stat} falls of to zero.

10.2.2 Temperature dependence of TF-μ-SR spectra

We applied 0.5T (a so-called high transverse field) to the sample above T_c and subsequently field cool the sample. This brings the sample into the mixed state, where we expect to have flux lines developed even though they might not be ordered into a lattice. Chang et al. [214] used small angle neutron scattering to look for a flux line lattice in this sample and was unable to detect one above 0.1T. At such fields, we expect the inter-vortex distance at this field to be suitable for observation of the Flux line properties [215]. In consistency with our analysis of the zero field measurements, we fit our transverse field data to the following two-component model

$$P_x(t) = \begin{cases} A_{\mathrm{m}} \exp\left(-\frac{1}{2}\sigma_{\mathrm{fast}}^2 t^2\right) \cos\left(\omega_{\mathrm{fast}} t + \delta\right) & \\ +A_{\mathrm{nm}} \exp\left(-\frac{1}{2}\sigma_{\mathrm{slow}}^2 t^2\right) \cos\left(\omega_{\mathrm{slow}} t + \delta\right) & \text{for} \quad T \leq T_c \\ A_{\mathrm{nm}} \exp\left(-\frac{1}{2}\sigma_{\mathrm{slow}}^2 t^2\right) \cos\left(\omega_{\mathrm{slow}} t + \delta\right) & \text{for} \quad T > T_c \end{cases} \tag{10.2}$$

The rapid relaxing oscillation represents muons stopping in magnetic regions of the sample. The magnetic volume fraction is given by $V_{\mathrm{m}} = A_{\mathrm{m}} / (A_{\mathrm{m}} + A_{\mathrm{mn}})$. Based on the zero field frequency the internal field should be around $\mu_0 H_{\mathrm{int}} = 0.023\mathrm{T}$, which is quite small compared to the external field. We fix the frequency of the fast oscillation to the value simply given by the external field $\omega_{\mathrm{fast}} = \gamma_\mu \mu_0 H_{\mathrm{ext}} = 67.5\mathrm{MHz}$. This data was taken with $\mu_0 \mathbf{H}_{\mathrm{ext}} || \mathbf{c}$, this means that the flux lines extent in the $(\mathbf{a}, \mathbf{b})$-plane, see figure 2.6, thus $1/T_2$ relaxation σ_{slow} depends on the in-plane magnetic penetration depth λ_{ab}. The phase is shared between both components. The remaining asymmetry represents the non-magnetic regions in the sample, and is described by a slowly relaxing oscillation. In the limit of $T \to 0$ we identify the fraction $A_{\mathrm{nm}}(T \to 0) / (A_{\mathrm{m}} + A_{\mathrm{mn}})$ as the superconducting volume fraction (V_{sc}).

Above the spin freezing temperature out data is well describe by single slowly relaxing oscillation.

Figure 10.3 shows some raw transverse field spectra at various temperatures. For clarity all spectra are shown in rotating reference frame with the frequency 67MHz, see chapter 7. At 1.6K the two components are directly visible from the data. At 8.6K and 10.6K they have become less pronounced. Above 10.6K we observe only one component. In consistency with our zero field data, the fit of our transverse field show a large magnetic volume fraction, which approximates 100%. The decrease of the rapid relaxation also follows a similar trent as our zero field λ_{stat}, see figure 10.4 A and B. Also shown in figure 10.3 the Fourier power spectrum (see chapter 7) for the 1.6K and 36.6K datasets are shown. The small shift due to the flux lines is just visible.

The slow relaxation rate $\sigma_{\mathrm{slow}}(T \to 0) = 1.2 \pm 0.1 \mu\mathrm{s}^{-1}$ follows a similar trend, as the zero field relaxation rate λ_{stat}. This is shown in figure 10.4 B. The value of $\sigma_{ab}(T \to 0)$ is in rough agreement with the expectation from the Uemura plot, see

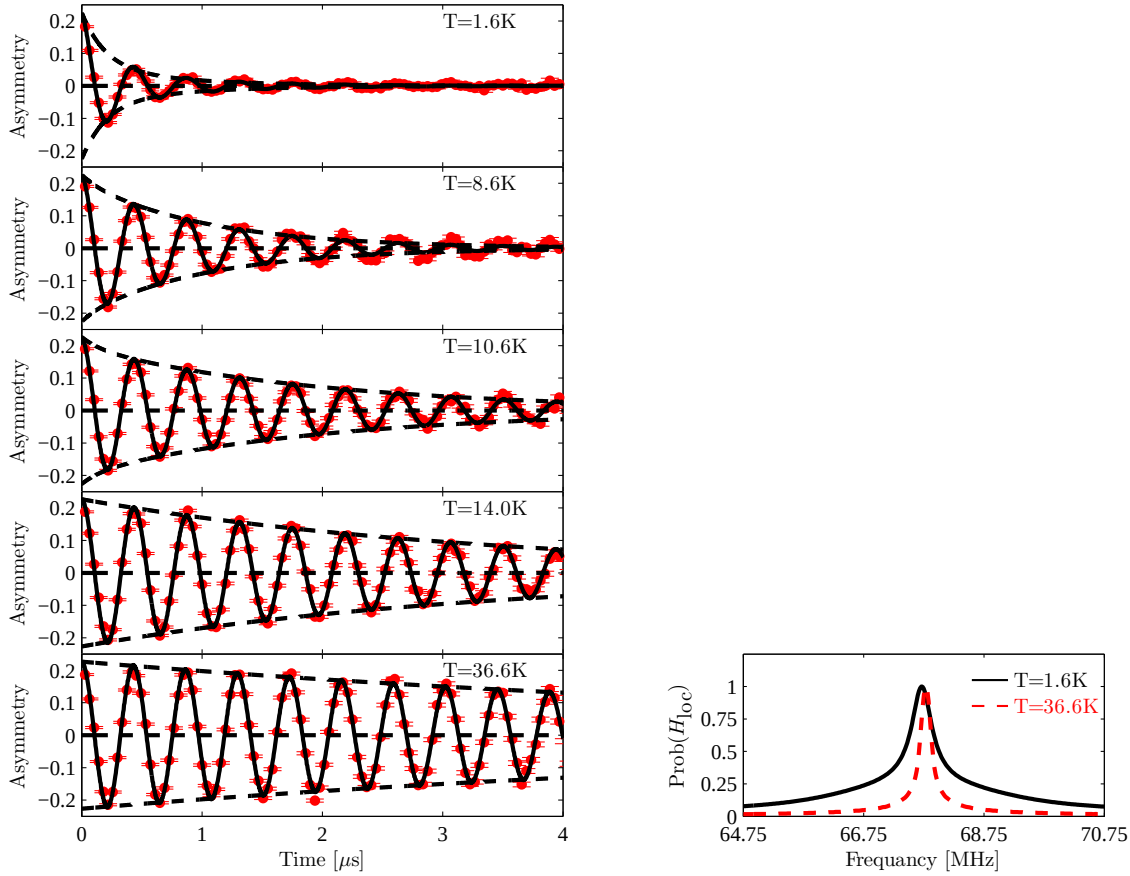

Figure 10.3: *Raw transverse field μ-SR data at various temperatures. At 1.6K we find two components in the data, one with a rapid relaxation and another with a slower relaxation. Above 10K only one component. In the bottom right the Fourier power spectrum for 1.6K and 36.6K respectively are shown. At 36.6K we observe only the well defined peak due to the external field, whereas at 1.6K we observe both the external field (slightly shifted down in frequency and broadened by the flux line field distribution) and the very broad 'peak' which corresponding to the magnetic part of the sample. The dashed line indicated the time evolution of the decay.*

chapter 7. however, if we consider the 'effective penetration depth' which smears out the difference between the penetration depth measured in an oriented single crystal and in a powder, following [1, 216], we find $\sigma\left(T\rightarrow 0\right)=\sigma_{ab}\left(T\rightarrow 0\right)/1.4=0.93\pm 0.07\mu\mathrm{s}^{-1}$, which is in excellent agreement with the Uemura plot. The slow relaxation rate decreases until the superconducting transition temperature, above which, it remains flat around $\sigma\left(T>T_c\right)\approx 0.25\mu\mathrm{s}^{-1}$. Similar values was observed in other LSCO systems [1]. The linear dependence on temperature could be an indication of a d-wave symmetric quasi particle energy gap in the superconducting state, see chapter 2, however the disorder these systems make it difficult to say anything with certainty, see e.g. the discussion in [183]. We fit the data below T_c to the expression, see chapter 7, $\lambda_{ab}^{-2}\left(T\right)=\lambda_{ab}^{-2}\left(0\right)\left[1+AT+BT^2\right]$ with fitting parameters $\lambda_{ab}\left(0\right)=0.274\pm 0.002\mu\mathrm{m}$,

$A = 0.112 \pm 0.005\mathrm{K}^{-1}$ and B fitted to zero within its errorbar. $\lambda_{ab}(0)$ value is in excellent agreement the values $\lambda_{ab} = 0.25 - 0.30\mu$m found from e.g. AC-susceptibility [217, 218].

The frequency of the slowly relaxing oscillation is shown in figure 10.4 C. It shows a decrease below the superconducting transition temperature due to the diamagnetic shielding currents around the flux lines, in full agreement with the theory explained in chapter 7. Both the decrease of the slow relaxation rate and the decrease of the frequency indicates that $T_c \approx 27$K, which is in agreement with Chang [83], but slightly below the value of 30K reported in [1]. Notice that nothing in these data show any influence of the spins freezing.

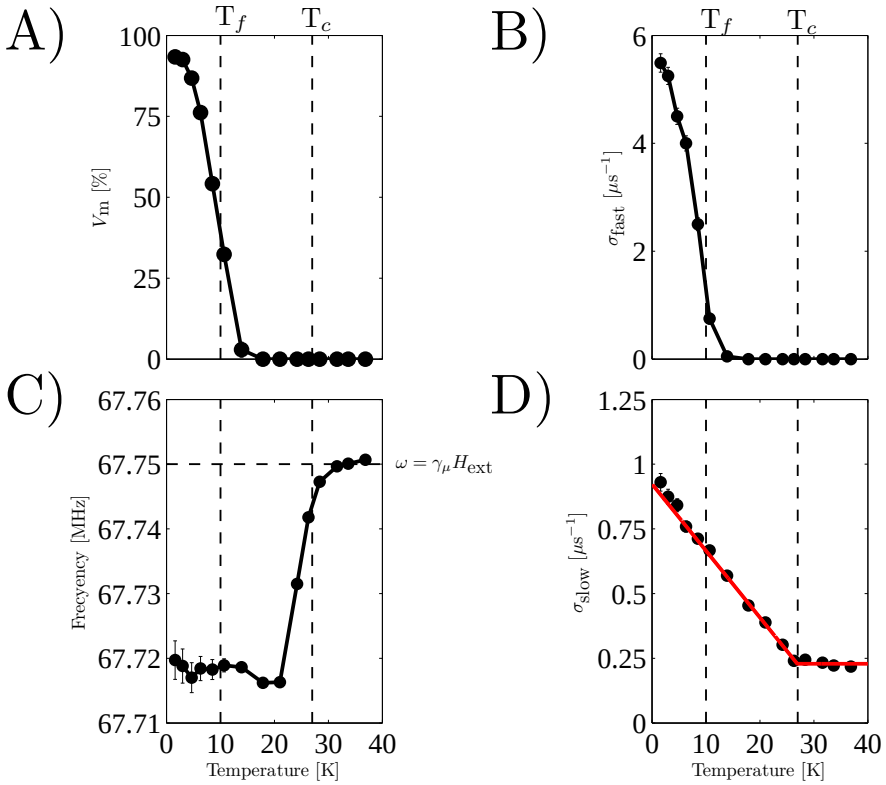

Figure 10.4: *(**A**) Magnetic volume fraction. (**B**) Fast relaxation rate, representing the magnetic regions of the sample. (**C**) The decrease in frequency below T_c and (**D**) Slow relaxation rate. We from out fit (red line) we obtain the penetration depth $\lambda_{ab}(0) = 0.274 \pm 0.002\mu m$. The vertical dashed lines represent the two important transition temperatures T_c and $T_f = T_{SDW}$ and the horizontal dashed line in (**C**) represents the frequency of the external field.*

10.3 Neutron Spin Echo results

In the previous section, we presented μ-SR experiments that, among other results, verified that $T_{SDW} = 10$K in LSCO12. This value is indeed lower than the equivalent phenomenon measured by neutron scattering using a triple axis spectrometer which finds $T_{SDW} = 27$K [83]. The proposed reason for this discrepancy, between neutron and μ-SR is that the time scale, where the electronic spin fluctuations become static, is not the same for the different techniques.

D. Haug et al. [206] reported how neutron spin-echo (NSE), with an energy resolution of $\sim 1\mu$eV, is a way to bridge the energy (time) scale of μ-SR, which have an energy scale similar to neutron spin-echo, and conventional neutron scattering, with a typical energy scale of 0.1meV. Haug demonstrated that the energy linewidth of the magnetic Bragg peaks in YBCO decrease with decreasing temperature, all the way to the energy resolution of the NSE technique.

We have performed a similar experiment on the same LSCO12 sample which was used for our muon studies presented in the previous section and hence in [83]. It is a large sample of mass ~ 10g. We used the resonant spin-echo triple-axis spectrometer (TRISP) located on the FRM II thermal source. The polarized neutron for TRIPS are delivered by a polarizing supermirror with a velocity selector to avoid higher order contamination. Pyrolytic-graphite (002) crystals were used to monochromate and analyze the neutron beam. We used $k_i = k_f = 2.51\text{Å}^{-1}$. We measured on the IC-AFM Bragg peak $Q = (0.88\,0.12\,0)$ (orthorhombic notation). The depolarization of the neutron beam is measured with a Heusler (111) analyzer.

As explained in section chapter 4, the effective magnetic field $\mu_0 H$ between the coils is converted into a 'spin-echo time' by the relation $\tau_{\text{NSE}} = 1.864 \times 10^{-12} \times \mu_0 H\,[\text{T}] \times L\,[\text{cm}] \times \lambda^3\,[\text{Å}]$ where $\lambda = 2\pi/k_i = 2.5$Åand L (the distance between the coils) are given by the instrumental setup. To measure the polarization for a specific spin-echo time, the effective field integral $\omega_2(L/v_2)$ of the second spectrometer arm is varied by translating the last rf coil a small distance ΔL. The transmission (I/I_0) through the Heusler analyzer is given by $T = (1 + P\cos(\phi))/2$ where P is the polarization of the neutron beam [120]. The perturbation of the last rf coil causes the intensity to oscillate according to the equation [219]

$$I(\delta L) = I_0 \left[1 + P(\tau_{\text{NSE}}) \cos\left(2\pi \frac{\Delta L - \Delta L_0}{\Delta L_{\text{p}}}\right)\right], \tag{10.3}$$

where I_0 is the average intensity, $\Delta L_p = 2\pi v_2/\omega_2$ is the oscillation period, and ΔL_0 is an offset. Every scan of ΔL runs through one such period and the typical size of ΔL is millimeters. While performing such a scan the (triple axis) spectrometer as a whole remains static on the position of the IC-AFM Bragg peak.

We fit our data to equation (10.3) to obtain the polarization as a function of spin-echo time. As explained in chapter 4, the polarization is expected to decay exponentially due to the Lorentzian broadening of a quasi elastic peak. We have determined the polarization for $\tau_{\text{NSE}} \in \{4.09\text{ps}, 32.25\text{ps}, 60.41\text{ps}\}$ in 3.5K, 10K and 15K respectively. These temperature values are chosen from the two following criteria; 1) all being be-

low the SDW-temperature found by cold neutron triple axis scattering and 2) being distributed around the SDW-temperature found by μ-SR. This will allow for a directly comparison of the two techniques. Unfortunately our best possible signal-to-noise ratio, $R = (I_{max} - I_{bg})/I_{bg}$ in our NSE experiment was only ~ 0.15 on the IC-AFM Bragg peak at $Q = (0.88\, 0.12\, 0)$, which is significantly less than what was found using the same sample in [83]. The consequence of this low signal-to-noise was that we had to count much longer than expected and it was only possible to obtain three temperature points. Figure 10.5 shows our ΔL scans, three values of spin-echo time and three temperatures. The reason for the low signal-to-noise ratio in this experiment relative to the findings in [83] is currently not understood. We known from our μ-SR analysis that the volume fraction in this sample is unaltered.

Figure 10.6 shows the extracted polarization as function of the spin-echo time. By fitting these points to (4.33) we obtain the exponential decay rate $\Gamma_{\rm NSE}$. The values are shown in table 10.1. Next we compare our NSE decay rates to the dynamic relaxation rate extracted from zero field μ-SR, where we have measured the dynamical relaxation rate $\lambda_{\rm dyn}$. In the limit of very rapid fluctuations, $\omega\tau_c << 1$, the expression (7.42) becomes independent of the applied field and directly proportional to τ_c

$$\begin{aligned} \lambda_{\rm dyn} &= \gamma_\mu^2 H_\perp^2 \tau_c \\ &= \omega_{\rm loc}^2 \tau_c, \end{aligned} \tag{10.4}$$

where the size of $\omega_{\rm loc}$ should be estimated from the local field in the limit $T \to 0$. The decay rate expected from μ-SR is readily obtained as $\Gamma_{\mu-{\rm SR}} = \hbar/\tau_c$. The values we obtain are shown in table 10.1. We find that at 3.5K the energy width extracted from zero field μ-SR is below the energy resolution of Neutron spin echo. Which is consistent with the small (negative) value we obtain, which is zero within its errorbar. At 10.5K the we are just on the resolution limit of spin echo, but at 15.0K the data shows an exponential decrease of the normalized neutron spin-echo polarization, which implies that the magnetic order is not static on the neutron spin echo timescale at this temperature. This is consistent with energy width we find from μ-SR.

T [K]	$\Gamma_{\rm NSE}$ [μeV]	$\Gamma_{\mu-{\rm SR}}$ [μeV]
3.5	-1.40 ± 2.71	0.42 ± 0.04
10.5	2.85 ± 3.23	0.88 ± 0.08
15.0	12.45 ± 3.81	12.14 ± 5.56

Table 10.1: *Quasi elastic linewidth of the IC-AFM Bragg peak at* $Q = (0.88\, 0.12\, 0)$ *in LSCO12, compared with values obtained from zero field muon spin rotation.*

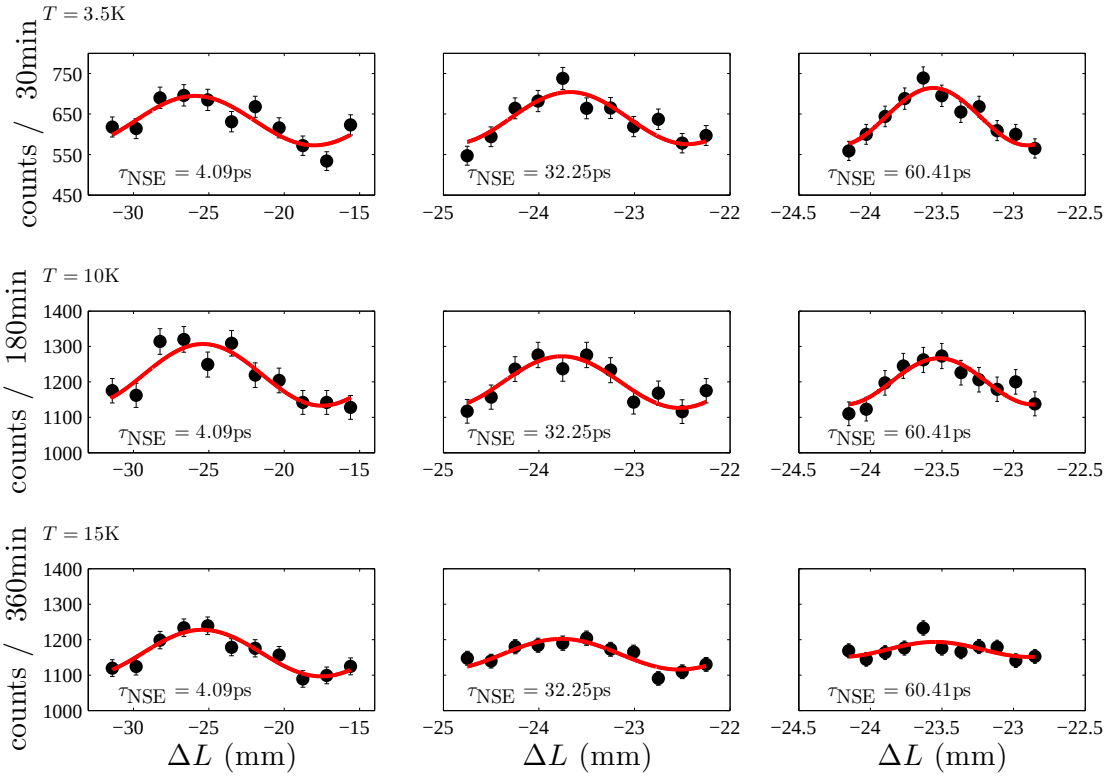

Figure 10.5: *These figures show the raw data from TRISP. The oscillation period is fixed and shared by all data sets. At 3.5K we observe that the oscillation amplitude is essentially unaltered as a function of spin echo time τ_{NSE}. This is in contrast with the 15K data where the amplitude clearly is suppressed at $\tau_{NSE} = 60.41$ relative to $\tau_{NSE} = 4.09$. A decreasing polarization is due to magnetism which is fluctuating on the spin echo time scale.*

10.4 Discussion and conclusion

In this chapter we reported a consistent analysis of new zero field and transverse field μ-SR experiments on the LSCO12 sample used by others for numerous investigations, e.g. [83, 205, 214, 75]. In full consistency with [83] we find a magnetic volume fraction approaching 100%, thus if this sample is phase separated, it is not detecable by muon spin resonance. This makes this sample different from the LSCO12 sample reported on by Savici et al. [1].

Also, Savici finds that the zero field μ-SR frequency is finite, and in some of the sample almost constant, until T_{SDW} where it the drops rapidly to zero, see e.g. figure 10.1. However, We observe a temperature regime of 10-15K with no zero field μ-SR frequency but still a rapid relaxation which we interpret as a dynamical relaxation originating from fluctuation magnetic order, and the Bragg peaks observed in this range are not static.

We performed a neutron spin echo study of the energy width of the an IC-AFM

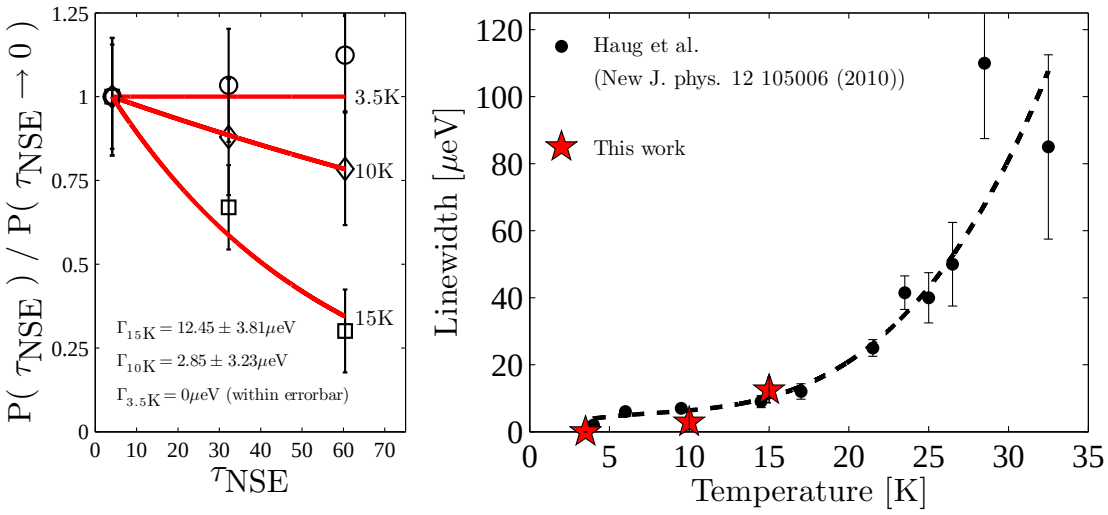

Figure 10.6: *Normalized neutron spin-echo polarization as function of spin-echo time. We observe at 3.5K, that the the quasi elastic energy width is 0 within its errorbar. The 15K data shows an exponential decrease of the normalized neutron spin-echo polarization, which implies that the magnetic order is not static on the neutron spin echo (and hence the μ-SR) timescale at this temperature.*

Bragg peak, and find that a finite broadening down to about 10K. Which supports our picture of fluctuating magnetic order which freezes on the time scale of μ-SR and neutron spin echo at 10K.

No anomalies connected to the spins freezing into this stripe order was detected on the superconducting properties. The transverse field frequency of muons stopping in the superconducting region of the sample is essentially unaltered, and so is the relaxation rate corresponding to the field distribution of magnetic flux lines. Instead, we are able to extract the penetration depth of the super conduction phase. We obtain $\lambda_{ab} = 0.274 \pm 0.002 \mu$m, which is consistent with the value expected for LSCO12 [217, 218].

CHAPTER 11

Conclusions

In this chapter I try to gather the results obtained in this thesis work. I present them in the order they appeared in the thesis.

11.0.1 $CoCl_2 \cdot 2D_2O$ and related $CoCl_2$ salts

We have successfully verified that the magnetic excitation in $CoCl_2 \cdot 2D_2O$ indeed goes soft with increasing field field. At H_c we observe no excitation above the elastic resolution of the spectrometer. However, we observe spin excitation emerging again above H_c, in the so-called quantum paramagnetic phase. Our data agrees well with the qualitative behavior of RPA theory, where the magnetic excitations are transverse spin waves, which are not present in the pure Ising model, and the domain wall excitation spectrum which, as described by [125], is characteristic of a one dimensional Ising system with weak interchain interactions, see figure 2.2, are not seen in $CoCl_2 \cdot 2D_2O$ in our experiments.

We have performed a density functional theory calculations of the ground state chemical structure of $CoCl_2 \cdot 2NH_3$ and used a simplified model of the dependence of the super exchange on the chemical bond length to estimate that the critical field of $CoCl_2 \cdot 2NH_3$ is $sim2$T lower that in $CoCl_2 \cdot 2D_2O$. However an experimental verification of the result have not been done at this point.

11.0.2 Y_9Co_7

With the best possible Y_9Co_7 sample available, we could confirm the previous report of phase separation, into itinerant ferromagnetism and low-temperature superconductivity, in this system from the work by Ansaldo et al. [188]. We also observed an anomaly in the zero field μ-SR frequency, which was not seen before, and we interpret this as further evidence of phase separation (See figure 8.4 and 8.6)

No effect is seen on the magnetic volume fraction upon cooling through T_c was observed, which further indicates that the nature of the co-existence is not microscopic.

11.0.3 $La_xSr_xCuO_{4+y}$

In consistency with previous zero field muon spin rotation and neutron scattering work on the three samples from the family $La_xSr_xCuO_{4+y}$, with $x = 0.04$, $x = 0.065$ and $x = 0.09$ [96, 97], we observed phase separation on a length scale which makes is directly visible to muon spin rotation. Our results from an analysis of transverse field muon spin rotation data confirms that $T_N \approx T_c \approx 40$K and that the superconducting phase in the three samples are indeed very similar.

We determine $T_N \approx 40$ by measuring the magnetic volume fraction in a high (~ 0.3T) transverse field, which goes to zero above T_N and we determine T_c by measuring both the decrease in frequency of the non-magnetic component due to the diamagnetic response of the superconducting state, which develops below T_c. The value of $\sigma\left(T \to 0\right) \approx 0.9\mu s^{-1}$ found in this study is in general agreement with the Uemura plot, see chapter 2. We also obtain values of the magnetic penetration depth $\lambda_{ab} \approx 0.40\mu$m which are of the same order of magnitude as for LSCO12 and optimally doped LSCO and very close to the value found in LCO+O , see e.g. [203]. The magnetic volume fraction found by zero field and weak transverse field found by Mohottala et al. [96], are consistent with the the values found in this work.

These samples show sharp incommensurate Bragg peaks, which indicates long ranged magnetic order that is similar to the stripe order in e.g. $La_{1.48}Nd_{0.4}Sr_{0.12}CuO_4$ and $La_{1.88}Ba_{0.12}CuO_4$. In addition, these samples are not reported to show any clear field enhancement of the elastic signal. This is also true for both $La_{1.48}Nd_{0.4}Sr_{0.12}CuO_4$ and $La_{1.88}Ba_{0.12}CuO_4$. However $La_{1.48}Nd_{0.4}Sr_{0.12}CuO_4$ and $La_{1.88}Ba_{0.12}CuO_4$ show no sign of phase separation [95].

11.0.4 $La_{1.88}Sr_{0.12}CuO_4$

We reported a consistent analysis of new zero field and transverse field μ-SR experiments on the $La_{1.88}Sr_{0.12}CuO_4$ sample used by others for numerous investigations, e.g. [83, 205, 214, 75]. This sample was different from the $La_{1.88}Sr_{0.12}CuO_4$ looked on by Savici et al. [1] in two major respects. First, in full consistency with [83] we find a magnetic volume fraction approaching 100%, thus if this sample is phase separated, it is not detecable by muon spin resonance. Savici on the other hand finds that it is phase seperated. Secondly, we observe a temperature regime of 10-15K with no zero field μ-SR frequency but still a rapid relaxation which we interpret as a dynamical relaxation originating from fluctuation magnetic order, and the Bragg peaks observed in this range are not static. This would indicate that the incommensurate antiferromagnetic order, seen in the work by e.g Rømer et al. [83, 75], does not corrospond to static order. This might instead the be inelastic on an energy scale smaller than 0.3meV (which is the lowest probed in [75]).

We performed a neutron spin echo study of the energy width of the an IC-AFM Bragg peak, and find that a finite broadening down to about 10K. Which supports our picture of fluctuating magnetic order which freezes on the time scale of μ-SR and neutron spin echo at 10K. However, below the freezing temperature, the magnetic order is very similar to the stripe order in e.g $La_{1.88}Sr_{0.12}CuO_4$ and $La_{1.88}Ba_{0.12}CuO_4$.

We observed no anomalies connected to the spins freezing into this stripe order was detected on the superconducting properties. The transverse field frequency of muons stopping in the superconducting region of the sample is essentially unaltered, and so is the relaxation rate corresponding to the field distribution of magnetic flux lines. Instead, we are able to extract the penetration depth of the super conduction phase. We obtain $\lambda_{ab} = 0.274 \pm 0.002\mu$m, which is consistent with the value expected for LSCO12 [217, 218].

Bibliography

[1] A. T. Savici et al. Static magnetism in superconducting stage−4 La_2CuO_{4+y} ($y = 0.12$). *Physica B.*, 289-290:338, 200.

[2] S. Blundell. *Magnetism in Condensed Matter*. Oxford University Press, 2007.

[3] Anderson P. W. New approach to the theory of superexchange interactions. *Phys. Rev.*, 115:2, 1959.

[4] Jensen J. and A. R. Mackintosh. *Rare earth magnetism: Structures and excitations*. Clarendon Press Oxford, 1991.

[5] K. W. H. Stevens. Matrix elements and operator equivalents connected with the magnetic properties of rare earth ions. *Proceedings of the Physical Society. Section A*, 65:209, 1951.

[6] G. Racah. Theory of complex spectra. II. *Phys. Rev.*, 62:438, 1942.

[7] M. T. Hutchings. Point charge calculations of energy levels of magnetic ions in crystalline electric fields. *Solid State Physics*, 16:227, 1964.

[8] et. al. Lea, K. R. The raising of angular momentum degeneracy of f−electron terms by cubic crystal fields. *J. Phys. Chem. Solids*, 23:1381, 1962.

[9] J. B. Goodenough. Theory of the role of covalence in the perovskite−type manganites [La, M (II)] MnO3. *Phys. Rev.*, 100:564, 1955.

[10] J. B. Goodenough. An interpretation of the magnetic properties of the perovskite−type mixed crystals $La_{1-x}Sr_xCoO_{3-\lambda}$. *J. Phys. Chem. Solids*, 6:287, 1958.

[11] Anderson P. W. Antiferromagnetism. theory of superexchange interaction. *Phys. Rev.*, 79:350, 1950.

[12] J. Kanamori. Superexchange interaction and symmetry properties of electron orbitals. *J. Phys. Chem. Solids*, 10:87, 1959.

[13] H. Weihe and H. U. Güdel. Quantitative interpretation of the goodenough-kanamori rules: A critical analysis. *Inorg. Chem.*, 36:3632, 1997.

[14] S. Sachdev. *Quantum Phase Transitions*. Cambridge University Press, 1999.

[15] D. N. Mermin and H. Wagner. Absence of ferromagnetism or antiferromagnetism in one− or two−dimensional isotropic heisenberg models. *Phys. Rev. Lett.*, 17:1136, 1966.

[16] P. C. Hohenberg. Existence of long−range order in one and two dimensions. *Phys. Rev.*, 158:383, 1967.

[17] S. Coleman. There are no goldstone bosons in two dimensions. *Comm. Math. Phys.*, 31:259, 1973.

[18] P. Jordan and E. Wigner. Über das paulische Äquivalenzverbot. *Zeitschrift für Physik*, 47:631, 1928.

[19] P. Pfeuty. The one−dimensional ising model with a transverse field. *Annals of Physics*, 57:79, 1970.

[20] E. Lieb et.al. Two soluble models of an antiferromagnetic chain. *Annals of Physics*, 16:407, 1961.

[21] R. J. Elliott. Ising model with a transverse field. *Phys. Rev. Lett.*, 25:443, 1970.

[22] A. Yaouanc and P. D. De Réotier. *Muon Spin Rotation, Relaxation and Resonance Applications to Condensed Matter*. Oxford Science publications, 2011.

[23] M. Suzuki. Relationship between d-dimensional quantal spin system and $(d+1)$-dimensional ising system. *Proc. Theo. Phys.*, 56:1454, 1976.

[24] J. A. Hertz. Quantum critical phenomena. *Phys. Rev. B*, 14:1165, 1976.

[25] N. W. Ashcroft and N. D. Mermin. *Solid State Physics*. Brooks/Cole, Thomson Learning, 1976.

[26] C. Kittel. *Introduction to Solid State Physics 8th edition*. John Wiley & Sons Ltd, 2005.

[27] M. Thinkham. *Introduction to superconductivity, second edition*. McGRAW-HILL international editions, 1996.

[28] K. Fossheim and A. Sudbø. *Superconductivity*. John Wiley & Sons Ltd, 2004.

[29] K. Onnes. Nobel talk: Investigations into the properties of substances at low temperatures, which have led, amongst other things, to the preparation of liquid helium. 1913.

[30] W. Meissner and R. Ochsenfeld. Ein neuer effekt bei eintritt der supraleitfähigkeit. *Naturwissenschaften*, 3:787, 1933.

[31] W. Meissner and R. Ochsenfeld. The electromagnetic equations of the supraconductor. *Proc. R. Soc. Lond. A*, 149:71, 1934.

[32] C. J. Gorter and H. B. G Casimir. The thermodynamics of the superconducting state. *Zeitschriftfuer Technische Physik*, 15:539, 1934.

[33] G. Burns. *High-Yemperature Superconductivity, An Introduction.* Academic Press, 1992.

[34] A. A. Abrikosov. On the magnetic properties of superconductors of the second group. *Soviet Physics JETP*, 5:1174, 1957.

[35] W. H. Kleiner et. al. Bulk solution of ginzburg-landau equations for type II superconductors: Upper critical field region. *Phys. Rev.*, 133:A1226, 1964.

[36] Cooper L. N. Bardeen, J. and J. R. Schrieffer. Theory of superconductivity. *Phys. Rev.*, 108:1175, 1957.

[37] L. N. Cooper. Bound electron pairs in a degenerate fermi gas. *Phys. Rev.*, 104:1189, 1956.

[38] H. Bruus and K. Flensberg. *Many-Body Quantum Theory in Condensed Matter Physics, An Introduction.* Oxford University Press, 2004.

[39] A. Altlands and B. Simons. *Condensed Matter Field Theory.* Cambridge University Press, 2006.

[40] J. Nagamatsu et. al. Superconductivity at 39k in magnesium diboride. *Nature*, 410:63, 2001.

[41] S. N. Kolodziejczyk et. al. Superconductivity, weak itinerant ferromagnetism and electronic band structure of Y_9Co_7. *Acta Phys. Pol. A*, 111:513, 2007.

[42] D. J. Scalapino. A common thread: The pairing interaction for unconventional superconductors. *Rev. Mod. Phys.*, 84:1383, 2012.

[43] J. G. Bednorz and K. A. Müller. Possible high tc superconductivity in the $Ba - La - Cu - O$ system. *Z. Phys. B Condensed Matter*, 64:189, 1986.

[44] C. W. Chu et. al. Evidence for superconductivity above 40K in the $La - Ba - Cu - O$ compound system. *Phys. Rev. Lett.*, 58:405, 1987.

[45] R. J. Cava. Bulk superconductivity at 36K in $La_{1.8}Sr_{0.2}CuO_4$. *Rev. Mod. Phys.*, 84:1383, 2012.

[46] M. K. Wu. Superconductivity at 93k in a new mixed-phase $Y - Ba - Cu - O$ compound system at ambient pressure. *Phys. Rev. Lett.*, 58:908, 1987.

[47] A. Schilling et. al. Superconductivity above 130K in the $Hg - Ba - Ca - Cu - O$ system. *Nature*, 363:57, 1993.

[48] L. Gao et. al. Study of superconductivity in the $Hg - Ba - Ca - Cu - O$ system. *Nature*, 213:261, 1993.

[49] Y. Kamihara et. al. Iron−based layered superconductor $La[O_{1-x}F_x]FeAs$ ($x = 0.05 - 0.12$) with $t_c = 26$K. *J. Am. Chem. Soc.*, 130:3296, 2008.

[50] L. Udby. *Ph.D. Thesis, University of Copenhagen*, 2009.

[51] A. A. Radaelli et al. Structural and superconducting properties of $La_{2-x}Sr_xCuO_4$ as a function of sr content. *Phys. Rev. B*, 49:4163, 1994.

[52] J. E. Greedan et al. Oxygen ordering in the crystal structure of the 93K superconductor $YBa_2Cu_3O_7$ using powder neutron diffraction at 298 and 79.5K. *Phys. Rev. B*, 35:8770, 1987.

[53] A. A. Jorgensen et al. Oxygen ordering and the orthorhombic-to-tetragonal phase transition in $YBa_2Cu_3O_{7-x}$. *Phys. Rev. B*, 36:3608, 1987.

[54] C. Niedermayer et al. Common phase diagram for antiferromagnetism in $La_{2-x}Sr_xCuO_4$ and $Y_{1-x}Ca_xBa_2Cu_3O_6$ as seen by muon spin rotation. *Phys. Rev. Lett.*, 80:3843, 1998.

[55] M. H. Julien et. al. Magnetic order and superconductivity in $La_{1.86}Sr_{0.14}CuO_4$: A review. *Physica B.*, 329−333:333, 2003.

[56] W. E. Pickett et. al. Electronic structure of the high-temperature oxide superconductors. *Rev. Mod. Phys*, 61:433, 1989.

[57] T. Timusk and B. Statt. The pseudogap in high-temperature superconductors: an experimental survey. *Rep. Prog. Phys.*, 62:61, 1999.

[58] T. Ito et. al. Systematic deviation from t-linear behavior in the in-plane resistivity of $YBa_2Cu_3O_{7-y}$ evidence for dominant spin scattering. *Phys. Rev. Lett.*, 70:3995, 1993.

[59] M. Vojta. Stripes and electronic quasiparticles in the pseudogap state of cuprate superconductors. *Physica C*, 481:178, 2012.

[60] D. LeBoeuf et. al. Lifshitz critical point in the cuprate superconductor $YBa_2Cu_3O_y$ from high-field hall effect measurements. *Phys. Rev. B*, 83:054506, 2011.

[61] N. Doiron-Leyruad et. al. Quantum oscillations and the fermi surface in an underdoped high$-\mathrm{t}_c$ superconductor. *Nature*, 447:565, 2007.

[62] D. LeBoeuf et. al. Electron pockets in the fermi surface of hole-doped high t_c superconductors. *Nature*, 450:533, 2007.

[63] V. J. Emery and S. A. Kivelson. Importance of phase fluctuations in superconductors with small superfluid density. *Nature*, 374:434, 1994.

[64] J. Hubbard. Electron correlations in narrow energy bands. *Proc. R. Soc. Lond. A.*, 276:238, 1963.

[65] F. C. Zhang and T. M. Rice. Effective hamiltonian for the superconducting Cu oxides. *Phys. Rev. B*, 37:3759, 1988.

[66] S. Raghu et. al. Superconductivity in the repulsive hubbard model: An asymptotically exact weak-coupling solution. *Phys. Rev. B*, 81:224505, 2010.

[67] S. Sorella et. al. Superconductivity in the two-dimensional t-J model. *Phys. Rev. Lett.*, 88:117002, 2002.

[68] D. Vaknin et. al. Antiferromagnetism in $\mathrm{La_2CuO_4}$. *Phys. Rev. Lett.*, 58:2802, 1987.

[69] P. W. Anderson. An approximate quantum theory of the antiferromagnetic ground state. *Phys. Rev.*, 86:694, 1952.

[70] E. Manousakis. The spin$-\frac{1}{2}$ heisenberg antiferromagnet on a square lattice and its application to the cuprous oxides. *Rev. Mod. Phys.*, 63:1, 1991.

[71] S. M. Hayden et al. Spin dynamics in the two-dimensional antiferromagnet $\mathrm{La_2CuO_4}$. *Phys. Rev. B*, 42:10220, 1990.

[72] G. Aeppli et al. Magnetic dynamics of $\mathrm{La_2CuO_4}$ and $\mathrm{La_{2-x}Ba_xCuO_4}$. *Phys. Rev. Lett.*, 62:2052, 1989.

[73] R. Coldea et al. Spin waves and electronic interactions in $\mathrm{La_2CuO_4}$. *Phys. Rev. Lett.*, 86:5377, 2001.

[74] J. M. Tranquada. *Handbook of High-Temperature Superconductivity: Theory and Experiment J.S. Brooks, eds., Springer, Amsterdam*, page 257, 2007.

[75] A. T. Rømer et al. Glassy low-energy spin fluctuations and anisotropy gap in $\mathrm{La_{1.88}Sr_{0.12}CuO_4}$. *Phys. Rev. B*, 87:144513, 2013.

[76] N. B. Christensen et al. Nature of the magnetic order in the charge-ordered cuprate $\mathrm{La_{1.48}Nd_{0.4}Sr_{0.12}CuO_4}$. *Phys. Rev. Lett.*, 98:197003, 2007.

[77] S. W. Cheong et. al. Incommensurate magnetic fluctuations in $\mathrm{La_{2-x}Sr_xCuO_4}$. *Phys. Rev. Lett.*, 67:1791, 1991.

[78] T. E. Mason et. al. Magnetic dynamics of superconducting $La_{1.86}Sr_{0.14}CuO_4$. *Phys. Rev. Lett.*, 68:1414, 1992.

[79] J. M. Tranquada et. al. Evidence for the stripe correlations of spins and holes in copper oxide superconductors. *Nature*, 375:561, 1995.

[80] K. Yamada et. al. Doping dependence of the spatially modulated dynamical spin correlations and the superconducting-transition temperature in $La_{2-x}Sr_xCuO_4$. *Phys. Rev. B*, 57:6165, 1998.

[81] S. Wakimoto et al. Observation of incommensurate magnetic correlations at the lower critical concentration for superconductivity in $La_{2-x}Sr_xCuO_4$ ($x = 0.05$). *Phys. Rev. B*, 60:R769, 1999.

[82] M. Matsuda et al. Static and dynamic spin correlations in the spin-glass phase of slightly doped $La_{2-x}Sr_xCuO_4$. *Phys. Rev. B*, 62:9148, 2000.

[83] J. Chang et. al. Tuning competing orders in $La_{2-x}Sr_xCuO_4$ cuprate superconductors by the application of an external magnetic field. *Phys. Rev. B*, 75:104525, 2008.

[84] S. Katano et al. Enhancement of static antiferromagnetic correlations by magnetic field in a superconductor $La_{2-x}Sr_xCuO_4$ with $x = 0.12$. *Phys. Rev. B*, 62:R14677, 2000.

[85] B. Lake et al. Antiferromagnetic order induced by an applied magnetic field in a high-temperature superconductor. *Nature*, 415:299, 2002.

[86] B Lake et al. Spins in the vortices of a high-temperature superconductor. *science*, 291:1759, 2001.

[87] J. M. Tranquada et al. Evidence for an incommensurate magnetic resonance in $La_{2-x}Sr_xCuO_4$. *Phys. Rev. B*, 69:174507, 2004.

[88] J. Chang et al.

[89] S. R. Dunsiger et al. Incommensurate spin ordering and fluctuations in underdoped $La_{2-x}Ba_xCuO_4$. *Phys. Rev. B*, 77:224410, 2008.

[90] M. Hücker et. al. Stripe order in superconducting $La_{2-x}Ba_xCuO_4$ for $0.095 \leq x \leq 0.155$. *Phys. Rev. B*, 83:104506, 2011.

[91] M. Fujuta et al. Stripe order, depinning, and fluctuations in $La_{1.875}Ba_{0.125}CuO_4$ and $La_{1.875}Ba_{0.075}Sr_{0.050}CuO_4$. *Phys. Rev. B*, 70:104517, 2004.

[92] J. Wen et al. Magnetic field induced enhancement of spin-order peak intensity in $La_{1.875}Ba_{0.125}CuO_4$. *Phys. Rev. B*, 78:212506, 2008.

[93] J. M. Tranquada et al. Neutron-scattering study of stripe-phase order of holes and spins in $La_{1.48}Nd_{0.4}Sr_{0.12}CuO_4$. *Phys. Rev. B*, 54:7489, 1996.

[94] Y. S. Lee et al. Neutron-scattering study of spin-density wave order in the superconducting state of excess−oxygen−doped La_2CuO_{4+y}. *Phys. Rev. B*, 60:7489, 2004.

[95] A. T. Savici et al. Muon spin relaxation studies of incommensurate magnetism and superconductivity in stage−4 $La_2CuO_{4.11}$ and $La_{1.88}Sr_{0.12}CuO_4$. *Phys. Rev. B*, 66:014524, 2002.

[96] H. R. De. S. E. Mohotalla et. al. Phase separation in superoxygenated $La_{2-x}Sr_xCuO_{4+y}$. *nature materials*, 5:377, 2006.

[97] L. Udby et al. Magnetic ordering in electronically phase-separated $La_{2-x}Sr_xCuO_{4+y}$: Neutron diffraction experiments. *Phys. Rev. B*, 80:014505, 2009.

[98] L. Udby et. al. Direct proof of generic magnetic and superconducting phases in a series of superoxygenated high-T_c cuprates. *Submitted to Phys. Rev. Lett.*, 2013.

[99] N. B. Christensen et al. unpublished results.

[100] B. Khaykovich et al.

[101] J. Chang et al. Magnetic-field-induced soft-mode quantum phase transition in the high-temperature superconductor $La_{1.855}Sr_{0.145}CuO_4$: An inelastic neutron-scattering study. *Phys. Rev. Lett.*, 102:177006, 2009.

[102] R. M. Martin. *Electronic Structure, Basic Theory and Practical Methods*. Cambridge University Press, 2004.

[103] J. Kohanoff. *Electronic Structure Calculations for Solids and Molecules*. Cambridge University Press, 2006.

[104] P. Hohenberg and W. Kohn. Inhomogeneous electron gas. *Phys. Rev.*, 136:864, 1964.

[105] W. Kohn and Sham L. J. Self-consistent equations including exchange and correlation effects. *Phys. Rev.*, 140:1133, 1965.

[106] Burke K. Perdew, J. P. and M. Ernzerhof. Generalized gradient approximation made simple. *Phys. Rev. Lett.*, 77:3865, 1996.

[107] Hansen L. B. Hammer, B. and J. K. Nørskov. Improved adsorption energetics within density-functional theory using revised perdew-burke-ernzerhof functionals. *Phys. Rev. B*, 59:7413, 1999.

[108] M. et. al. Dion. Van der waals density functional for general geometries. *Phys. Rev. Lett.*, 92:246401, 2004.

[109] Bowler D. R. Klime, J. and A. Michaelides. Chemical accuracy for the van der waals density functional. *J. Phys: Condensed Matter*, 22:022201, 2010.

[110] J. Wellendorff and T. Bligaard. On the importance of gradient-corrected correlation for van der waals density functionals. *Topics in Catalysis*, 54:1143, 2011.

[111] C. Nordling. Presentation speech of the 1994 nobel prize ceremony in physics. 1994.

[112] G. L. Squires. *Introduction to the Theory of Thermal Neutron Scattering*. Dover Publications, inc., 1996.

[113] Mesot J. Strässle T. Furrer, A. *Neutron Scattering in Condensed Matter Physics*. World Scientific, 2009.

[114] Shapiro S. M. Tranquada J. M. Shirane, G. *Neutron Scattering with a Triple-Axis Spectrometer Basic Techniques*. Cambridge University Press, 2002.

[115] J. J. Sakurai. *Modern Quantum Mechanics*. Addison-Wesley Publishing Company, 1994.

[116] L. Van Hove. Correlations in space and time and born approximation scattering in systems of interacting particles. *Phys. Rev.*, 95:249, 1954.

[117] S.N. Klausen et. al. Simulations and experiments on RITA − 2 at PSI. *Applied Physics A*, 74:1508, 2002.

[118] C.R.H. Bahl et. al. The monochromatic imaging mode of a RITA−type neutron spectrometer. *Nuclear Instruments and Methods in Physics Research B*, 226:667, 2004.

[119] C.R.H. Bahl et. al. Inelastic neutron scattering experiments with the monochromatic imaging mode of the RITA-II spectrometer. *Nuclear Instruments and Methods in Physics Research B*, 246:452, 2006.

[120] F. Mezei. *Neutron Spin Echo Spectroscopy, Basics, Trends and Applications*. Springer, Lecture Notes in Physics, 2003.

[121] Golub R. Keller, T. and R. Gähler. *Neutron Spin Echo − A technique for high resolution neutron scattering*. Notes, 2000.

[122] J. B. Torrance and M. Tinkham. Excitations of multiple−magnon bound states in $CoCl_2 \cdot 2H_2O$. *Phys. Rev.*, 187:595, 1969.

[123] M. Tinkham. Microscopic dynamics of metamagnetic transitions in an approximate ising system $CoCl_2 \cdot 2H_2O$. *Phys. Rev.*, 188:967, 1969.

[124] H. Mollymoto and M. Motokawa. High field transverse magnetization of ising antiferromagnet $CoCl_2 \cdot 2H_2O$. *J. Phys. Soc. Japan*, 49:108, 1980.

[125] R. Coldea et. al. Quantum criticality in an ising chain: Experimental evidence for emergent E_8 symmetry. *Science*, 327:177, 2010.

[126] et. al. Montfrooij, W. Spin dynamics of the quasi-one-dimensional ferromagnet $CoCl_2 \cdot 2D_2O$. *Phys. rev. B*, 64:134426, 2001.

[127] B. Morosin and J. Graeber. A reinvestigation of the crystal structure of $CoCl_2 \cdot 2H_2O$. *Acta. Cryst.*, 16:1176, 1963.

[128] et. al. Cox, D. E. The magnetic structure of $CoCl_2 \cdot 2D_2O$. *Phys. Lett.*, 17:103, 1965.

[129] A. Abragam and M. H. L. Pryce. The theory of paramagnetic resonance in hydrated cobalt salts. *Proc. R. Soc. Lond. A*, 206:173, 1951.

[130] Jacob Larsen. *Master Thesis, Quantum Phase Transformation of the Near−Ising Antiferromagnet* $CoCl_2 \cdot 2H_2O$.

[131] A. Narath. Antiferromagnetism in $CoCl_2 \cdot 2D_2O$. i. magnetic structure. *Phys. Rev*, 136:766, 1964.

[132] A. Narath. Antiferromagnetism in $CoCl_2 \cdot 2D_2O$. ii. chlorine nuclear magnetic resonance and paramagnetic susceptibility. *Phys. Rev*, 140:552, 1965.

[133] J. K. Kjems and J. Als-Nielsen. Spin−wave dispersion in $CoCl_2 \cdot 2D_2O$: A system of weakly coupled ising spins. *Phys. Rev. B*, 12:5190, 1975.

[134] T. Oguchi. Theory of magnetism in $CoCl_2 \cdot 2D_2O$. *J. Phys. Soc. Japan*, 20:2236, 1965.

[135] P. A. Lindgård Mogensen and A. Kowalska. *Risø Report No. 127: Diagonalization Procedure for a Bose-System Hamiltonian.* Danish Atomic Energy Commission Research Establishment Risø, 1966.

[136] et. al. Christensen, N. B. Magnetic bloch oscillations in the near-ising antiferromagnet $CoCl_2 \cdot 2D_2O$. *Physica B*, 276−278:784, 2000.

[137] J. Kanamori. Magnetization process in an ising spin system. *Proc. Theo. Phys.*, 35:16, 1966.

[138] J. Kanamori. Magnetization process in antiferromagnets with a strong uniaxial anisotropy energy. *Proc. Theo. Phys.*, 38:541, 1967.

[139] C. Heid et. al. Magnetic phase diagram of $CoNb_2O_6$: A neutron diffraction study. *Jour. Magn. Magn. Mat.*, 151:123, 1995.

[140] G. Cao et. al. Partial antiferromagnetism in spin−chain $Sr_5Rh_4O_{12}$, $Ca_5Ir_3O_{12}$ and Ca_4IrO_6.

[141] W. Scharf et. al. Magnetic structure of $CoNb_2O_6$. *J. Magn. Magn. Mat.*, 13:121, 1979.

[142] J. P. Goff et. al. Exchange mixing and soliton dynamics in the quantum spin chain $CsCoCl_3$. *Phys. Rev. B*, 52:15992, 1995.

[143] H. J. Schulz. Dynamics of coupled quantum spin chains. *Phys. Rev. Lett.*, 77:2790, 1996.

[144] S. T. Carr. Spectrum and correlation functions of a quasi−one−dimensional quantum ising model. *Phys. Rev. Lett.*, 90:177206, 2003.

[145] P. Lee et. al. Interplay of quantum criticality and geometric frustration in columbite. *Nature Physics*, 6:702, 2010.

[146] Private communication. *Georg Ehlers.*

[147] Private communication. *Jens Jensen.*

[148] Private communication. *Rasmus Toft-Petersen.*

[149] J. S. Hummelshøj et. al. Density functional theory based screening of ternary alkali-transition metal borohydrides: A computational material design project. *J. Chem. Phys.*, 131:014101, 2009.

[150] A. Leineweber et. al. $Co(NH_3)_2Cl_2$ and $Co(ND_3)_2Cl_2$: Order-disorder behaviiour of $N(H,D)_3$ and antiferromagnetic structure. *Z. Anorg. Allg. Chem*, 627:2063, 2001.

[151] B. E. Blöhl et al. Projected augmented-wave method. *Phys. Rev. B*, 50:17953, 1994.

[152] H. J. Monkhorst and J. D. Park. Special points for brillouin-zone integrations. *Phys. Rev. B*, 13:5188, 1976.

[153] F. Jensen. *Introduction to Computational Chemistry, 2nd Edition.* John Wiley & Sons Ltd, 2007.

[154] T. Frederiksen et al. Inelastic transport theory from first principles: Methodology and application to nanoscale devices. *Phys. Rev. B*, 75:205413, 2007.

[155] J. S. Hummelshøj. *Ph.D. Thesis, Thechnical University of Denmark*, 2009.

[156] G. A. Sawatzky et al. Magnetic interactions and covalency effects in mainly ionic compounds. *Journal of Magnetism and Magnetic Materials*, 3:37, 1976.

[157] G. A. Mishra and S. Satpathy. Electronic structure and exchange interactions in the manganese-based pyrochlore oxides. *Phys. Rev. B*, 58:7585, 1998.

[158] T. Shimizu et al. Cu−o−cu bond-angle dependence of magnetic interactions in antiferromagnetic cuprates. *Physica B*, 329−333:765, 2003.

[159] D. Bloch. The 10/3 law for the volume dependence of superexchange. *J. Phys. Chem. Solids*, 27:881, 1966.

[160] K. N. Shrivastava and V. Jaccarino. Variation of superexchange with interatomic distance. i. the T_2g system $v^{++} - f^{-} - v^{++}$. *Phys. Rev. B*, 13:299, 1976.

[161] L. J. De Jongh et. al. On the exchange interaction in some $3d$-metal ionic compounds. *Physica B.*, 79:568, 1975.

[162] R. E. Coffman et. al. A limit function for long range ferromagnetic and antiferromagnetic superxchange. *J. Phys. Chem.*, 83:2397, 1979.

[163] C. Yasuda et. al. Néel temperature of quasi-low-dimensional heisenberg antiferromagnets. *Phys. Rev. B*, 94:217201, 2005.

[164] A. Schenck. *Muon Spin Rotation Spectroscopy: Principles and Applications in Solid State Physics*. Institute of Physics Publishing, 1985.

[165] K. Nagamine. *Introductory Muon Science*. Cambridge Science publications, 2003.

[166] S. H. Neddermeyer and C. D. Anderson. Note on the nature of cosmic-ray particles. *Phys. Rev.*, 51:884, 1937.

[167] J. C. Street and E. C. Stevenson. New evidence for the existence of a particle of mass intermediate between the proton and electron. *Phys. Rev.*, 52:1003, 1937.

[168] J. L. Tallon et. al. Muon spin relaxation studies of superconducting cuprates. *Supercond. Sci. Technol.*, 10:A38, 1997.

[169] C. Niedermayer. Muon spin rotation study of the correlation between tc and n_s/m^* in overdoped $Tl_2Ba_2CuO_{6+d}$. *Phys. Rev. Lett.*, 71:1764, 1993.

[170] J. E. Sonier. High-field μsr studies of superconducting and magnetic correlations in cuprates above T_c. *J. Phys: Condens. Matter*, 22:203202, 2010.

[171] J. E. Sonier. Magnetic penetration depth and condensate density of cuprate high-T_c superconductors determined by muon-spin-rotation experiments. *Phys. Rev. B*, 52:10488, 1995.

[172] A. Amato and H. Luetkens. Gps user guide. 2011.

[173] C. S. Wu et al. Experimental test of parity conservation in beta decay. *Phys. Rev.*, 105:1413, 1957.

[174] R. L. Garwin et al. Observations of the failure of conservation of parity and charge conjugation in meson decays: the magnetic moment of the free muon. *Phys. Rev.*, 105:1415, 1957.

[175] A. Kerena et. al. Universal superconducting and magnetic properties of the $(Ca_xLa_{1-x})(Ba_{1.75-x}La_{0.25+x})Cu_3O_y$ system: a μsr investigation. *Solid State Comm.*, 126:39, 2003.

[176] L. P. Le et al. Muon-spin-rotation and relaxation studies in $(TMTSF)_2 - X$ compounds. *Phys. Rev. B*, 48:7284, 1993.

[177] R. Kubo and T. Toyabe. A stochastic model for low field resonance and relaxation. *Colloque Ampére XIV, North-Holland Pibl. Co.*, page 810, 1967.

[178] E. H. Brandt. Flux distribution and penetration depth measured by muon spin rotation in high-T_c superconductors. *Phys. Rev.*, 37:2349, 1988.

[179] A. D. Sidorenko et al. Muonic study of type ii superconductor. *Hyperfine Interaction*, 63:49, 1990.

[180] Y. J. Uemura. Universal correlations, pseudo-gaps and condensation mechanisms in high-T_c superconductors. *Hyperfine Interactions*, 105:35, 1997.

[181] Y. J. Uemura et al. Universal correlations between T_c and n_s/m^* (carrier density over effective mass) in high-T_c cuprate superconductors. *Phys. Rev. Lett.*, 62:2317, 1989.

[182] Y. J. Uemura et al. Basic similarities among cuprate, bismuthate, organic, chevrel-phase, and heavy-fermion superconductors shown by penetration-depth measurements. *Phys. Rev. Lett.*, 66:2665, 1991.

[183] J. E. Sonier et al. New muon-spin-rotation measurement of the temperature dependence of the magnetic penetration depth in $YBa_2Cu_3O_{6.95}$. *Phys. Rev. Lett.*, 72:744, 1994.

[184] P. J. Hirschfeld and N. Goldenfeld. Effect of strong scattering on the low-temperature penetration depth of a d-wave superconductor. *Phys. Rev. B*, 48:4219, 1993.

[185] http://lmu.web.psi.ch/facilities/software.html. musrfit user manual.

[186] Tanya Riseman. *Ph.D. Thesis, University of British Columbia*, 1993.

[187] E. B. Karlsson. *Solid State Phenomena: As Seen by Muons, Protons, and Excited Nuclei*. Clarendon Press, 1995.

[188] E. J. Ansaldo et. al. Study of the hybrid state of Y_9Co_7. *Solid State Comm.*, 55:193, 1985.

[189] Private communication. *Tomasz Klimczuk*.

[190] T. Klimczuk et al. Structure and paramagnetism in weakly correlated Y_8Co_5. *J. Phys. Condens. Matter*, 25:125701, 2013.

[191] A. K. Grover et al. The Y-Co system: A partial phase diagram study. *J. Less Common Met*, 86:29, 1982.

[192] M. Takigawa et. al. Itinerant electron ferromagnetism in $Y_4Co_3 - 59Co$ NMR. *J. Phys. Soc. Japan*, 52:3318, 1983.

[193] S. Wada and T. Kohara. NMR study of Y_4Co_3 compound. *Solid State Comm.*, 48:5, 1983.

[194] S. N. Kolodziejczyk et. al. Magnetism and superconductivity in a transition metal compound: Y_4Co_3. *J. Phys. F. Metal. Phys*, 10:L333, 1980.

[195] B. V. B. Sarkissian and J. L. Tholence. The critical fields of the magnetic superconductor Y_9Co_7. *J. Magn. Magn. Matter*, 54-57:1525, 1986.

[196] L. C. Hebel and C. P. Slichter. Nuclear spin relaxation in normal and superconducting aluminum. *Phys. Rev.*, 113:513, 1959.

[197] R. F. Kiefl et. al. Coherence peak and superconducting energy gap in Rb_3C_{60} observed by muon spin relaxation. *Phys. Rev. Lett.*, 70:3987, 1993.

[198] W. A. MacFarlane et. al. Muon-spin-relaxation studies of the alkali−fulleride superconductors. *Phys. Rev. B*, 58:1004, 1998.

[199] L. Udby et al. Incommensurate spin fluctuations in high-transition temperature superconductors. *Science*, 277:1067, 1997.

[200] X. Xiong et al. Evidence of in-plane superstructure formation in phase-separated and staged single crystal La_2CuO_{4+d}. *Phys. Rev. Lett.*, 76:2997, 1996.

[201] H. R. De. S. E. Mohottala. Ph.d. thesis, university of connecticut. 2006.

[202] A. Suter. *Memorandum The Skewed Gaussian*. Notes, 2008.

[203] E. J. Ansaldo et. al. Magnetic properties of the superconducting 'superoxide' La_2CuO_{4+d}. *Phys. Rev. B*, 40:2555, 1989.

[204] G. M. Luke et al. Magnetic field penetration depth in single crystal $La_{1.85}Sr_{0.15}CuO_4$ and $Nd_{1.85}Ce_{0.15}CuO_4$. *Physica C*, 282-287:1465, 1997.

[205] J. Chang et al. Electronic structure near the 1/8−anomaly in la-based cuprates. *New J. Phys.*, 10:103016, 2008.

[206] D. Haug et. al. Neutron scattering study of the magnetic phase diagram of underdoped $YBa_2Cu_3O_{6+x}$. *New J. Phys.*, 12:105006, 2010.

[207] D. R. Harshman et al. Freezing of spin and charge in $La_{2-x}Sr_xCuO_4$. *Phys. Rev. B*, 38:852, 1988.

[208] B. J. Sternlieb et al. Muon-spin-relaxation and neutron-scattering studies of magnetism in single-crystal $La_{1.94}Sr_{0.06}CuO_4$. *Phys. Rev. B*, 41:8866, 1990.

[209] K. Kumagai et al. μsr and nmr investigations on electronic and magnetic state around $x = 0.12$ in $La_{2-x}Sr_xCuO_4$ and $La_{2-x}Ba_xCuO_4$. *Hyperfine Interactions*, 86:473, 1994.

[210] E. Demler et. al. Spin-ordering quantum transitions of superconductors in a magnetic field. *Phys. Rev. Lett.*, 87:067202, 2001.

[211] S. B. Sulaiman et al. Location and associated hyperfine properties of μ^+ in La_2CuO_4. *Hyperfine Interactions*, 79:901, 1993.

[212] S. B. Sulaiman et al. Theory of location and associated hyperfine properties of the positive muon in La_2CuO_4. *Hyperfine Interactions*, 84:87, 1994.

[213] P. Dalmas de Réotier and A. Yaouanc. Muon spin rotation and relaxation in magnetic materials. *J. Phys. Condens. Matter*, 9:9113, 1997.

[214] J. Chang et al. Spin density wave induced disordering of the vortex lattice in superconducting $La_{2-x}Sr_xCuO_4$. *Phys. Rev. B*, 85:134520, 2012.

[215] Private communication. *Christof Niedermayer*.

[216] W. Barford and J.M.F Gunn. The theory of the measurement of the london penetration depth in uniaxial type ii superconductors by muon spin rotation. *Physics C*, 156:515, 1988.

[217] C. Panagopoulos et al. Superfluid response in monolayer high-T_c cuprates. *Phys. Rev. B*, 67:220502, 2003.

[218] Q. Li et al. Magnetic penetration depth of $(La_{1-x}Sr_x)_2CuO_4$ single crystals. *Phys. Rev. B*, 47:2854, 1993.

[219] K. Habicht et. al. Temperature-dependent phonon lifetime in lead investigated with neutron-resonance spin-echo spectroscopy. *Phys. Rev. B*, 69:104301, 2004.

Inorganic Chemistry

Article

pubs.acs.org/IC

Spin $^1/_2$ Delafossite Honeycomb Compound Cu_5SbO_6

E. Climent-Pascual,*[,†] P. Norby,[‡] N.H. Andersen,[‡] P.W. Stephens,[§] H.W. Zandbergen,[⊥] J. Larsen,[‡] and R.J. Cava[†,‡]

[†]Department of Chemistry, Princeton University, Princeton, New Jersey 08544, United States

[‡]Materials Research Division, Risø DTU, Technical University of Denmark, DK-4000 Roskilde, Denmark

[§]Department of Physics and Astronomy, Stony Brook University, Stony Brook, New York 11794, United States

[⊥]National Centre for HREM, Delft University of Technology, 2628 CJ Delft, The Netherlands

ABSTRACT: Cu_5SbO_6 is found to have a monoclinic, Delafossite-derived structure consisting of alternating layers of O−Cu(I)−O sticks and magnetic layers of Jahn−Teller distorted $Cu(II)O_6$ octahedra in an edge sharing honeycomb arrangement with $Sb(V)O_6$ octahedra. This yields the structural formula $Cu(I)_3Cu(II)_2Sb(V)O_6$. Variants with ordered and disordered layer stacking are observed, depending on the synthesis conditions. The spin $^1/_2$ Cu^{2+} ions form dimers in the honeycomb layer. The magnetic susceptibility measured between 5 and 300 K is characteristic of the presence of a singlet−triplet spin gap of 189 K. High resolution synchrotron X-ray diffraction studies indicate that changes in the intra- or interdimer distances between 300 and 20 K, such as might indicate an increase in strength of the Peierls-like distortion through the spin gap temperature, if present, are very small. A comparison to the $NaFeO_2$-type Cu^{2+} honeycomb compounds $Na_3Cu_2SbO_6$ and $Na_2Cu_2TeO_6$ is presented.

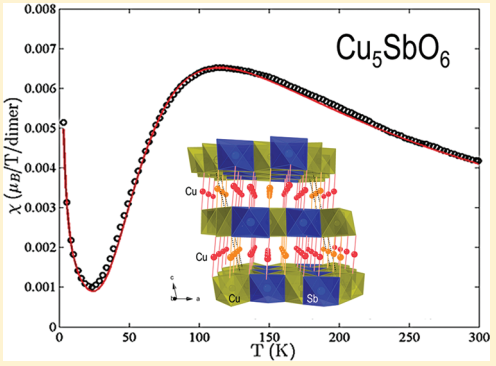

1. INTRODUCTION

Compounds with magnetic ions arranged in 1- or 2-dimensional sublattices continue to be of interest in the study of magnetism, especially in the context of geometric magnetic frustration.[1] Among these, compounds based on Cu^{2+} are especially appealing because at spin $^1/_2$, quantum effects are expected to be important in determining the magnetic properties. Recent observations of the properties of mineral-based cuprates[2,3] based on kagome lattices are of particular interest in this regard. Although not generally appreciated to be frustrated, magnetic ions on honeycomb lattices frequently display nontrivial types of magnetic ordering at low temperatures because of frustration that arises from the presence of strong competition between nearest neighbor and second nearest neighbor magnetic interactions.[4,5] The Jahn−Teller distortion for $3d^9$ Cu^{2+} frequently prevents the formation of ideal magnetic lattice geometries, and, in the case of the two honeycomb layer cuprates known, $NaFeO_2$-derived $Na_3Cu_2SbO_6$ and $Na_2Cu_2TeO_6$,[6,7] results in the presence of strong $S = 0$ Cu−Cu dimers across a subset of the shared edges of the octahedra in the honeycomb plane.

A compound variously reported as having composition Cu_5SbO_6 or $Cu_4SbO_{4.5}$ is known to occur in the Cu−Sb−O chemical system,[8−11] but its crystal structure and magnetic properties have not previously been reported. Here we show that the compound has the formula Cu_5SbO_6 and has a Delafossite-derived structure, with planes of O−Cu(I)−O sticks alternating with planes of edge sharing MO_6 octahedra; the ordering of Cu^{2+} and Sb^{5+} octahedra in a 2:1 ratio results in a honeycomb geometry for the Cu ions and leads to a triple Delafossite formula unit; octahedral distortions and shifts in the stacking of neighboring planes lead to monoclinic symmetry. Similar structures are found for other Delafossite honeycomb compounds either synthesized directly or via ion exchange from $NaFeO_2$-derived starting materials.[12−14] We find that the plane stacking in Cu_5SbO_6 can be regular or disordered, with the disordered stacking variant stable on synthesis at 1000 °C, and the ordered stacking variant favored just below the melting point of 1160 °C in air. Overall monoclinic symmetry and disordered stacking are commonly found in $NaFeO_2$-type derivatives with triangular and honeycomb magnetic layers;[15−17] we do not observe the 3R versus 2H polytypism frequently seen in Delafossites.[18,19] Our magnetic characterization shows Cu_5SbO_6 to display a singlet−triplet gap of ∼189 K, which we attribute to the presence of the Cu−Cu dimers in the honeycomb layers. Our structural studies show that the dimerization is weaker than is seen in the previously known Cu honeycomb compounds $Na_3Cu_2SbO_6$ and $Na_2Cu_2TeO_6$, and we therefore studied the crystal structure by high resolution synchrotron X-ray diffraction at 20 K and ambient temperature, to determine whether the dimerization increases in strength on cooling, that is, whether there is significant magnetostructural coupling as the spins localize in the $S = 0$ state at low temperatures. No enhancement of the structural dimerization because of the spin singlet formation is observed.

Received: September 21, 2011
Published: December 15, 2011

   dx.doi.org/10.1021/ic202066n | *Inorg. Chem.* 2012, 51, 557−565

2. EXPERIMENTAL SECTION

Synthesis. Samples were prepared by conventional solid state methods. High purity CuO (Alfa Inorganics, 99.99%) and Sb_2O_5 (Alfa Inorganics, 99.9%) were intimately mixed, in a stoichiometric ratio to yield 5Cu:1Sb, and placed in high purity alumina crucibles. Samples were then heated in air to 950 at 100 °C per hour, held for 16 h, cooled, reground, and then pelletized and reheated in air at 1000 °C for 24 h to yield the disordered stacking variant of the phase. The disordered stacking variant was obtained on heating to temperatures up to about 1130 °C above which temperature the ordered stacking variant is found. The most highly crystallized sample of the ordered stacking variant, with the smallest amount of disordered stacking present, was obtained from a sample with an excess of 3 wt % of CuO, with the same heating and soaking cycle, but then cooled at 5 °C per hour to 1040 °C before turning off the furnace. Variation of the composition indicated that single phase samples of the Delafossite honeycomb structure phase could be obtained only for a 5:1 ratio of Cu:Sb.

Characterization Techniques. The reactions were monitored in the laboratory by X-ray powder diffraction (XRPD) using Philips Panalytical X'Pert MPD (Cu $K_{\alpha 1}$) and Bruker D8 FOCUS (Cu $K_{\alpha 1,2}$) diffractometers. High resolution XRPD data for structure analysis were taken at beamline X16C at the National Synchrotron Light Source at Brookhaven National Laboratory. The samples for the high resolution studies were loaded in a glass capillary (ϕ = 0.3 mm) and/or on a plate, and diffraction patterns ($\lambda \approx 0.69889$ Å) were collected for the low temperature and high temperature variants at both 20 and 300 K. Indexing of the powder pattern was performed by means of the successive dichotomy method[20] with the *DICVOL* program.[21] The possible space groups were found from systematic extinctions, and the structure for the ordered Cu_5SbO_6 variant was solved by direct-space methods using the FOX program[22] and refined by the Rietveld method using the FullProf program integrated within the FullProf Suite of programs.[23] Diffraction maxima were fit with the Thompson–Cox–Hastings pseudo-Voigt function, and the background was defined using linear interpolation between a set of fixed points. Simulation of the stacking disorder–order was performed with DIFFaX.[24] This allows for calculation of the powder diffraction pattern based on rigid layer-like building blocks and corresponding stacking operators. For this simulation, the structure of a single building block was taken from the result of the Rietveld refinement of the ordered variant. Electron microscopy was performed on an aberration corrected ($C_S \sim 0$) TITAN high-resolution transmission electron microscope operating at 300 kV. Thin areas were obtained by gently dry crushing the specimens and next making a suspension with ethanol and depositing a few drops on a holey carbon Cu grid.

Magnetic susceptibility measurements were performed by vibrating sample magnetometry (VSM) in a CRYOGENIC cryogen free measurement system (CFMS) with a base temperature of 1.6 K, 16 T maximum magnetic field, and sensitivity of 10^{-6} emu. Polycrystalline sample powders of 300 mg approximate weight were employed. Specific heat measurements were performed by the heat-relaxation method in the temperature range between 2 and 250 K using a Quantum Design physical property measurement system (PPMS). The sample was fixed to the sapphire platform of the sample holder by a small amount of Apiezon grease. The specific heat of the sample holder and the grease was measured separately under the same conditions, and this addendum was subtracted from the experimental values to obtain the specific heat of the ordered variant of Cu_5SbO_6. To subtract the phonon contribution to the specific heat a reference sample of the nonmagnetic structural/chemical analogue $Cu_3Zn_2SbO_6$ was used.[12] Electron Paramagnetic Resonance (EPR) spectra were obtained at 4 K with the samples placed in 4-mm-o.d. quartz tubes in a Bruker EMX spectrometer operating in the X-band utilizing microwave frequencies around 9.5 GHz. The determination of the *g* values was made through the use of the simulation program SimFonia provided with the Bruker EMX EPR spectrometer.

3. RESULTS AND DISCUSSION

Crystal Structure. Representative regions of the XRPD patterns at 300 K for disordered (upper panel) and (lower panel) ordered Cu_5SbO_6 are presented in Figure 1. The fact

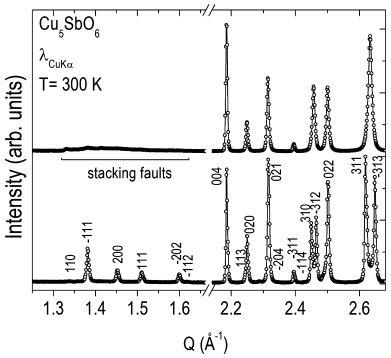

Figure 1. Selected regions of the XRPD (Cu $K_{\alpha 1}$) patterns at 300 K for disordered (upper panel) and ordered (lower panel) variants of Cu_5SbO_6. The patterns are clearly related, though the differences are significant. A broad peak in the disordered form near Q = 2.64 $Å^{-1}$ splits into two narrow peaks, and peaks at lower Q, in the region 1.3–1.6 $Å^{-1}$ are clearly present in the ordered form but are broadened, weaker, and display an asymmetric shape in the disordered form. The indexing of the diffraction lines for the ordered variant is based on a monoclinic cell $a \sim 8.93$ Å, $b \sim 5.60$ Å, $c \sim 11.85$ Å, and $\beta = 103.6°$.

that the two forms are strongly related can be seen by simple visual comparison. The indexing of the diffraction peaks for the ordered variant, based on the monoclinic cell of $a \sim 8.93$ Å, $b \sim 5.60$ Å, $c \sim 11.85$ Å, and $\beta = 103.6°$, is shown in the lower panel. Two important features can be seen indicating that the two forms are related, although they display differences in the perfection of the stacking of the honeycomb layers. First, the disordered variant displays some peaks that are broader than those in the ordered form (e.g., the peaks near Q = 2.63 $Å^{-1}$), while others (e.g., the peak indexed as the (004) near Q = 2.18 $Å^{-1}$) are equally sharp. Second, there is a low angle region for which a broad feature is seen in the diffraction pattern for the disordered variant (for Q between 1.3 and 1.6 $Å^{-1}$, marked as "stacking faults") whereas distinct peaks are observed in this region for the ordered variant. This anisotropic diffraction peak broadening led us to study the two variants by selected area electron diffraction (SAED). The results of this study are seen in Figure 2, which shows [010] SAED patterns for the disordered

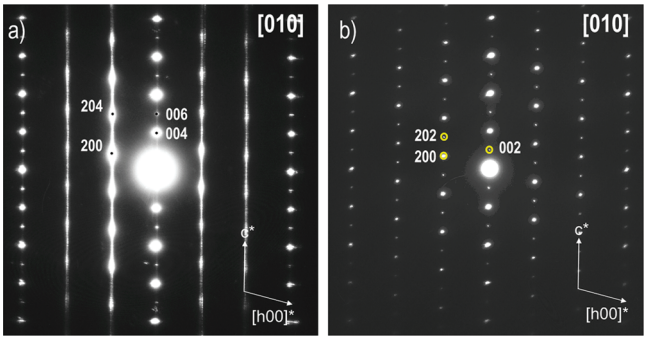

Figure 2. SAED patterns in the [010] reciprocal lattice plane for the disordered (a) and ordered (b) variants of Cu_5SbO_6. The stacking direction is vertical in the figure. Streaking of the diffraction peaks along the stacking direction is clearly seen in panel (a) indicating the presence of layer stacking disorder.

dx.doi.org/10.1021/ic202066n | *Inorg. Chem.* 2012, 51, 557–565

(2a) and ordered (2b) variants of Cu_5SbO_6. It is immediately apparent that the ordered variant displays sharp electron diffraction spots, while the disordered one shows the presence of lines of strongly streaked peaks in the reciprocal lattice direction perpendicular to the honeycomb layers, a strong and unambiguous proof of stacking disorder of the planes.

The detailed structural analysis was performed on the ordered stacking phase, because in an X-ray diffraction measurement of the average structure the lack of long-range order between the layers in the disordered form effectively averages the positions of the Sb(V) and Cu(II) cations in the honeycomb, therefore preventing the acquisition of structural information to the precision desired to investigate the possibility of magneto-structural coupling. To obtain a structural model for the ordered variant that is sufficiently high in quality to answer questions about such possible coupling, accommodation had to be made in its observed synchrotron X-ray diffraction pattern for the presence of the disordered variant.

Thus, as a first step, the XRPD pattern of the disordered variant had to be modeled precisely so that its impact on the detailed refinements of the ordered variant could be accommodated. Since this faulted phase is a minor "impurity" in the high temperature ordered phase, and the determination of its average crystal structure is not useful for current purposes, the XRPD data set for the disordered variant was analyzed by a Le Bail profile fit.[24] The characteristic diffraction pattern for the disordered variant was accurately modeled using an orthorhombic unit cell with dimensions of a = 2. 97450(3) Å, b = 5. 59209(6) Å, and c = 11. 51660(13) Å, and the *Pbnn* (#52) space group (Figure 3a). To model the severe peak broadening for this faulted phase, we employed a phenomenological model that describes the broadening of the peaks by a linear combination of ninth order spherical harmonics (SPH).[26,27] This model is implemented in the Rietveld code of the FullProf program, allowing the treatment to account for the anisotropic size-like broadening in terms of refinable real spherical harmonics coefficients that contribute to the Lorentzian component of the Voigt function employed. Although this has been used to model the broadening caused by stacking faults,[28] the SPH approach is too general to treat strong anisotropic broadening. To employ the diffraction data for the disordered variant quantitatively, a reference mixture (80 wt % disordered variant and 20 wt % α-Al_2O_3) was analyzed. Using the measured intensities on this sample, a refinement was carried out of the relative proportion of the phases until the known proportion was reproduced. This allows the values of the structure factors for the disordered phase to be determined in absolute units.[29] In this refinement, the scale factor of the disordered phase was refined by assuming the composition Cu_5SbO_6 for the disordered variant and keeping the relative intensities constant. Other parameters, such as cell parameters, profile shape, global temperature factor, and asymmetry were also refined. α-Al_2O_3 was treated in the normal fashion. The fit obtained provides the structural information contained in the *hkl* integrated intensities as well as the microstructural information that is included in the peak shape.[29] The structure factors were then used to model the integrated intensities of the disordered variant in the sample of the ordered variant that was analyzed quantitatively; the quantitative contribution of the disordered phase to the diffraction pattern of the high temperature ordered variant (see below) could therefore be estimated. Because we are concerned

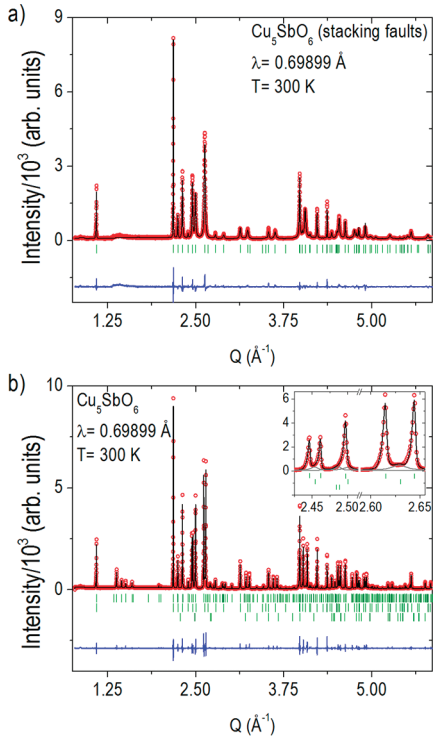

Figure 3. Observed (open circles), calculated (solid line), and difference (lower solid line) high resolution synchrotron XRPD profiles for the disordered (a) and ordered (b) variants of Cu_5SbO_6 at 300 K. The upper panel shows one set of tick marks that indicates the calculated Bragg positions (Le Bail method) for the disordered form. The lower panel, showing the data on which the quantitative structural analysis (Rietveld refinement) is based, shows three sets of tick marks. The upper and middle rows of tick marks show the Bragg positions for the ordered and disordered forms of Cu_5SbO_6, respectively, while the third row shows the calculated positions for CuO. The inset in the lower panel shows the part of the diffraction pattern clearly affected by the presence of small quantities of the disordered variant and CuO in the ordered variant.

only with accommodating the presence of the relatively weak diffraction from the disordered "impurity" in the diffraction pattern of the ordered variant, this approach works very well.

The crystal structure of Cu_5SbO_6 in its ordered stacking phase was found from the structure refinements to be monoclinic, $C2/c$ space group (#15), with unit cell parameters at 300 K a = 8.92346(3) Å, b = 5.592776(16) Å, c = 11.84459(4) Å, and β = 103.58453(17)°. The final fitted synchrotron XRPD pattern at 300 K for the ordered variant of Cu_5SbO_6 is shown in Figure 3b; the figure shows the excellent fit of the data by the structural model. There is no overall change in symmetry of the structure between 300 and 20 K, and therefore a similar fit to the low temperature synchrotron XRPD data, obtained at 20 K, was also performed. The refined structural parameters at 300 and 20 K are presented in Table 1. The inset in Figure 3b shows details of regions in the diffraction pattern from the ordered variant where the presence of the disordered variant and the CuO impurity (this sample was synthesized with an excess of CuO, as described) are the most pronounced. Inspection of the region near Q = 2.63 $Å^{-1}$ shows the presence of a small and broad peak from the disordered variant (middle set of tick marks) between two peaks from the ordered variant. The phase content of this disordered variant

dx.doi.org/10.1021/ic202066n | *Inorg. Chem.* 2012, 51, 557–565

Table 1. Refined Lattice Parameters, Atomic Positions, and Overall Debye-Waller Factor (B_{ov}) of the Ordered Cu_5SbO_6 in Monoclinic $C2/c$ ($Z = 4$) at 300 and 20 K[a]

				T (K)	
				300	20
a (Å)				8.92346(3)	8.90920(3)
b (Å)				5.592776(16)	5.585598(18)
c (Å)				11.84459(4)	11.84986(4)
β (deg.)				103.58453(17)	103.6007(3)
V (Å^3)				574.590(3)	573.151(3)
O(1)	O^{2-}	8*f*: *x*,*y*,*z*	*x*	0.6164(12)	0.6185(13)
			y	0.3762(15)	0.3809(16)
			z	0.5964(9)	0.5955(11)
O(2)	O^{2-}	8*f*: *x*,*y*,*z*	*x*	0.2215(12)	0.2236(13)
			y	0.9280(16)	0.9165(19)
			z	0.9182(8)	0.9120(10)
O(3)	O^{2-}	8*f*: *x*,*y*,*z*	*x*	0.4473(13)	0.4523(12)
			y	0.1192(17)	0.1178(18)
			z	0.0913(10)	0.1009(10)
Cu(1)	Cu^{+}	8*f*: *x*,*y*,*z*	*x*	0.4165(2)	0.4166(3)
			y	0.7494(5)	0.7499(8)
			z	0.0021(2)	0.0012(2)
Cu(2)	Cu^{2+}	8*f*: *x*,*y*,*z*	*x*	0.8281(3)	0.8298(3)
			y	0.0953(3)	0.0991(3)
			z	0.2422(2)	0.2449(2)
Cu(3)	Cu^{2+}	4*e*: 0,*y*,1/4	*y*	0.6292(5)	0.6220(5)
Sb(1)	Sb^{5+}	4*c*: 3/4,3/4,0			
B_{ov} (Å^2)				0.112(18)	0.071(22)
R_{Bragg} (%)				3.36	6.58
R_P (%)				7.49	11.2
wR_P (%)				10.1	14.6
χ^2				11.00	8.30

[a]Agreement factors (R_{Bragg}, R_P, wR_P, and χ^2) are also given.

was found to be at approximately the 20 wt % level. The region of the pattern near $Q = 2.48$ Å^{-1} similarly shows the presence of a small amount (3 wt %) of CuO (bottom tick marks). Figure 4 shows a HREM image that presents a real space confirmation of the stacking order in the ordered variant. The lines of white spots of medium intensity aligned at the β angle of ~103 degrees from the dominant horizontal lines of spots show a region of monoclinic stacking. This monoclinic stacking was observed to be followed regularly over large parts of the sample, not shown in this figure. An image simulation was done with the refined structural model from the synchrotron XRPD data at 300 K (Table 1), shown on the left for the monoclinic stacking. A good fit is obtained between the experimental and simulated images.

To investigate the stacking disorder further, DIFFaX modeling was performed using the layer structure determined from the Rietveld refinement of the ordered Cu_5SbO_6 structure. A double layer was described in an orthorhombic unit cell related to the monoclinic unit cell as $a_O = a_M$, $b_O = b_M$, $c_O = c_M \times \sin \beta$. The monoclinic symmetry was obtained by using one stacking vector ($c_M \times \cos \beta/a_M$, 0, 1). The disordered structure was calculated using the same structural element, but with a 50% stacking probability for each of the vectors ($c_M \times \cos \beta/a_M$, 0, 1) and ($-c_M \times \cos \beta/a_M$, 0, 1). Figure 5 shows the DIFFaX-simulated and observed X-ray diffraction patterns using disordered (Figure 5a) and ordered stacking (Figure 5b). A rather good agreement is seen between position, intensity,

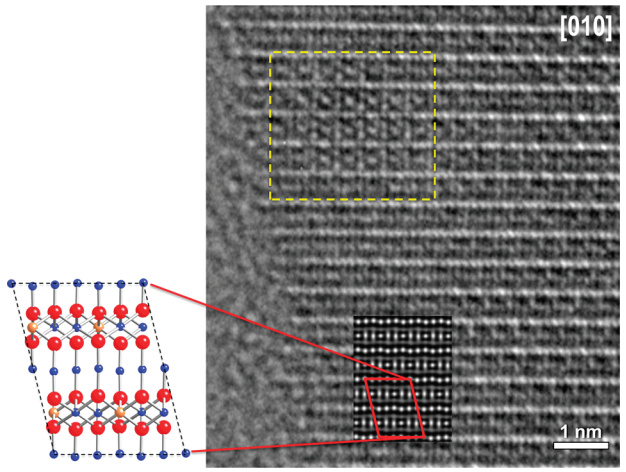

Figure 4. HRTEM image of Cu_5SbO_6 presenting a real space confirmation of the stacking order in the ordered variant. In the highlighted part, the lines of medium intensity white spots are aligned at the β angle of ~103 degrees from the dominant horizontal lines of spots. This monoclinic stacking was observed also over a larger part, not shown in this figure. Image simulation ($E = 300$ kV, $C_S = 0$, convergence 0.15 mrad, focus spread 5 nm, defocus $\Delta f = +5$ nm, mechanical vibration 0.03 nm, and thickness $t = 4$ nm) was done by using the model shown on the left for the ordered monoclinic stacking (large blue circles, Cu, large green circles, Sb, large red circles). The dashed-yellow square shows the presence of disordered regions in the ordered variant.

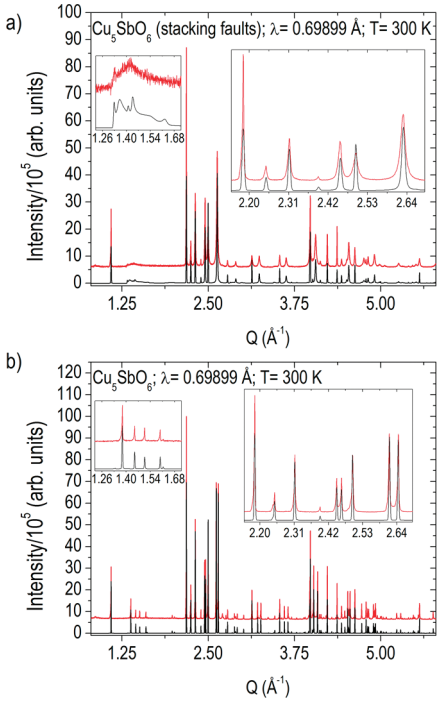

Figure 5. High resolution synchrotron XRPD patterns and DIFFaX simulations for the disordered (upper panel) and ordered (lower panel) variants of Cu_5SbO_6 at 300 K. Raw data and simulated curves are shown as red and black solid lines, respectively. The insets in the upper and lower panels show the parts of the diffraction patterns most affected by the disorder.

anisotropic line broadening, and discontinuities observed in the disordered phase. Notice especially the reproduction of the broad feature between $Q = 1.3$ and 1.6 Å^{-1}, and the disappearance of the ordered-phase peak-splitting at a Q value of about 2.45 and 2.64 Å^{-1}. Although the powder diffraction

dx.doi.org/10.1021/ic202066n | Inorg. Chem. 2012, 51, 557–565

pattern of the disordered phase is not fully reproduced using this simple model, the good agreement confirms the structure as a heavily disordered modification of the monoclinic ordered phase. The electron microscopy images show that the disordered phase can be understood in terms of the presence of disordered regions within the ordered structure, rather than in terms of a discrete phase, as can be seen in the small yellow square in Figure 4.

Figure 6 shows the crystal structure of Cu_5SbO_6. Figure 6a shows the geometry of the honeycomb Cu_2SbO_6 layer, which is

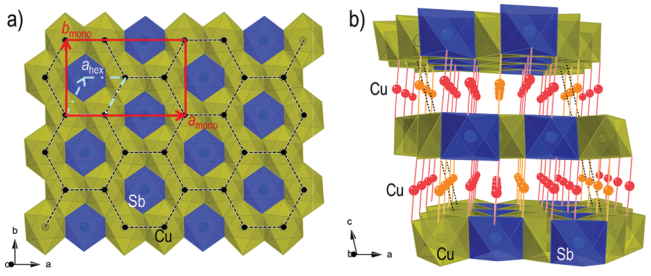

Figure 6. Delafossite honeycomb crystal structure of Cu_5SbO_6. (a) View perpendicular to the honeycomb layer with the Cu^{2+} honeycomb arrangement emphasized (black dashed lines and dots). $Sb(V)O_6$ octahedra are shown in blue (dark) while $Cu(II)O_6$ octahedra are shown in yellow (light). A schematic illustration of the relationship of the unit cell axes between the hexagonal (light-gray dashed-dot arrows) and monoclinic (red solid arrows) cells is also included. (b) View parallel to the honeycomb layers. The two types of O−Cu(I)−O sticks that separate the planes are shown, and the unit cell is shown by black dotted lines.

made from Cu^{2+} and Sb^{5+} (Cu(1) and Sb(1), located on 8*f* and 4*c* sites in Table 1) octahedra sharing edges in a 2:1 ratio. The Cu^{2+} honeycomb lattice is emphasized. The Cu^{2+} and Sb^{5+} ions are coplanar, but do not form an ideal equilateral triangle lattice geometry. The close packed layers of oxygen (O(1), O(2), and O(3) located on 8*f* sites in Table 1) above and below the metal plane are irregular in shape and slightly puckered, accommodating the Jahn−Teller (J-T) distortion of the $3d^9$ Cu^{2+} ions, as described below. The crystallographic monoclinic unit cell in this plane, shown in the figure by red solid lines, deviates from the ideal pseudohexagonal plane ($a_{hex} \sim b_{hex} \sim 3.1$ Å) where $a_{mono} \approx 3a_{hex}$, $b_{mono} \approx \sqrt{3}a_{hex}$, shown in the figure by light-gray dashed lines, by a shortening of ~8% along *a* because of the Cu−O J-T distortion. Figure 6b shows the stacking of the layers. Cu^+ ($3d^{10}$) ions in the expected stick geometry are found between planes, connecting all oxygens in the honeycomb planes above and below. The cell symmetry dictates that there are two independent Cu^+ ions (Cu(2) and Cu(3) located on 8*f* and 4*e* in Table 1) in these spacer layers, in a 2:1 ratio; all connect honeycomb plane oxygens that are shared by two $Cu(II)O_6$ octahedra and one $Sb(V)O_6$ octahedron. The monoclinic cell, with a β angle of ~103.58 degrees, is shown by the dotted line. Given the J-T distortion that always accompanies Cu^{2+} in octahedral geometry, and the required accompanying distortion in the shape of the honeycomb plane, an ideal hexagonal or rhombohedral symmetry structure is not possible for Cu_5SbO_6. Thus, the lower symmetry allows the structure to relax. The stacking of several layers of the honeycomb, abstracted to their simple form for the metal atoms in the honeycomb only, is presented in Figure 7a and b. The figure shows that the honeycomb metal layers are staggered, not eclipsed, in a fashion that repeats after 1.5 cells,

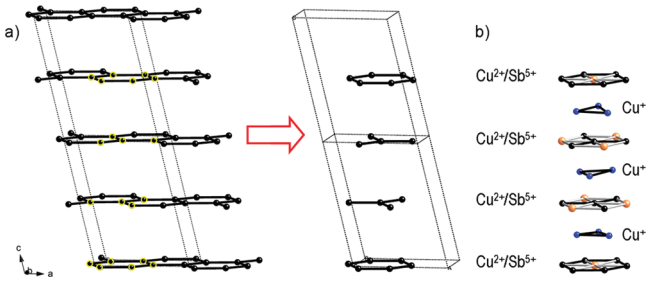

Figure 7. (a) Schematic view of arrangement of the metal atoms in the honeycombs in Cu_5SbO_6 when viewed in a direction parallel to the layers. (b) The honeycombs are staggered, and the layer sequence repeats after 3 translations making this, if considering the metal atoms in the honeycomb layer only, effectively a pseudo-3R Delafossite structure.

forming a pseudo 3R-polytype honeycomb RMO_2 Delafossite compound. An ideal 3R polytype has been reported for the related compound $Cu_3Ni_2SbO_6$ where the effects of the J-T distortion are not present.[11]

A selection of chemically relevant bond angles and distances at room temperature and 20 K is presented in Table 2. All

Table 2. Selected Bond Distances (Å) and Angles (deg.) Found for Cu_5SbO_6 from the Rietveld Analysis of the XRPD Data at 300 and 20 K[a]

		T (K)	
		300	20
Cu	d_{ax}	2.309(14)	2.335(10)
		2.376(11)	2.350(9)
	d_{eq}	1.968(12)	1.968(12)
		1.984(10)	1.986(11)
		1.996(10)	1.990(12)
		2.050(10)	2.039(10)
	Θ_{ax}	177.9(3)	179.2(4)
	Θ_{eq}	171.2(4), 171.1(4)	172.5(5), 173.8(5)
	Θ_{hc1},Θ_{hc2},Θ_{hc3}	92.6(4), 93.9(5), 95.8(4)	93.4(4), 92.7(5), 93.13(9)
	Δ_d	0.595	0.566
		1.103[b]	
		1.400[c]	
	d_{hc1}	2.960(3)	2.946(3)
	d_{hc2}	3.169(4)	3.170(5)
		3.181(4)	3.179(5)
Sb	d_{ax}	2.032(9) × 2	2.100(10) × 2
	d_{eq}	1.966(12) × 2	2.003(10) × 2
		1.978(13) × 2	2.007(10) × 2
	Δ_d[d]	0.021	0.048
		0.050[b]	
		0.026(Te)[c]	

[a] d_{ax} (×2) and d_{eq} (×4) denote the local axial and equatorial Cu(1)−O and Sb(1)−O bond lengths in the octahedra. Θ_{ax} and Θ_{eq} (×2) indicate the local axial and equatorial O−Cu(1)−O bond angles in the octahedra. d_{hc1} and d_{hc2} (×2), and Θ_{hc1}, Θ_{hc2}, and Θ_{hc3} indicate the Cu(1)−Cu(1) bond distances and Cu(1)−O(1,2,3)-Cu(1) bond angles in the honeycomb layers, respectively. The mean square deviations from ideal octahedral symmetry (Δ_d, %) are also included. [b]And $Na_3Cu_2TeO_6$. [c]Ref 6, 7. [d]$\Delta_d = (1/6)\sum_{n=1,6}[(d_n - \langle d\rangle)/\langle d\rangle]^2 \times 100$; Δ_d's for $Na_3Cu_2SbO_6$.

Cu−O bond lengths are as expected (1.96−2.40 Å) and nearly equivalent at the two temperatures. The $Cu(II)O_6$ octahedra are distorted, again as expected, with a J-T distortion

dx.doi.org/10.1021/ic202066n | *Inorg. Chem.* 2012, 51, 557−565

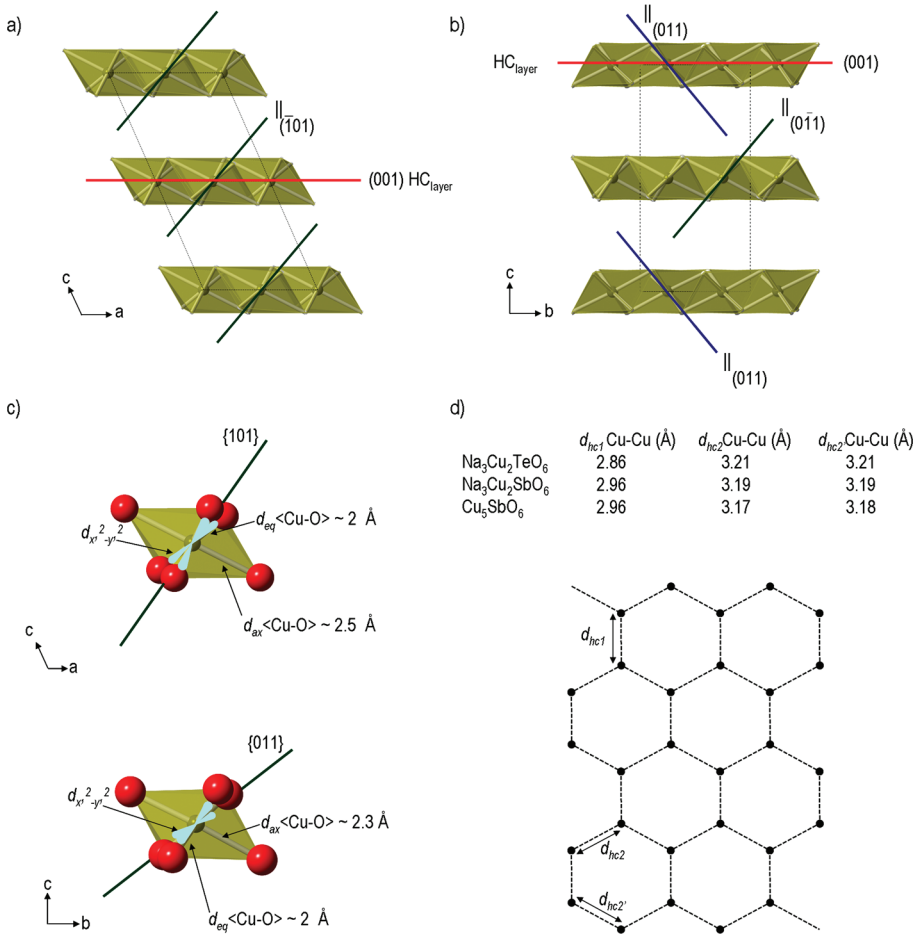

	d_{hc1} Cu-Cu (Å)	d_{hc2} Cu-Cu (Å)	d_{hc2} Cu-Cu (Å)
$Na_3Cu_2TeO_6$	2.86	3.21	3.21
$Na_3Cu_2SbO_6$	2.96	3.19	3.19
Cu_5SbO_6	2.96	3.17	3.18

Figure 8. Important structural characteristics of Cu_5SbO_6 compared to those in $Na_3Cu_2SbO_6$ and $Na_2Cu_2TeO_6$ (5,6). In panels a–c, the brown and blue solid lines denote the orientations of the Cu $d_{x^2-y^2}$ orbital planes in the J-T distorted octahedra. (a and b) The honeycomb planes, with the Cu–O octahedra fully rendered. Within the individual layers, all the Cu $d_{x^2-y^2}$ orbital planes are aligned. In $NaFeO_2$-derived $Na_2Cu_2TeO_6$ and $Na_3Cu_2SbO_6$, (a), the $d_{x^2-y^2}$ orbital planes are parallel in all the layers, while in Delafossite-derived Cu_5SbO_6, (b), the $d_{x^2-y^2}$ orbital planes in adjacent layers are approximately perpendicular. (c) The relative sizes, shapes, and orientations of the Cu(II)O_6 octahedra in $Na_3Cu_2(Te,Sb)O_6$ (upper) and Cu_5SbO_6 (lower). (d) Schematic comparison of the Cu^{2+} honeycomb lattices for the three compounds, with the Cu–Cu distances tabulated.

characterized by average $d_{z'^2}$ (z' indicates a local octahedron axis) and $d_{x'^2-y'^2}$ (x' and y' indicate local octahedron axes) bond lengths of ~2.34 and ~2.00 Å, respectively. The Sb(V)O_6 octahedra are also slightly distorted no doubt to accommodate the Cu^{2+}, with bond lengths varying from ~2.03 to ~1.98 Å. Employing the expression for the mean square deviation from ideal octahedral symmetry often employed to describe such distortions in perovskites,[30] we find mean square deviations of $\Delta_d \sim 0.6\%$ for the Cu(II)O_6 octahedra and $\Delta_d \sim 0.02\%$ for the Sb(V)O_6 octahedra. The deviations for the Cu(II) are much lower than is seen for the Cu(II) in the $NaFeO_2$-like honeycomb compounds $Na_3Cu_2SbO_6$ and $Na_2Cu_2TeO_6$, where they are 1.1% and 1.4%, respectively.

A comparison of several important aspects of the structures of $Na_2Cu_2TeO_6$, $Na_3Cu_2SbO_6$, and Cu_5SbO_6 is shown in Figure 8. Figures 8a ($Na_2Cu_2TeO_6$, $Na_3Cu_2SbO_6$) and 8b (Cu_5SbO_6) show only the honeycomb planes, with the Cu–O octahedra fully rendered. The solid lines mark the orientations of the Cu $d_{x^2-y^2}$ orbital planes in the J-T distorted octahedra within the layers. Within an individual layer in both structure types, all the Cu $d_{x^2-y^2}$ orbital planes and thus the J-T elongations are aligned. When considering adjacent layers, however, there is a major difference between $NaFeO_2$-derived $Na_2Cu_2TeO_6$ and $Na_3Cu_2SbO_6$ and Delafossite-derived Cu_5SbO_6: In the former case (8a) the $d_{x^2-y^2}$ orbital planes are all parallel, while in the later case (8b) they are approximately perpendicular. This may result in subtle differences in the magnetic coupling between layers in the two families of compounds. A comparison of the shapes of the Cu(II)O_6 octahedra in $Na_2Cu_2TeO_6$, $Na_3Cu_2SbO_6$, and Cu_5SbO_6 is also shown in Figure 8c. The J-T distortions are large and very similar in the $NaFeO_2$-derived phases, while in Delafossite-derived Cu_5SbO_6 the J-T distortion is considerably weaker.

For the purpose of understanding the magnetism of Cu_5SbO_6 and the $NaFeO_2$-derived Cu honeycomb phases, several interatomic distances involving the Cu ions are of interest. These distances are shown in the context of the honeycomb lattice in Figure 8d. In all three compounds, two pairs of the Cu in the six-membered rings are substantially closer to each other than would be present for a uniform ring. These are the Cu dimers that form the magnetic singlet state. These dimers repeat in a triangular lattice, but the relative orientations of the dimers do not result in a 3 or 3*m* in-plane symmetry; rather the in-plane symmetry is 2*mm*. The degree of the Cu–Cu dimerization can be easily seen in the difference in separations between the closest Cu's in the ring and the average Cu separation in the ring; the dimerization is larger in the $NaFeO_2$-derived honeycomb phases than in the honeycomb

dx.doi.org/10.1021/ic202066n | *Inorg. Chem.* 2012, 51, 557–565

Delafossite. In $Na_2Cu_2TeO_6$ this difference is $|2.8584 - (2.8584 + 2 \times 3.2136)/3| = 0.2368$ Å, in $Na_3Cu_2SbO_6$ it is $|2.9559 - (2.9559 + 2 \times 3.1993)/3| = 0.1623$ Å, and in Cu_5SbO_6 it is slightly lower, at $|2.9602 - (2.9602 + 3.1686 + 3.1805)/3| = 0.1429$ Å. Thus, while Cu_5SbO_6 has the weakest dimerization at ambient temperature of the three known honeycomb phases, the dimerization is still significant, as can be seen in the deviation from the ideal hexagonal symmetry $a_{mono}/(\sqrt{3}b_{mono}) = 0.921$. This excludes Cu_5SbO_6 as being a good example of an ideal spin $^1/_2$ honeycomb lattice, which is expected to display interesting quantum magnetism because of a resonating valence bond state.[31]

The weaker Cu−Cu dimerization in the honeycomb in Cu_5SbO_6 motivated us to determine the crystal structure of the phase to high precision well below the transition to the fully localized magnetic singlet state (see next section) to determine whether there is any subtle magnetostructural coupling present, that is, whether there is an increasing Peierls-like structural distortion on the honeycomb lattice when the singlet state is fully formed. The results of the low temperature refinement showed that the degree of dimerization changed from |0.1429| Å at room temperature to |0.1395| Å at 20 K. This difference is very small, approximately at the experimental precision, though it is in the expected direction if the dimer does become stronger on cooling through the singlet formation temperature. Thus, any magnetostructural changes that might accompany the development of the full singlet state in Cu_5SbO_6 are very weak, if present.

Magnetic Properties. The temperature dependent magnetic susceptibilities for the ordered and disordered variants of Cu_5SbO_6 between 300 and 2 K are shown in Figure 9. The data have been fitted with the expression for a dimer and a Curie−Weiss term for the impurity ions assumed to be "free" Cu^{2+} ions:

$$\chi = C1/T(3 + \exp(\delta/T)) + C2/(T - \theta) + C3 \quad (1)$$

Where χ is taken as $M/(\mu_0 H)$ at 0.5 T (M vs $\mu_0 H$ is linear in field up to the measurement field of 0.5 T at all temperatures), C1 is the Curie Constant for the bulk spins, δ is the value of the spin gap for excitations of the dimers from the singlet to paramagnetic state, C2 is the Curie Constant for the impurity spins, θ is their Curie−Weiss temperature, and C3 is a temperature independent term. C3 = 0 within error for all samples and was omitted from the final fits. Data are shown in Figure 9a for one sample of the disordered variant of Cu_5SbO_6, and for one sample of the ordered variant (the sample with approximately 20 wt % disordered variant as an "impurity" phase) in Figure 9b. The crystal structure analysis shows one Cu−Cu dimer per formula unit of Cu_5SbO_6 (i.e., $Cu^{1+}{}_3Cu^{2+}{}_2SbO_6$). The value of C1 then contains only one adjustable parameter, namely, the g-factor for Cu. C2 allows for the determination of the concentration of "free" Cu ions/formula unit, that is, those not locked into the singlet state through dimerization because of defects in the crystal structure (we assume $g = 2$ and $S = 1/2$ for the "free" Cu spins). The fits to the data yield, for the disordered variant: $\delta = 191$ K and $g = 2.05$ for the bulk spins, and 2.2% "free" Cu ions with $\theta = -6.6$ K. For the ordered variant, we find $\delta = 186$ K and $g = 2.09$ for the bulk spins, and 2.9% free Cu ions, with $\theta = -0.8$ K. The data are well described by the simple dimer model as shown in Figure 8; the origin of the relatively high θ for the impurity spins in the disordered variant is not currently known. The similar percentages of "free spins" for both variants

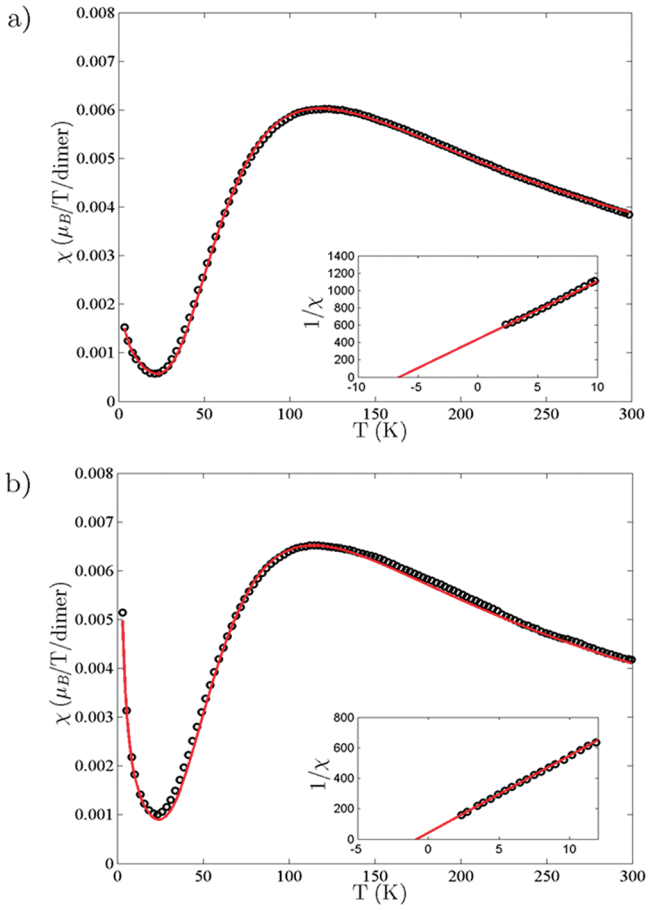

Figure 9. Magnetic susceptibilities measured by VSM at a field of 0.5 T in the temperature range between 2 and 300 K. Open circles are experimental data, the lines are fits using $\chi = C1/T(3 + \exp(\delta/T)) + C2/(T - \theta) + C3$, the dimer susceptibility plus a low temperature Curie−Weiss susceptibility for "free" impurity ions, assumed to be Cu^{2+}. C1 is the Curie Constant for the bulk spins from which we derive g, δ is the value of the spin gap, C2 is the Curie Constant for the impurity spins, and θ is their Curie−Weiss temperature. C3 = 0 within error for all samples. For the disordered variant: $\delta = 191$ K and $g = 2.05$ for the bulk spins, and there are 2.2% "free" Cu ions with $\theta = -6.6$ K. For the ordered variant: $\delta = 186$ K and $g = 2.09$ for the bulk spins, and there are 2.9% free Cu ions, with $\theta = -0.8$ K. The fits for the disordered and ordered samples are shown in panels (a) and (b), respectively. The insets show the inverse susceptibility at low temperatures verifying the Curie−Weiss behavior of the impurity spins.

indicate that the stacking faults do not affect the perfection of the Cu/Sb ordering in the honeycomb layers. The g values obtained are within two standard deviations of that determined from the EPR measurements, where $g = 2.18$ for both variants of the phase.

The temperature dependence of the specific heats for Cu_5SbO_6 and the nonmagnetic analogue Cu_3ZnSbO_6 are shown in Figure 10. Comparison of the data shows the presence of excess specific heat in Cu_5SbO_6 arising from the magnetic entropy released because of the localization of the Cu spins in the Cu−Cu dimers in the temperature range around 100 K. Subtraction of the specific heat for Cu_3ZnSbO_6 from that observed for Cu_5SbO_6 and then integrating in the usual fashion to obtain the magnetic entropy released as a function of temperature yields the plot shown in the inset to Figure 10. The data shows the release of entropy in

dx.doi.org/10.1021/ic202066n | Inorg. Chem. 2012, 51, 557−565

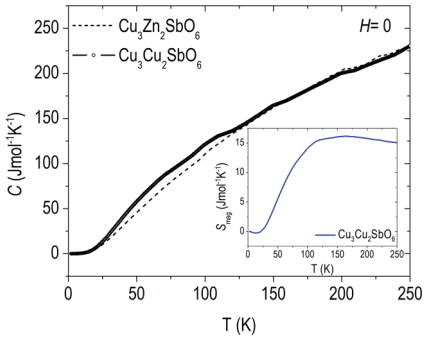

Figure 10. Main panel, the temperature dependent specific heats for the ordered variant of Cu_5SbO_6 and for the nonmagnetic analogue $Cu_3Zn_2SbO_6$. Comparison of the data show the presence of specific heat in excess of that due to phonons for Cu_5SbO_6. The excess specific heat is released in the temperature range of 25−125 K. The inset shows the integrated entropy released, obtained from $\Delta S = \int [C_p(Cu_5SbO_6) - C_p(Cu_3Zn_2SbO_6)]/T \, dT$.

the expected fashion in the temperature range expected from the magnetic susceptibility. The total entropy released, about 15 J/(mol K), is larger than that expected for 2 Cu per formula unit each releasing R ln 2 J/K, which would be about 11.5 J/(mol K). This suggests that there may be entropy in excess of that due to magnetism alone released in the formation of the singlet state in Cu_5SbO_6, a possible indication of subtle structural or vibrational changes accompanying the formation of the singlet state.

4. CONCLUSIONS

Cu_5SbO_6 is found to display a Delafossite-derived crystal structure with the 2:1 ordering of Cu^{2+} and Sb^{5+} in edge sharing octahedra in the triangular metal planes resulting in a magnetic Cu^{2+} honeycomb geometry. Strong Jahn−Teller distortions of the Cu(II)O_6 octahedra are present, resulting in the monoclinic overall symmetry, and the formation of Cu^{2+}−Cu^{2+} dimers. The dimers form in a dimensionally triangular lattice, but their relative orientations make the in-plane lattice rectangular rather than triangular. The structural dimers lead to the observation of the classic temperature dependent magnetic susceptibility for a dimerized system in which the ground state is a spin singlet. Thus, the susceptibility data for temperatures up to 300 K can be modeled in detail by considering only a single antiferromagnetic interaction forming the singlet−triplet state with an energy gap of about 189 K. Further studies of the magnetic properties are of interest. The very similar nature of the magnetic susceptibilities for the ordered and disordered stacking variants of the phase indicates that the magnetism is highly dominated by the magnetism due to the dimers and that any influence of interplanar coupling must be very small. Comparison to the previously known $NaFeO_2$-derived Cu^{2+} honeycomb compounds $Na_2Cu_2TeO_6$ and $Na_3Cu_2SbO_6$ reveals significant structural differences, but these differences do not appear to be significant enough to change the basic magnetic properties. A hint of magnetostructural coupling resulting from the low temperature singlet formation is found in the comparison of the low and high temperature structures of Cu_5SbO_6, but it is comparable to the precision of the measurements; this possibility is also suggested in the analysis of the entropy released during the singlet formation. Continuing search for compounds displaying Cu^{2+} honeycomb lattices, and the possibility that they might display predicted resonating valence bond physics,[31] should be of significant future interest.

AUTHOR INFORMATION

Corresponding Author

*E-mail: ecliment@princeton.edu.

ACKNOWLEDGMENTS

The work at Princeton was supported by the Department of Energy, Division of basic Energy Sciences, Grant DE-FG02-08ER46544. Use of the National Synchrotron Light Source, Brookhaven National Laboratory, was supported by the U.S. Department of Energy, Office of Science, Office of Basic Energy Sciences, under Contract No. DE-AC02-98CH10886. R.J.C. gratefully acknowledges the support for his work at Risø DTU by the Velux Visiting Professor Program 2009-2010. We also thank Dr. Carlos Pacheco (Department of Chemistry, Princeton University) for his assistance in performing the EPR measurements.

REFERENCES

(1) Lacroix, C.; Mendels, P.; Mila, F. *Introduction to Frustrated Magnetism: Materials, Experiments and Theory*; Springer-Verlag: Berlin, Germany, 2011.
(2) Yamashita, S.; Moriura, T.; Nakazawa, Y.; Yoshida, H.; Okamoto, Y.; Hiroi, Z. *J. Phys. Soc. Jpn.* **2010**, *79*, 083710.
(3) Helton, J. S.; Matan, K.; Shores, M. P.; Nytko, E. A.; Bartlett, B. M.; Yoshida, Y.; Takano, Y.; Suslov, A.; Qiu, Y.; Chung, J.-H.; Nocera, D. G.; Lee, Y. S. *Phys. Rev. Lett.* **2007**, *98*, 107204.
(4) Regnault, L. P.; Rossat-Mignod, J. *Magnetic Properties of Layered Transition Metal Compounds*; Kluwer Academic Pub: Dortrecht, The Netherlands, 1989.
(5) Smirnova, O.; Azuma, M.; Kumada, N.; Kusano, Y.; Matsuda, M.; Shimakawa, Y.; Takei, T.; Yonesaki, Y.; Kinomura, N. *J. Am. Chem. Soc.* **2009**, *131*, 8313.
(6) Xu, J.; Assoud, A.; Soheilnia, N.; Derakhshan, S.; Cuthbert, H. L.; Greedan, J. E.; Whangbo, M. H.; Kleinke, H. *Inorg. Chem.* **2005**, *44*, 5042.
(7) Smirnova, O. A.; Nalbandyan, V. B.; Petrenko, A. A.; Avdeev, M. *J. Solid State Chem.* **2005**, *178*, 1165.
(8) Kol'tsova, T. N.; Chastukhin, A. E. *Inorg. Mater.* **2002**, *38*, 1228.
(9) Shimada, S.; Mackenzie, K. J. D. *Thermochim. Acta.* **1982**, *56*, 73.
(10) Shimada, S.; Mackenzie, K. J. D.; Kodaira, K.; Matsushita, T.; Ishii, T. *Thermochim. Acta* **1988**, *73*, 133.
(11) Stan, M.; Mihaiu, S.; Crisan, D.; Zaharescu, M. *Eur. J. Solid State Inorg. Chem.* **1998**, *35*, 243.
(12) Nagarajan, R.; Uma, S.; Jayaraj, M. K.; Tate, J.; Sleight, A. W. *Solid State Sci.* **2002**, *4*, 787.
(13) Hosogi, Y.; Kato, H.; Kudo, A. *J. Mater. Chem.* **2008**, *18*, 647.
(14) Politaev, V. V.; Nalbandyan, V. B.; Petrenko, A. A.; Shukaev, I. L.; Volotchaev, V. A.; Medvedev, B. S. *J. Solid State Chem.* **2010**, *183*, 684.
(15) O'Malley, M. J.; Verweij, H.; Woodward, P. M. *J. Solid State Chem.* **2008**, *181*, 1803.
(16) Kobayashi, H.; Kanno, R.; Kawamato, Y.; Tabuchi, M.; Nakamura, O.; Takano, M. *Solid State Ionics* **1995**, *82*, 25.
(17) Kimber, S. A. J.; Ling, C. D.; Morris, D. J. P.; Chemseddine, A.; Henry, P. F.; Argyriou, D. N. *J. Mater. Chem.* **2010**, *20*, 8021.
(18) Ingram, B. J.; González, G. B.; Mason, T. O.; Shahriari, D. Y.; Barnabe, A.; Ko, D.; Poeppelmeier, K. R. *Chem. Mater.* **2004**, *16*, 5616.
(19) Isawa, K.; Yaegashi, Y.; Komatsu, M.; Nagano, M.; Sudo, S.; Karppinen, M.; Yamauchi, H. *Phys. Rev. B* **1997**, *56*, 3457.
(20) Louër, D.; Louër, M. *J. Appl. Crystallogr.* **1972**, *5*, 271.
(21) Boultif, A.; Louër, D. *J. Appl. Crystallogr.* **2004**, *37*, 724.
(22) Favre-Nicolin, V.; Černý, R. *J. Appl. Crystallogr.* **2002**, *35*, 734.
(23) Rodríguez-Carvajal, J.; Roisnel, T. *FullProf, WinPLOTR*, and accompanying programs; 2008; http://www.ill.eu/sites/fullprof/index.html (accessed January 2011).
(24) Treacy, M. M. J.; Newsam, M. J.; Deem, M. W. *Proc. R. Soc. A* **1991**, *433*, 499.

(25) Le Bail, A.; Duroy, H.; Fourquet, J. L. *Mater. Res. Bull.* **1988**, *23*, 447.
(26) Popa, N. C. *J. Appl. Crystallogr.* **1998**, *31*, 176.
(27) Popa, N. C.; Balzar, D. *J. Appl. Crystallogr.* **2008**, *41*, 615.
(28) Casas-Cabanas, M.; Palacín, M. R.; Rodríguez-Carvajal, J. *Powder Diffr.* **2005**, *20*, 334.
(29) Taylor, J. C.; Rui, Z. *Powder Diffr.* **1992**, *7*, 152.
(30) Alonso, J. A.; Martinez-Lope, M. J.; Casais, M. T.; Fernandez-Diaz, M. T. *Inorg. Chem.* **2000**, *39*, 922.
(31) Banerjee, A.; Damle, K.; Paramekanti, A. arXiv:1012.4546v2, 2010.

Muon spin rotation study of magnetism and superconductivity in $Ba(Fe_{1-x}Co_x)_2As_2$ single crystals

C. Bernhard,[1] C. N. Wang,[1] L. Nuccio,[1,2] L. Schulz,[1,*] O. Zaharko,[3,4] J. Larsen,[3,4] C. Aristizabal,[2] M. Willis,[2] A. J. Drew,[2] G. D. Varma,[5] T. Wolf,[6] and Ch. Niedermayer[3]

[1]*University of Fribourg, Department of Physics and Fribourg Centre for Nanomaterials, Chemin du Musée 3, CH-1700 Fribourg, Switzerland*

[2]*Queen Mary University of London, School of Physics and Astronomy, Mile End Road, London E1 4NS, United Kingdom*

[3]*Laboratory for Neutron Scattering, Paul Scherrer Institut, CH-5232 Villigen, Switzerland*

[4]*Department of Physics, Technical University of Denmark, 2800 Lyngby, Denmark*

[5]*Department of Physics, Indian Institute of Technology Roorkee, Roorkee 247667, India*

[6]*Karlsruher Institut für Technologie, Institut für Festkörperphysik, D-76021 Karlsruhe, Germany*

(Received 1 July 2012; revised manuscript received 12 October 2012; published 14 November 2012)

Using muon spin rotation (μSR) we investigated the magnetic and superconducting properties of a series of $Ba(Fe_{1-x}Co_x)_2As_2$ single crystals with $0 \leqslant x \leqslant 0.15$. Our study details how the antiferromagnetic order is suppressed upon Co substitution and how it coexists with superconductivity. In the nonsuperconducting samples at $0 < x < 0.04$ the antiferromagnetic order parameter is only moderately suppressed. With the onset of superconductivity this suppression becomes faster and it is most rapid between $x = 0.045$ and 0.05. As was previously demonstrated by μSR at $x = 0.055$ [P. Marsik *et al.*, Phys. Rev. Lett. **105**, 57001 (2010)], the strongly weakened antiferromagnetic order is still a bulk phenomenon that competes with superconductivity. The comparison with neutron diffraction data suggests that the antiferromagnetic order remains commensurate whereas the amplitude exhibits a spatial variation that is likely caused by the randomly distributed Co atoms. A different kind of magnetic order that was also previously identified [C. Bernhard *et al.*, New J. Phys. **11**, 055050 (2009)] occurs at $0.055 < x < 0.075$ where T_c approaches the maximum value. The magnetic order develops here only in parts of the sample volume and it seems to cooperate with superconductivity since its onset temperature coincides with T_c. Even in the strongly overdoped regime at $x = 0.11$, where the static magnetic order has disappeared, we find that the low-energy spin fluctuations are anomalously enhanced below T_c. These findings point toward a drastic change in the relationship between the magnetic and superconducting orders from a competitive one in the strongly underdoped regime to a constructive one in near-optimally and overdoped samples.

DOI: 10.1103/PhysRevB.86.184509 PACS number(s): 76.75.+i, 74.25.Ha, 74.70.Xa

I. INTRODUCTION

The discovery of high-temperature superconductivity in the iron arsenides in 2008 (Ref. 1) with T_c values as high as 55 K in $ReFeAsO_{1-x}F_x$ (Re = Sm, Nd, and Gd)[2,3] has prompted intense experimental and theoretical efforts to explore their electronic properties. It turned out that similar to the cuprates, superconductivity emerges here in close proximity to an antiferromagnetic (AF) state. In the most commonly investigated system $(Ba,Sr)Fe_2As_2$, for which large single crystals are readily available, superconductivity can be likewise introduced by electron doping as in $(Ba,Sr)(Fe_{1-x}Co_x)_2As_2$,[4] by hole doping as in $(Ba,Sr)_{1-x}K_xFe_2As_2$,[5,6] with external pressure,[7,8] or with internal chemical pressure as in $(Ba,Sr)(Fe_{1-x}Ru_x)_2As_2$.[9] It is commonly observed that the long-range AF order of the undoped parent compound $(Ba,Sr)Fe_2As_2$ becomes suppressed and superconductivity emerges even before the magnetic order has entirely disappeared.[10] The critical temperature of the superconducting state rises at first in the so-called underdoped regime where it coexists with a strongly weakened AF order. The highest critical temperature is obtained close to the critical point where the static magnetic order vanishes. Upon further doping or pressure, T_c decreases again and finally disappears in the so-called overdoped regime. Since T_c is maximal right at the point where static magnetism disappears and presumably low-energy magnetic spin fluctuations are most pronounced, it is widely believed that the AF spin fluctuations are playing an important role in the superconducting pairing mechanism.

Nevertheless, it is still debated whether the coexistence of AF order and superconductivity in the underdoped regime occurs in all iron arsenide superconductors. A true coexistence and competition between short-ranged but bulk AF order and superconductivity has been established in underdoped samples of Sm-1111[11,12] and especially in single crystals of $Ba(Fe_{1-x}Co_x)_2As_2$.[13–16] Such a coexistence was not observed in La-1111.[17] Moreover, in $Ba_{1-x}K_xFe_2As_2$ (Refs. 18 and 19) and in $SmFe_{1-x}Ru_xAsO_{0.85}F_{0.15}$ (Ref. 20) and $Ba(Fe_{1-x}Ru_x)_2As_2$ (Ref. 21), it was reported to involve a macroscopically phase-segregated state. Albeit, for $Ba_{1-x}K_xFe_2As_2$ a recent study established that the macroscopic phase segregation does not occur in high-quality samples where the AF and superconducting orders truly coexist on the nanometer scale.[22] This suggests that the macroscopic phase segregation previously reported for $Ba_{1-x}K_xFe_2As_2$ single crystals[18,19] is of chemical origin, likely due to a variation in the K content.[23]

Even for the $Ba(Fe_{1-x}Co_x)_2As_2$ system, which is rather well investigated thanks to the availability of sizable and fairly homogeneous single crystals, it remains to be investigated in detail how exactly the magnetic order evolves and disappears around optimum doping.

Here we present such a detailed muon spin rotation (μSR) study of the dependence of the magnetic properties on Co doping in a series of $Ba(Fe_{1-x}Co_x)_2As_2$ single crystals with $0 \leqslant x \leqslant 0.15$. We show that the magnetic order parameter is anomalously suppressed as superconductivity emerges in the underdoped regime. We also detail how the static magnetic

correlations disappear around optimum doping, and present evidence that slow spin fluctuations persist in the overdoped regime. Notably, we find that a competition between the static AF order and superconductivity occurs only in the underdoped regime, whereas near-optimum doping and even in the overdoped regime there are signatures of a cooperative relationship between inhomogeneous static or slowly fluctuating magnetic correlations and superconductivity. We remark that our results confirm previous μSR work which already reported the coexistence and competition of bulk magnetic and superconducting orders for the underdoped sample at $x = 0.055$ (Ref. 15) as well as the development of an inhomogeneous magnetic state right below T_c in a near-optimally doped sample.[24]

II. MATERIALS AND METHODS

The $Ba(Fe_{1-x}Co_x)_2As_2$ single crystals were grown from self-flux in glassy carbon crucibles. As described in Refs. 25 and 26, their Co content was determined by energy dispersive x-ray spectroscopy with an accuracy of about 0.005. The superconducting transition temperature, T_c, as shown in Fig. 1 was determined from resistivity and dc magnetization measurements that were performed using a physical property measurement system (PPMS) from Quantum Design (Model QD6000). The antiferromagnetic transition temperature, T_N, was deduced from the μSR experiments (as shown below). The obtained phase diagram of T_c and T_N as shown in Fig. 1 agrees reasonably well with previous reports.[27–31] The $x = 0.055$ sample has been already previously investigated with μSR and infrared spectroscopy.[15] Infrared measurements have also been performed at $x = 0.065$.[32] Specific heat measurements on crystals from the same or similar growth batches are reported in Ref. 26. These measurements suggest a bulk superconducting state of the samples in the Co doping range of $0.035 \leqslant x \leqslant 0.13$ with a maximum transition temperature $T_{c,\,max} = 24.5$ K at $x = 0.065$.

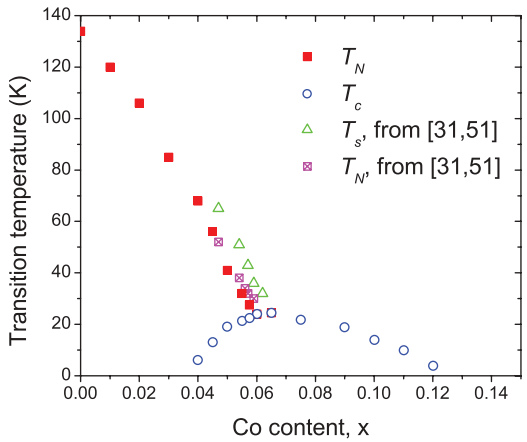

FIG. 1. (Color online) Phase diagram of the magnetic transition temperature, T_N, as determined with μSR and the superconducting critical temperature, T_c, obtained from resistivity and magnetic susceptibility measurements as well as from the specific heat data of Ref. 26. Shown for comparison are the magnetic and structural transition temperatures of Refs. 31 and 51.

The μSR measurements have been performed on large single crystals or on mosaics of several smaller pieces with freshly cleaved surfaces. The zero-field (ZF), longitudinal-field (LF), and transverse-field (TF) measurements have been conducted with the general purpose spectrometer (GPS) setup at the πM3 beamline of the Swiss Muon Source (SμS) at the Paul Scherrer Institut (PSI) in Villigen, Switzerland.

The μSR technique measures the time-resolved spin polarization of an ensemble of muons that reside on interstitial lattice sites of the studied material. A beam of fully spin-polarized so-called surface muons is produced at a proton accelerator and implanted with an average energy of about 4.2 MeV in the sample where it thermalizes rapidly without a significant loss in spin polarization. In the iron arsenides the muons have been shown to stop at well-defined interstitial lattice sites close to an As ion.[33] The average muon implantation depth (and thus the spread of the muon stopping sites) is about 100–200 μm; the magnetic and superconducting properties probed by the muon ensemble are therefore representative of the bulk.

The muon spin polarization is recorded via the detection of the asymmetry of the emission of the positrons that arise from the radioactive decay of the muons. The obtained μSR spectra cover a time window of about 10^{-6}–10^{-9} s. With the gyromagnetic ratio of the positive muons of $\gamma_\mu = 2\pi \times 135.5\ \mathrm{MHz\,T^{-1}}$, this means that internal magnetic fields between 0.1 G and several teslas are detectable. The muon spins are precessing in the local magnetic field, B_μ, with a frequency of $\nu_\mu = \gamma_\mu B_\mu / 2\pi$. The positive muons decay within an average lifetime of $\tau_\mu \approx 2.2\,\mu$s into two neutrinos and a positron. The latter is preferentially emitted along the direction of the muon spin at the instant of decay. By tracing the time dependence of the spatial asymmetry of the positron emission rate, the time-resolved spin polarization $P(t)$ of the muon ensemble is thus obtained. The initial asymmetry is 27%–28% for the measurements performed in ZF geometry and 21%–22% for the ones performed in TF geometry (since the spin rotator at the GPS beamline rotates the muon spin only by 56°). The indicated, small differences in the initial asymmetry arise from a variation in the size and mounting of the samples as well as from the so-called veto counter that was used for the smaller samples. More details regarding the μSR technique can be found in Refs. 34–36.

The μSR technique yields the magnetic-field distribution on a microscopic scale and is therefore very well suited for the investigation of the magnetic and superconducting properties of new materials. In particular, it enables a reliable determination of the volume fractions of the magnetic and superconducting phases and it can also be used to determine the temperature and doping dependence of the magnetic and superconducting order parameters. It has previously been very successfully applied to study the coexistence of magnetism and superconductivity in a variety of unconventional superconductors such as the underdoped cuprates,[37–40] the ruthenate cuprates,[41] the triplet superconductor Sr_2RuO_4 (Ref. 42), or more recently the iron arsenides[11,12,15,17,19,20,43–47] and iron selenides.[48–50]

The neutron diffraction experiments were performed at the thermal four-circle single-crystal diffractometer TRICS at the spallation neutron source SINQ at PSI. A pyrolytic

graphite (PG-002) monochromator was used with neutron wavelength $\lambda = 2.4$ Å. The crystal was mounted in a closed-cycle refrigerator and the intensities of 15 accessible magnetic Bragg peaks were measured.

Additional neutron diffraction experiments were performed at the cold neutron triple-axis spectrometer RITA-II to measure selected magnetic Bragg peaks with a higher accuracy and better resolution. A wavelength $\lambda = 4.04$ Å from a PG-002 monochromator was used and the crystal was mounted in a helium cryostat in two different orientations allowing for scans in reciprocal space along the **a** (longitudinal) and **b** (transverse) directions through the magnetic Bragg peak at $\mathbf{Q}_{\mathrm{AFM}} = (1,0,3)$ in orthorhombic notation. The scan directions are explained in detail in Ref. 51.

III. RESULTS AND DISCUSSION

A. Magnetism in nonsuperconducting samples at $0 \leqslant x \leqslant 0.03$

Figure 2 shows representative low-temperature ZF-μSR spectra of the $Ba(Fe_{1-x}Co_x)_2As_2$ crystals that give an overview of how the AF order evolves as a function of the Co substitution. In the undoped parent compound, at $x = 0$, it has been established by magnetic neutron diffraction that a long-range AF order with an Fe moment of about 0.9–1 μ_B develops below $T_N = 134$ K.[13,52–55] The corresponding ZF-μSR spectrum in Fig. 2(a) is also characteristic of a bulk, long-range ordered AF state. Its oscillatory signal has a large amplitude and a small relaxation rate similar to that in previous μSR experiments.[22,56,57] The fit shown by the solid line has been obtained with the function

$$P(t) = P(0)\left[\sum_{i=1}^{2} A_i \cdot \cos(\gamma_\mu B_{\mu,i}\, t + \varphi) \cdot \exp(-\lambda_i t) + A_3 \cdot \exp(-\lambda_3 t)\right], \quad (1)$$

where P, A_i, $B_{\mu,i}$, φ, λ_i are the polarization of the muon spin ensemble, the relative amplitudes of the different signals, the local magnetic field at the muon sites, the initial phase of the muon spin, and the exponential relaxation rates, respectively. The first two terms yield oscillation frequencies of about 28.4 and 7 MHz. It was previously shown for the 1111 system that these two precession frequencies arise from different interstitial muon sites that are located within or between the FeAs layer, respectively.[33] By analogy we assume that two similar muon sites exist for the $Ba(Fe_{1-x}Co_x)_2As_2$ system. The nonoscillatory and slowly relaxing signal described by the third term arises due to the nonorthogonal orientation of the muon spin polarization, **P**, and the local magnetic field $\mathbf{B}_\mu$. In polycrystalline samples with randomly oriented grains (and thus randomly oriented $\mathbf{B}_\mu$) this yields a so-called "one-third tail" with $A_3 = 1/3$. For single crystals A_3 varies between zero and unity as the orientation between $\mathbf{B}_\mu$ and **P** changes from parallel to perpendicular. At $x = 0$ we obtain $A_3 \approx 0.3$ which suggests that the angle between $\mathbf{B}_\mu$ and **P** is about 70°. This value does not change much upon Co substitution at $0 \leqslant x \leqslant 0.055$ where the samples maintain a bulk magnetic state at low temperature that is established from TF-μSR experiments as shown below (in Fig. 8) and for the same $x = 0.055$ sample in Ref. 15.

Figures 2(b) and 2(c) show that the ZF-μSR spectra for the nonsuperconducting samples at $x = 0.02$ and 0.03 are only moderately affected by the Co substitution. The highest precession frequency, which is well resolved and measures the magnitude of the AF order parameter, decreases only by about 10% from 28.4 MHz at $x = 0$ (where neutron diffraction yields a magnetic moment of $0.9-1\,\mu_B$)[13,52–55] to 24.8 MHz at $x = 0.03$. The Co doping still gives rise to a sizable increase of the relaxation rate from 3.3 μs^{-1} at $x = 0$ to about 25 μs^{-1} at $x = 0.03$ which indicates a significant broadening of the distribution of the local magnetic fields. These trends are shown in Fig. 3 which displays the doping dependence of the normalized value of the

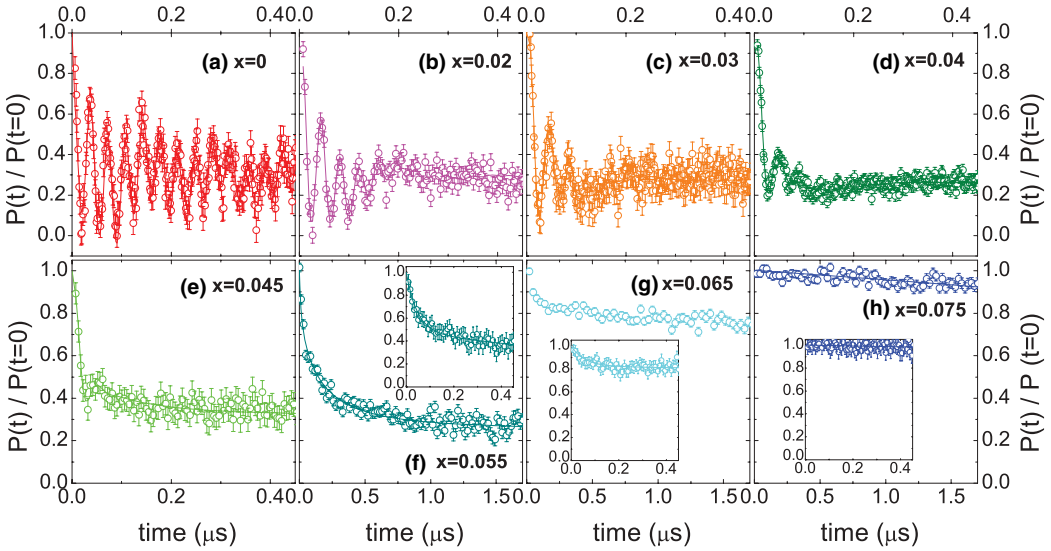

FIG. 2. (Color online) Low-temperate ZF-μSR spectra of $Ba(Fe_{1-x}Co_x)_2As_2$ single crystals with $0 \leqslant x \leqslant 0.075$ showing how the magnetic order is suppressed by the Co substitution. Insets in (f)–(h) show the spectra at early times as in (a)–(e).

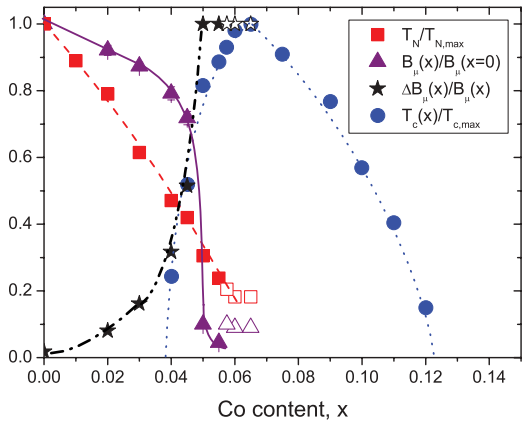

FIG. 3. (Color online) Phase diagram showing the Co dependence of the normalized magnetic and superconducting transition temperatures, T_N and T_c, and the normalized values of the average magnetic field at the muon site, B_μ and of its relative spread, ΔB_μ. The open symbols show the magnetic properties in the spatially inhomogeneous magnetic state near optimum doping. For samples $0 \leqslant x \leqslant 0.045$ with an oscillatory signal in the ZF-μSR time spectra B_μ and ΔB_μ have been obtained by fitting with the function in Eq. (1). For samples $0.05 \leqslant x \leqslant 0.065$ where the oscillatory signal is completely overdamped (see Fig. 2) only exponential relaxation functions were used and B_μ was estimated from the relaxation rate according to $\lambda^{ZF} = \gamma B_\mu$. The latter estimate agrees with the one obtained from the TF-μSR data as shown in Fig. 4(b) for $x = 0.05$.

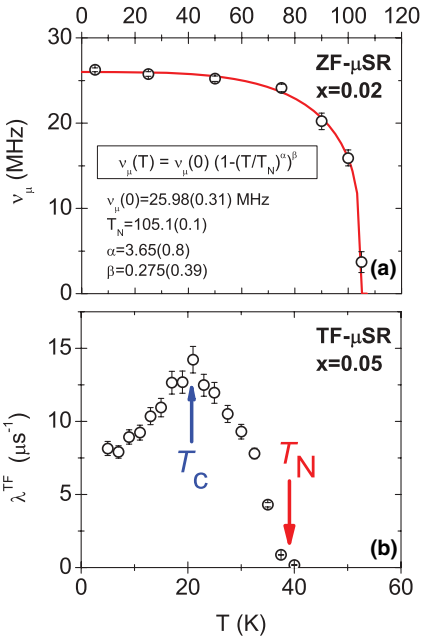

FIG. 4. (Color online) (a) T dependence of the highest ZF-μSR precession frequency, ν_μ, at $x = 0.02$. The fit (solid line) shows the determination of the low-temperature value of the local magnetic field, $B_\mu(T = 0) = 2\pi/\gamma\,\nu_\mu(T = 0)$ with $\gamma = 851.4$ MHz T^{-1}, and the AF transition temperature, T_N. (b) T dependence of the transverse-field ($H^{ext} = 3$ kOe) relaxation rate, λ^{TF}, at $x = 0.05$. The sharp increase of λ^{TF} marks T_N. The decrease of λ^{TF} below T_c arises due to the competition between the magnetic and superconducting orders. From the value of $\lambda^{TF}(T_c)$ and the relationship $\lambda^{TF} = \gamma/\sqrt{2}B_\mu$ we obtained an independent estimate of B_μ that agrees with the one obtained from the ZF-μSR data as shown in Fig. 3.

internal magnetic field, $B_\mu(x)/B_\mu(x = 0)$, and of its relative spread, $\Delta B_\mu(x)/B_\mu(x)$. Figure 4(a) shows an example of the $x = 0.02$ sample how the values of T_N and B_μ have been deduced from the T dependent ZF-μSR data.

B. Coexistence of bulk magnetism and superconductivity in underdoped samples at $0.04 \leqslant x \leqslant 0.055$

The ZF spectra in Figs. 2(d)–2(f) and the evolution of $B_\mu(x)$ and $\Delta B_\mu(x)$ in Fig. 3 highlight that the suppression of the AF order parameter and its spatial variation start to evolve much more rapidly as soon as superconductivity emerges at $x \geqslant 0.04$. The sample at $x = 0.04$ with $T_c = 6$ K is a borderline case where our μSR data do not provide solid proof that superconductivity is a bulk phenomenon. Nevertheless, already at $x = 0.045$ our μSR data provide firm evidence for a bulk superconducting state. Figure 5(a) shows a so-called TF-μSR pinning experiment which confirms that a strongly pinned superconducting vortex lattice develops in the entire sample's volume. The sample was initially cooled in an external field of $H^{ext} = 500$ Oe to $T = 1.6$ K $\ll T_c = 13$ K. The first TF-μSR measurement was then performed under regular field-cooled conditions at $T = 1.6$ K. The so-called μSR line shape, as obtained from a fast-Fourier transformation of the TF-μSR time spectrum, is shown by the solid symbols. It details the distribution of the local magnetic field that is probed by the muon ensemble. This line shape consists of a very narrow peak due to about 2%–3% of background muons that stop outside the sample, in the sample holder, or the cryostat walls and windows. The muons stopping inside the sample give rise to the very broad main peak whose unusually large width is caused by the static magnetic order which persists throughout the entire sample volume. The broadening due to the superconducting vortex lattice is in comparison much smaller and completely overwhelmed by the magnetic contribution. The magnetic order is documented by the ZF-μSR spectrum in Fig. 5(b) which reveals a strongly damped, oscillatory signal with an average frequency of 20.4 MHz. Before the second TF-μSR measurement (open symbols) the external magnetic field was increased by 250 Oe to $H^{ext} = 750$ Oe while the temperature was kept at 1.6 K $\ll T_c$. It is evident from Fig. 5(a) that only the narrow peak due to the background muons follows the change of H^{ext} whereas the broad peak due to the muon inside the sample remains almost unchanged. This observation, that the magnetic flux density inside the sample remains unchanged, is the hallmark of a bulk type-II superconductor with a strongly pinned vortex lattice. Notably, this bulk superconducting vortex state coexists with an antiferromagnetic order that is also a bulk phenomenon. The combined ZF-μSR and TF-μSR data thus provide unambiguous evidence that the superconducting and magnetic orders coexist on a nanometer scale. A corresponding pinning effect due to a superconducting vortex lattice that exists in the presence of a bulk magnetic order has also been observed at $x = 0.05$ (not shown) and it was previously demonstrated for a crystal at $x = 0.055$.[15]

Clear signatures of the competition between the magnetic and superconducting orders have already been reported from neutron diffraction[13,14] and later from TF-μSR

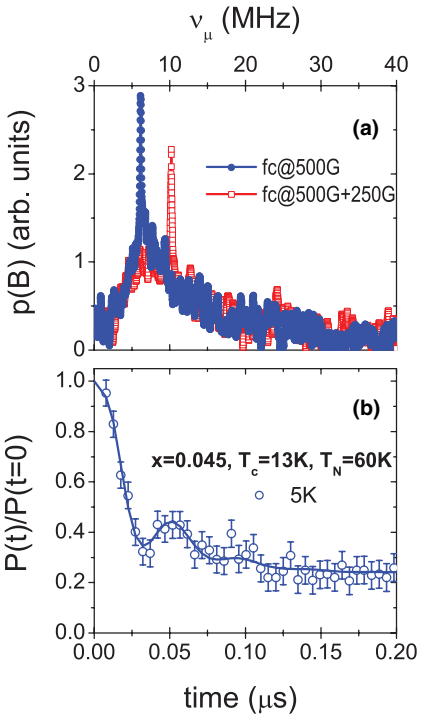

FIG. 5. (Color online) (a) TF-μSR line shapes at $x = 0.045$ obtained during a so-called "pinning experiment" showing the presence of a strongly pinned, bulk superconducting vortex lattice. The sample was initially cooled to $T = 1.6\,\mathrm{K} \ll T_c = 13\,\mathrm{K}$ in a transverse field of $H^{\mathrm{ext}} = 500$ Oe. The first TF-μSR line shape (blue symbols) was measured under standard field-cooled conditions. Before the second TF-μSR line-shape measurement (red symbols), the field was increased to 750 Oe at 1.6 K. The pinning of a bulk vortex lattice is evident since only the narrow peak, due to the background muons stopping outside the sample, follows the change of H^{ext}, whereas the broader part of the μSR line shape, due to the muons that stop inside the sample, remains almost unchanged. (b) Corresponding ZF-μSR spectrum at 5 K showing a large oscillatory signal that is characteristic of a bulk magnetic order.

measurements.[15] The combined neutron and μSR data revealed that the magnitude of the magnetic order parameter is anomalously suppressed below T_c while the volume fraction of the magnetic phase remains close to 100%.[15] In Fig. 6 we compare a set of magnetic neutron diffraction and μSR data that have been obtained on the very same single crystal with $x = 0.05$. Transverse and longitudinal scans through the magnetic Bragg peak at $\mathbf{Q}_{\mathrm{AFM}} = (1,0,3)$ in orthorhombic notation are shown in Figs. 6(a) and 6(b), respectively. Single, resolution-limited peaks are observed in both scan directions, indicating commensurate antiferromagnetic order with a correlation length in excess of 300 Å. The diffraction data obtained at $T = 5$ K are consistent with a stripe-type C-antiferromagnetic structure with an ordered Co moment of $\sim 0.1\,\mu_B$ per Fe ion. The moment is thus reduced by about a factor of 10 from the value in the parent compound $BaFe_2As_2$.[55] This agrees well with the value deduced from the μSR relaxation rate as shown in Fig. 3. Figure 6(c) compares the T dependence of the peak intensity (solid symbols) with the one of the TF-μSR relaxation rate λ^{TF} (open symbols). The neutron and μSR data consistently reveal the onset of the static magnetic order below $T_N \approx 40$ K. They both also exhibit a pronounced anomaly around $T_c \approx 19$ K which signifies the superconductivity-induced suppression of the magnetic order parameter.

The direct comparison of the neutron diffraction and μSR data also yields important information with respect to the magnetic order. The observation of well-defined, resolution-limited Bragg peaks in magnetic neutron diffraction, as shown in Figs. 6(a) and 6(b), demonstrates that the AF order is commensurate and fairly long ranged. It is not in agreement with the incommensurate AF order which has been reported from NMR experiments.[58,59] The incommensurability of $\varepsilon \approx 0.04$ as reported in Ref. 59 would be well beyond the resolution limit of the neutron diffraction experiment presented in this paper and is therefore clearly not observed. On the other hand, the rapid exponential relaxation of the ZF-μSR signal in Fig. 6(d), with no trace of an oscillation, implies that the spread

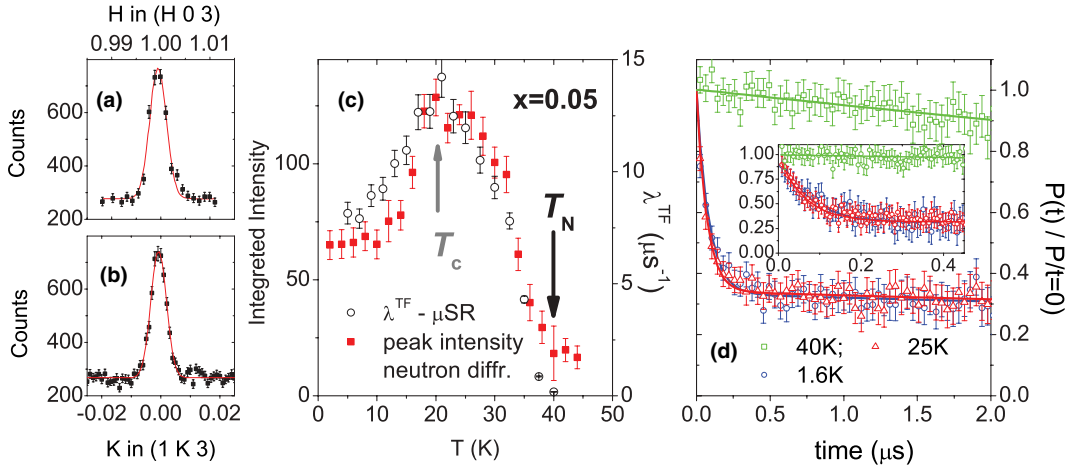

FIG. 6. (Color online) (a) and (b) Neutron diffraction data at $x = 0.05$ showing the antiferromagnetic Bragg peak at the commensurate (1,0,3) position (in orthorhombic notation). (c) Comparison of the T dependence of the intensity of the Bragg peak from neutron diffraction and the relaxation rate, λ^{TF}, of the TF-μSR experiment. The good agreement confirms that they both probe the same bulk magnetic order parameter that is partially suppressed below T_c since it competes with superconductivity. (d) ZF-μSR spectra at $x = 0.05$ showing a rapid depolarization without any trace of an oscillatory signal. Inset: Magnification of the fast relaxation at early times.

of the local magnetic field must be fairly large. The neutron and μSR techniques appear to be probing the same kind of magnetic order since they yield the same onset temperature $T_N = 40$ K, the same anomalous suppression around T_c, and very similar values of the order moment of $\sim$0.09–0.1 μ_B per Fe ion. A likely explanation therefore is in terms of a sizable spatial variation of the amplitude of the commensurate AF order. This variation could be induced by the randomly distributed Co atoms which give rise to a spatial variation of the magnitude of the antiferromagnetic order parameter. We note that a similar conclusion was obtained from previous NMR experiments on Ni-substituted Ba-122.[60]

Further information about the role of the Co-induced disorder in the suppression of the magnetism can be obtained from the comparison with the μSR data on the hole-doped $Ba_{1-x}K_xFe_2As_2$.[22] The substitution-induced disordering effects should be significantly weaker here since the K ions are incorporated on the Ba sites where they do not directly disturb the iron arsenide layers. The relaxation rate of the oscillatory signal in the ZF-μSR spectrum of the $Ba_{1-x}K_xFe_2As_2$ sample with $x = 0.19$ in Ref. 22 is indeed significantly smaller than the one of the $Ba(Fe_{1-x}Co_x)_2As_2$ crystal at $x = 0.045$ which is in a similarly underdoped state with $T_c \approx 0.5T_{c,\,max}$. Nevertheless, in both the K- and the Co-substituted samples the μSR precession frequency and thus the magnetic order parameter are only moderately reduced as long as the samples are not yet superconducting or remain strongly underdoped with $T_c \leqslant 0.5T_{c,\,max}$. This common behavior suggests that the disorder effects in the Co-substituted samples are not governing the general features of the magnetic and superconducting phase diagram. Figure 3 also shows that in $Ba(Fe_{1-x}Co_x)_2As_2$ the magnetic order parameter is very rapidly suppressed between $x = 0.045$ and $x = 0.05$ where the Co concentration increases by a relatively small amount. It was previously shown that the weak magnetic state at $x = 0.055$ remains a bulk phenomenon[15] with a well-defined commensurate order.[13,14] These observations rather point toward an intrinsic origin of the transition, for example, due to a change of the Fermi-surface topology as was observed in this doping range with the angle-resolved photoemission spectroscopy (ARPES).[61] A corresponding μSR study of homogeneous $Ba_{1-x}K_xFe_2As_2$ samples in the weakly underdoped regime with $0.5T_{c,\,max} < T_c < T_{c,\,max}$, to the best of our knowledge, is still lacking.

Another interesting feature concerns the very different doping dependences of T_N and B_μ. Figure 3 displays the monotonous and almost linear suppression of T_N in the range $0 \leqslant x \leqslant 0.055$ with no sign of an anomaly between $x = 0.045$ and 0.05 where B_μ is suddenly reduced from $\sim$70% to $\sim$10% of its value at $x = 0$. Such a qualitatively different behavior of T_N and B_μ is rather surprising since the thermodynamic properties such as the transition temperature, T_N, should be governed by the magnetic order parameter. It implies that the actual value of T_N is much lower than the upper bound that is set by the magnetic order parameter. It has indeed been found that T_N is closely linked to the structural transition temperature, T_s, where the crystal symmetry changes from tetragonal to orthorhombic. The T_N values are always slightly below or at best equal to T_s, which suggests that the orthorhombic distortion is a prerequisite for the static magnetic order to develop.[31,62,63] It is still debated whether the orthorhombic transition itself is caused by an electronic instability. The proposed explanations range from the scenario of an orbital polarization due to a different occupation of the Fe d_{xz} and d_{yz} orbitals[64,65] to a nematic instability of the electronic system that is driven by the anisotropic magnetic fluctuations.[63] In the presence of a sizable magnetoelastic coupling,[31] the former model naturally explains that T_N is tied to T_s and thus may not be strongly affected by the rapid suppression of the magnetic order parameter. In the context of the nematic model such a different behavior of T_N and B_μ is less obvious since the magnetic correlations are at the heart of both the structural and the magnetic transitions. As outlined in Ref. 63, the hierarchy of the nematic and the magnetic transition is determined by their different sensitivity to fluctuation effects. The nematic transition is less sensitive since it breaks only a discrete lattice symmetry whereas the AF transition requires in addition that the continuous rotational symmetry is broken. While this may explain that the anomaly in T_N is considerably weaker than the one in B_μ, it still makes it difficult to understand that this anomaly is essentially absent.

C. Spatially inhomogeneous magnetic order around optimum doping at $0.055 < x < 0.075$

Next, we address the question of how the static magnetic order vanishes around optimal doping. We show that this involves a spatially inhomogeneous magnetic state for which the magnetic volume fraction decreases systematically with increasing Co content and finally vanishes at $x \geqslant 0.075$. Notably, we find that this inhomogeneous magnetic state develops right below T_c, which suggests that it may have a constructive rather than a competitive relationship with superconductivity. The evolution of the magnetic properties in the range from $x = 0.055$ to $x = 0.075$ is captured in Fig. 7, which displays the temperature dependence of the ZF-μSR spectra, and in Fig. 8, which shows the corresponding low-temperature TF-μSR spectra. The ZF-μSR spectra at $T > T_N$ have been fitted with a so-called Kubo-Toyabe function which describes the weak depolarization due to the nuclear moments. This function has been multiplied with an exponential function with a relaxation rate λ^{ZF} to account for an additional relaxation due to slow magnetic fluctuations. The spectra at $T < T_N$ were fitted with a sum of two exponential functions, one of which has a large relaxation rate to describe the rapidly depolarizing part of the signal. The amplitude of this rapidly relaxing signal is shown in Figs. 7(e)–7(h) as a function of doping and temperature. The obtained normalized values of T_N and B_μ in the spatially inhomogeneous phase are shown by the open symbols in Fig. 3.

In the bulk magnetic state at $x = 0.055$, the rapidly depolarizing ZF-μSR signal develops below $T_N \approx 32$ K and its amplitude reaches about 65% as shown in Figs. 7(a) and 7(e). As discussed above, the slowly relaxing part of the ZF-μSR signal of about 35% arises in these single crystals because the muon spin polarization and $\mathbf{B}_\mu$ are not orthogonal. This is confirmed by the TF-μSR data in Fig. 8 where at $x = 0.055$ the entire TF-μSR signal depolarizes very rapidly (except for a small fraction due to the background muons that stop outside the sample). Figures 7(b) and 7(c) show that the

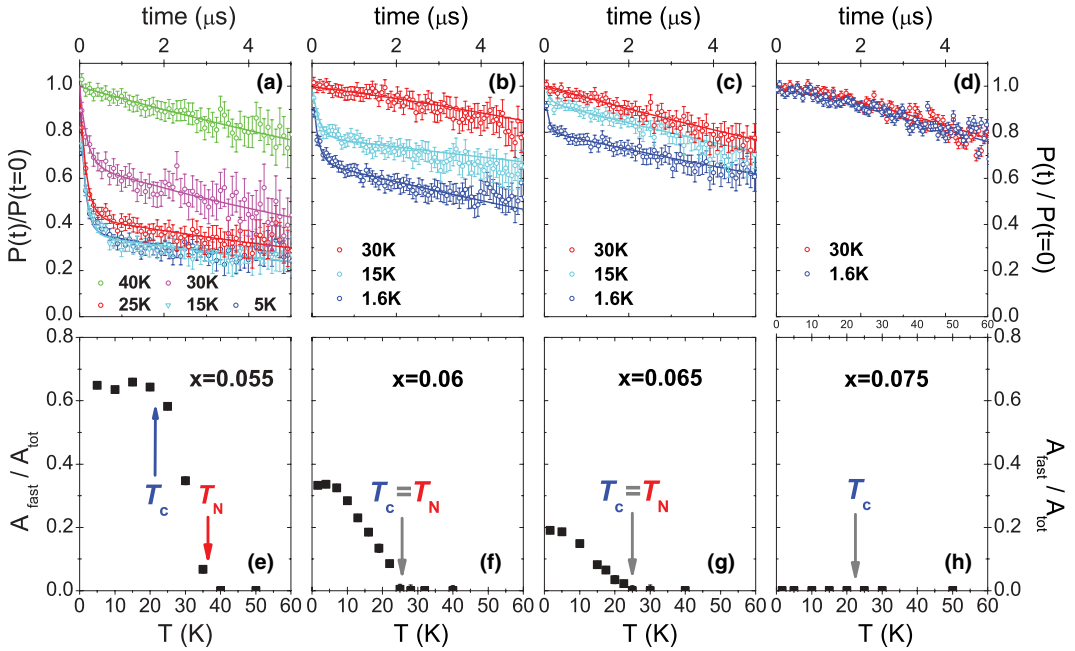

FIG. 7. (Color online) ZF-μSR spectra in the range of $0.055 \leqslant x \leqslant 0.075$ showing that the final suppression of the magnetic order around optimum doping involves a spatially inhomogeneous state with a reduced magnetic volume fraction.

ZF-μSR spectra at $x = 0.06$ and 0.065 exhibit a noticeably different behavior since the amplitude of the magnetic signal is significantly reduced here. This trend is also evident from the TF-μSR data in Fig. 8 where the amplitude of the rapidly depolarizing signal also decreases systematically. The solid lines show a two-component fit with a rapidly depolarizing component that describes the magnetic regions and a more slowly depolarizing one that accounts for the nonmagnetic regions. In the latter the relaxation is dominated by the superconducting vortex lattice which apparently develops in both the nonmagnetic and the magnetic regions as is evident from additional pinning experiments (not shown). From the fits of the TF-μSR data we deduced that the volume fraction of the magnetic phase decreases from essentially 100% at $x = 0.055$ to ~50% at $x = 0.06$ and ~30% at $x = 0.065$.

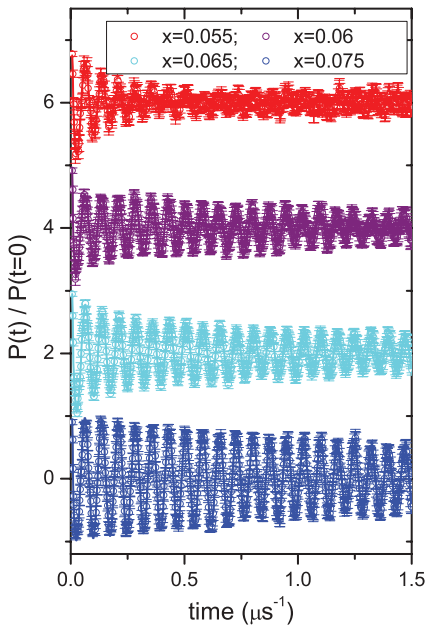

FIG. 8. (Color online) TF-μSR spectra of the near optimally doped crystals at $T = 1.6\,\mathrm{K} \ll T_c$. The spectra are shifted up by $+6$ for $x = 0.055$, $+4$ for $x = 0.06$, and $+2$ for $x = 0.065$. The spectra were obtained at $H^{\mathrm{ext}} = 3$ kOe and are shown in a rotating reference frame corresponding to $H^{\mathrm{rot}} = 2$ kOe.

Notably, we find that this spatially inhomogeneous magnetic order develops only in the superconducting state. Figures 7(f) and 7(g) show indeed that the onset of the magnetic signal coincides with T_c. This curious coincidence was observed in several other near-optimally doped crystals with T_c values close to $T_{c,\,\mathrm{max}} = 25$ K; an early example is reported in Ref. 24. Some of these crystals may have contained impurity phases and their Co content may not always have been well controlled and characterized; they still establish the general trend that the onset of this inhomogeneous magnetic order coincides with T_c. Figures 7(d) and 7(h) show that this inhomogeneous magnetic order is finally absent in the crystal with $x = 0.075$ that is moderately overdoped with $T_c \approx 21.7$ K. It is also not observed in the more strongly overdoped crystals at $x = 0.09$, 0.11, and 0.12.

The systematic decrease of the magnetic volume fraction within the fairly narrow window of $0.055 \leqslant x < 0.075$ around optimum doping makes it seem unlikely that a magnetic impurity phase is responsible for the spatially inhomogeneous magnetic order. This could also not explain the observation that the onset of the magnetic order coincides with T_c.

The same arguments apply against the scenario that the magnetic order may be a muon-induced effect, either due to its positive charge or a lattice distortion. There is no obvious reason why such an effect should only occur in the superconducting state and if so only in parts of the sample volume. Besides, we note that at $x = 0.05$ we obtained good

agreement between the neutron diffraction and the μSR data (see Fig. 4) which confirms that the muons do not noticeably disturb the magnetic order. This is despite the rapid change of the magnetic properties in the range of $0.045 < x < 0.055$ which should enhance the susceptibility to any muon-induced effects.

The magnetic neutron scattering experiments revealed a change of the magnetic ground state between $x = 0.055$ and 0.06. The AF order is reported here to become incommensurate[51] and eventually to exhibit a reentrant behavior.[31] A similar behavior was recently reported for Ni-substituted crystals where also a sudden transition from a commensurate to an incommensurate AF order was observed.[66] The latter was still found to develop at $T_N > T_c$ and to compete with superconductivity. From Fig. 7 it can be seen that our μSR data at $0.055 < x < 0.075$ show no evidence of such a reentrant behavior where the magnetic order is weakened or even vanishes at low temperature. Instead, at $x = 0.06$ and 0.065 we find that the magnetic order develops right below T_c with the amplitude of the magnetic signal increasing toward low temperature. A possible explanation for these different trends may be that the spatially inhomogeneous magnetic state seen by μSR around optimal doping is strongly disordered and yields magnetic Bragg peaks that are very broad and difficult to observe in neutron diffraction. This broadening may be enhanced in the superconducting state such that the reentrant behavior reported in near-optimally doped samples in Ref. 31 may actually arise from a broadening of the magnetic Bragg peaks. Clearly, further efforts should be undertaken to investigate this inhomogeneous magnetic state at $0.055 < x < 0.075$ with magnetic neutron diffraction.

D. Superconductivity-induced enhancement of spin fluctuations in overdoped samples

Finally, we show that an anomalous, superconductivity-induced enhancement of the low-energy spin fluctuations occurs even in strongly overdoped samples. Figure 9 shows the ZF- and LF-μSR data for an overdoped crystal with $x = 0.11$ and $T_c = 10$ K. From the ZF-μSR spectra in Fig. 9(a) it can already be seen that the relaxation rate in the superconducting state is slightly larger than the one in the normal state. The effect is relatively weak since the relaxation in these ZF spectra is dominated by the contribution of the randomly oriented nuclear magnetic moments, described by a so-called Kubo-Toyabe function. It is well known that a small longitudinal field (LF) can be used to reduce this static nuclear contribution as to reveal the weaker dynamical relaxation due to low-energy spin fluctuations.[36] The corresponding LF-μSR data for small longitudinal fields of 5 and 10 Oe are shown in Figs. 9(b) and 9(c), respectively. They exhibit small yet clearly visible changes that are characteristic of an increase of the dynamical relaxation rate at low temperature. Figure 9(d) details the temperature dependence of the dynamical relaxation rate, λ^{LF}, for $H^{LF} = 10$ Oe which exhibits a clear anomaly at $T_c \approx 10$ K. The sudden increase of λ^{LF} below T_c signifies a superconductivity-induced enhancement of the low-energy spin fluctuations in this strongly overdoped crystal. The inset of Fig. 9(d) shows how this SC-induced increase in relaxation

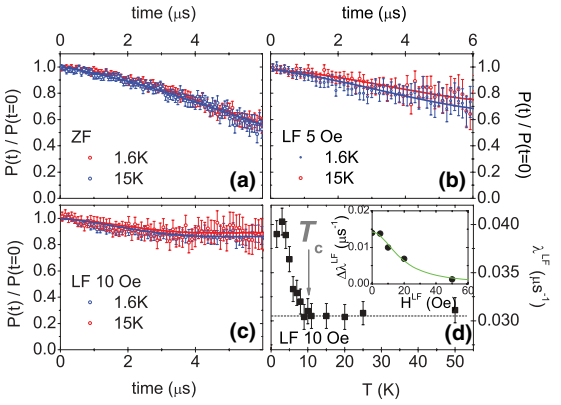

FIG. 9. (Color online) (a)–(c) ZF-μSR and weak LF-μSR spectra for the strongly overdoped crystal with $x = 0.11$ and $T_c \approx 10$ K. (d) Temperature dependence of the LF-μSR relaxation rate at $H^{LF} = 10$ Oe showing a sudden increase below T_c which reveals a superconductivity-induced enhancement of the low-energy spin fluctuations. Inset: Superconductivity-induced enhancement of the relaxation rate, $\Delta\lambda^{LF}$, as a function of the longitudinal field. The green line shows a fit with the so-called Redfield function as shown in Eq. (2) and discussed in the text.

rate, $\Delta\lambda^{LF}$, evolves as a function of the longitudinal field. The green line shows a fit with the so-called Redfield function,

$$\Delta\lambda^{LF} = 2(\gamma\mu_o H_\mu)^2\tau_c/[1 + (\gamma\mu_o H^{LF}\tau_c)^2], \qquad (2)$$

which describes a relaxation process due to fluctuating local fields[36] with a magnitude, $\mu_o H_\mu = 0.16$ G, and a correlation time, $\tau_c = 0.65\,\mu$s.

In this context we recall a related trend in the TF-μSR data where it was noticed that in the superconducting state the μSR line shape exhibits an anomalous paramagnetic shift.[46,48,67] This superconductivity-induced paramagnetic shift of the TF-μSR line shape, which has also been consistently observed in the present optimally and overdoped single crystals (not shown), is most likely related to the superconductivity-induced enhancement of the low-energy spin fluctuations.

The μSR data thus provide compelling evidence that even in the optimally doped and overdoped samples, the magnetic correlations and/or the low-energy spin fluctuations are noticeably enhanced in the superconducting state. A similar behavior was previously observed in materials with a spin-triplet superconducting order parameter that breaks time reversal symmetry, as in Sr_2RuO_4,[42] $PrOs_4Sb_{12}$,[68] or $LaNiC_2$.[69] However, such a spin-triplet state does not seem to be realized in $Ba(Fe_{1-x}Co_x)_2As_2$ for which NMR Knight shift measurements revealed a pronounced superconductivity-induced reduction of the Knight shift that is a hallmark of a spin-singlet superconducting state.[70,71] Therefore, it appears that alternative explanations for the enhanced spin correlations in the superconducting state of optimally doped and overdoped $Ba(Fe_{1-x}Co_x)_2As_2$ need to be explored. This issue is beyond the scope of our present μSR study.

IV. SUMMARY

With muon spin rotation (μSR) we investigated the magnetic and superconducting phase diagram of a series of

$Ba(Fe_{1-x}Co_x)_2As_2$ single crystals with $0 \leqslant x \leqslant 0.15$. We showed that the magnetic order parameter is initially only weakly reduced at $x \leqslant 0.04$, whereas it exhibits a much more rapid suppression as superconductivity emerges at $x > 0.04$. In most of the underdoped regime we observed a weakened, yet bulk magnetic order that coexists and competes with superconductivity. The comparison with neutron diffraction data suggests that this AF order remains commensurate. The Co atoms likely induce a random variation of the amplitude which leads to a large μSR depolarization rate. The final suppression of the magnetic order toward optimum doping involves a spatially inhomogeneous magnetic state. The magnetic volume fraction becomes rapidly reduced at $x > 0.055$ and it vanishes at $x = 0.075$. Notably, this inhomogeneous magnetic order develops right below T_c and therefore does not seem to compete with superconductivity but rather seems to have a constructive relationship. Even in a strongly overdoped sample at $x = 0.11$ the μSR experiments reveal signatures of a superconductivity-induced enhancement of the low-energy spin fluctuations. Our observations highlight a versatile relationship between magnetism and superconductivity that is competitive on the underdoped side of the Co-doping phase diagram whereas it appears to be cooperative in optimally doped and overdoped samples.

ACKNOWLEDGMENTS

We acknowledge fruitful discussions with Dr. Christoph Meingast. The μSR experiments were performed at the Swiss muon Source (SμS) at the Paul Scherrer Institut, Villigen, Switzerland where we benefitted from the technical support of Dr. Alex Amato and Dr. Hubertus Lütkens. We appreciate Bente Lebech for helping us with the refinement of the magnetic neutron diffraction data to obtain absolute values of the magnetic moment. The work at University of Fribourg has been supported by the Swiss National Science Foundation (SNF) Grants No. 200020-129484 and No. 200020-140225, by the NCCR MaNEP, and by Project No. 122935 of the Indo-Swiss Joint Research Program (ISJRP). The work in QMUL was supported by the Leverhulme Trust, and C.A. was funded by an EPSRC Doctoral Training Award. The work in Karlsruhe was supported by the Deutsche Forschungsgemeinschaft (DFG) through SPP 1458. The financial support from D.S.T. (Government of India) is highly acknowledged.

*Present address: Microelectronics Research Center, The University of Texas at Austin, Austin, TX 78758, USA.

[1] Y. Kamihara, T. Watanabe, M. Hirano, and H. Hosono, J. Am. Chem. Soc. **130**, 3296 (2008).

[2] X. H. Chen, T. Wu, G. Wu, R. H. Liu, H. Chen, and D. F. Fang, Nature **453**, 761 (2008).

[3] Ren Zhi-An, L. Wei, Y. Jie, Y. Wei, Shen Xiao-Li, Li Zheng-Cai, Che Guang-Can, Dong Xiao-Li, Sun Li-Ling, Zhou Fang, and Zhao Zhong-Xian, Chin. Phys. Lett. **25**, 2215 (2008).

[4] A. S. Sefat, R. Jin, M. A. McGuire, B. C. Sales, D. J. Singh, and D. Mandrus, Phys. Rev. Lett. **101**, 117004 (2008).

[5] M. Rotter, M. Tegel, and D. Johrendt, Phys. Rev. Lett. **101**, 107006 (2008).

[6] N. Ni, S. L. Bud'ko, A. Kreyssig, S. Nandi, G. E. Rustan, A. I. Goldman, S. Gupta, J. D. Corbett, A. Kracher, and P. C. Canfield, Phys. Rev. B **78**, 014507 (2008).

[7] P. L. Alireza, Y. T. C. Ko, J. Gillett, C. M. Petrone, J. M. Cole, G. G. Lonzarich, and S. E. Sebastian, J. Phys.: Condens. Matter **21**, 012208 (2009).

[8] S. A. J. Kimber, A. Kreyssig, Y. Z. Zhang, H. O. Jeschke, R. Valenti, F. Yokaichiya, E. Colombier, J. Yan, T. C. Hansen, T. Chatterji, R. J. McQueeney, P. C. Canfield, Goldman, and D. N. Argyriou, Nat. Mater. **8**, 471 (2009).

[9] A. Thaler, N. Ni, A. Kracher, J. Q. Yan, S. L. Bud'ko, and P. C. Canfield, Phys. Rev. B **82**, 014534 (2010).

[10] J. Paglione and R. L. Greene, Nat. Phys. **6**, 645 (2010).

[11] A. J. Drew, Ch. Niedermayer, P. J. Baker, F. L. Pratt, S. J. Blundell, T. Lancaster, R. H. Liu, G. Wu, X. H. Chen, I. Watanabe, V. K. Malik, A. Dubroka, M. Rössle, K. W. Kim, C. Baines, and C. Bernhard, Nat. Mater. **8**, 310 (2009).

[12] S. Sanna, R. De Renzi, G. Lamura, C. Ferdeghini, A. Palenzona, M. Putti, M. Tropeano, and T. Shiroka, Phys. Rev. B **80**, 052503 (2009).

[13] A. D. Christianson, M. D. Lumsden, S. E. Nagler, G. J. MacDougall, M. A. McGuire, A. S. Sefat, R. Jin, B. C. Sales, and D. Mandrus, Phys. Rev. Lett. **103**, 087002 (2009).

[14] D. K. Pratt, W. Tian, A. Kreyssig, J. L. Zarestky, S. Nandi, N. Ni, S. L. Bud'ko, P. C. Canfield, A. I. Goldman, and R. J. McQueeney, Phys. Rev. Lett. **103**, 087001 (2009).

[15] P. Marsik, K. W. Kim, A. Dubroka, M. Rössle, V. K. Malik, L. Schulz, C. N. Wang, Ch. Niedermayer, A. J. Drew, M. Willis, T. Wolf, and C. Bernhard, Phys. Rev. Lett. **105**, 57001 (2010).

[16] M.-H. Julien, H. Mayaffre, M. Horvatić, C. Berthier, X. D. Zhang, W. Wu, G. F. Chen, N. L. Wang, and J. L. Luo, Europhys. Lett. **87**, 37001 (2009).

[17] H. Luetkens, H.-H. Klauss, M. Kraken, F. J. Litterst, T. Dellmann, R. Klingeler, C. Hess, R. Khasanov, A. Amato, C. Baines, M. Kosmala, O. J. Schumann, M. Braden, J. Hamann-Borrero, N. Leps, A. Kondrat, G. Behr, J. Werner, and B. Büchner, Nat. Mater. **8**, 305 (2009).

[18] J. T. Park, D. S. Inosov, Ch. Niedermayer, G. L. Sun, D. Haug, N. B. Christensen, R. Dinnebier, A. V. Boris, A. J. Drew, L. Schulz, T. Shapoval, U. Wolff, V. Neu, X. Yang, C. T. Lin, B. Keimer, and V. Hinkov, Phys. Rev. Lett. **102**, 117006 (2009).

[19] T. Goko, A. A. Aczel, E. Baggio-Saitovitch, S. L. Bud'ko, P. C. Canfield, J. P. Carlo, G. F. Chen, Pengcheng Dai, A. C. Hamann, W. Z. Hu, H. Kageyama, G. M. Luke, J. L. Luo, B. Nachumi, N. Ni, D. Reznik, D. R. Sanchez-Candela, A. T. Savici, K. J. Sikes, N. L. Wang, C. R. Wiebe, T. J. Williams, T. Yamamoto, W. Yu, and Y. J. Uemura, Phys. Rev. B **80**, 024508 (2009).

[20] S. Sanna, P. Carretta, P. Bonfà, G. Prando, G. Allodi, R. De Renzi, T. Shiroka, G. Lamura, A. Màrtinelli, and M. Putti, Phys. Rev. Lett. **107**, 227003 (2011).

[21] Y. Laplace, J. Bobroff, V. Brouet, G. Collin, F. Rullier-Albenque, D. Colson, and A. Forget, Phys. Rev. B **86**, 020510(R) (2012).

[22]E. Wiesenmayer, H. Luetkens, G. Pascua, R. Khasanov, A. Amato, H. Potts, B. Banusch, H. H. Klauss, and D. Johrendt, Phys. Rev. Lett. **107**, 237001 (2011).
[23]W. K. Yeoh, B. Gault, X. Y. Cui, C. Zhu, M. P. Moody, L. Li, R. K. Zheng, W. X. Li, X. L. Wang, S. X. Dou, G. L. Sun, C. T. Lin, and S. P. Ringer, Phys. Rev. Lett. **106**, 247002 (2011).
[24]C. Bernhard, A. J. Drew, L. Schulz, V. K. Malik, M. Rössle, Ch. Niedermayer, Th. Wolf, G. D. Varma, G. Mu, H.-H. Wen, H. Liu, G. Wu, and X. H. Chen, New J. Phys. **11**, 055050 (2009).
[25]F. Hardy, P. Adelmann, T. Wolf, H. v. Löhneysen, and C. Meingast, Phys. Rev. Lett. **102**, 187004 (2009).
[26]F. Hardy, T. Wolf, R. A. Fisher, R. Eder, P. Schweiss, P. Adelmann, H. v. Lohneysen, and C. Meingast, Europhys. Lett. **91**, 47008 (2010).
[27]N. Ni, M. E. Tillman, J. Q. Yan, A. Kracher, S. T. Hannahs, S. L. Bud'ko, and P. C. Canfield, Phys. Rev. B **78**, 214515 (2008).
[28]J. H. Chu, J. G. Analytis, C. Kucharczyk, and I. R. Fisher, Phys. Rev. B **79**, 014506 (2009).
[29]F. Rullier-Albenque, D. Colson, A. Forget, and H. Alloul, Phys. Rev. Lett. **103**, 057001 (2009).
[30]F. L. Ning, K. Ahilan, T. Imai, A. S. Sefat, M. A. McGuire, B. C. Sales, D. Mandrus, P. Cheng, B. Shen, and H. H. Wen, Phys. Rev. Lett. **104**, 037001 (2010).
[31]S. Nandi, M. G. Kim, A. Kreyssig, R. M. Fernandes, D. K. Pratt, A. Thaler, N. Ni, S. L. Bud'ko, P. C. Canfield, J. Schmalian, R. J. McQueeney, and A. I. Goldman, Phys. Rev. Lett. **104**, 057006 (2010).
[32]K. W. Kim, M. Rössle, A. Dubroka, V. K. Malik, T. Wolf, and C. Bernhard, Phys. Rev. B **81**, 214508 (2010).
[33]H. Maeter, H. Luetkens, Yu. G. Pashkevich, A. Kwadrin, R. Khasanov, A. Amato, A. A. Gusev, K. V. Lamonova, D. A. Chervinskii, R. Klingeler, C. Hess, G. Behr, B. Büchner, and H. H. Klauss, Phys. Rev. B **80**, 094524 (2009).
[34]A. Schenck, *Muon Spin Rotation Spectroscopy: Principles and Applications in Solid State Physics* (Adam Hilger Ltd., Bristol-Boston, 1985).
[35]*Muon Science: Proceedings of the 51st Scottish Universities Summer School in Physics: NATO Advanced Study Institute on Muon Science, 17–28 August, 1998*, edited by S. L. Lee, R. Cywinski, and S. H. Kilcoyne (Institute of Physics, Bristol, UK, 1999).
[36]J. H. Brewer, *in Encyclopedia of Applied Physics*, edited by G. L. Trigg, Vol. 11 (VCH, New York, 1994), p. 23.
[37]A. Weidinger, Ch. Niedermayer, A. Golnik, R. Simon, E. Recknagel, J. I. Budnick, B. Chamberland, and C. Baines, Phys. Rev. Lett. **62**, 102 (1989).
[38]R. F. Kiefl, J. H. Brewer, J. Carolan, P. Dosanjh, W. N. Hardy, R. Kadono, J. R. Kempton, R. Krahn, P. Schleger, B. X. Yang, Hu Zhou, G. M. Luke, B. Sternlieb, Y. J. Uemura, W. J. Kossler, X. H. Yu, E. J. Ansaldo, H. Takagi, S. Uchida, and C. L. Seaman, Phys. Rev. Lett. **63**, 2136 (1989).
[39]Ch. Niedermayer, C. Bernhard, T. Blasius, A. Golnik, A. Moodenbaugh, and J. I. Budnick, Phys. Rev. Lett. **80**, 3843 (1998).
[40]S. Sanna, G. Allodi, G. Concas, A. D. Hillier, and R. De Renzi, Phys. Rev. Lett. **93**, 207001 (2004).
[41]C. Bernhard, J. L. Tallon, Ch. Niedermayer, Th. Blasius, A. Golnik, E. Brücher, R. K. Kremer, D. R. Noakes, C. E. Stronach, and E. J. Ansaldo, Phys. Rev. B **59**, 14099 (1999).
[42]G. M. Luke, Y. Fudamoto, K. M. Kojima, M. I. Larkin, J. Merrin, B. Nachumi, Y. J. Uemura, Y. Maeno, Z. Q. Mao, Y. Mori, H. Nakamura, and M. Sigrist, Nature **394**, 558 (1998).
[43]A. J. Drew, F. L. Pratt, T. Lancaster, S. J. Blundell, P. J. Baker, R. H. Liu, G. Wu, X. H. Chen, I. Watanabe, V. K. Malik, A. Dubroka, K. W. Kim, M. Rössle, and C. Bernhard, Phys. Rev. Lett. **101**, 097010 (2008).
[44]H. H. Klauss, H. Luetkens, R. Klingeler, C. Hess, F. J. Litterst, M. Kraken, M. M. Korshunov, I. Eremin, S. L. Drechsler, R. Khasanov, A. Amato, J. Hamann-Borrero, N. Leps, A. Kondrat, G. Behr, J. Werner, and B. Büchner, Phys. Rev. Lett. **101**, 077005 (2008).
[45]Y. J. Uemura, Nat. Mater. **8**, 253 (2009).
[46]T. J. Williams, A. A. Aczel, E. Baggio-Saitovitch, S. L. Bud'ko, P. C. Canfield, J. P. Carlo, T. Goko, H. Kageyama, A. Kitada, J. Munevar, N. Ni, S. R. Saha, K. Kirschenbaum, J. Paglione, D. R. Sanchez-Candela, Y. J. Uemura, and G. M. Luke, Phys. Rev. B **82**, 094512 (2010).
[47]D. R. Parker, M. J. P. Smith, T. Lancaster, A. J. Steele, I. Franke, P. J. Baker, F. L. Pratt, M. J. Pitcher, S. J. Blundell, and S. J. Clarke, Phys. Rev. Lett. **104**, 057007 (2010).
[48]M. Bendele, P. Babkevich, S. Katrych, S. N. Gvasaliya, E. Pomjakushina, K. Conder, B. Roessli, A. T. Boothroyd, R. Khasanov, and H. Keller, Phys. Rev. B **82**, 212504 (2010).
[49]Z. Shermadini, A. Krzton-Maziopa, M. Bendele, R. Khasanov, H. Luetkens, K. Conder, E. Pomjakushina, S. Weyeneth, V. Pomjakushin, O. Bossen, and A. Amato, Phys. Rev. Lett. **106**, 117602 (2011).
[50]C. N. Wang, P. Marsik, R. Schuster, A. Dubroka, M. Rössle, Ch. Niedermayer, G. D. Varma, A. F. Wang, X. H. Chen, T. Wolf, and C. Bernhard, Phys. Rev. B **85**, 214503 (2012).
[51]D. K. Pratt, M. G. Kim, A. Kreyssig, Y. B. Lee, G. S. Tucker, A. Thaler, W. Tian, J. L. Zarestky, S. L. Bud'ko, P. C. Canfield, B. N. Harmon, A. I. Goldman, and R. J. McQueeney, Phys. Rev. Lett. **106**, 257001 (2011).
[52]J. Zhao, W. Ratcliff, II, J. W. Lynn, G. F. Chen, J. L. Luo, N. L. Wang, J. Hu, and P. Dai, Phys. Rev. B **78**, 140504 (2008).
[53]Q. Huang, Y. Qiu, W. Bao, M. A. Green, J. W. Lynn, Y. C. Gasparovic, T. Wu, G. Wu, and X. H. Chen, Phys. Rev. Lett. **101**, 257003 (2008).
[54]Y. Su, P. Link, A. Schneidewind, T. Wolf, P. Adelmann, Y. Xiao, M. Meven, R. Mittal, M. Rotter, D. Johrendt, T. Brueckel, and M. Loewenhaupt, Phys. Rev. B **79**, 064504 (2009).
[55]M. D. Lumsden and A. D. Christianson, J. Phys.: Condens. Matter **22**, 203203 (2010).
[56]A. Jesche, N. Caroca-Canales, H. Rosner, H. Borrmann, A. Ormeci, D. Kasinathan, H. H. Klauss, H. Luetkens, R. Khasanov, A. Amato, A. Hoser, K. Kaneko, C. Krellner, and C. Geibel, Phys. Rev. B **78**, 180504 (2008).
[57]A. A. Aczel, E. Baggio-Saitovitch, S. L. Bud'ko, P. C. Canfield, J. P. Carlo, G. F. Chen, P. Dai, T. Goko, W. Z. Hu, G. M. Luke, J. L. Luo, N. Ni, D. R. Sanchez-Candela, F. F. Tafti, N. L. Wang, T. J. Williams, W. Yu, and Y. J. Uemura, Phys. Rev. B **78**, 214503 (2008).
[58]F. L. Ning, K. Ahilan, T. Imai, A. S. Sefat, R. Jin, M. A. McGuire, B. C. Sales, and D. Mandrus, Phys. Rev. B **79**, 140506 (2009).
[59]Y. Laplace, J. Bobroff, F. Rullier-Albenque, D. Colson, and A. Forget, Phys. Rev. B **80**, 140501 (2009).

[60] A. P. Dioguardi, N. apRoberts-Warren, A. C. Shockley, S. L. Bud'ko, N. Ni, P. C. Canfield, and N. J. Curro, Phys. Rev. B **82**, 140411 (2010).

[61] C. Liu, A. D. Palczewski, R. S. Dhaka, T. Kondo, R. M. Fernandes, E. D. Mun, H. Hodovanets, A. N. Thaler, J. Schmalian, S. L. Budko, P. C. Canfield, and A. Kaminski, Phys. Rev. B **84**, 020509(R) (2011).

[62] R. M. Fernandes, D. K. Pratt, W. Tian, J. Zarestky, A. Kreyssig, S. Nandi, M. G. Kim, A. Thaler, Ni Ni, P. C. Canfield, R. J. McQueeney, J. Schmalian, and A. I. Goldman, Phys. Rev. B **81**, 140501 (2010).

[63] R. M. Fernandes and J. Schmalian, Supercond. Sci. Technol. **25**, 084005 (2012).

[64] J.-H. Chu, J. G. Analytis, K. De Greve, P. L. McMahon, Z. Islam, Y. Yamamoto, and I. R. Fisher, Science **329**, 824 (2010).

[65] T.-M. Chuang, M. P. Allan, J. Lee, Y. Xie, N. Ni, S. L. Bud'ko, G. S. Boebinger, P. C. Canfield, and J. C. Davis, Science **327**, 181 (2010).

[66] H. Luo, R. Zhang, M. Laver, Z. Yamani, M. Wang, X. Lu, M. Wang, Y. Chen, S. Li, S. Chang, J. W. Lynn, and P. Dai, Phys. Rev. Lett. **108**, 247002 (2012).

[67] R. Khasanov, A. Maisuradze, H. Maeter, A. Kwadrin, H. Luetkens, A. Amato, W. Schnelle, H. Rosner, A. Leithe-Jasper, and H. H. Klauss, Phys. Rev. Lett. **103**, 067010 (2009).

[68] Y. Aoki, A. Tsuchiya, T. Kanayama, S. R. Saha, H. Sugawara, H. Sato, W. Higemoto, A. Koda, K. Ohishi, K. Nishiyama, and R. Kadono, Phys. Rev. Lett. **91**, 067003 (2003).

[69] A. D. Hillier, J. Quintanilla, and R. Cywinski, Phys. Rev. Lett. **102**, 117007 (2009).

[70] F. Ning, K. Ahilan, T. Imai, A. S. Sefat, R. Jin, M. A. McGuire, B. C. Sales, and D. Mandrus, J. Phys. Soc. Jpn. **77**, 103705 (2008).

[71] M. Yashima, H. Nishimura, H. Mukuda, Y. Kitaoka, K. Miyazawa, P. M. Shirage, K. Kiho, H. Kito, H. Eisaki, and A. Iyo, J. Phys. Soc. Jpn. **78**, 103702 (2009).

nature physics

LETTERS

PUBLISHED ONLINE: 14 OCTOBER 2012 | DOI: 10.1038/NPHYS2456

Direct observation of competition between superconductivity and charge density wave order in $YBa_2Cu_3O_{6.67}$

J. Chang[1,2]*, E. Blackburn[3], A. T. Holmes[3], N. B. Christensen[4], J. Larsen[4,5], J. Mesot[1,2], Ruixing Liang[6,7], D. A. Bonn[6,7], W. N. Hardy[6,7], A. Watenphul[8], M. v. Zimmermann[8], E. M. Forgan[3] and S. M. Hayden[9]

Superconductivity often emerges in the proximity of, or in competition with, symmetry-breaking ground states such as antiferromagnetism or charge density waves[1–5] (CDW). A number of materials in the cuprate family, which includes the high transition-temperature (high-T_c) superconductors, show spin and charge density wave order[5–7]. Thus a fundamental question is to what extent do these ordered states exist for compositions close to optimal for superconductivity. Here we use high-energy X-ray diffraction to show that a CDW develops at zero field in the normal state of superconducting $YBa_2Cu_3O_{6.67}$ ($T_c = 67$ K). This sample has a hole doping of 0.12 per copper and a well-ordered oxygen chain superstructure[8]. Below T_c, the application of a magnetic field suppresses superconductivity and enhances the CDW. Hence, the CDW and superconductivity in this typical high-T_c material are competing orders with similar energy scales, and the high-T_c superconductivity forms from a pre-existing CDW environment. Our results provide a mechanism for the formation of small Fermi surface pockets[9], which explain the negative Hall and Seebeck effects[10,11] and the 'T_c plateau'[12] in this material when underdoped.

Charge density waves in solids are periodic modulations of conduction electron density. They are often present in low-dimensional systems such as $NbSe_2$ (ref. 4). Certain cuprate materials such as $La_{2-x-y}Nd_ySr_xCuO_4$ (Nd-LSCO) and $La_{2-x}Ba_xCuO_4$ (LBCO) also show charge modulations that suppress superconductivity near $x = 1/8$ (refs 6,7). In some cases, these are believed to be unidirectional in the CuO_2 plane, and have been dubbed 'stripes'[2,3]. There is now a mounting body of indirect evidence that charge and/or spin density waves (static modulations) may be present at high magnetic fields in samples with high T_c: quantum oscillation experiments on underdoped $YBa_2Cu_3O_y$ (YBCO) have revealed the existence of at least one small Fermi surface pocket[9,10], which may be created by a charge modulation[11]. More recently, nuclear magnetic resonance (NMR) studies have shown a magnetic-field-induced splitting of the Cu2F lines of YBCO (ref. 13). An important issue is the extent to which the tendency towards charge order exists in high-T_c superconductors[2,3].

Here we report a hard (100 keV) X-ray diffraction study, in magnetic fields up to 17 T, of a detwinned single crystal of $YBa_2Cu_3O_{6.67}$ (with ortho-VIII oxygen ordering[8,12], $T_c = 67$ K and $p = 0.12$, where p is the hole concentration per planar Cu). We find that a CDW forms in the normal state below $T_{CDW} \approx 135$ K. The charge modulation has two fundamental wave vectors $\mathbf{q}_{CDW} = \mathbf{q}_1 = (\delta_1, 0, 0.5)$ and $\mathbf{q}_2 = (0, \delta_2, 0.5)$, where $\delta_1 \approx 0.3045(2)$ and $\delta_2 \approx 0.3146(7)$, with no significant field- or temperature-dependence of these values. The CDW gives rise to satellites of the parent crystal Bragg peaks at positions such as $\mathbf{Q} = (2 \pm \delta_1, 0, 0.5)$. Although the satellite intensities have a strong temperature and magnetic field dependence, the CDW is not field-induced and is unaffected by field in the normal state. Below T_c it competes with superconductivity, and a decrease of the CDW amplitude in zero field becomes an increase when superconductivity is suppressed by field. A very recent paper[14] reports complementary resonant soft X-ray scattering experiments performed on $(Y, Nd)Ba_2Cu_3O_{6+x}$ as a function of doping and in the absence of a magnetic field. The results are broadly in agreement with our zero field data.

Figure 1a,g shows scans through the $(2-\delta_1, 0, 0.5)$ and $(0, 2-\delta_2, 0.5)$ positions at $T = 2$ K. Related peaks were observed at $(2+\delta_1, 0, 0.5)$ and $(4-\delta_1, 0, 0.5)$ (see Supplementary Fig. S3). The incommensurate peaks are not detected above 150 K (Fig. 1c). From the peak width we estimate that the modulation has an in-plane correlation length $\xi_a \approx 95 \pm 5$ Å (at 2 K and 17 T—see Methods). The existence of four similar in-plane modulations $(\pm\delta_1, 0)$ and $(0, \pm\delta_2)$ indicates that the modulation is associated with the (nearly square) CuO_2 planes rather than the CuO chains. The present experiment cannot distinguish between $1-\mathbf{q}$ and $2-\mathbf{q}$ structures, that is, we cannot tell directly whether modulations along the a and b directions co-exist in space or occur in different domains of the crystal. However, Bragg peaks from the two CDW components have similar intensities and widths (Fig. 1b,g) despite the orthorhombic crystal structure, which breaks the symmetry between them. This suggests that $\mathbf{q}_1$ and $\mathbf{q}_2$ are coupled, leading to the co-existence of multiple wave vectors, as seen in other CDW systems such as $NbSe_2$ (ref. 4). The scan along the c^* direction in Fig. 1d has broad peaks close to $l = \pm 0.5$ reciprocal lattice units (r.l.u.), indicating that the CDW is weakly correlated along the c direction, with a correlation length ξ_c of approximately 0.6 lattice units.

[1]Institut de la Matière Complexe, Ecole Polytechnique Fedérale de Lausanne (EPFL), CH-1015 Lausanne, Switzerland, [2]Paul Scherrer Institut, Swiss Light Source, CH-5232 Villigen PSI, Switzerland, [3]School of Physics and Astronomy, University of Birmingham, Birmingham, B15 2TT, UK, [4]Department of Physics, Technical University of Denmark, DK-2800 Kongens Lyngby, Denmark, [5]Laboratory for Neutron Scattering, Paul Scherrer Institut, CH-5232 Villigen PSI, Switzerland, [6]Department of Physics and Astronomy, University of British Columbia, Vancouver, Canada, [7]Canadian Institute for Advanced Research, Toronto, Canada, [8]Hamburger Synchrotronstrahlungslabor (HASYLAB) at Deutsches Elektronen-Synchrotron (DESY), 22603 Hamburg, Germany, [9]H. H. Wills Physics Laboratory, University of Bristol, Bristol, BS8 1TL, UK. *e-mail: johan.chang@epfl.ch.

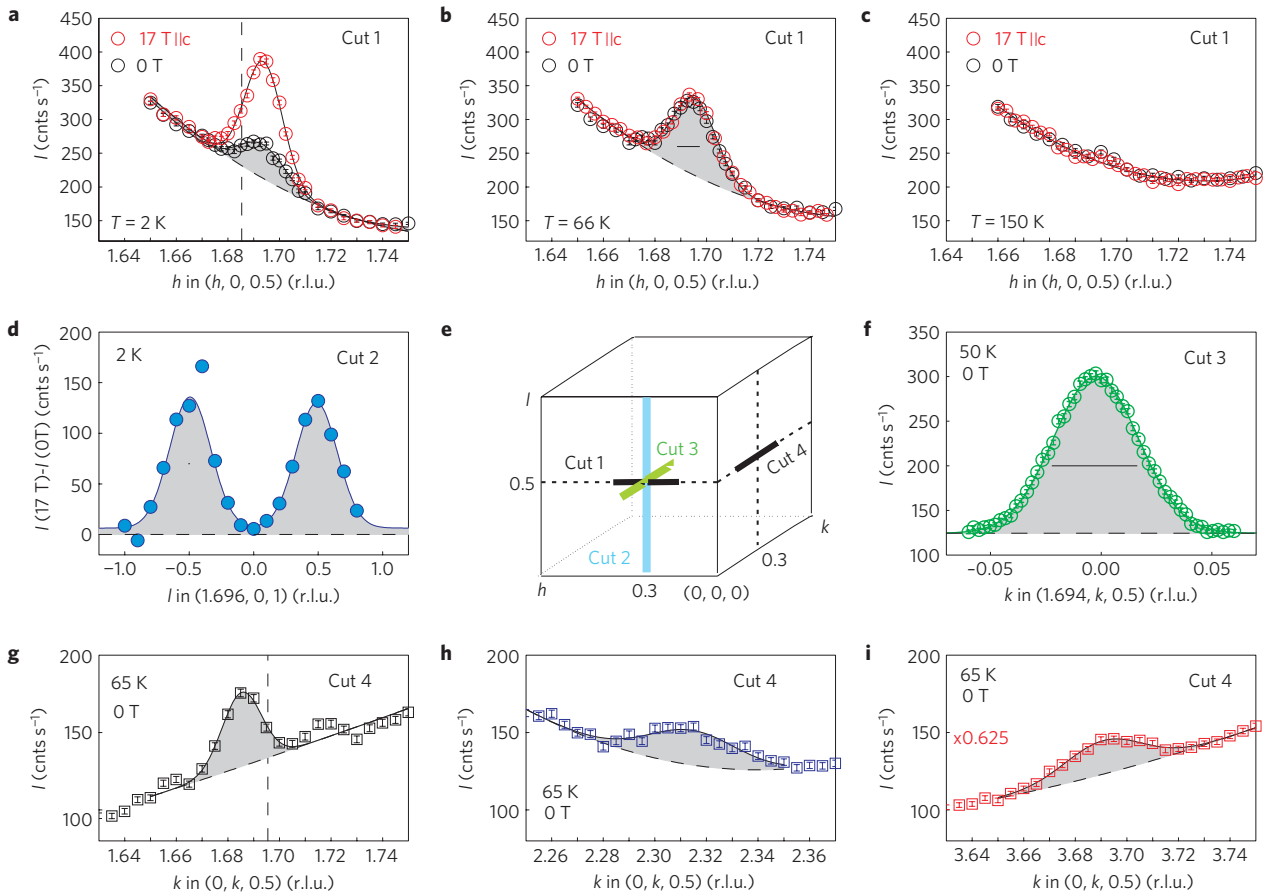

Figure 1 | Incommensurate charge-density-wave order. Diffracted intensity in reciprocal space $\mathbf{Q} = (h, k, l) = h\mathbf{a}^* + k\mathbf{b}^* + l\mathbf{c}^*$ where $a^* = 2\pi/a$, $b^* = 2\pi/b$ and $c^* = 2\pi/c$, with lattice parameters $a = 3.81$ Å, $b = 3.87$ Å (Supplementary Fig. S1), $c = 11.72$ Å. Four different scans in reciprocal space, projected into the first Brillouin zone, are shown schematically in **e**. **a**–**c**, Scans along $(h, 0, 0.5)$ for temperatures and magnetic fields (applied along the crystal c-direction) as indicated. An incommensurate lattice modulation, peaked at $(2 - \delta_1, 0, 0)$, where $\delta_1 = 0.3045(2)$, emerges as the temperature is lowered below 135 K. The intensity of the satellite in **b** is of the order 2×10^{-6} weaker than the (2, 0, 0) reflection. This becomes field-dependent below the zero-field superconducting transition temperature $T_c = 67$ K. The full-width half-maximum instrumental resolution is shown by horizontal lines in **b**,**f**. By deconvolving the resolution from the Gaussian fits to the data taken at 17 T and 2 K, an h-width of $\sigma_a = 6.4 \times 10^{-3}$ r.l.u. corresponding to a correlation length $\xi_a = 1/\sigma_a$ of 95 ± 5 Å was found (see Methods). **d**, The field-induced signal $I(17\text{ T}) - I(0\text{ T})$ at $T = 2$ K is modulated along (1.695, 0, l) and peaks at approximately $l = \pm 0.5$. **f**, Scan along (1.695, k, 0.5). The poor resolution along the k-direction did not allow accurate determination of the width along (1.695, k, 0.5), but we estimate a value of 0.01 r.l.u., comparable to that along (h, 0, 0.5), indicating similar coherence lengths along a- and b-axis directions. **g**–**i**, Scans along (0, k, 0.5). Incommensurate peaks are found in several Brillouin zones, for example, at positions $\mathbf{Q} = (0, 2 \pm \delta_2, 0.5)$ and $(0, 4 - \delta_2, 0.5)$, where $\delta_2 = 0.3146(7)$, see also Supplementary Fig. S3. The vertical dashed line in **g** indicates δ_1 whereas the line in **a** indicates δ_2. The lattice modulation was fitted to a Gaussian function (solid lines in **a**–**d**,**f**–**i**) on a background (dashed lines) modelled by a second-order polynomial. Error bars are determined by counting statistics.

In zero field, the intensity of the CDW Bragg peak (Fig. 2) grows on cooling to T_c, below which it is partially suppressed. For $T > T_c$, a magnetic field applied along the c direction has no effect. Below T_c it causes an increase of the intensity of the CDW signal (Figs 1a and 2). At $T = 2$ K, the intensity grows with applied magnetic field (Fig. 2b) and shows no signs of saturation up to 17 T. The magnetic field also makes the CDW more long-range ordered (Fig. 2c). In zero magnetic field, the **q**-width varies little with temperature. However, below T_c in a field, the CDW order not only becomes stronger, but also becomes more coherent, down to a temperature T_{cusp} below which the intensity starts to decrease (Figs 2 and 4). All of this is clear evidence for competition between CDW and superconducting orders.

Non-resonant X-ray diffraction is sensitive to modulations of charge density and magnetic moments. In our case, the expected magnetic cross-section is several orders of magnitude smaller than our observed signal, which must therefore be due to charge scattering. NMR measurements on a sample of the same composition as ours[13] indicate that the CDW is not accompanied by magnetic order, and this is confirmed by soft X-ray measurements, which would also be sensitive to fluctuating order[14]. Charge density modulations in solids will always involve both a modulation of the electronic charge and a periodic displacement of the atomic positions[15]. We are more sensitive to the atomic displacements than to the charge modulation because ions with large numbers of electrons (as in YBCO) dominate the scattering (see Supplementary Information).

NMR data[13] suggest that CDW order only appears below $T \approx 67$ K and $H > 9$ T, whereas with X-rays we observe CDW order in zero field up to 135 K. This apparent discrepancy may arise from differing timescales of various probes (see Supplementary Information for further discussion). X-ray diffraction experiments are usually interpreted as measuring the static order of a given structure, but, if performed with wide energy acceptance, are also sensitive to short-lived structures. Thus, it is possible that the observed CDW is quasi-static and only frozen on the NMR timescale (≈3 ns) at high fields and lower temperatures.

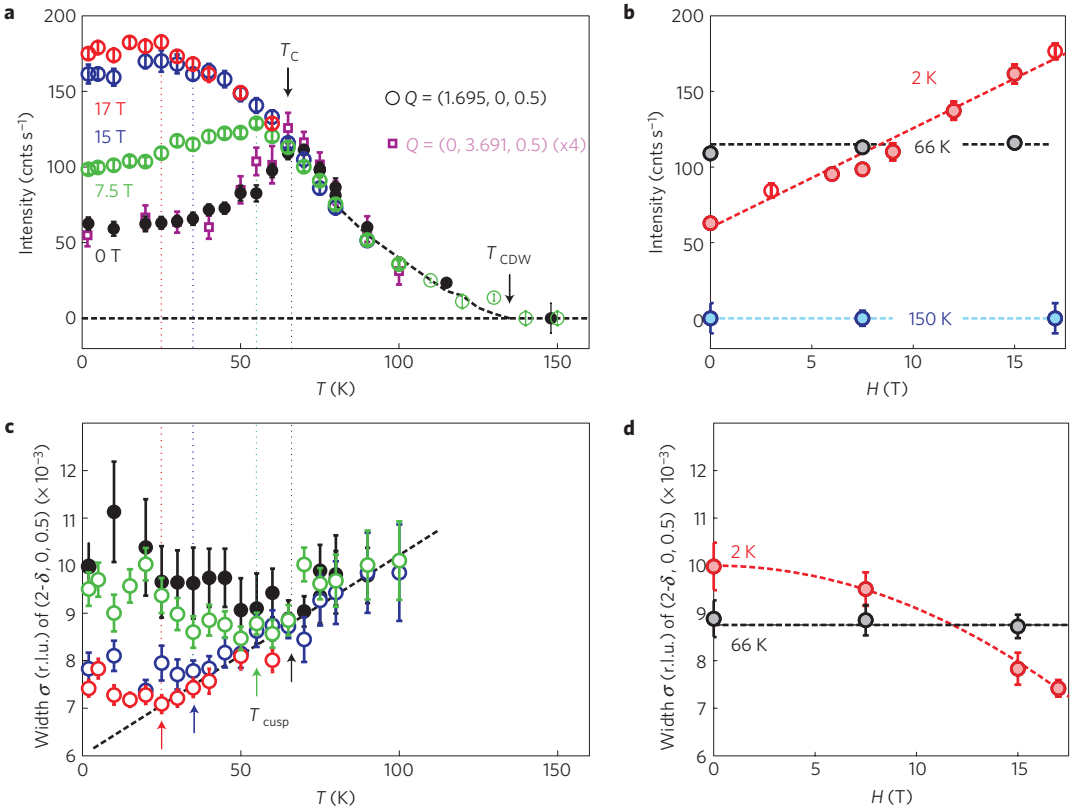

Figure 2 | Competition between charge-density-wave order and superconductivity. a, Temperature dependence of the peak intensity at (1.695, 0, 0.5) (circles) and (0, 3.691, 0.5) (squares) for different applied magnetic fields. The square data points have been multiplied by a factor of four. In the normal state, there is a smooth onset of the CDW order. In the absence of an applied magnetic field there is a decrease in the peak intensity below T_c. This trend can be reversed by the application of a magnetic field. **b**, Magnetic field dependence of the lattice modulation peak intensity at (1.695,0,0.5) for different temperatures. At $T = 2$ K, the peak intensity grows approximately linearly with magnetic field up to the highest applied field. **c**,**d**, Gaussian linewidth of the (1.695, 0, 0.5) CDW modulation plotted versus temperature and field respectively. The raw linewidth, including a contribution from the instrumental resolution, is field-independent in the normal state ($T > T_c$). In contrast, the CDW order becomes more coherent below T_c, once a magnetic field is applied. This effect ceases once the amplitude starts to be suppressed owing to competition with superconductivity. The vertical dashed lines in **a**,**c** illustrate the connection between these two features of the data that define the T_{cusp} temperatures. All other lines are guides to the eye. Error bars indicate standard deviations of the fit parameters described in Methods.

The intensities of the incommensurate Bragg peaks are sensitive to atomic displacements parallel to the total scattering vector **Q**. The comparatively small contribution to **Q** along the c^* direction from $l = 0.5$ r.l.u. means that our signal for a (h, 0, 0.5) peak is dominated by displacements parallel to the a direction. (There will also be displacements parallel to the c direction but we are essentially insensitive to them in our present scattering geometry). Our data indicate that the incommensurate peaks are much stronger if they are satellites of strong Bragg peaks of the form ($\boldsymbol{\tau} = (2n, 0, 0)$) at positions such as $\boldsymbol{\tau} \pm \mathbf{q}_1$. This indicates that the satellites are caused by a modulation of the parent crystal structure. The fact that the scattering is peaked at $l = \pm 0.5$ r.l.u. means that neighbouring bilayers are modulated in antiphase. The two simplest structures (Fig. 3a,b) compatible with our data (see Supplementary Information) involve the neighbouring CuO_2 planes in the bilayer being displaced in the same (bilayer-centred) or opposite (chain-centred) directions, resulting in the maximum amplitude of the modulation being on the CuO_2 planes or CuO chains respectively. In their $2-\mathbf{q}$ form, these structures would lead to the in-plane 'checkerboard' pattern shown in Fig. 3c. Scanning tunnelling microscopy studies of other underdoped cuprates[16] and of field-induced CDW correlations in vortex cores[17] also support the tendency towards checkerboard formation[18], although disorder can cause small stripe domains to mimic checkerboard order[19]. Our observation of a CDW may be related to phonon anomalies[20], which suggest that in YBCO near $p \approx 1/8$ there are anomalies in the underlying charge susceptibility for $\mathbf{q} \approx (0, 0.3)$.

Cuprate superconductors show strong spin correlations, and the interplay between spin and charge correlations may be at the heart of the high-T_c phenomenon. The spin correlations are largely dynamic, with energies up to several hundred meV. $YBa_2Cu_3O_{6+x}$ and $La_{2-x}(Ba, Sr)_xCuO_{4+\delta}$ show incommensurate magnetic order, which can be enhanced by suppressing superconductivity with an applied magnetic field[21–24]; this has some analogies with the CDW order observed here. The magnetic order is static on the ~1 meV frequency scale of neutron diffraction and has been detected in lightly doped $YBa_2Cu_3O_{6+x}$ for $p \leq 0.082$ (ref. 21), and moderately doped $La_{2-x}Sr_xCuO_4$ for $p \leq 0.14$ (ref. 24). The $YBa_2Cu_3O_{6.67}$ ($p \approx 1/8$) sample studied here is expected to have a relatively large spin gap, $\hbar\omega \approx 20$ meV (ref. 25), in its magnetic excitations at low temperature, making it unlikely that it orders magnetically. As discussed earlier, this is confirmed by other measurements[13,14], so the CDW does not seem to be accompanied by spin order. Moreover, there is no obvious relationship between $\mathbf{q}_{CDW}$ and the wave vector of the incipient spin fluctuations $\mathbf{q}_{SF} \approx (0.1, 0)$ of similarly doped samples[25].

It is interesting to note that T_{CDW} corresponds approximately with T_H (Fig. 4), the temperature at which Hall effect measurements suggest that Fermi surface reconstruction begins[26]. A CDW that

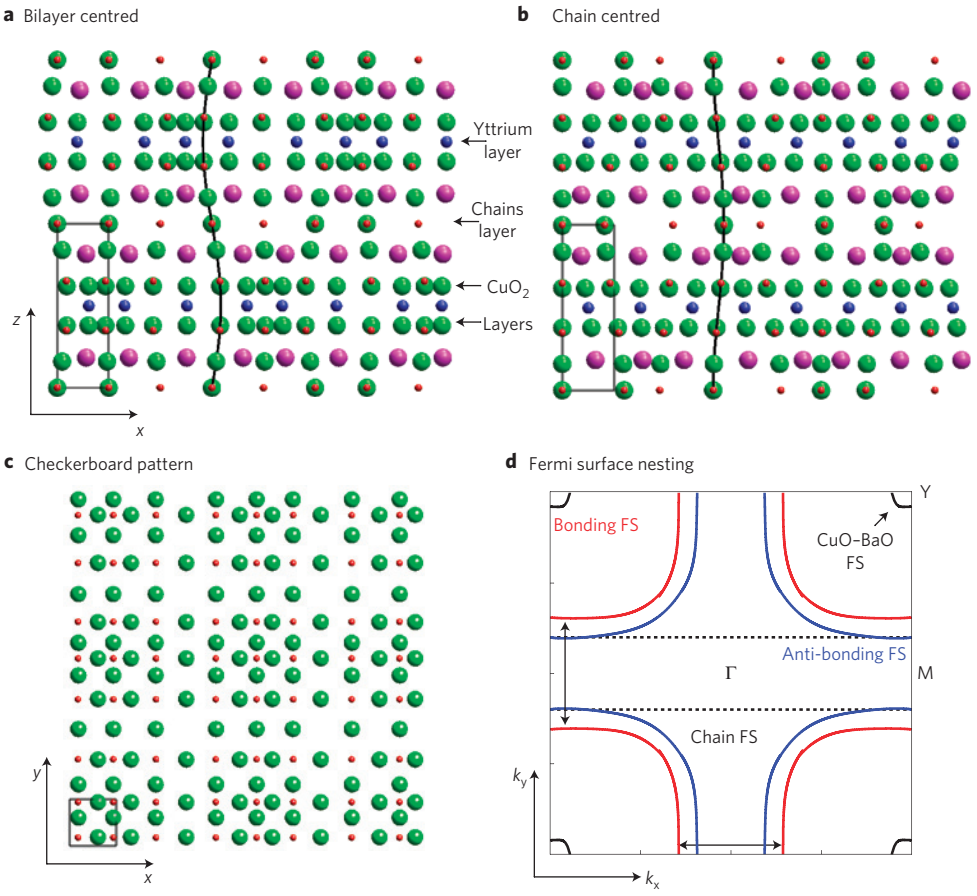

Figure 3 | Real space and reciprocal space pictures. a,**b**, One dimensional atomic displacements (exaggerated for clarity—the estimated amplitude is ~0.003 Å, see Supplementary Information) in the unit cell of YBCO ortho-VIII. The positions of yttrium (blue), barium (purple), copper (red) and oxygen (green) atoms are shown as a function of *x* (Cu–O bond direction) and *z* perpendicular to the CuO_2 planes. The structure in **a** has maximal displacement on the yttrium site and the displacement is the same in the two bilayer CuO_2 planes. In **b**, the structure has maximal displacement at CuO-chain positions and the displacement is opposite within the bilayer planes. Notice that the displacements in neighbouring bilayers are in anti-phase and the CuO chains are modulated with the ortho-VIII structure. **c**, Modulations along both Cu–O bond directions (*x* and *y*) lead to a checkerboard structure. **d**, Schematic of the Fermi surface (FS) of YBCO (based on ref. 28–see Supplementary Information). It consists of bonding (red) and anti-bonding (blue) sheets originating from the CuO_2 bilayer planes, one-dimensional open sheets from the oxygen chains and possible small pockets around the *Y*-point from the CuO–BaO layers. Coupling of the bonding states (indicated by vertical and horizontal arrows) favours the bilayer-centred structure, although this is in competition with intra-bilayer Coulomb effects (see Supplementary Information). Recent resonant X-ray scattering on an ortho-III sample also suggests that the CDW originates from the CuO_2 planes[32]. The arrows connecting the bonding bands near the zone boundary are compatible with the CDW vectors $\mathbf{q}_1 = (\delta_1, 0, 0.5)$ and $\mathbf{q}_2 = (0, \delta_2, 0.5)$ if the Fermi surface has a small dispersion along $\mathbf{k}_z$.

breaks translational symmetry provides a natural mechanism for Fermi surface reconstruction and the formation of pockets. From the negative Hall and Seebeck coefficients[10,11,26], it was inferred that the Fermi pocket observed by quantum oscillations[9] is electron-like[10]. The exact structure of the low-temperature reconstructed Fermi surface is still debated, although recent high-field specific heat experiments place constraints on the possibilities and suggest a small number of pockets[27] (see Supplementary Information). It is interesting to compare the LDA Fermi surface of YBCO (ref. 28) with $\mathbf{q}_{CDW}$ (Fig. 3d and Supplementary Information). The electronic states most obviously connected by $\mathbf{q}_{CDW}$ are the bonding bands at and near the zone boundary, which lie near the anti-nodal region of the superconducting gap, where the pseudogap is also maximized.

Our results have important implications for the phenomenology and phase diagram of the cuprates (Fig. 4). A simple Landau theory (see Supplementary Information) shows that T_c will be suppressed below the value it would have in the absence of the CDW. We speculate that this is reflected in the shape of the superconducting dome[12] (Fig. 4). One of the defining properties of underdoped cuprates such as ortho-VIII YBCO is the pseudogap. This develops at the 'crossover' temperature T^* (for $YBa_2Cu_3O_{6.67}$, $T^* \approx 220$ K), where there is a suppression of low-energy electronic states, evidence for '$Q = 0$' magnetic order[29] and rotational anisotropy appears in various physical properties, such as the Nernst effect[30]. The CDW reported here develops at $T_{CDW} \approx 135$ K, inside the pseudogap state. From Fig. 2a,c we can identify the temperature $T_{cusp}(H)$ where the suppression of the CDW begins. The level of this competition indicates that the CDW and superconductivity have similar energy scales (10–30 meV), unlike $NbSe_2$ where the CDW order is not significantly suppressed by superconductivity[4]. $T_{cusp}(H)$ (Fig. 4) seems to correspond to the temperature $T_n(H)$ at which superconductivity in the mixed state can be identified from transport measurements rather than the appearance of zero resistance.

We draw attention to the situation in the cuprates that many different kinds of order, such as superconductivity, pseudogap, CDW and antiferromagnetism, occur on comparable temperature scales. When they compete, they do so on an almost equal footing. We may suspect that this is not accidental, and that

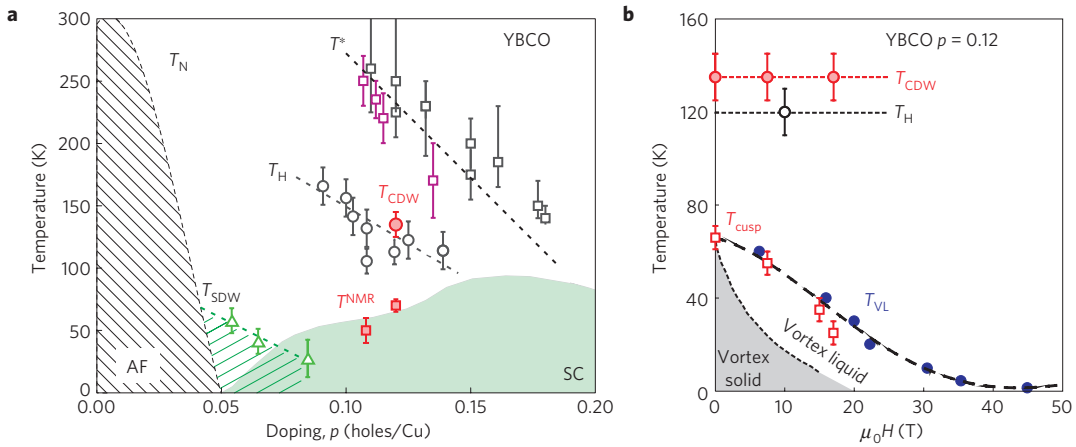

Figure 4 | Phase diagram of $YBa_2Cu_3O_{7-x}$. **a**, Doping dependence of the antiferromagnetic ordering temperature T_N, the incommensurate spin-density wave order T_{SDW} (green triangles; ref. 21), the superconducting temperature T_c and the pseudogap temperature T^* as determined from the Nernst effect[30] (black squares) and neutron diffraction[29] (purple squares). Notice that the Nernst effect[30] indicates a broken rotational symmetry inside the pseudogap region, whereas a translational symmetry preserving magnetic order is found by neutron scattering[29]. Below temperature scale T_H (black circles), a larger and negative Hall coefficient was observed[26] and interpreted in terms of a Fermi surface reconstruction. Our X-ray diffraction experiments show that in YBCO $p = 0.12$ incommensurate CDW order spontaneously breaks the crystal translational symmetry at a temperature T_{CDW} that is twice as large as T_c. T_{CDW} is also much larger than T^{NMR} (red squares), the temperature scale below which NMR observes field-induced charge order[13]. **b**, Field dependence of T_{CDW} (filled red circles) and T_{cusp} (open squares), the temperature below which the CDW is suppressed by superconductivity, compared with T_H (open black circle) and T_{VL} (filled blue circles), the temperature where the vortex liquid state forms[26]. Error bars on T_{SDW}, T_H, T_{NMR}, and T^* are explained in refs 21,26,30,33. The error bars on T_{CDW} and T_{cusp} reflect the uncertainty in determining the onset and suppression temperature of CDW order from Fig. 2.

these various orders are 'intertwined'[31]. In this context, we can view our present results as indicating that the electron system has a tendency towards two ground states: a charge density wave, which breaks translational symmetry and involves electron–hole correlations, versus superconductivity, which breaks gauge symmetry and involves electron–electron correlations. We note that the **q**-vectors of the CDW lie close to the separation of pieces of Fermi surface that have maximum superconducting gap at optimal doping and have the same sign of the order parameter.

Methods

Our experiments used 100 keV hard X-ray synchrotron radiation from the DORIS-III storage ring at DESY, Hamburg, Germany. We installed a recently developed 17 T horizontal cryomagnet designed for beamline use on the triple-axis diffractometer at beamline BW5. The sample was mounted by gluing it over a hole in a temperature-controlled aluminium plate within the cryomagnet vacuum and was thermally shielded by thin Al and aluminized mylar foils glued to this plate. The sample temperature could be controlled over the range ~2–300 K. The incoming and outgoing beams passed through 1 mm thick aluminium cryostat vacuum windows, which gave a maximum of $\sim \pm 10°$ input and output angles relative to the field direction, which was parallel to the sample c axis within $<1°$. Between the beam access windows and the sample plate, there were further aluminium foil thermal radiation shields at liquid nitrogen temperature. A 2 mm square aperture collimated the incoming beam, so that it passed mainly through the part of the sample over the hole in the aluminium plate, greatly reducing background scattering by the plate. Further slits before the analyser and the detector removed scattering by the cryostat windows and nitrogen shields. The scattering plane (a^*–c^*) was horizontal. The cryomagnet was mounted on a rotation stage with a goniometer giving χ tilt about the field axis. The sample was initially mounted with its a axis nearly horizontal. The χ goniometer allowed the exact alignment of this axis using the (2 0 0) Bragg peak and could also be used for low-resolution scans in the b^* direction. Magnetic fields were applied with the sample heated above T_c; it was then field-cooled to base temperature. When fields were applied, minor changes in the position and angle of the sample holder were observed; these were corrected by use of horizontal and vertical motion stages under the cryostat rotation stage, and by realigning on the (2 0 0) Bragg peak. During temperature scans, realignment on the (2 0 0) Bragg peak was performed automatically at every temperature point to ensure that all measurements were centred. After results had been obtained with the a axis horizontal, the sample was remounted with the b axis horizontal for further measurements. The $YBa_2Cu_3O_{6.67}$ sample had dimensions $a \times b \times c = 3.1 \times 1.7 \times 0.6\ mm^3$ and mass 18 mg. The superconducting transition temperature $T_c = 67$ K (width: 10%–90% = 1.1 K) was derived from a zero-field-cooled magnetization curve at 0.1 mT. The single crystal was 99% detwinned and the Cu–O chains were ordered with the ortho-VIII structure by standard procedures[12].

The diffracted intensities from the CDW, shown in Fig. 1, are composed of an incommensurate lattice modulation peak on a smoothly varying background. The background along (h, 0, 0.5) mainly originates from the tails of the ortho-VIII peaks (see Supplementary Information). It varies strongly from one Brillouin zone to another; for example, the background around (2.7, 0, 0.5) is an order of magnitude larger than around (1.7, 0, 0.5). The background has essentially no field dependence (Fig. 1a–c) so subtracting the zero-field from high-field data is a simple way to eliminate the background. This reveals the field-enhanced signal inside the superconducting state (Fig. 1a–d).

As there is a weak temperature dependence in the background (Fig. 1a–c), it is not possible to eliminate it by subtracting a high-temperature curve. Therefore, to obtain the temperature dependences shown in Fig. 2, we fitted the data to a Gaussian function $G(Q)$ and modelled the background by a second-order polynomial $B(Q) = c_0 + c_1 Q + c_2 Q^2$. The constants c_0, c_1 and c_2 have a small but significant temperature dependence. The low counting statistics resulted in Gaussians fitting equally well as other possible lineshapes such as Lorentzians.

The signal-to-background ratio is best for the $(2-\delta_1, 0, 0.5)$ peak due the weaker structural ortho-VIII peak (see Supplementary Fig. S2). From the Gaussian fits to the $(2-\delta_1, 0, 0.5)$ satellite peak at 2 K and 17 T we can estimate the correlation length ξ along the three crystal axis directions. We define $\xi = 1/\sigma$, where $\sigma = (\sigma^2_{meas} - \sigma^2_R)^{0.5}$ is the measured Gaussian standard deviation corrected for the instrument resolution σ_R and expressed in $Å^{-1}$. Along the a axis direction, we find $\sigma = 6.4 \times 10^{-3}$ r.l.u. $\equiv 1.1 \times 10^{-2}\ Å^{-1}$, and hence $\xi_a = 95 \pm 5$ Å. Deconvolving the poor instrumental resolution along the b axis direction for the $(2-\delta_1, 0, 0.5)$ peak yields a similar correlation length $\xi_b \sim \xi_a$.

Received 18 June 2012; accepted 18 September 2012; published online 14 October 2012

References

1. Mathur, N. D. *et al.* Magnetically mediated superconductivity in heavy fermion compounds. *Nature* **394,** 39–43 (1998).
2. Kivelson, S. A. *et al.* How to detect fluctuating stripes in the high-temperature superconductors. *Rev. Mod. Phys.* **75,** 1201–1241 (2003).
3. Vojta, M. Lattice symmetry breaking in cuprate superconductors: Stripes, nematics, and superconductivity. *Adv. Phys.* **58,** 699–820 (2009).
4. Moncton, D. E., Axe, J. D. & DiSalvo, F. J. Neutron scattering study of the charge–density wave transitions in 2H–$TaSe_2$ and 2H–$NbSe_2$. *Phys. Rev. B* **16,** 801–819 (1977).
5. Demler, E., Sachdev, S. & Zhang, Y. Spin-ordering quantum transitions of superconductors in a magnetic field. *Phys. Rev. Lett.* **87,** 067202 (2001).
6. Tranquada, J. M. *et al.* Evidence for stripe correlations of spins and holes in copper oxide superconductors. *Nature* **375,** 561–563 (1995).

7. Fujita, M., Goka, H., Yamada, K., Tranquada, J. M. & Regnault, L. P. Stripe order, depinning, and fluctuations in $La_{1.875}Ba_{0.125}CuO_4$ and $La_{1.875}Ba_{0.075}Sr_{0.05}CuO_4$. *Phys. Rev. B* **70,** 104517 (2004).
8. Von Zimmermann, M. *et al.* Oxygen-ordering superstructures in underdoped $YBa_2Cu_3O_{6+x}$ studied by hard x-ray diffraction. *Phys. Rev. B* **68,** 104515 (2003).
9. Doiron-Leyraud, N. *et al.* Quantum oscillations and the Fermi surface in an underdoped high-T_c superconductor. *Nature* **447,** 565–568 (2007).
10. LeBoeuf, D. *et al.* Electron pockets in the Fermi surface of hole-doped high-T_c superconductors. *Nature* **450,** 533–536 (2007).
11. Laliberté, F. *et al.* Fermi-surface reconstruction by stripe order in cuprate superconductors. *Nature Commun.* **2,** 432 (2011).
12. Liang, R. *et al.* Evaluation of CuO_2 plane hole doping in $YBa_2Cu_3O_{6+x}$ single crystals. *Phys. Rev. B* **73,** 180505 (2006).
13. Wu, T. *et al.* Magnetic-field-induced charge-stripe order in the high-temperature superconductor $YBa_2Cu_3O_y$. *Nature* **477,** 191–194 (2011).
14. Ghiringhelli, G. *et al.* Long-range incommensurate charge fluctuations in $(Y,Nd)Ba_2Cu_3O_{6+x}$. *Science* **337,** 821–825 (2012).
15. Abbamonte, P. Charge modulations versus strain waves in resonant x-ray scattering. *Phys. Rev. B* **74,** 195113 (2006).
16. Schmidt, A. R. *et al.* Electronic structure of the cuprate superconducting and pseudogap phases from spectroscopic imaging. *New J. Phys.* **13,** 065014 (2011).
17. Hoffman, J. E. *et al.* A four unit cell periodic pattern of quasi-particle states surrounding vortex cores in $Bi_2Sr_2CaCu_2O_{8+\delta}$. *Science* **295,** 466–469 (2002).
18. Wise, W. D. *et al.* Charge-density-wave origin of cuprate checkerboard visualized by scanning tunnelling microscopy. *Nature Phys.* **4,** 696–699 (2008).
19. Robertson, J. A. *et al.* Distinguishing patterns of charge order: Stripes or checkerboards. *Phys. Rev. B* **74,** 134507 (2006).
20. Reznik, D. *et al.* Electron-phonon coupling reflecting dynamic charge inhomogeneity in copper oxide superconductors. *Nature* **440,** 1170–1173 (2006).
21. Haug, D. *et al.* Neutron scattering study of the magnetic phase diagram of underdoped $YBa_2Cu_3O_{6+x}$. *New J. Phys.* **12,** 105006 (2010).
22. Lake, B. *et al.* Antiferromagnetic order induced by an applied magnetic field in a high-temperature superconductor. *Nature* **415,** 299–302 (2002).
23. Khaykovich, B. *et al.* Enhancement of long-range magnetic order by magnetic field in superconducting La_2CuO_{4+y}. *Phys. Rev. B* **66,** 014528 (2002).
24. Chang, J. *et al.* Tuning competing orders in $La_{2-x}Sr_xCuO_4$ cuprate superconductors by the application of an external magnetic field. *Phys. Rev. B* **78,** 104525 (2008).
25. Dai, P., Mook, H. A., Hunt, R. D. & Dogan, F. Evolution of the resonance and incommensurate spin fluctuations in superconducting $YBa_2Cu_3O_{6+x}$. *Phys. Rev. B* **63,** 054525 (2001).
26. LeBoeuf, D. *et al.* Lifshitz critical point in the cuprate superconductor $YBa_2Cu_3O_y$ from high-field Hall effect measurements. *Phys. Rev. B* **83,** 054506 (2011).
27. Riggs, S. C. *et al.* Heat capacity through the magnetic-field-induced resistive transition in an underdoped high-temperature superconductor. *Nature Phys.* **7,** 332–335 (2011).
28. Carrington, A. & Yelland, E. A. Band-structure calculations of Fermi-surface pockets in ortho-II $YBa_2Cu_3O_{6.5}$. *Phys. Rev. B* **76,** 140508 (2007).
29. Li, Y. *et al.* Unusual magnetic order in the pseudogap region of the superconductor $HgBa_2CuO_{4+\delta}$. *Nature* **455,** 372–375 (2008).
30. Daou, R. *et al.* Broken rotational symmetry in the pseudogap phase of a high-T_c superconductor. *Nature* **463,** 519–522 (2010).
31. Berg, E., Fradkin, E., Kivelson, S. A. & Tranquada, J. M. Striped superconductors: How spin, charge and superconducting orders intertwine in the cuprates. *New J. Phys.* **11,** 115004 (2009).
32. Achkar, A. J. *et al.* Distinct charge orders in the planes and chains of ortho-III ordered $YBa_2Cu_3O_{6+\delta}$ identified by resonant elastic x-ray scattering. Preprint at http://arxiv.org/abs/1207.3667.
33. Chang, J. *et al.* Nernst effect in the cuprate superconductor $YBa_2Cu_3O_y$: Broken rotational and translational symmetries. *Phys. Rev. B* **84,** 014507 (2011).

Acknowledgements

We thank B. L. Gyorffy, M. W. Long, J. A. Wilson, A. J. Schofield, J. R. Cooper, J. W. Loram, S. A. Kivelson, L. Taillefer, C. Bourbonnais, C. Proust and A. Kapitulnik for discussions and R. Nowak, G. R. Walsh and J. Blume for technical assistance. This work was supported by the EPSRC (grant numbers EP/G027161/1 and EP/J015423/1), the Wolfson Foundation, the Royal Society, the Danish Agency for Science, Technology and Innovation under DANSCATT and the Swiss National Science Foundation through NCCR-MaNEP and grant number PZ00P2_142434. J.C., N.B.C. and J.M. are grateful to L. Braicovich, G. Ghiringhelli, B. Keimer and M. Le Tacon for communicating their results to them after this experiment was completed.

Author contributions

D.A.B., W.N.H. and R.L., prepared the samples. E.B., J.C., N.B.C., E.M.F., S.M.H., M.v.Z. and A.W. conceived and planned the experiment. E.B., J.C., N.B.C., E.M.F., S.M.H., A.T.H., J.L. and M.v.Z. carried out the experiment. J.C., E.M.F. and S.M.H. carried out data analysis and modelling. E.B, J.C., N.B.C., E.M.F and S.M.H. wrote the paper. J. M. was responsible for research direction and planning at PSI. All authors discussed the results and commented on the manuscript.

Additional information

Supplementary information is available in the online version of the paper. Reprints and permissions information is available online at www.nature.com/reprints. Correspondence and requests for materials should be addressed to J.C.

Competing financial interests

The authors declare no competing financial interests.

Direct proof of unique magnetic and superconducting phases in superoxygenated high-T_c cuprates

L. Udby,[1] J. Larsen,[2] N. B. Christensen,[2] M. Boehm,[3] Ch. Niedermayer,[4] H. E. Mohottala,[5]
T. B. S. Jensen,[2] R. Toft-Petersen,[2,6] F. C. Chou,[7] N. H. Andersen,[2] K. Lefmann,[1] and B. O. Wells[8]

[1] *Nanoscience Center, Niels Bohr Institute, University of Copenhagen, DK-2100 Copenhagen, Denmark*
[2] *Department of Physics, Technical University of Denmark, DK-2800 Kgs. Lyngby, Denmark*
[3] *Institut Laue-Langevin, 38042 Grenoble Cedex 9, France*
[4] *Laboratory for Neutron Scattering, Paul Scherrer Institut, CH-5232 VIlligen PSI, Switzerland*
[5] *University of Hartford, West Hartford, Connecticut 06117, USA*
[6] *Helmholtz Zentrum Berlin für Materialien und Energie, D-14109 Berlin, Germany*
[7] *Center for Condensed Matter Sciences, National Taiwan University, Taipei 10617, Taiwan*
[8] *Department of Physics, University of Connecticut, Storrs, Connecticut 06269-3046, USA*

We present a combined magnetic neutron scattering and muon spin rotation study of the nature of the magnetic and superconducting phases in electronically phase separated $La_{2-x}Sr_xCuO_{4+y}$, x = 0.04, 0.065, 0.09. For all samples, we find long-range modulated magnetic order below $T_N \simeq Tc$ = 39 K. In sharp contrast with oxygen-stoichiometric $La_{2-x}Sr_xCuO_4$, we find that the magnetic propagation vector as well as the ordered magnetic moment is independent of Sr content and consistent with that of the 'striped' cuprates. Our study provides direct proof that superoxygenation in $La_{2-x}Sr_xCuO_{4+y}$ allows the spin stripe ordered phase to emerge and phase separate from superconducting regions with the hallmarks of optimally doped oxygen-stoichiometric $La_{2-x}Sr_xCuO_4$.

PACS numbers: 74.72.Gh, 74.25.Ha, 75.25.-j,74.10.+v

The many active degrees of freedom in transition metal oxides lead to intrinsic complexity with different electronic states being nearly degenerate. As a consequence nanoscale phase separation can be observed in such different materials as the CMR manganites and high-temperature superconducting (HTSC) cuprates [1, 2]. A central challenging theme is how dopant disorder influences the details of the phase separation in otherwise electronically similar systems and e.g. pins fluctuating order [3]. We adress this issue by investigating the electronic properties of a HTSC system with two essentially different mechanisms of charge-carrier doping i.e. mobile oxygen ions and immobile Sr ions.

Starting from the Mott insulating and antiferromagnetic parent compound La_2CuO_4 (LCO), replacement of La by Sr leads to superconductivity above $x = 0.055$ in $La_{2-x}Sr_xCuO_4$ (LSCO) with the highest superconducting transition temperature, $T_c = 38$ K at $x \simeq 0.15$ (optimal doping) [4]. On the other hand, intercalation of a sufficient amount of excess oxygen in Sr-free samples to produce La_2CuO_{4+y} (LCO+O) leads to even higher $T_c \simeq 42$ K [5] and less flux-pinning [6]. The origin of the differences in superconducting properties lies in the nature of the doping-processes: When oxygen-stoichiometric LSCO is formed by cooling through the liquid-solid phase transition at temperatures far above room temperature, a homogeneous but quenched disordered distribution of Sr on La sites is produced. By contrast, intercalated oxygen remains mobile down to much lower temperatures [7] where it tends to organise in well-ordered superstructures that can be observed in diffraction experiments [8], and over which there is a partial degree of control [9, 10]. Combining magnetisation and muon spin rotation, we have recently discovered that even in samples containing quenched disordered Sr, intercalated oxygen facilitates optimal superconducting properties ($T_c^{onset} \simeq 40$ K and weak pinning) [11, 12]. It does so by promoting phase separation between regions of the sample that are non-magnetic (and superconducting) and regions with magnetic order. The local magnetic fields around the muon stopping site are similar [11] to those of the so-called stripe ordered materials $(La,Nd)_{15/8}Sr_{1/8}CuO_4$ (LNSCO) and $La_{15/8}Ba_{1/8}CuO_4$ (LBCO) [13]. From elastic neutron scattering (ENS) experiments on these materials it is known that the magnetic order is characterised by two incommensurate magnetic propagation vectors, corresponding to two domains of modulated antiferromagnetic order [14–16]. An ENS study on LSCO+O, $x = 0.09$ reveal similar peaks [17], but a systematic exposition of the nature and possible evolution of magnetic and superconducting states in LSCO+O has been lacking.

In this Letter we present a ENS study of the magnetic properties of LSCO+O single crystals covering a broad range of Sr content, and investigate the superconducting properties using high transverse field muon spin rotation (HTF-μSR). Using neutrons as a bulk-sensitive probe of magnetism, we provide direct evidence for the identity of the magnetic phases of our LSCO+O samples in terms of propagation vector and ordered magnetic moment. Moreover, we show that these characteristics are the same as those of stripe-ordered LNSCO and LBCO. Further, we find that the superconducting penetration depth of all samples are identical within our experimen-

tal errors and of a magnitude similar to that of optimally doped oxygen-stoichiometric LSCO.

All samples studied are the same single crystals also used in [11] with $x = 0.04, 0.065, 0.09$. They were float-zone grown in an optical furnace and post-oxidised (superoxygenated) through wet-chemical methods [5, 8]. The intercalation process was stopped after a long period of oxidation, always after the sample showed a single transition of T_c^{onset} ∼40 K as recorded by SQUID measurements. The ENS studies were performed at the cold triple-axis spectrometers RITA-II and IN14 at the Paul Scherrer Institute (PSI), Switzerland and the Institut Laue-Langevin, France, respectively. Both spectrometers employed elastic scattering mode with $E_i = E_f = 5$ meV and 40' horizontal collimation before and after the sample. Be-filters removed higher-order contamination scattering from the monochromators. All Miller indices in this work refer to the orthorhombic *Bmab* notation in reciprocal lattice units [rlu] based on the low temperature lattice parameters [18]. The muon data were recorded at the General Purpose Surface-Muon Instrument at PSI using a high (0.3 T) transverse field after fast (>1 K/min) cooling, since the SC properties are known not to change with cooling rate for the investigated crystals.

To set the stage for LSCO+O, we start by summarising the magnetic properties of oxygen-stoichiometric LSCO: In the magnetic phase the modulation period and direction depends strongly on Sr content x and a quartet of peaks are detected by ENS with $\delta \propto x$ [19] away from the anti-ferromagnetic position corresponding to modulated anti-ferromagnetic (m-AFM) order in the CuO planes. For $0.024 \lesssim x \lesssim 0.055$ the spin structure is rotated i.e modulated diagonally with respect to the Cu-O bonds [20–22]. For $x > 0.055$ the modulation is parallel to the Cu-O bonds with incommensurability saturating at $\delta \simeq 1/8$ for $x \simeq 1/8$ [19]. Long-range magnetic order with correlation length $\xi > 100$ Å is only found for $x \simeq 1/8$. In striking contrast with these characteristics of LSCO, Figure 1 shows several key results of our study: In all the investigated superoxygenated LSCO+O samples through the Sr doping range $x = 0.04 - 0.09$ at $T \sim 2$ K, we have observed a quartet of peaks by ENS at the *same* positions. The peaks at $\mathbf{Q} = (1 + \delta_H, \delta_K, 0)$ are compared in the left panel of Figure 1. We find for all x that the peaks are located $\delta_H \sim \delta_K \sim \delta = 0.123 \pm 0.004$ away from the antiferromagnetic point. This corresponds to m-AFM with periodicity of 8.1(3) unit cells parallel the Cu-O bonds as is also found in oxygen-stoichiometric LSCO $x \simeq 1/8$. That the incommensurability δ and the modulation direction is always the same in LSCO+O regardless of Sr doping x is however opposed to what is observed in oxygen-stoichiometric LSCO. The peaks of LSCO+O are sharp and instrumentally resolved for $x < 0.09$ as seen in the left panel of Figure 1. For $x = 0.09$ there is however a ∼30% broadening which we previously found to result from the finite size of the m-AFM domains in the sample [17, 23]. These domains are, however, at least 300−400 Å for all x. This periodicity and long correlation lengths of the m-AFM signal are similar to those of the zero-field magnetic signal observed in LCO+O [24, 25], oxygen stoichiometric LSCO with $x \simeq 1/8$ and the parallel stripes found in LNSCO and LBCO [14–16]. The spin correlation lengths in our LSCO+O samples are however much larger than in oxygen stoichiometric LSCO samples with comparable Sr content [19]. The temperature dependence of the m-AFM peak intensity for LSCO+O is shown in the right panel of Figure 1. It follows the same power-law dependence for all $x = 0.04 - 0.09$ with transition temperature $T_N = 39(3)$ K [26] which is also in contrast to oxygen stoichiometric LSCO where the intensity does not follow the usual power-law dependence for the lowest dopings [27] and T_N is much smaller and varies in the same Sr doping range [28].

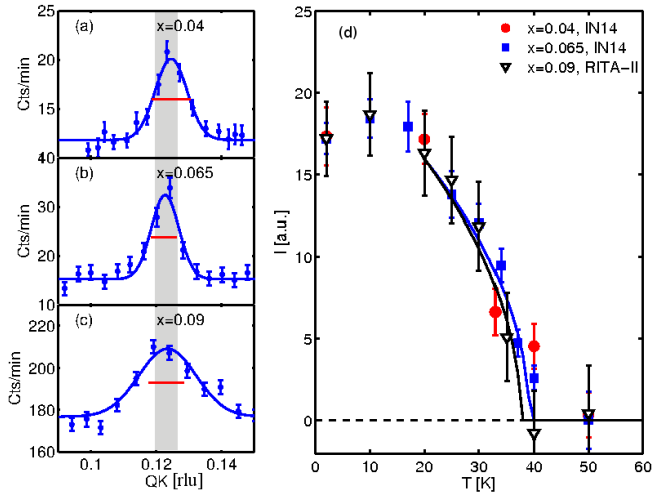

FIG. 1. (Color online) (a-c) ENS scans in reciprocal space through the m-AFM peak at $\mathbf{Q}$=(1+δ_H, δ_K, 0). All data were taken at $T = 2$ K at IN14. Solid lines are Gaussian fits and the horizontal red lines show the resolution as found by corresponding scans through Bragg peaks. The grey shaded region indicates the average peak position as described in the text. (d) Temperature dependence of the intensity of the m-AFM peaks. The intensities are scaled at 2 K. In order to locate T_N, power-law fits with a fixed exponent $\eta = 0.5$ were conducted (lines).

In order to find the magnitude of the ordered magnetic moments from the ENS data we need knowledge of the magnetic volume fractions which can be provided by μSR experiments. The muons stop at specific lattice positions and provide a random sampling of the internal field distribution both in the magnetic volume fraction and the vortex state of the superconducting volume fraction. All μSR data presented in this Letter were fitted with a three-component model for the assymetry following the procedure outlined in [29]. Two of the components are temperature dependent and related to the sample. A third component models the background orig-

inating from e.g. muons stopping in the cryostat walls or sample holder and is assumed to be temperature independent. For details see the supplementary information [18]. The first temperature dependent component models the muons which are rapidly relaxing, i.e. they are being depolarised by the ordered moments in the magnetic volume fraction of each sample for which the derived temperature dependence is shown in the top panels of Figure 2. We note that the magnetic volume fractions begin to grow at the same temperatures at which ENS reveals the onset of m-AFM order, see Figure 1(d), indicating that truly static magnetic order sets in below T_N. The second temperature dependent component is slowly relaxing and originates from the non-magnetic part of the sample. Its temperature dependence is also shown for each sample in the top panels of Figure 2. A slight decrease in precession frequency of this component [18] marks the superconducting onset transition at T_c. At base temperature we assume that all of this component originates from the flux-line lattice in the superconducting volume of the sample. The temperature dependence of the relaxation rate in the non-magnetic volume is shown in Figure 2. For all samples we observe a similar temperature dependence with $\sigma(T \to 0) \sim 0.9\ \mu\mathrm{s}^{-1}$. This value is the expected relaxation value for a superconducting volume with a penetration depth of at least $\lambda \sim 1500$ Å [30] in an optimally doped LSCO sample with a rigid 3D vortex lattice. It is seen from these data that the relaxation rate increases below 40 K in all samples, coinciding with the superconducting transition temperature $T_c = 39(1)$ K. We have confirmed this by AC susceptibility measurements, regardless of the cooling rate. The magnetic and superconducting volume fractions and their transition temperatures are compiled in Table I. We note that the magnetic and superconducting transition temperatures coincide for all x.

x	V_m[%]	V_{SC}[%]	T_N[K]	T_c[K]
0.04	56(4)	44(1)	∼40	39(1)
0.065	19(1)	81(1)	39(1)	38.7(7)
0.09	47(1)	53(1)	38(2)	37.1(5)

TABLE I. Collected μSR results for the magnetic and superconducting base temperature volume fractions, V_m and V_{SC}, respectively, of each sample. T_N and T_c are determined from ENS (Fig. 1) and μSR (Fig. 2 (d-f)), respectively.

We now return to the derivation of the magnetic moment from the ENS data based on the aquired knowledge of the magnetic volume fractions. Table II shows the integrated, mass-normalised peak areas of the m-AFM peaks from the ENS data, and it it seen that the intensity varies substantially, probably due to differences in both magnetic volume fraction and sample mosaic details. Hence, we normalise the m-AFM peaks to the integrated area of a Bragg peak and divide by the magnetic volume fraction to obtain the constant A listed in Table II. It is seen that A is the same for all LSCO+O samples within errors, thus implying they have the same ordered magnetic moment if the same model for the magnetic order can be assumed. We thus turn to the specifics of the symmetry-related peaks in order to motivate a model for the spin-structure. For all LSCO+O samples we have observed peaks at the same positions $\mathbf{Q}_m = (1 \pm \delta_H, 0 \pm \delta_K, 0)$ and $(0 \pm \delta_H, 1 \pm \delta_K, 0)$ indicating a similar spin structure. For the $x = 0.09$ sample, full scans at all above mentioned positions were performed and the data fitted to Gaussian lineshapes as shown in Figure 3. The intensities and widths of all the m-AFM peaks are found to be the same

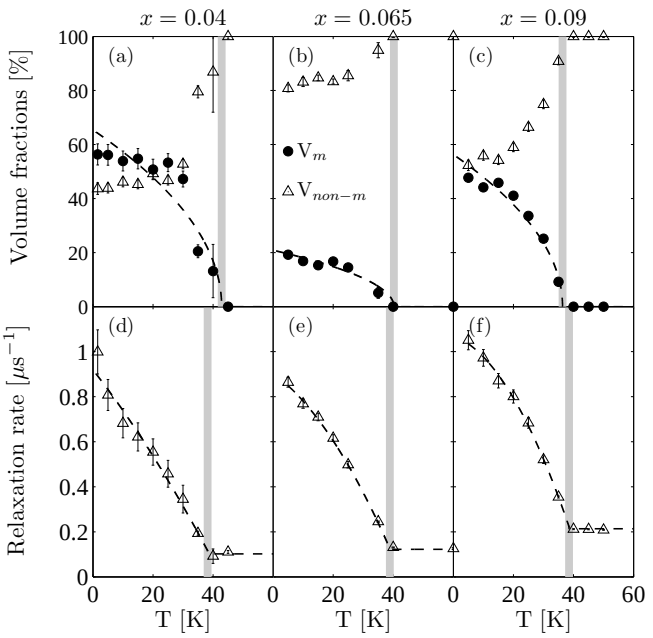

FIG. 2. Results of HTF-μSR experiments. If not visible, the statistical errors are smaller than the datapoint markers. (a-c) Temperature dependence of the magnetic and non-magnetic volume fractions of the sample. Dashed lines are guides to the eye and grey shaded regions mark T_N. (d-f) Temperature dependence of the spin relaxation rate for muons stopping in the superconducting regions of the sample. Following [31] the dashed lines are fits to the function $\sigma_0(1 - aT - bT^2)$ for $T < T_c$. Grey shaded regions mark T_c.

x	m [g]	$I_{IC}[\frac{\mathrm{cts}}{\mathrm{min}\cdot\mathrm{g}}]$	$I_{200}[\frac{\mathrm{cts}}{\mathrm{min}\cdot\mathrm{g}}]$	$A = \frac{I_{IC}}{I_{200}\cdot V_m}$
0.04	0.035	2.9(5)	$3.7(3)\cdot10^4$	$1.4(3)\cdot10^{-4}$
0.065	0.091	2.0(3)	$6.4(2)\cdot10^4$	$1.6(3)\cdot10^{-4}$
0.09	0.415	1.7(3)	$2.0(1)\cdot10^4$	$1.8(3)\cdot10^{-4}$

TABLE II. Mass (m), mass-normalized IC AFM and nuclear Bragg peak intensities, I_{IC} and I_{200}, respectively. The intensities derive from Gaussian fits to data taken under identical experimental conditions at IN14. The last column shows I_{IC} normalized by the product of I_{200} and the magnetic volume fraction V_m.

within two standard deviations as is also observed for the spin stripes in LNSCO [16] and LBCO [32]. We therefore assume, analogously to LNSCO, that the m-AFM peaks in LSCO+O in one direction can be represented by a simple collinear spin stripe model and the other set of peaks in the quartet are generated by 90° rotation beween alternating CuO planes. For each CuO plane we consider a 8×2 Cu-site unit cell $[\uparrow\downarrow\uparrow \cdot \downarrow\uparrow\downarrow \cdot ; \downarrow\uparrow\downarrow \cdot \uparrow\downarrow\uparrow \cdot]$ where the moments are lying in the CuO plane with angle β with $\mathbf{Q}_m$. Then the magnetic structure factor is given by $|F_m|^2 = p^2 f_m^2 \mu^2 \sin^2\beta |\tilde{F}_m|^2$. For S=1/2 spins we have $p = 0.2696 \cdot 10^{-14}$ m, and the form factor for Cu^{2+} and geometrical structure factor take the values $f_m = 0.90(5)$ [33] and $|\tilde{F}_m|^2 = 93.25$ at the m-AFM points. Details of this and the following calculations are shown in the supplematary material [18]. Based on the experimentally determined factor A in Table II we find the ordered moment in units of Bohr magnetons to be

$$\mu = \sqrt{|F_m|^2 / p^2 f_m^2 \sin^2\beta \left|\tilde{F}_m\right|^2} = 0.10(2)\sqrt{C}/\sin\beta \quad (1)$$

Assuming that the spins are weakly correlated between neighboring CuO planes, the vertical resolution correction gives $C \simeq 1.4$ [18] and we obtain $\mu = 0.12(2)\mu_B$ for spins oriented along [010] ($\sin\beta = 0.99$) as in La_2CuO_4 [34] and $\mu = 0.14(3)\mu_B$ for spins oriented along [110] ($\sin\beta = 0.7(1)$), as observed in LNSCO [16]. If the scattering intensity is approximately constant along c^* (scattering rods) due to e.g. twinning as seen in LCO+O [24] we have $C \simeq 2.7$ and the quoted ordered moments must be corrected by a numerical factor ~ 1.4. In the absence of experimental information about the c-axis magnetic correlations, we restrain ourselves to the conclusion that the ordered magnetic moments in the magnetic volume fractions of LSCO+O are of the same order of magnitude as the those determined for LCO+O ($\mu = 0.15(5)\mu_B$ [24]) and stripe ordered LNSCO ($\mu = 0.10(3)\mu_B$ [35]).

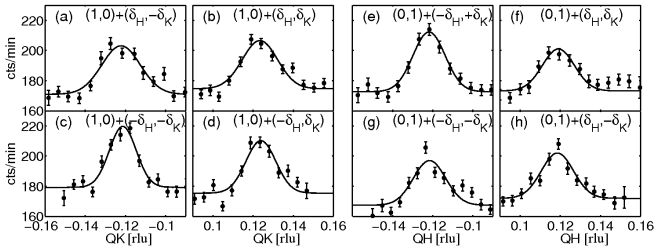

FIG. 3. (a-h) Rocking curve scans through the IC AFM peaks of LSCO+O $x = 0.09$. All lines represent Gaussian fits.

We summarise our results of LSCO+O through a range of Sr dopings to conclude that superoxygenation facilitates the same type of long-range m-AFM order, with same periodicity $\delta \sim 1/8$, moment and transition temperature $T_N = 39(3)$ K within errors. This is in contrast to oxygen stoichiometric LSCO [19, 21, 28]. Furthermore, the magnetic transition temperatures of the studied LSCO+O crystals are the same within errors whether determined using the local μSR probe or bulk-sensitive neutron scattering. This is also in contrast to oxygen stoichiometric LSCO where the transition temperature as observed by μSR is significantly lower than the one observed by neutron scattering due to gradual freezing of the moments [36]. These observations are evidence of the existence of a single and long-range ordered m-AFM phase thoughout the Sr doping range $0.04 \leq x \leq 0.09$ in LSCO+O which is similar to the striped systems LBCO [14, 32] and LNSCO [15, 16, 37, 38]. Since our LSCO+O crystals stay orthorhombic at low temperatures, the stripe-like magnetic order is not pinned by the strong ordering field of the low temperature tetragonal (LTT) phase as in LBCO and LNSCO[14, 15]. However, the commensurate nature of the ordering still implies a strong coupling to the lattice. We expect that the difference here is that since LSCO+O has a weaker, random disordering field from the Sr dopants it also does not require the stronger lattice ordering field associated with the LTT phase. This picture is consistent with our observation that the LSCO+O sample with the highest Sr content $x = 0.09$ has slightly reduced magnetic correlation length.

Regarding the superconducting phase of LSCO+O, the transition temperature $T_c = 39(1)$ K is the same within errors and coinciding with the magnetic transition temperature for all samples in contrast to $T_c \propto x$ in oxygen-stoichiometric LSCO [19]. T_c is also not suppressed as in the anomalous 1/8 state of LNSCO [39] and LBCO [40] suggesting phase separation rather than competition between the two phases in the same areas of the sample. Furthermore the penetration depth is similar in the superoxygenated system thoughout the investigated Sr range and has value corresponding to that of optimally doped LSCO. This is in contrast to oxygen stoichiometric LSCO where the penetration depths for superconducting samples increase with x [41]. The similarity of the temperature dependence of the relaxation rate in LSCO+O indicates that the superconducting gap symmetry is similar thoughout the Sr doping range.

These observations prove that a long-range electronic phase separation occurs in LSCO+O between a 1/8 stripe-like magnetic phase and a superconducting phase which is similar to optimally doped LSCO. A recent report on pressure studies of LBCO [42] has μSR and magnetisation data similar to our earlier work [11] revealing phase separation between stripe-like magnetism and superconductivity. Despite these striking similarilies between LSCO+O and pressurised LBCO, the latter seems to favor an underdoped, reduced T_c superconducting phase perhaps by depinning the charge order [43]. This differs from the superoxygenated samples we describe here where the separate phases appear to have different effective charge densities.

We thank Brian M. Andersen for helpful discussions. This work was supported by the Danish Agency for Science Technology and Innovation under the Framework Programme on Superconductivity and the Danish Research Council FNU through the instrument center DANSCATT. Work at the University of Connecticut was supported by the U.S. Department of Energy under Contract No. DE-FG02-00ER45801. This work is based on experiments performed partly at the Institut Laue-Langevin, Grenoble, France and partly atthe Swiss spallation neutron source SINQ, Paul Scherrer Institute, Villigen, Switzerland.

[1] E. Dagotto, Science **309**, 257 (2005).
[2] G. Alvarez, M. Mayr, A. Moreo, and E. Dagotto, Phys. Rev B **71**, 014514 (2005).
[3] S. A. Kivelson, I. P. Bindloss, E. Fradkin, V. Oganesyan, J. M. Tranquada, A. Kapitulnik, and C. Howald, Rev. Mod. Phys. **75**, 1201 (2003).
[4] H. Takagi, T. Ido, S. Ishibashi, M. Uota, S. Uchida, and Y. Tokura, Phys. Rev. B **40**, 2254 (1989).
[5] A. Wattiaux, J.-C. Park, J.-C. Grenier, and M. Pouchard, C. R. Acad. Sci. Paris **310**, 1047 (1990).
[6] F. Chou, D. Johnston, S.-W. Cheong, and P. Canfield, Physica C **216**, 66 (1993).
[7] X. Xiong, P. Wochner, S. C. Moss, Y. Cao, K. Koga, and M. Fujita, Phys. Rev. Lett. **76**, 2997 (1996).
[8] B. O. Wells, R. J. Birgeneau, F. C. Chou, Y. Endoh, D. C. Johnston, M. A. Kastner, Y. S. Lee, G. Shirane, and J. M. Tranquada, Z. Phys. B **100**, 535 (1996).
[9] Y. S. Lee, F. C. Chou, A. Tewary, M. A. Kastner, S. H. Lee, and R. J. Birgeneau, Phys. Rev. B **69**, 020502 (2004).
[10] M. Fratini, N. Poccia, A. Ricci, G. Campi, M. Burghammer, G. Aeppli, and A. Bianconi, Nature **466**, 841 (2010).
[11] H. E. Mohottala, B. O. Wells, J. I. Budnick, W. A. Hines, C. Niedermayer, L. Udby, C. Bernhard, A. R. Moodenbaugh, and F. C. Chou, Nature Mat. **5**, 377 (2006).
[12] H. E. Mohottala, B. O. Wells, J. I. Budnick, W. A. Hines, C. Niedermayer, and F. C. Chou, Phys. Rev. B **78**, 064504 (2008).
[13] B. Nachumi *et al.*, Phys. Rev. B **58**, 8760 (1998).
[14] M. Fujita, H. Goka, K. Yamada, J. M. Tranquada, and L. P. Regnault, Phys. Rev. B **70**, 104517 (2004).
[15] J. M. Tranquada, B. J. Sternlieb, J. D. Axe, Y. Nakamura, and S. Uchida, Nature **375**, 561 (1995).
[16] N. B. Christensen, H. M. Rønnow, J. Mesot, R. A. Ewings, N. Momono, M. Oda, M. Ido, M. Enderle, D. F. McMorrow, and A. T. Boothroyd, Phys. Rev. Lett. **98**, 197003 (2007).
[17] L. Udby, N. H. Andersen, F. C. Chou, N. B. Christensen, S. B. Emery, K. Lefmann, J. W. Lynn, H. E. Mohottala, C. Niedermayer, and B. O. Wells, Phys. Rev. B **80**, 014505 (2009).
[18] See Supplemental Material [URL by publisher].
[19] K. Yamada *et al.*, Phys. Rev. B **57**, 6165 (1998).
[20] M. Fujita, K. Yamada, H. Hiraka, P. M. Gehring, S. H. Lee, S. Wakimoto, and G. Shirane, Phys. Rev. B **65**, 064505 (2002).
[21] S. Wakimoto *et al.*, Phys. Rev. B **61**, 3699 (2000).
[22] M. Matsuda, M. Fujita, K. Yamada, R. J. Birgeneau, M. A. Kastner, H. Hiraka, Y. Endoh, S. Wakimoto, and G. Shirane, Phys. Rev. B **62**, 9148 (2000).
[23] L. Udby, P. K. Willendrup, E. Knudsen, C. Niedermayer, U. Filges, N. B. Christensen, E. Farhi, B. O. Wells, and K. Lefmann, Nucl. Instr. Meth. A **634**, 138 (2011).
[24] Y. S. Lee, R. J. Birgeneau, M. A. Kastner, Y. Endoh, S. Wakimoto, K. Yamada, R. W. Erwin, S. H. Lee, and G. Shirane, Phys. Rev. B **60**, 3643 (1999).
[25] B. Khaykovich, Y. S. Lee, R. W. Erwin, S.-H. Lee, S. Wakimoto, K. J. Thomas, M. A. Kastner, and R. J. Birgeneau, Phys. Rev. B **66**, 014528 (2002).
[26] We have too few points in the ENS data to fit a proper T_N for the small $x = 0.04$ crystal, but $T_N \sim 40$K is consistent with the μSR data as discussed later in the text.
[27] S. Wakimoto *et al.*, Phys. Rev. B **60**, R769 (1999).
[28] K. Hirota, Physica C **357-360**, 61 (2001).
[29] E. J. Ansaldo, J. H. Brewer, T. M. Riseman, J. E. Schirber, E. L. Venturini, B. Morosin, D. S. Ginley, and B. Sternlieb, Phys. Rev B **40**, 2555 (1989).
[30] Y. J. Uemura *et al.*, Phys. Rev. B **38**, 909 (1988).
[31] J. E. Sonier *et al.*, Phys. Rev. Lett. **72**, 744 (1994).
[32] M. Fujita, Physica C **481**, 23 (2012).
[33] S. Shamoto, M. Sato, J. M. Tranquada, B. J. Sternlieb, and G. Shirane, Phys. Rev. B **48**, 13817 (1993).
[34] D. Vaknin, S. K. Sinha, D. E. Moncton, D. C. Johnston, J. M. Newsam, C. R. Safinya, and H. E. King, Phys. Rev. Lett. **58**, 2802 (1987).
[35] J. M. Tranquada, J. D. Axe, N. Ichikawa, Y. Nakamura, S. Uchida, and B. Nachumi, Phys. Rev. B **54**, 7489 (1996).
[36] M.-H. Julien, Physica. B **329-333**, 693 (2003).
[37] J. Chang *et al.*, Phys. Rev. B **78**, 104525 (2008).
[38] J. Wen, Z. Xu, G. Xu, J. M. Tranquada, G. Gu, S. Chang, and H. J. Kang, Phys. Rev. B **78**, 212506 (2008).
[39] M. K. Crawford, R. L. Harlow, E. M. McCarron, W. E. Farneth, J. D. Axe, H. Chou, and Q. Huang, Phy. Rev. B **44**, 7749 (1991).
[40] A. R. Moodenbaugh, Y. Xu, M. Suenaga, T. J. Folkerts, and R. N. Shelton, Phys. Pev B **38**, 4596 (19988).
[41] Y. J. Uemura *et al.*, Phys. Rev. Lett. **62**, 2317 (1989).
[42] Z. Guguchia, A. Maisuradze, G. Ghambashidze, R. Khasanov, A. Shengelaya, and H. Keller, *arXiv:1303.3865v1* (2013).
[43] M. Hücker, M. v. Zimmermann, M. Debessai, J. S. Schilling, J. M. Tranquada, and G. D. Gu, Phys. Rev Lett. **104**, 057004 (2010).

DRAFT to be submitted

Interplay of structure and magnetism in Hydrated Cobalt salts studied by DFT

Jacob Larsen[a,b], Steen Lysgaard[c], Niels Bech Christensen[a], Tejs Vegge[c]

[a]Department of Physics, Technical University of Denmark, DK-2800 Kgs. Lyngby
[b]Laboratory for Neutron Scattering, Paul Scherrer Institut, CH-5232 Villigen
[c]Department of Energy Conversion and Storage, Technical University of Denmark, Frederiksborgvej 399 DK-4000 Roskilde

Abstract Using density functional theory we present a comparison of the ground state crystal structures of $CoCl_2{\cdot}2H_2O$ and $CoCl_2{\cdot}2NH_3$, which are candidate materials for observing the quantum criticality expected for systems of exchange-coupled Ising spins subjected to a transverse magnetic field. We employ a simple model for the dependence of magnetic superexchange interactions on bond lengths and angles, and use this to predict the change in the critical field expected in $CoCl_2{\cdot}2NH_3$ relative to the experimentally known value for $CoCl_2{\cdot}2H_2O$. Our model indicates that $CoCl_2{\cdot}2NH_3$ should have a critical field smaller than that of $CoCl_2{\cdot}2H_2O$ by approximately 2 Tesla.

1 Introduction

Density functional theory (DFT) is a highly successful numerical technique when dealing with the electron structure of solids [1,2]. With the recent introduction of hybrid functionals, and the inclusion of the non-local, long-range Van der Waals interaction into the framework of DFT, chemical accuracy has been achieved in systems such as metal ammines and hydrates. For example, with their prospects as hydrogen storage materials in mind, the stable structural phases were recently investigated in such systems, see e.g. [3].

Once consistency between experiments and simulations has been firmly established, one major advantage of DFT is that large-scale screening studies can be performed to search for the optimal compound for a given application within a well-defined class of materials. For a recent review see Ref [4].

Here we address whether or not a simple approach based on DFT calculations might be a useful and fast screening procedure, when searching for magnetic materials with similar structural features and magnetic ground state properties, but characterized by different energy scales.

Quantum phase transitions (QPT's) are phase transitions taking place at T=0 K, driven by e.g. applied pressure, changes in chemical composition through doping, or applied magnetic field. The physical properties near QPTs are governed by quantum fluctuations, but the quantum critical point exerts its influence at finite temperatures too [5].

Possibly the simplest example of a QPT is realized in the one dimensional transverse field Ising model described by the spin Hamiltonian $H = \Sigma_{<ij>} J S_i^z S_j^z + \Sigma_i B^x S_i^x$ [5], where the first summation runs over pairs of nearest neighbor Ising spins, coupled by the exchange interaction strength J. The second sum represents the Zeeman energy in an external field applied along the x-axis. In zero applied field, $B^x = 0$, all spins are oriented along the easy z-axis. Qualitatively, the application of a transverse field induces quantum tunneling between the two single-ion spin states $S_i^z = 1/2$ and $S_i^z = -1/2$. At a sufficiently high critical field, $B^x_c = J$, magnetic orderdisappears altogether, and the system enters magnetically disordered, but quantum mechanically correlated phase.

Experimentally, the quantum phase transition predicted for the transverse field Ising model, has been studied in the dipolar-coupled ferromagnet $LiHoF_4$ [6] and in $CoNb_2O_6$ [7]. From the perspective of magnetism, the latter material consists of chains of ferromagnetically coupled Co^{2+} ions, running along the crystallographic c-axis. The ferromagnetic chains are coupled to neighboring chains by weak antiferromagnetic interactions, leading to overall antiferromagnetic order below T_N=2.95 K [7].

Neutron scattering has revealed a surprisingly rich magnetic excitation spectrum in $CoNb_2O_6$. In particular, just below the critical field B_c=5.5T, and in agreement with theoretical predictions, the highest-order mathematical symmetry group, E_8, is reflected in the magnetic excitation spectrum [7]. The observations reported for $CoNb_2O_6$ call for further experimental investigations of similar materials, focusing, in particular, on identifying the key characteristic magnetic properties needed to promote exotic excitation spectra.

One such candidate material is the hydrated salt $CoCl_2 \cdot 2H_2O$ [8]. Its monoclinic crystal structure is shown in Figure 1. The combined effects of the crystal field and a sizeable spin-orbit coupling in $CoCl_2 \cdot 2H_2O$ result in a strongly uniaxial magnetic ground state with an anisotropic g-tensor. Below T_N = 17.2K the magnetic moments of the Co^{2+} ions order along the crystallographic b-direction and form a three dimensional magnetic ground state of ferromagnetic chains running along the crystallographic c-axis with an antiferromagnetic superexchange interchain couplings along the [110] direction [9]. Mollymoto and coworkers showed that for magnetic fields applied transverse to the easy b-axis, i.e. in the ac-plane, the magnetization of $CoCl_2 \cdot 2H_2O$ (after correction for admixing of ground and excited Kramers doublets) depends linearly on the field, H, with the extremal critical fields $\mu_0 H_{c,min}$ = 16.2± 0. 5T and $\mu_0 H_{c,max}$ = 37.0±1.5 T found for H along the two Co-O bond directions [10]. Above these fields, the system can be described as a fully polarized paramagnet. Starting form the low-temperatures commensurate antiferromagnetic state and increasing the transverse magnetic field towards the critical fields given above, the spin wave excitation spectrum is expected to soften gradually, with the (Ising) gap in the excitation spectrum going to zero at H_c.

Neutron scattering is the ideal tool to study this quantum phase transitions as the spin excitations can be studied over large portions of momentum and energy transfer. Indeed, neutron scattering has been used to study the zero-field spin waves in $CoCl_2 \cdot 2H_2O$ [11,12,13]. However, even reaching the smallest transverse critical field, $\mu_0 H_{c,min}$=16.2T, of $CoCl_2 \cdot 2H_2O$ is a challenge since sample environment suites at most neutron scattering facilities are limited to fields smaller than 15T. There is therefore a case for searching for materials with the same salient structural and magnetic features as $CoCl_2 \cdot 2H_2O$, but with smaller critical fields.

Combining DFT with simple model considerations for the dependence of the exchange interactions on bond-angles and bond-lengths, this paper estimates how the critical field of $CoCl_2 \cdot 2H_2O$ is changed by replacing all H_2O molecules by NH_3.

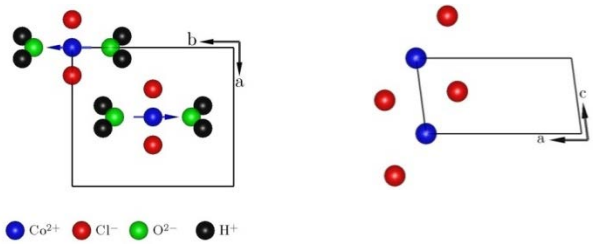

Figure 1: Illustration of the monoclinic crystal structyre of $CoCl_2 \cdot 2H_2O$ as seen along the c* (left) and b directions, respectively. The blue arrows represent the spins of Co^{2+} ions, that are oriented along the easy b-axis direction for temperatures lower than T_N=17.2K [9]

2 Computational methods

The DFT calculations for $CoCl_2 \cdot 2NH_3$ were initialized using the structural information available for $CoCl_2.2H_2O$ [8] shown in table I. H_2O was exchanged by NH_3 by placing the Nitrogen atom at the 4g sites. Subsequently, the atomic positions were relaxed to determine the structure and thermodynamic properties of the emergent amine phase.

The calculations were performed in the ASE framework [14] using the GPAW code [15,16], which a real-space projector-augmented wave (PAW) method [17,18]. We use a vdW-DF [19] exchange correlation functional that accounts for the non-local van der Waals forces, which are essential in weakly bound systems as the metal halide hydrates and amines containing a large amount of hydrogen and which have long bond-lengths. All reported structures were tested for convergence of the energy for both *k*-points and grid spacing. The Brillouin-zone was sampled using a Monkhorste-Pack grid [20] with 6 *k*-points, the grid spacing was 0.18Å and all initial structures were allowed to relax the atomic coordinates by a quasi-Newton type optimization algorithm [21] using the calculated DFT forces. All calculations were performed both with and without spin polarization.

The energies of H_2O(g) and NH_3(g) were calculated by placing a molecule in a cube with a side length of 8Å, removing the periodic boundary conditions and using the grid spacing described above. Finite enthalpy and entropy values are calculated by adding the calculated zero point energy and finite temperature corrections. For solids, the correction is found by summation of the mean energies of the vibrational frequencies calculated in the harmonic approximation.

3 Results

3.1 $CoCl_2 \cdot 2H_2O$

Due to rotational ordering of the H_2O spacer molecule about Co-O bond direction, which creates a doubling of

the unit cell along the [001] direction, the crystal structure of $CoCl_2 \cdot 2H_2O$ belongs to the monoclinic space group #12 ($C_{2/m}$) with room temperature lattice constants a=7.25Å, b=5.58Å and c=3.55Å and the monoclinic angle β_m=97.5 degrees [8]

The relaxed atomic positions are shown in table I. The crystal structure of $CoCl_2 \cdot 2H_2O$ stabilizes two inequivalent Co-Cl bond lengths, Co-Cl_x and Co-Cl_y, coinciding with the magnetic easy ($H_{c,min}$) and hard ($H_{c,max}$) transverse axes, respectively. However, for computational simplicity, our calculations assume an orthorhombic unit cell. This brings the short and long Co-Cl bond lengths closer together.

Atom	Wyckoff	x/a	y/b	z/c
Co	2a	0	0	0
Cl	4i	1.730	0.191	1.895
		-1.722	0.202	-1.893
O	4g	-0.238	2.099	0.063
		0.255	-2.100	-0.060
H	8j	0.486	2.657	0.430
		-0.664	2.621	-0.654
		0.684	-2.614	0.661
		-0.461	-2.668	-0.426

Table I: Relaxed atomic position for one chemical formula unit of $CoCl_2 \cdot 2H_2O$.

The calculated bond lengths, listed in table II, are all slightly smaller than the literature values [8]. In particular, the interchain Cl-Cl bond is reduced by 11%. The ionic radii of Co (0.698Å) and Cl (1.810Å) yield a bond length comparable to our results [22]. The ordered magnetic moment of the relaxed $CoCl_2 \cdot 2H_2O$ structure is found to be $\mu_{DFT}=2.52\mu_B$/Co [9]

3.2 $CoCl_2 \cdot 3NH_3$

The structure calculated for $CoCl_2.2NH_3$ displays an increase of all bond lengths relative to the $CoCl_2.2H_2O$ structure described in the previous section, see table 2. Surprisingly, the ordered moment computed for the relaxed $CoCl_2.2NH_3$ structure amounts to only $\mu_{DFT}=0.92\mu_B$/Co, a value much lower than computed for $CoCl_2.2H_2O$ and also much smaller than the value $\mu_{exp}=3.60(5)\ \mu_B$/Co found experimentally [10].

3.3 Chemical binding energies

As a validation of our approach, we calculate the chemical binding energies of water and ammonia relative to the empty salt. The binding energy of water is defined as

(1) $$\Delta E_{binding} = E_{CoCl2.2H2O} - (E_{CoCl2(s)} + 2 \times E_{H2O(g)}),$$

with an equivalent expression for ammonia. The calculations were performed per chemical formula unit using the van der Waals functional. We obtained binding energies of 82.44 kJ/mole for H_2O and 78.18 kJ/mole for NH_3. These values are in good agreement with those previously determined for similar systems.

	Bond length [Å] CoCl2.2H2O ([8.])	Bond length [Å] CoCl2.2NH3 ([23])	Relative difference
Co-Co(inter)	5.61 (5.62)	5.71 (5.86)	+1.7% (+4.3)
Co-Co(intra)	3.59 (3.55)	3.69 (3.71)	+2.6% (+4.5)
Co-Co(a)	7.27 (7.26)	7.59 (7.99)	+4.4% (+10.1)
Co-Cl(long)	2.57 (2.63)	2.56 (2.60)	-0.4% (-1.1)
Co-Cl(short)	2.42 (2.33)	2.48 (2.48)	+2.5% (+6.4)
Cl-Cl(inter)	3.89 (4.31)	4.27 (4.03)	+9.8% (-6.5)
Cl-Cl(a)	3.85 (3.84)	4.18 (4.53)	+8.6% (+18.0)

Table II: A comparison between bond lengths calculated for $CoCl_2 \cdot 2H_2O$ and $CoCl_2.2NH_3$ as described in the text. In the columns quoting calculated bond lengths for $CoCl_2 \cdot 2H_2O$ and $CoCl_2.2NH_3$ the experimental values determined in Refs [8] and [23], respectively, are given. The final column gives the relative changes in calculated bond lengths with experimental differences in parentheses.

4 Dependence of the superexchange interaction on bond lengths and angles.

As is well-known, superexchange interaction is an indirect exchange between two non-neighbor magnetic ions. The origin of superexchange is the kinetic energy gain related to electrons making virtual jumps to neighboring sites. Assuming that the Coulomb energy cost of electrons hopping to neighboring sites is U and that the kinetic energy is t, the superexchange interaction J is proportional to t^2/U. The hopping matrix element t generally depends directly on the interatomic distance, r, as $r^{-\alpha}$. For *d*-orbital wavefunctions, it has been shown that $\alpha = 5$ [24]. Thus, we expect J to depend on r as $r^{-\beta}$ where $\beta=2\alpha$ is the equal to 10. In experiments, however, values of β have been reported in the interval $10 \le \beta \le 12$ [25, 26].

The angle between the interacting orbitals is also known to have a significant effect on the nature of the resulting exchange interaction. This is usually expressed through the semi empirical Goodenough-Kanamori-Anderson rules [27,28,29]. The ferromagnetially aligned cobalt ions that are arranged along the c-axis in the $CoCl_2$ salts considered here, interact via chlorine ions configurations where the bonding angle is close to 90°. Following [30,31] we will assume the following simple form of for the dependence of J on the bond length, r, and the Cl-Co-Cl bond angle θ

(2) $$J(r) = J_0 r^{-\beta} \cos^2(\theta)$$

The $\cos^2(\theta)$ dependence is a simplification, but experimental investigation on e.g cuprate materials [31] indicates a similar behavior.

5 Critical field calculations

The crystal field splitting of $CoCl_2.2H_2O$, including the spin orbit coupling, result in a double degenerate ground state with effective S=½ and anisotropic g values i.e $g^{\alpha\alpha}\mu_B S$ = 1.68, 0.94 and 3.39 $\mu_B/Co2^+$ for α = x y and z respectively [10]. Following [10] the effective Hamiltonian, H_{eff}, for this system in a transverse field, say the α direction, assumes the form

$$H_{eff} = -2\sum_i\sum_\delta \mathbf{S}_i\mathbf{J}_\delta\mathbf{S}_{i+\delta} - \mu_B\sum_i S^\alpha g^{\alpha\alpha}H^\alpha \quad (3)$$

where δ = 0,1,2,3,... represent interactions between Co^{2+} ions listed in order of their magnitude. For each of these the exchange tensor is given by

$$\mathbf{J}_\delta = \begin{pmatrix} J_\delta^{xx} & 0 & 0 \\ 0 & J_\delta^{yy} & 0 \\ 0 & 0 & J_\delta^{zz} \end{pmatrix}. \quad (4)$$

The values for J_c^{xx}, J_c^{yy} and J_c^{zz} can be determined by inelastic neutron scattering. Denoting the easy axis (the crystallographic *b* direction in the case of $CoCl_2.2H_2O$) by z, the critical field along the transverse α direction, was derived by Mollymoto et al [12]

$$\mu_0 H_c = \frac{\left(J_0^{zz} - J_0^{\alpha\alpha} + 2(|J_1^{zz}| + |J_0^{\alpha\alpha}|)\right)}{g^{\alpha\alpha}\mu_B S} \quad (5)$$

where we have only included the δ = 0 and 1 terms because since further neighbor interactions are very small, and hence will not contribute much to the value of H_c.

Using equation (2) and the DFT results in table II, we may estimate by how much the relevant exchange interactions are reduced in $CoCl_2.2NH_3$ compared with $CoCl_2.2H_2O$. Employing equation (5) we can then determine the expected change in critical field of $CoCl_2.2NH_3$ relative to $CoCl_2.2H_2O$. Normalizing the calculated critical fields to the experimental values $\mu_0H_{c,min}$ = 16.2T and $\mu_0H_{c,max}$ = 37.0T for $CoCl_2.2D_2O$, we obtain the results summarized in tabel IV. For the minimum critical transverse field, we obtain values in the range 13.9 to 14.2 T depending on the value used for the exponent β in equation (2).

$\mu_0H_{c,min}$ β=10	$\mu_0H_{c,min}$ β=12	$\mu_0H_{c,max}$ β=10	$\mu_0H_{c,max}$ β=12
14.2T	13.9T	32.2T	31.5T

Table IV: Computed minimum and maximum critical transverse fields $\mu_0H_{c,min}$ and $\mu_0H_{c,max}$, respectively, determined from the relaxed crystal structures of CoCl2.2D2O and CoCl2.NH3. Both fields are calculated for β=10 and β=12.

6 Conclusions

We have performed DFT calculations of the ground state crystal structures and ordered moments of $CoCl_2.2H_2O$ and $CoCl_2.NH_3$. The calculated bond lengths for $CoCl_2.2H_2O$ differ only slightly from the literature values. The discrepancies are mainly due to the use of an orthorhombic unit cell in the calculations, instead of the experimentally determined monoclinic structure. We find that both the inter- and intra-chain bond lengths increase when water is exchanged by ammonia. The consequence of this increase is that the critical field, $\mu_0H_{c,min}$, of the transverse field Ising quantum phase transition is expected to be reduced from 16.2T to a value in the range 13.9-14.2T. The reduced value of H_c is far better suited for neutron scattering experiments and $CoCl_2.2NH_3$ might therefore be better suited for studies of transverse field Ising quantum criticality than $CoCl_2.2H_2O$.

References

[1] P. Hohenberg and W. Kohn. Physical Review 1964;136;3B:864-71
[2] W. Kohn and L. J. Sham. Physical Review 1965;140;4A:1133-8
[3] S. Lysgaard et al. International journal of hydrogen energy, 37, 18927, 2012
[4] S. Curtarolo et al, Nature Materials **12**, 191 (2013)
[5] S. Sachdev. *Quantum Phase Transitions*. Cambridge University Press
[6] H. M. Rønnow et al. Science 2005;308:389-92
[7] R. Coldea et al., Science 2010;327:177-80
[8] B. Morosin and Graeber Atca. Cryst., 16, 1176 (1963)
[9] D. E. Cox, B. C. Frazer and G. Shirane, Phys. Lett. **17**, 103 (1965)
[10] H. Mollymoto et al. , J. Phys. Soc Japan 1980;49;1:108-14
[11] J. K. Kjems et al, Phys Rev. B. **12**, 5190 (1975)
[12] N. B. Christensen et al, Physica B **276**, 784 (2000)
[13] W. Montfrooij et al, Phys. Rev. B **64**, 134426 (2001)
[14] S. R. Bahn and K. W. Jacobsen. An object-oriented scripting interface to a legacy electronic structure code. Computing in Science & Engineering 2002;4(3):56-66.

[15] J. J. Mortensen. Real-space grid implementation of the projector augmented wave method. Phys. Rev. B. 2005;71:035109
[16] J. Enkovaara et al. Electronic structure calculations with GPAW: a real-space implementation of the projector augmented-wave method. J. Phys: Condensed Matter. 2010;22;25:253202
[17] P. E. Blöchl. Projector augmentation-wave method. Phys. Rev. B. 1994;50;24:17953-79
[18] P. E. Blöchl. Projector augmented wave method: *ab initio* molecular dynamics with full wave functions. Bull. Mater. Sci. 2003;26;1:33-41
[19] M. Dion et al. Van der Waals Density Functional for General Geometries. Phys. Rev. Lett. 2004;92;24:246401-4
[20] H. J. Monkhorst and J. D. Park. Special points for Brillouin-zone integrations. Phys. Rev. B. 1976;13;12:5188-92
[21] P. Maragakis et al. Adaptive nudged elastic band approach for transition state calculation. J. Chem. Phys. 2002;117;10:4651-8
[22] R. D. Shannon Revised effective ionic radii and systematic studies of interatomic distances in halides and chalcogenides. Acta Cryst. A. 1976;32:751-67
[23] A. Leineweber et al. $Co(NH_3)_2Cl_2$ and $Co(ND_3)_2Cl_2$ Order-Disorder Behaviour of N(H,D)3 and Antiferromagnetic Structure. Z. Anorg Allg. Chem 2001:627:2063-9
[24]Dávila1992: Phys. Rev. B., 46, 10432 1992
[25]DeJongh1975: Physica B., 79, 568, 1975
[26]Sawatzky1976: JMMM, 3, 37, 1976
[27]Buettner1979: The Journal of Physical Chemistry, 83, 2387, 1979
[28]Goodenough1955: Phys. Rev., 100, 564, 1955
[29]Goodenough1958: J. Phys. Chem. Solids, 6, 287, 1958
[30]Kanamori1959: J. Phys. Chem. Solids, 10, 87, 1959
[31]Shimizu2003: Physica B., 329-333, 765, 2003